

Nonlocal correlations between freely propagating pairs of atoms

Dongki Shin

A thesis submitted for the degree of
Doctor of Philosophy of
The Australian National University

December 2020

© Dongki Shin 2020

Except where otherwise indicated, this thesis is my own original work.

Dongki Shin
25 December 2020

In memory of my grandmother, who called me Dr. Shin when I was little.

Acknowledgments

I am grateful to have so many nice people around me. These people have all directly or indirectly helped to make this PhD possible.

I would first like to thank my supervisors – Andrew Truscott, Sean Hodgman, and Ken Baldwin – for providing expert guidance. My thanks go to Ken for the various support and opportunities I received throughout my PhD. Indeed my PhD journey started with Ken, when near the end of my summer internship with the ANU group, Ken asked whether I was interested in doing a PhD in the group, and subsequently helped me to apply for the Australian government scholarship. My thanks are to Sean, for his door has always been open for a conversation, and I am thankful to be able to rely on his sharp intuition and opinions, which seems to have grown into a habit. His whiteboard would probably still be stained with layers of our scribbled thoughts and plans of experiments. I am especially grateful to Andrew, for leading many researchers at ANU before my time to build the world class Helium BEC machine, for welcoming me into the team more than five years go, and all the while fostering each member’s unique creativity and research interest. Thanks for giving me the keys to the BEC machine, it looked so mystifying when I started, and (in hindsight) your recommendation for a generous amount of elbow grease. When the magic surrounding the machine gradually faded, I was mesmerised to uncover the physics beneath.

Two other people who have wrangled the subtleties in this thesis are my lab partners and treasured friends, Bryce Henson and Jacob Ross. In discussing all the ideas and problems during my PhD, Bryce and Jake has never failed to shine in their passion for scientific method and knowledge. I could not have asked for more admirable companions in this journey. So here is to you guys! I am also appreciative of the company of other lab members and colleagues at the Research School of Physics: Kieran, Roman , Tamara, Danny, Abbas, Mohammed, Rohit, Inseok, Yonghwan, Thomas, Sam, and other unmentioned ex-AMPL (Atomic and Molecular Physics Laboratories) staff and students. Not only were they willing to share their unique set of skills (and tools), they have made the Physics school and Canberra an enjoyable and social place during my PhD.

My last thanks for the team at ANU goes to the talented technicians – Colin Dedman (electron whisperer) and Ross Tranter (mechanical wizard) – whose fingerprints are all over the experimental apparatus! Colin and Ross were never hesitant to explain the complex machines they built, which made their labs always an exciting place to stop by.

Outside of physics, many friends and family have supported me in incredible ways. My thanks to friends in Canberra, who have shared many embarrassing mem-

ories usually made over a couple of drinks too many. For letting me look after their loving Labrador Bronte, making Canberra a home for me, and treating me as their family, I am especially indebted to the Farleys for my time in Canberra.

To friends and family back in New Zealand, I would like to send my warm thanks for their love and support from home. I am especially grateful to my parents, Boontak and Yongheon, for encouraging and supporting me to follow my dreams ever since I was young. The person who is most excited about this thesis is probably my realist fiancé Kate. My heartfelt gratitude goes to you for your patience over the five years we spent apart, encouragement to overcome obstacles, and *dak doritang*¹ for the soul.

¹Dak doritang is a traditional Korean chicken stew, and is my favourite Korean dish.

Abstract

Since the formulation of quantum theory in the early twentieth century, its counter-intuitive description of nature has shifted dramatically from being considered its weakness, to opening up vibrant fields of research and enabling classically untenable technologies. Perhaps the most striking aspect of quantum mechanics is exhibited in the infamous Einstein-Podolsky-Rosen (EPR) paradox, as the violation of locality from distant entangled particles. Due to many stringent technical requirements in the test of quantum nonlocality however, experimentalists have only recently demonstrated the nonlocal nature of quantum mechanics. Such well-controlled physical systems were few just a decade ago. This thesis contributes to the exponentially growing diversity of physical systems exhibiting quantum nonlocality, specifically between freely propagating massive particles, realised from an elastic collision of two helium atoms. This work investigates the entanglement between internal states of the scattered atom pairs, which opens up many exciting avenues to studying entanglement in motional variables of massive particles as well, since both types of entanglement are prepared in a collision.

The thesis is composed of three projects, starting with an upgrade to the existing experimental apparatus to more stably produce ultracold gases of metastable helium. Massive particles such as atoms exhibit a wave-like behaviour at ultracold temperatures, typically requiring micro-Kelvin temperatures for a dilute gas. Laser cooling and trapping techniques in ultrahigh vacuum chambers are the workhorse of achieving such temperatures in atomic gases. The master laser system for the experimental apparatus was designed on an external-cavity diode laser, and is central to preparing Bose-Einstein condensates (BEC) of the dilute gas of metastable helium.

BECs exhibit coherence in interference experiments which earn the term macroscopic matter-waves. As such, replicating classical optics phenomena with matter-waves has been of great interest since the first experimental realisation and manipulation of BECs. Here we study quantum correlations arising from a collision of BECs. In the particle picture counter-propagating pairs of atoms scatter, and quantum mechanically these pairs are expected to be entangled in their momentum and spin from conservation rules. The spins of spatially separate pairs are experimentally verified to be entangled, and exhibit EPR's "spooky" nonlocal correlations.

Finally, we demonstrate the spatially separated entanglement in the freely propagating pairs of atoms in an application to quantum sensing. In this task the magnetic field gradient along the pairs' trajectories causes the atomic pair's correlation to oscillate. The pairwise entanglement enables the measurement to decouple from a common noise source, such as spatial uniform fluctuations in the magnetic field, and surpass the classical limit of measurement sensitivity.

x

List of publications

- *Ghost imaging with atoms*
R. I. Khakimov, B. M. Henson, D. K. Shin, S. S. Hodgman, R. G. Dall, K. G. H. Baldwin, A. G. Truscott
Nature 540100 (2016)
- *Widely tunable, narrow linewidth external-cavity gain chip laser for spectroscopy between $1.0 - 1.1 \mu m$*
D. K. Shin, B. M. Henson, R I. Khakimov, J. A. Ross, C. J. Dedman, S. S. Hodgman, K. G. H. Baldwin, A. G. Truscott
Optics Express 2427403 (2016)
- *Bogoliubov-Cherenkov radiation in an atom laser*
B. M. Henson, X. Yue, S. S. Hodgman, D. K. Shin, L. A. Smirnov, E. A. Ostrovskaya, X. W. Guan, A. G. Truscott
Physical Review A 97063601 (2018)
- *Approaching the adiabatic timescale with machine learning*
B. M. Henson, D. K. Shin, K. F. Thomas, J. A. Ross, M. R. Hush, S. S. Hodgman, A. G. Truscott
Proceedings of the National Academy of Sciences 11513216–13221 (2018)
- *Bell correlations between spatially separated pairs of atoms*
D. K. Shin, B. M. Henson, S. S. Hodgman, T. Wasak, J. Chwedenczuk, A. G. Truscott
Nature Communications 104447 (2019)
- *Entanglement-based 3D magnetic gradiometry with an ultracold atomic scattering halo*
D. K. Shin, J. A. Ross, B. M. Henson, S. S. Hodgman, A. G. Truscott
New Journal of Physics 22013002 (2020)
- *Direct Measurement of the Forbidden $2^3S_1 \rightarrow 3^3S_1$ Atomic Transition in Helium*
K.F. Thomas, J. A. Ross, B. M. Henson, D. K. Shin, K. G. H. Baldwin, S. S. Hodgman, A. G. Truscott
Physical Review Letters 125013002 (2020)

Contents

Acknowledgments	vii
Abstract	ix
1 Introduction	1
1.1 Overview	3
2 Background	5
2.1 Quantum nonlocality	5
2.1.1 EPR-Bohm paradox	6
2.1.2 Quantum nonlocality and its hierarchy	10
2.1.3 Role of quantum nonlocality in quantum technology	19
2.1.4 Experimental demonstrations	20
2.2 Entanglement via atomic collisions	23
2.2.1 Types of nonclassical atomic ensembles	24
2.2.2 Theory of pairwise entanglement by collision	26
2.2.3 Quantum correlations and nonlocality observed in atomic ensembles	46
2.3 Experimental apparatus	47
2.3.1 Metastable helium	48
2.3.2 He [*] BEC machine	53
2.3.3 Coherent manipulation of momentum and spin of single He [*] atoms	58
2.3.4 Single atom detection	69
3 Master laser system for cooling and trapping metastable helium	73
3.1 Design and operation of the master laser	74
3.1.1 External-cavity laser	74
3.1.2 Laser design	76
3.1.3 Laser system setup	79
3.2 Wavelength tunability	80
3.2.1 Tuning range	80
3.2.2 Fast modulation	81
3.2.3 Thermal sensitivity	83
3.3 Stabilisation to an atomic reference	83
3.3.1 Saturated absorption spectroscopy of He [*]	84
3.3.2 Frequency stabilisation by acousto-optic modulation	86

3.4	Frequency stability	87
3.4.1	Laser linewidth	89
3.4.2	Long-term stability	90
4	Nonlocal spin correlations across pairs of spatially separated atoms	93
4.1	Introduction	93
4.2	Theory of nonlocal correlations in a scattering halo	93
4.2.1	Collision of oppositely spin-polarised BECs	94
4.2.2	Nonlocal correlations in the s-wave scattering halo	95
4.3	Experimental methods	103
4.3.1	Experimental sequence	104
4.3.2	Data analysis	108
4.4	The atomic pair source	112
4.4.1	The s-wave scattering halo	112
4.4.2	Correlated pairs	114
4.5	Coherent control of atomic spin	116
4.6	Experimental observation of quantum nonlocality	124
4.6.1	Symmetrically rotated spin correlation	125
4.6.2	Nonlocal spin correlations	125
4.7	Conclusion	128
5	Entanglement-based 3D magnetic gradiometry with an ultracold atomic scattering halo	131
5.1	Quantum metrology in a nutshell	132
5.1.1	Phase estimation of a single qubit and classically correlated ensembles	132
5.1.2	Quantum enhancement in measurement sensitivity by entanglement	134
5.2	Quantum sensors and quantum magnetic microscopes	135
5.2.1	Atom pairs in a magnetic field	136
5.2.2	The trajectory of atoms in the scattering halo	138
5.3	Entanglement-based 3D magnetic gradiometry	140
5.3.1	Methods and concept	140
5.3.2	Generalised collective spin correlation	143
5.3.3	Scattering angle dependence in pairwise correlations	145
5.3.4	Entanglement-based 3D magnetic gradiometry	145
5.4	3D magnetic field tomography	149
5.4.1	Methods and concept	149
5.4.2	Experimental results	150
5.5	Conclusion	151
6	Conclusions and Outlook	153
6.1	Conclusions	153
6.2	The Bell test and loopholes	153

6.3 Hyperentanglement	154
6.4 A quantum test of general relativity	155
A Theory of stimulated Raman transition	157
B Notes on the ECL	161
B.1 Alignment procedure	161
B.1.1 Positioning the lens in XYZ degree of freedom	161
B.1.2 Aligning the collimation lens	161
B.2 List of parts and instruments	162
C Notes on correlations	165
C.1 Sum uncertainty relation for angular momentum	165
C.2 CHSH Bell inequality	165
C.3 Generalised bipartite correlation coefficient for many-body states	167
C.4 LHV model supports EPR-steering correlation	167
C.5 Combinatorial algorithm for evaluating correlation functions	171
References	175

Introduction

Information has been important to individuals and society throughout history. Technology for storing, transporting, and processing information has developed from ancient tools to the most modern realisation as the manipulation of individual particles in quantum technologies. The translation of quantum mechanics from a fundamental theory of nature into real world applications is widely believed to bring a technological revolution in computing, sensing and communication, to name a few known uses. The main driver of this radical shift lies in the deepest aspect of quantum mechanics which is incompatible with the previously held tenet in classical physics of locality and realism (local realism), called quantum nonlocality. With advances in technology and better understanding of physical systems, experiments have recently been able to put local realism under stringent tests [1].

The first sign of the tension between locality and quantum mechanics (QM) was identified by Einstein, Podolsky and Rosen (EPR) in 1935 [2] with just two particles prepared in a superposition of states perfectly correlated simultaneously in two non-commuting observables. Under the prevailing principle of locality the perfect knowledge of the outcome of the distant counterpart without disturbance from measuring the local particle results in a clear violation of the uncertainty principle for the non-commuting observables concerned. This curious property demonstrated by the EPR pairs was coined by Schrödinger [3] as *entanglement*, whereby one's measurement of their particle is theorised to *steer* that of the distant counterpart. These contradictory interpretations by EPR and Schrödinger remained largely unexplored until Bell in 1964 showed that the notion of locality can be experimentally tested against the prediction of QM [4]. Many experiments soon began to explore the so-called *Bell test*, firstly with pairs of entangled photons emitted from an atomic cascade emission (first by Freedman and Clauser in 1972 [5] and significantly improved by Aspect and co-workers in 1982 [6] using time-varying analysers). Although the experimental results from these early Bell tests seemed to agree with the QM prediction, they were also strictly compatible with local realism, since the experiments were open to various loopholes [7]. For instance, the most simple type of a loophole in Bell tests exists when the individual measurements on the counterparts are not carried out independently, such that the observed pairwise correlations cannot distinguish nonlocal effects from locally propagated influences. In order to overcome this so-called locality loophole, the entangled pair must therefore be ad-

equally spatially separated, while maintaining its coherence and isolated from its environment. This herculean challenge only recently culminated in the loophole-free violation of local realism [8, 9, 10, 11] in support of quantum mechanics, and thereby put a last word to the long standing classical axioms. Such nonlocal correlations cannot be mimicked by any means of classically hidden information and randomness, and are based on the quantum entanglement of a delocalised collection of particles, which forms the basis for a much more complex network of correlations in many-body quantum systems [12]. Therefore, quantum nonlocality currently appears to be a necessary resource in a variety of quantum information technologies [1], including absolutely secure communication [13], quantum teleportation [14], and quantum computation [15]. The foundational mathematical formalism introduced by Bell was recently extended to formulate the nonlocality dismissed in EPR's argument [16], referred to as EPR-steering nonlocality, which introduces an aspect of asymmetry into the correlations. EPR-steering is gaining a lot of interest for its closely related ties into realistic applications of quantum communication [17], in particular when there exists asymmetry of trust in quantum communication networks [18].

This thesis investigates nonlocal correlations between two helium atoms which have undergone a collision and presents the first direct observation of collision induced entanglement between a pair of neutral atoms. From the wave-particle duality in quantum mechanics, massive particles such as atoms can behave wavelike and interfere [19], but to observe such quantum effects they must be extremely well isolated from the environment and prepared close to their ground state. This typically requires the atom to be prepared in a dilute gas, held in an ultrahigh vacuum chamber, and be cooled down to ultracold temperatures around $1\text{ }\mu\text{K}$ [20]. Ultracold temperatures in atomic gases are achieved predominantly by laser cooling and trapping techniques [21], and for the experimental investigation in this thesis we begin with the development of the master laser system for the experimental apparatus. This laser, designed and fabricated in-house, is a central tool we use to prepare an ultracold gas of metastable helium in a quantum state called a Bose-Einstein condensate (BEC).

Collisions of BECs have become a useful method for generating correlated atom pairs [22]. Such collisions basically scatter pairs of atoms into opposite directions by conservation laws as in the classical picture. Quantum mechanically however, each pair will scatter to a superposition of every possible directions, and therefore be entangled in momentum. Although a collision can generate quantum entanglement (one of the most profound concepts in QM) in such a conceptually trivial manner, no direct evidence of this phenomenon has yet been found. Here we experimentally verify that the spins of the atom pairs are entangled while they are spatially separated, and investigate nonlocal correlations in the outcome from a realisation of the EPR paradox.

Historically nonclassical squeezed states of light have received lots of interest in quantum optics [23], and are now applied to laser interferometry for gravitational wave detection [24], where minimising photon shot noise is crucial. Recently nonclassical states of atoms have gained a wide popularity in quantum enhanced sens-

ing [25]. This is due to a myriad of interactions and fundamental physical properties measurable with atoms, including electromagnetic and gravitational fields, as well as enabling the testing of general relativity to quantum mechanical parameter regimes, and the fundamental standard of time keeping. In this regard, correlated atomic pairs provide a unique source for exploring matterwaves experiments in the few particle regime. In the time evolution of the spin correlation between the pairs, as they separated, we made a serendipitous discovery that the entanglement in spin allows a method of measuring the magnetic field gradient with no classical analogy, which is furthermore intrinsically insensitive to common-mode fluctuations of the magnetic field.

1.1 Overview

- Chapter 2 introduces the background material to accompany this thesis. First, the concept of quantum nonlocality is formalised and the hierarchical structure of nonlocality is explored with a concrete example with two qubits. Then, nonclassical states of atomic ensembles are discussed, based on the entangling mechanism in atom-atom collisions, and it is found that the scattering product in a collision of ultracold gases are just like pairs of qubits with nonlocal correlations. Lastly, an overview is given of the main experimental apparatus, the metastable helium Bose-Einstein condensate machine, and the crucial tools required in the investigation of quantum correlations, including the coherent control of atoms and the single-atom detector.
- Chapter 3 presents the design and characterisation of the new master laser system for the experimental apparatus, which is responsible for the laser cooling and trapping of metastable helium, and is therefore a critical instrument for the preparation of BEC of metastable helium. Based on a single-angled facet semiconductor gain chip in an external-cavity laser design, this laser system achieves excellent performance at low-cost and allows for in-house fabrication and maintenance.
- Chapter 4 presents the experimental verification of entanglement and the observation of quantum nonlocality between pairs of spatially separated helium atoms. Briefly, a collision of two BECs generates the spin entangled pairs of atoms and correlations between the pairs' spins are measured along various directions. The observed correlations agree with the theoretical prediction of a Bell triplet state, and a violation of EPR-steering inequality is observed.
- Chapter 5 investigates the spatially delocalised entanglement in the counter-propagating pairs of atoms for an application into quantum sensing of magnetic field. A novel method of magnetic gradiometry is presented based on the evolution of pairwise correlation, which is insensitive to common-mode fluctuations of the magnetic field. Furthermore, ballistic expansion of the scattering

ensemble allows a 3D reconstruction of the interrogated field without the need for a conventional scanning probe mechanism.

- Chapter 6 provides an outlook to future investigations on entangling collisions for cold atoms and a summary of the thesis. A direct extension to this work could look towards realising a Bell test and addressing experimental loopholes from a number of technical limitations. Further goals are the investigation of motional entanglement of the atom pairs and the generation of mass entangled atom pairs by collision of different atomic species.

Background

Non-classical states of matter have been generated and manipulated in labs for over a decade. Recent realisations include squeezed states and correlated pairs of ultracold atoms. Quantum nonlocality is a deeply non-classical aspect of nature, and is a central resource in quantum technologies. It exhibits in a hierarchy of correlations allowed by quantum mechanics, and historically finds roots in the Einstein-Podolsky-Rosen paradox. The metastable helium BEC machine has been developed to provide suitable control and detection capabilities for tests of Bell inequalities with freely-propagating atoms.

This chapter gives the background for this thesis in three parts. First, I present a theoretical overview of quantum nonlocality. Second, non-classical states of matter realisable in ultracold atomic systems are introduced, and the theory behind collision-based entangling process is discussed. Third, I describe the experimental apparatus used in this thesis to create correlated pairs of freely propagating atoms, and probe quantum nonlocal correlations.

2.1 Quantum nonlocality

Nonlocality is the signature of quantum mechanics (QM) that goes hand in hand with entanglement. This property of QM is most strikingly presented by Bell's theorem and its experimental realisations, drawing the conclusion that locality and realism, two long-held core principle of classical physics, are an unsatisfactory base for understanding nature. Aside from the fundamental research interest in quantum physics, nonlocality is now widely deemed a key resource for a broad range of quantum technologies concerning information [1] and communication [26]. For example the task of demonstrating the violation of Bell inequality between two networked parties allows the absolute verification of the security of the quantum communication channel, while a quantum sensor that is internally prepared in a correlated (entangled) state can show improved sensitivity over an uncorrelated one, called quantum enhanced metrology [27]. The recent discovery of a new class of quantum nonlocality, called EPR-steering, has gained interest as hybridising the nonlocality of Bell states and entanglement, and unravelling a hierarchical structure to quantum nonlocality [16].

2.1.1 EPR-Bohm paradox

Here we illustrate the EPR paradox [2] modified by Bohm for a pair of spatially separated spin-1/2 particles [28], and by extension to any two level system/qubit¹. Notably we make the particular choice for the pair state, namely the Bell triplet

$$|\Psi^+\rangle = \frac{1}{\sqrt{2}}(|\uparrow\rangle_A |\downarrow\rangle_B + |\downarrow\rangle_A |\uparrow\rangle_B). \quad (2.1)$$

For completeness we note that the Bell states (also called EPR states) are four maximally entangled states of two qubits, which form an orthonormal basis, defined by

$$|\Psi^\pm\rangle = \frac{1}{\sqrt{2}}(|\uparrow\downarrow\rangle \pm |\downarrow\uparrow\rangle) \quad (2.2)$$

$$|\Phi^\pm\rangle = \frac{1}{\sqrt{2}}(|\uparrow\uparrow\rangle \pm |\downarrow\downarrow\rangle). \quad (2.3)$$

$|\Psi^-\rangle$ is the singlet with zero total angular momentum ($S = 0$), and the rest span the triplet ($S = 1$), although notice that the Bell basis is not the common eigenbasis of \vec{S}^2 and \hat{S}_z . In Eq. (2.3) A/B labelling of the qubit is omitted for simplicity, since its meaning is obvious from the order of kets. Since different types of correlation arises depending on the choice of the pair state, the EPR paradox is most commonly illustrated with the particles either in the singlet $|\Psi^-\rangle$ or the $|\Phi^+\rangle$ triplet, due to their simplicity in pairwise correlation.

Let us consider a pair of spin-1/2 particles which are spatially separated at A and B, as illustrated in Fig. 2.1. In quantum theory the pair may take on a superposition of any tensor product state that describes each particle's state at A and B. As such, the $|\Psi^+\rangle$ state in Eq. (2.1) represents an equal superposition of two spins which are oppositely polarised along the z -direction.

In QM the outcome at A is fundamentally a probability distribution given by the density matrix which is partially traced over the unobserved system B² (vice versa for B)

$$\hat{\rho}_A = \text{Tr}_B(|\Psi^+\rangle\langle\Psi^+|) = \frac{1}{2}(|\uparrow\rangle\langle\uparrow| + |\downarrow\rangle\langle\downarrow|)_A = \frac{\mathbb{I}_2}{2}. \quad (2.4)$$

Therefore without the knowledge of its entangled counterpart, the particle at A is a complete statistical mixture, that has an equiprobable chance of returning each outcome (here 50% spin up and 50% spin down). Measurements in general are described

¹ We adopt the conventional notation throughout the thesis. $\vec{\sigma} = \left(\begin{bmatrix} 0 & 1 \\ 1 & 0 \end{bmatrix}, \begin{bmatrix} 0 & -i \\ i & 0 \end{bmatrix}, \begin{bmatrix} 1 & 0 \\ 0 & -1 \end{bmatrix} \right)$ denotes the Pauli vector, where the Pauli matrices are represented in the $\hat{\sigma}_z$ -basis $\{|\uparrow\rangle, |\downarrow\rangle\}$, and spin-1/2 operators are $\vec{S} = (\hbar/2)\vec{\sigma}$.

²The partial trace of ρ gives a *marginal* quantum state ρ_S , such that any correlation to the unobserved/unknown subsystem E is statistically averaged and lost. It is defined as

$$\rho_S = \text{Tr}_E \rho \equiv \sum_i \langle \rho | i_E | \rho \rangle$$

, where $\{|i_E\rangle\}$ is an orthonormal basis of E .

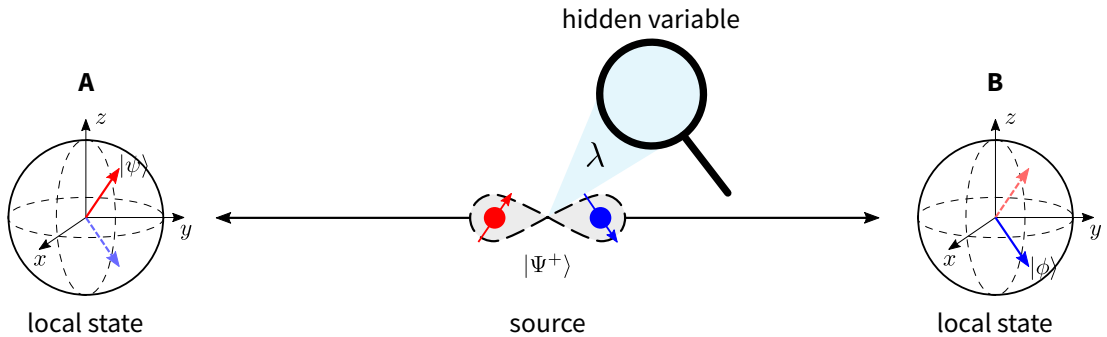


Figure 2.1: Schematic of the EPR thought-experiment with two spin-1/2 particles. A source prepares two spin-1/2 particles in the $|\Psi^+\rangle$ state, which is spatially separated between A and B. When the spin of one particle is measured to be $|\psi\rangle$ at A, say (illustrated on the Bloch sphere), QM states that the counterpart at B will instantaneously collapse to a definite state $|\phi\rangle$ (this Bloch vector is a reflection of $|\psi\rangle$ about the xy plane). EPR's paper was the first to notice such a nonlocal effect in QM, and assuming it to be counter-physical, argued that quantum theory is incomplete. EPR suggested that a complete theory may uncover physical variables λ hidden to QM that could explain the seemingly probabilistic nature of microscopic particles.

in QM by positive operator-valued measure (POVM) [29]: for every measurement \mathcal{M} one may make on a system ρ (e.g. observables $\hat{S}_z, \hat{S}_x^{(A)} \otimes \hat{S}_x^{(B)}$) and the set of all possible outcomes $\{m_i\}$ (e.g. $\{\pm\hbar/2\}, \{\pm\hbar^2/4\}$), there is a corresponding set of positive operators $\{\hat{E}_i^{\mathcal{M}}\}$ which gives the probability for each outcome by

$$P(m_i | \mathcal{M}; \rho) = \text{Tr}(\hat{E}_i^{\mathcal{M}} \rho), \quad (2.5)$$

and satisfying $\sum_i \hat{E}_i^{\mathcal{M}} = 1$ for the normalisation of probability.

Let us explicitly show how the spin of the particle, at location l , is determined along an arbitrary direction \mathbf{n} according to QM. This measurement exactly corresponds to the spin observable $\hat{S}_{\mathbf{n}}^{(l)}$, giving the binary outcomes spin *up* or *down* along every measurement angle \mathbf{n} , denoted $|\uparrow_{\mathbf{n}}\rangle$ and $|\downarrow_{\mathbf{n}}\rangle$ (subscript is omitted for \hat{S}_z basis without ambiguity). Labelling the two outcomes $\uparrow, \downarrow \equiv +1, -1$, we arrive at the corresponding orthogonal projectors $\Pi_{+1}^{\mathbf{n}} = |\uparrow_{\mathbf{n}}\rangle\langle\uparrow_{\mathbf{n}}|$ and $\Pi_{-1}^{\mathbf{n}} = |\downarrow_{\mathbf{n}}\rangle\langle\downarrow_{\mathbf{n}}|$, which form the desired POVM. Since the density matrix for each partial system is proportional to the identity matrix, we arrive at an important result that the outcome for each particle is completely random (50% spin up and 50% spin down) regardless of the measurement direction.

A little more interesting feature of $|\Psi^+\rangle$ we can immediately notice from Eq. (2.1) is that when both measurements at A and B are chosen along z , their joint outcomes are perfectly anti-correlated: 50% (\uparrow^A, \downarrow^B) and 50% (\downarrow^A, \uparrow^B). Therefore although individually the outcomes along z at A and B are uncertain, measuring one particle makes the other's outcome completely known.

An even more surprising correlation is observed in the x and y directions. These correlations are less trivial to obtain than for the z -measurement, which is obvious from the definition, see Eq. (2.1). But since the system is restricted to just two qubits, this question can be exactly answered for arbitrary measurements at A and B. Let us restrict the measurement configuration for the two qubits to be *symmetric*, such that the spin measurement direction at A and B are identically \mathbf{n} . It would indeed be sufficient to express $|\Psi^+\rangle$ explicitly as a superposition of the symmetrically rotated basis $\{|\uparrow_{\mathbf{n}}\uparrow_{\mathbf{n}}\rangle, |\uparrow_{\mathbf{n}}\downarrow_{\mathbf{n}}\rangle, |\downarrow_{\mathbf{n}}\uparrow_{\mathbf{n}}\rangle, |\downarrow_{\mathbf{n}}\downarrow_{\mathbf{n}}\rangle\}$, since then we can just read off the probability amplitudes corresponding to a particular event. Note that the spin-1/2 eigenstates are related by

$$\begin{aligned} |\uparrow_{\mathbf{n}}\rangle &= \cos\phi/2|\uparrow\rangle + e^{i\theta}\sin\phi/2|\downarrow\rangle \\ |\downarrow_{\mathbf{n}}\rangle &= -e^{-i\theta}\sin\phi/2|\uparrow\rangle + \cos\phi/2|\downarrow\rangle, \end{aligned} \quad (2.6)$$

where θ and ϕ corresponds to the azimuthal and polar angles of \mathbf{n} , respectively.³ The $|\Psi^+\rangle$ state along symmetrically rotated basis is then given by

$$|\Psi^+\rangle = \frac{1}{\sqrt{2}} \left(e^{-i\theta}\sin\phi |\uparrow_{\mathbf{n}}\uparrow_{\mathbf{n}}\rangle + \cos\phi |\uparrow_{\mathbf{n}}\downarrow_{\mathbf{n}}\rangle + \cos\phi |\downarrow_{\mathbf{n}}\uparrow_{\mathbf{n}}\rangle - e^{i\theta}\sin\phi |\downarrow_{\mathbf{n}}\downarrow_{\mathbf{n}}\rangle \right). \quad (2.7)$$

Thus, when the spin is measured orthogonal to the z -axis ($\phi = \pi/2$), such as in the x - and y -oriented spin measurements, the anti-correlated terms completely vanish. Specifically in this case, the particles' spins are identical, in other words perfectly correlated, as their joint outcomes are given according to 50% (\uparrow^A, \uparrow^B) and 50% ($\downarrow^A, \downarrow^B$).

Before we discuss the significance of the above result for $|\Psi^+\rangle$, let us briefly mention a well known result for the singlet state $|\Psi^-\rangle$. Since the singlet has zero total spin, the individual spin projections ($s_1, s_2 = \pm 1/2$) will always be anti-correlated ($s_1 = -s_2$) when projected along the same axis, since the total projection ($s_1 + s_2$) must be vanish. Compared to the algebraic manipulations we used to determine the correlations for $|\Psi^+\rangle$, the symmetrically rotated correlations of the singlet is much more intuitive, and as such conventionally used to study quantum nonlocality. Note that whenever we discuss a general result, we illustrate an example related to $|\Psi^+\rangle$, which can be significantly different to those more familiar with the singlet case.

As it turns out, the above set of correlations predicted by QM are a phenomenon of quantum nonlocality, analogous to the demonstration of the EPR paradox. Furthermore, the main goal of this thesis will be to experimentally realise distant pairs of atoms entangled in $|\Psi^+\rangle$ states, and demonstrate the above quantum correlations. A formal discussion of what we mean by nonlocality, and as such a proof of our above claim, requires some preamble that will be introduced in the following section. Fortunately however, even without consulting precise definitions, we can still come to appreciate non-classical features of the strong correlations through two arguments I

³Note that the polar angle is the angle measured from the positive z -axis, and that some notations in literature interchange the symbols θ and ϕ to represent polar and azimuthal angles, respectively.

present below.

First let us compare the QM correlation result from the spins of $|\Psi^+\rangle$ against a *reasonable* classical theory for magnetic dipole moments of particles. Then, to exhibit the perfect anti-correlation along the z -axis requires each particle's dipole moment to have been initially prepared oppositely polarised along z . Now when each particle's dipole moment is projected orthogonally, since the orthogonal component is zero, it must either polarise along or against the axis by an equi-probable chance. Since each particle is independent, this implies that the pair's correlation along x and y must also vanish, which is in contradiction to the QM phenomenon. Strictly speaking, this argument begs the question as to whether it was necessary to include randomness into the description of projections. Indeed, classical theories may utilise extra physical properties to exactly reproduce the QM correlations, and furthermore eliminate randomness. An analysis covering this perspective, called the hidden variable theory, will be given in the next section, but it still turns out to be insufficient to completely reproduce QM! For the sake of getting an early insight into nonlocal aspects of QM, it is safe to set aside such ad hoc refashioning of classical theories.

The second argument follows the style of the EPR paradox, where we presume nature to be local. More precisely, the principle of *locality* states that any event cannot influence, and be influenced by, others that happen sufficiently far away in space [30]. From special relativity, the independent events should be space-like separated, meaning that neither event lies inside the future light cone of the other, where causal influences may exist. Contrariwise, if the two particles of a $|\Psi^+\rangle$ state, for instance, are spatially overlapped, or interrogated one after the other with sufficiently long delay (enough for some sub-/luminal signalling to travel between events), then under locality the outcomes cannot be guaranteed to be independent of each other.

The core of the EPR paradox is found in the interplay of locality and quantum entanglement. Recall that the measurement postulate of QM does not distinguish whether a composite system is localised or separated. Revisiting the entangled state Eq. (2.1), QM states that when one particle of $|\Psi^+\rangle$ is measured to be $|\uparrow\rangle$ ($|\downarrow\rangle$), the other particle instantaneously collapses to a perfectly anti-correlated state $|\downarrow\rangle$ ($|\uparrow\rangle$). Indeed given that locality holds, this result must imply that at every realisation of $|\Psi^+\rangle$, the two particles must have shared a predetermined arrangement of spins. Since otherwise, there could be no sub-/luminal signal from one measurement to inform the counterpart to influence its outcome. Following a similar argument, a perfect correlation along x and y axes implies predetermined spin variables in these measurement configurations (this will be formalised in the next section with the definition of local hidden variable/quantum state models). We have therefore established that the spin variable for each particle in $|\Psi^+\rangle$ (in particular the x,y,z -components simultaneously) as an *element of reality*, although the quantum theory famously does not allow an observer to measure it without a disturbance.

Now it is worth emphasising this point with a powerful generalisation: given that locality and QM hold together, perfect correlations over space-like separations from maximally entangled states can be used to show that complementary variables are elements of reality. This is exactly the principle of *realism*, stating that all physical

quantities have definite, objective properties [30]. Indeed, it is well known that determinism goes directly against the QM uncertainty principle, so we have arrived at a contradiction, which is the essence of EPR paradox. For completeness, let us show with an explicit example, how this self-contradiction arises in QM.

In fact, locality can be exploited by a diverse range of entangled states to immediately result in a violation of the uncertainty principle, such as the famous position-momentum relation $\Delta\hat{x}\Delta\hat{p} \geq \hbar/2$,⁴ and thus to the self-contradiction of quantum theory. With $|\Psi^+\rangle$ observe that, according to the locality principle, non-commuting spin components measured at B (e.g. $\hat{S}_i^{(B)}$ for $i = x, z$) can be simultaneously determined by measuring one component directly at B and the other at A (experimentally this requires the measurement of A and B to be sufficiently separated in spacetime). This clearly violates an uncertainty relation for spin-1/2 systems given by $(\Delta\hat{S}_i)^2 + (\Delta\hat{S}_j)^2 \geq \hbar^2/4$ for any pair of perpendicular axes i, j (see Section C.1 for a derivation).

Strong supporters of quantum theory on the other hand, seriously considered whether locality should be trusted. In fact in the reply to EPR's argument in the same year [3], Schrödinger coined the quantum correlated state as entangled, and furthermore suggested (although crucially did not believe himself) that measuring a part of an entangled state instantaneously *steers* the counterpart to what QM predicted.

As such, the so-called EPR paradox as presented here is a thought-experiment that seriously opened up QM to dismissal as a fundamental theory as locality was both an intuitive and central principle of classical physics. Without a definite way to test the locality principle itself, it remained just that until a breakthrough idea would appear.

2.1.2 Quantum nonlocality and its hierarchy

It turns out that (certain) experimentally observable correlations predicted by quantum theory are incompatible with any theory respecting locality and hidden variables. Beginning with a proper definition of entanglement, we formalise quantum nonlocality as first achieved by Bell demonstrating the strongest such form, called Bell nonlocality. Then we revisit the nonlocality in the EPR paradox and illustrate the recent theoretical achievement [16] that led to the explicit formulation of the unique and least understood type of nonlocality. EPR-steering nonlocality opened up the realisation of the EPR paradox and consequently the demonstration of Schrödinger's steering in laboratories. The three classes of nonlocality — entanglement, EPR-steering, and Bell nonlocality — form a hierarchy and individually play a key role in quantum technologies, as illustrated in Fig. 2.2. We emphasise the strict hierarchy by considering a family of mixed states, to include realistic, noisy factors that modify the ideal, pure $|\Psi^+\rangle$ state. We find noise must be sufficiently low to observe quantum nonlocality, furthermore these limits are quantified.

⁴Throughout this thesis ΔO will denote root mean squared (rms) uncertainty of the variable O such that variance is written $(\Delta x)^2 \equiv \langle (x - \bar{x})^2 \rangle$, with the brackets sometimes omitted Δx^2 .

Let us represent the noisy Bell state by a linear combination of $|\Psi^+\rangle$ and a completely mixed state $\mathbb{I}_4/4$

$$\hat{\rho}_+ = p |\Psi^+\rangle\langle\Psi^+| + (1-p)\mathbb{I}_4/4 \quad (2.8)$$

where $p \in [0, 1]$ is the visibility parameter. The family of two-qubit states $\hat{\rho}_+$ is a modified version of the two-qubit Werner state [31], obtained by replacing $|\Psi^-\rangle$ with $|\Psi^+\rangle$. Indeed since $\hat{\rho}_+$ is just the two-qubit Werner state with a local basis transformation, they are identical in nonlocal nature. Fortunately, the quantum correlations of Werner states, including the relationship between the visibility parameter to nonlocality, are well understood, due to their unique covariant properties [31, 16]. The hierarchical nature of quantum nonlocality is exemplified by the increasingly nonlocal correlation manifested by $\hat{\rho}_+$ with respect to p , as shown in Fig. 2.2.

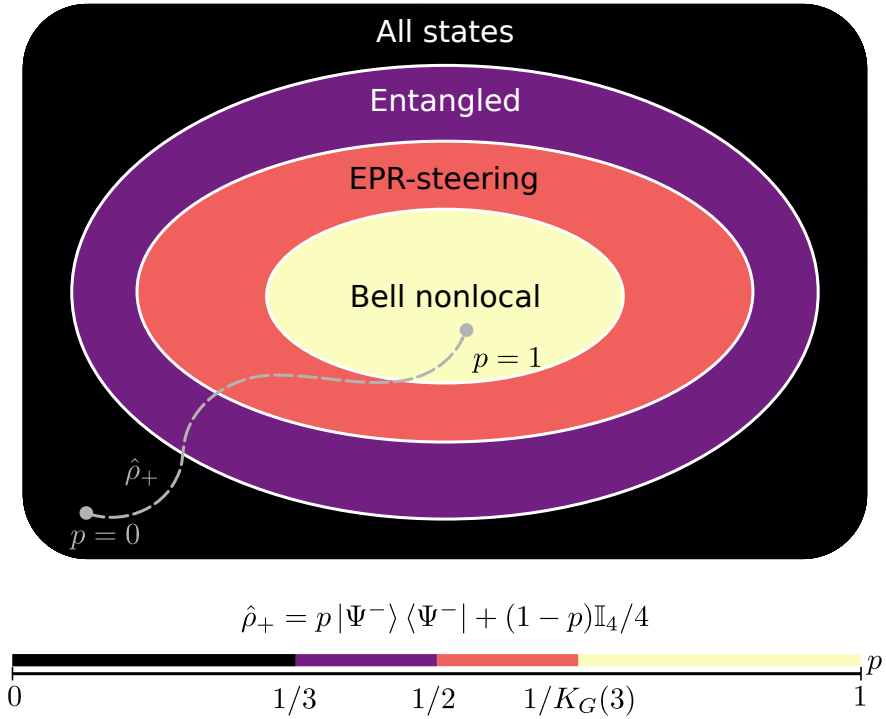


Figure 2.2: Hierarchy of quantum nonlocality. Quantum states are classified according to different classes of nonlocality (entanglement, EPR-steering, and Bell nonlocality), and the complementary class of separable states, shown as a Venn diagram. The dashed grey curve shows the family of two-qubit states $\hat{\rho}_+$ as p runs from 0 to 1. $\hat{\rho}_+$ is entangled if and only if (iff) $p > 1/3$, EPR-steering iff $p > 1/2$, and Bell nonlocal iff $p > 1/K_G(3) \approx 1/1.5$.

Entanglement

A bipartite pure state $|\Psi\rangle_{AB}$, composed of two distinct subsystems A and B, is *separable* iff it is a product of pure states in each subsystem, thus written $|\Psi\rangle_{AB} = |\psi\rangle_A \otimes |\phi\rangle_B$, and *entangled* otherwise. A separable state, therefore, has a simple physical interpretation that each subsystem has a corresponding well-defined quantum state. For an entangled system, however, no such interpretation exists, so that the system's characteristic must be treated as a whole, and not as a sum of its parts. Happily, we are already familiar with entangled states. The Bell states Eq. (2.3) are the archetypal examples of entangled states of two qubits, since they cannot be factorised into two separate qubit states (we will prove it using a different method for $|\Psi^+\rangle$ in this section).

A natural extension of separability of a pure state to mixed state then leads to the definition of bipartite entanglement for arbitrary states: a state $\rho^{(AB)}$ in $A \otimes B$ is separable iff it can be represented as a linear combination of product states, such that

$$\rho_{\text{sep}}^{(AB)} = \sum_i p_i \rho_i^{(A)} \rho_i^{(B)} \quad (2.9)$$

for some ensemble $\{(p_i, \rho_i^{(A)} \rho_i^{(B)})\}$. Otherwise the state is defined entangled, where

$$\rho_{\text{ent}}^{(AB)} \neq \sum_i p_i \rho_i^{(A)} \rho_i^{(B)}, \quad (2.10)$$

such that no such factorised ensemble exists. The definition and characteristic of entanglement, as well as quantum nonlocality [1], in multipartite systems is much richer [32], but such scenarios are outside the scope of this thesis. Now we formalise correlations between the subsystems A and B (interchangeably denoted by spatially separated observers Alice and Bob, respectively), beginning by comparing the difference between a separable and entangled quantum system.

Due to their spatial separation, Alice and Bob can only measure their own *particle* (a subsystem of ρ), which corresponds to local observables $\{\mathcal{A}\}$ and $\{\mathcal{B}\}$ in the measurement. According to QM, their *joint probability distribution* for the outcome a, b under the *measurement configuration* \mathcal{A}, \mathcal{B} is given by $P(a, b | \mathcal{A}, \mathcal{B}; \rho) = \text{Tr}(E_a^{\mathcal{A}} E_b^{\mathcal{B}} \rho)$, where $\{E_m^{\mathcal{M}}\}$ is the POVM (see Eq. (2.5)) acting only on one particle. For a separable state the equality holds in Eq. (2.10), therefore

$$\begin{aligned} P_{\text{sep}}(a, b | \mathcal{A}, \mathcal{B}; \rho) &= \sum_{\lambda} \text{Tr} \left(E_a^{\mathcal{A}} \rho_{\lambda}^{(A)} \right) \text{Tr} \left(E_b^{\mathcal{B}} \rho_{\lambda}^{(B)} \right) p_{\lambda} \\ &= \sum_{\lambda} P_Q(a | \mathcal{A}; \rho_{\lambda}^{(A)}) P_Q(b | \mathcal{B}; \rho_{\lambda}^{(B)}) p_{\lambda}, \end{aligned} \quad (2.11)$$

for some ensemble $\{(p_{\lambda}, \rho_{\lambda}^{(A)} \rho_{\lambda}^{(B)})\}$ for all measurement-outcomes $(\mathcal{A}, \mathcal{B}; a, b)$, where we have introduced a subscript notation P_Q to explicitly indicate that the probability function is quantum mechanical, as defined in Eq. (2.5), in the anticipation of predictions from hidden variable models discussed later. The separation of joint outcomes

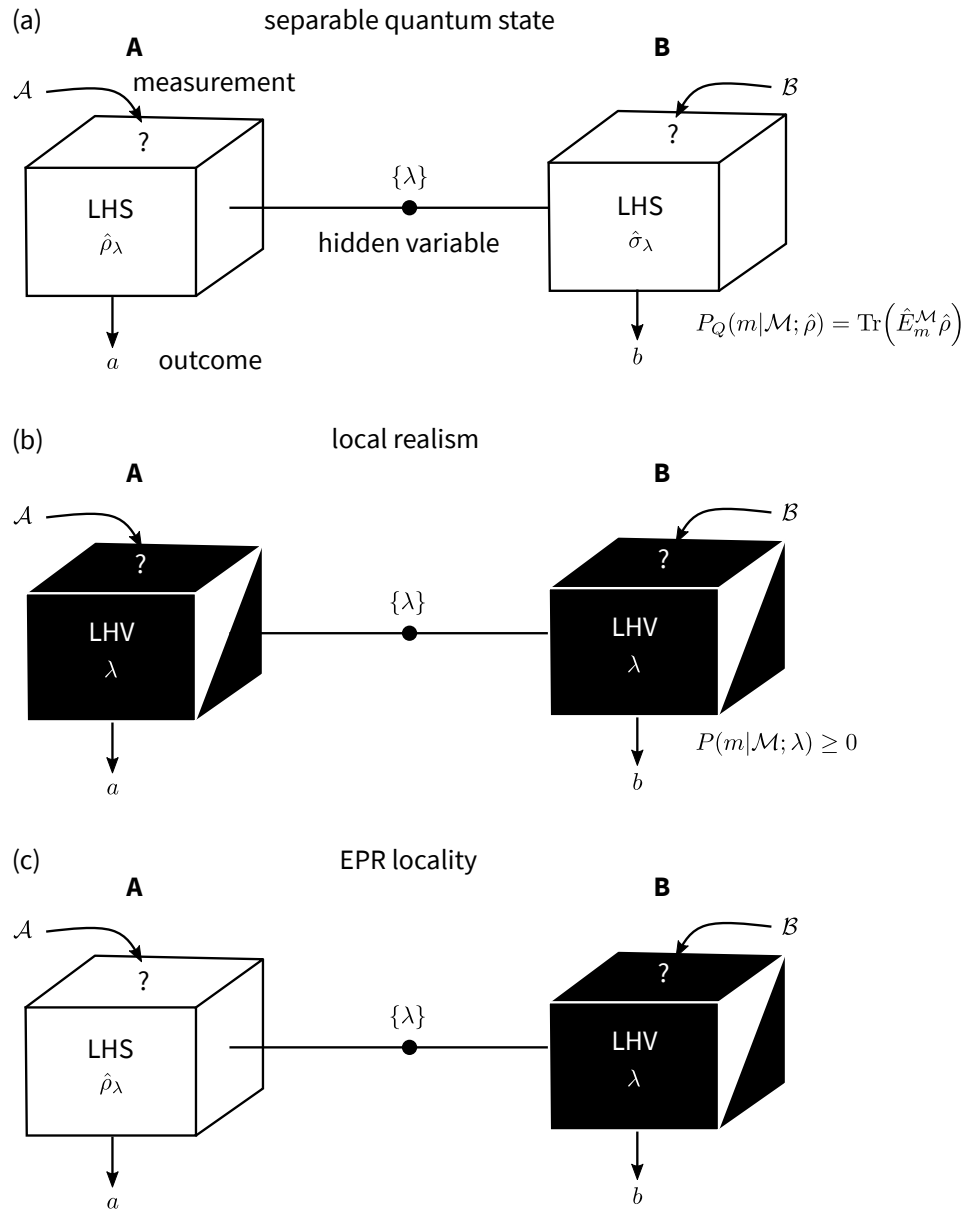


Figure 2.3: Formulation of bipartite locality classes. Individual subsystem's outcomes are determined from its internal model (white/black box denote quantum/general probability model) and a shared hidden variable λ . (a) All statistical correlations arising from a separable quantum state shared between A and B can be modelled by a pair of local hidden states (LHS) $\hat{\rho}_\lambda, \hat{\sigma}_\lambda$, with some common hidden correlation λ generated at the source. (b) Any theory respecting local realism is a local hidden variable (LHV) model. (c) A hybrid LHS-LHV model formalises locality assumptions in EPR paradox.

by definite quantum states (albeit which state among many $\{\rho_\lambda\}$ is hidden to the observer), as in the last line of Eq. (2.11) and illustrated in Fig. 2.3(a), is called the *local hidden (quantum) state* (LHS) model for A and B⁵. Since for any entangled state, no such separation of local quantum probability distributions exists by definition, no LHS model can completely reproduce correlations arising from entangled states. This is the basis of quantum nonlocality.

Now we discuss how to test whether a prepared system is entangled or separable, called the *separability problem*. For this task the operational definition of entanglement Eq. (2.11) provides no improvement over the density matrix-based form Eq. (2.10). This effort is however the key first step in the formalisation of quantum nonlocality, since the latter expression allows us to directly question and solve for other theories than QM. Indeed, the form of Eq. (2.11) lends itself naturally to a unified operational definition of the remaining classes of quantum nonlocality, by the modification of probability distribution of the individual subsystem.

The necessary and sufficient condition for the two-qubit $\hat{\rho}_+$ states to become entangled is $p > 1/3$ (see Fig. 2.2), which follows from a trivial modification of Werner's original proof [31]. In fact, entanglement is well understood in the general two-qubit system [32] – there exists a necessary and sufficient separability criterion (Peres-Horodecki criterion), and a measure to quantify the degree of entanglement (entanglement of formation). For higher dimensional or multipartite systems, characterising entanglement remains notoriously difficult [32].

To solve the separability problem involves the derivation of necessary conditions for a state to be separable, called *separability criteria* [34]. Typically a separability criterion is formulated as an inequality, for a function of a density matrix, that is satisfied by all separable states, and therefore its violation indicates that the state is entangled. Furthermore, if the inequality is derived from the expectation value of an observable, namely $\text{Tr}(\mathcal{W}\rho_{\text{sep}}) \geq 0$ satisfied for all separable ρ_{sep} , then \mathcal{W} is called an entanglement witness [34].

We should note carefully that, in general, separability and similar locality criteria express *sufficient* conditions for a particular test property, and as such the corresponding inequalities are often called *no-go* theorems. A notable feature of such criteria is that a non-violation result cannot be used to distinguish the test property (i.e. some, but not all, entangled states will satisfy a separability criterion). Despite this drawback, such criteria are the key tools used in the verification of quantum nonlocality, where a diverse range of them are found for different systems [32]. In practice an experimentalist has an approximate idea about their prepared system, such as $\hat{\rho}_+$ for our case, but may not have independent control of qubits, or the time, to perform a full state tomography of the density matrix [35], which grows exponentially with the number of qubits. It turns out that for every entangled state there is an entanglement witness which identifies it [34]. Therefore by a clever choice of an entanglement wit-

⁵The local hidden state formalism was introduced by Wiseman and coworkers in Ref. [16] to refer to a local quantum state/LHV hybrid model discussed in Section 2.1.2. However for clarity in our overview of quantum nonlocality, we use *LHS* to strictly mean a general, black box model of a localised QM state, complementing *LHV*, as the original authors explained in Ref. [33].

ness or a separability criterion, a restricted set of measurements can be sufficient to prove that the system is (to some amount) entangled.

It is instructive to see the separability criterion in action, and we defer the derivation to Chapter 4 when the complete physical system and its capabilities are explained. A separability criterion that identifies our two-qubit system $|\Psi^+\rangle$ is

$$\mathcal{S}_{\text{sep}} \equiv |E(\theta, \theta) - E(\theta', \theta')| \leq 1, \quad (2.12)$$

where

$$\begin{aligned} E(\theta, \phi) &\equiv \sum_{a,b=\pm 1} ab P_Q(a, b | \mathcal{A}(\theta), \mathcal{B}(\phi); \rho) \equiv \langle (\vec{\sigma}^{(A)} \cdot \hat{\mathbf{n}}(\theta)) \otimes (\vec{\sigma}^{(B)} \cdot \hat{\mathbf{n}}(\phi)) \rangle \\ &= \sum_{a,b=\pm 1} ab \text{Tr} [(\Pi_a^{\mathbf{n}(\theta)} \otimes \Pi_b^{\mathbf{n}(\phi)}) \rho] \end{aligned} \quad (2.13)$$

is the QM prediction for the *pairwise correlation function* of spins, and $\hat{\mathbf{n}}(\alpha) \equiv \cos \alpha \hat{\mathbf{z}} + \sin \alpha \hat{\mathbf{x}}$ denotes the unit vector along the direction of spin measurement (recall the notation from Eq. (2.5), and see Chapter 4 for a proof of the separability criterion). Indeed this separability criterion Eq. (2.12) does not identify every single two-qubit entangled state, since it is trivially satisfied by the two Bell states $|\Phi^+\rangle$ and $|\Psi^-\rangle$ which are invariant under symmetrically rotated measurements ($\theta = \phi$) giving $E(\theta, \theta) = \pm 1$, respectively, and $\mathcal{S}_{\text{sep}} = 0$. On the other hand, a maximum violation of the inequality is reached by the other two Bell states $|\Psi^+\rangle$ and $|\Phi^-\rangle$, since along the two orthogonal directions $(\theta, \theta') = (0, \pi/2)$ the pair flips between the perfect anti-correlation ($E(0, 0) = \mp 1$) and identical correlation ($E(\pi/2, \pi/2) = \pm 1$), therefore giving $\mathcal{S}_{\text{sep}} = 2$. By construction no separable state can violate the inequality (proved in Chapter 4), but notice that some separable states may saturate it (the equality holds), as simple as for instance $|\uparrow\downarrow\rangle$ and $|\uparrow\uparrow\rangle$ from the orthogonal measurement angles.

For completeness, let us use the above separability criterion to investigate $\hat{\rho}_+$. First, note that for a completely mixed state, the correlator defined in Eq. (2.13) vanishes trivially, since regardless of the measurement axis each qubit independently gives a 50:50 projection. Therefore the correlator for $\hat{\rho}_+(p)$ is just that of $|\Psi^+\rangle$ reduced by the visibility parameter p , such that the maximum of the separability parameter is $\max \mathcal{S}_{\text{sep}}(\hat{\rho}_+) = 2p$.

So our separability criterion demonstrates that a subset of $\hat{\rho}_+(p)$ for $p > 1/2$ are entangled. For $p = 0$ we have the completely mixed state which is trivially separable. Notice that we cannot be certain as to whether this subset captures all the entangled states! In fact, our particular choice of the entanglement witness Eq. (2.12) is not *optimal* [34], and the true cutoff for p , that correctly divides $\hat{\rho}_+$ into such subsets, lies below 1/2. Without going into the details outside the scope of our thesis, there exists a rather simple necessary and sufficient criterion to test the separability of two qubits, called the Peres-Horodecki criterion [36] which states that all separable states' density matrices remain positive after a partial transpose operation on the subsystem. As we mentioned before, such a powerful tool requires a complete knowledge of the

density matrix, and is generally unavailable outside the simplest kind of composite systems, such as that of our two qubit and the qubit-qutrit system [32]. Using the Peres-Horodecki criterion, we find directly that $\hat{\rho}_+$ is entangled if and only if (iff) $p > 1/3$. Figure 2.2 illustrates this important result over all quantum states classified as either separable or entangled, as a first entry in the anticipation of other types of nonlocality that we will subsequently encounter.

Local realism and Bell's theorem

Recall from the EPR paradox, if locality is assumed to hold then QM quickly breaks down as an inconsistent theory as a result of the strong correlations between entangled systems. Since a complete description of physical observables are both unexplained and unaccounted for in the quantum theory, EPR thus concludes that QM cannot be a complete theory of nature. Consider whether a deeper theory of nature respecting locality could be found from the unaccounted for *hidden variables*, called the *local hidden variable* (LHV) theory, that would outdo QM by completely eliminating its probabilistic features. Indeed, it is intuitive to picture the fundamental mechanics of nature as a set of deterministic rules governing a complete list of variables. This establishes the central principles of classical physics that is worth reiterating: (1) *realism*, which states for all physical objects to possess an element of reality, and (2) *locality*, which limit cause and effect phenomena to propagate no faster than light, which as a combination is called *local realism* [30]. Here we illustrate the landmark discovery by Bell [4], which spurred on the formalisation of local realism [37], quantified the bound of all LHV theories, and ultimately resulted in the experimentally falsifiable test of QM versus local realism.

The local realist joint probability distribution for Alice and Bob is given by

$$P(a, b | \mathcal{A}, \mathcal{B}; W) = \sum_{\lambda} P(a, b | \mathcal{A}, \mathcal{B}; \lambda) p_{\lambda}, \quad (2.14)$$

where λ is the hidden variable for a particular realisation, and the effective result is summed over the probability distribution p_{λ} , given by the ensemble $W = \{(p_{\lambda}, \lambda)\}$ shared by A and B, and $(\mathcal{A}, \mathcal{B}; a, b)$ the measurement-outcome, as discussed previously. Observe that identifying λ and specifying the outcome probability $P(a, b | \mathcal{A}, \mathcal{B}; \lambda)$ for all λ under all measurement-outcomes gives a particular hidden variable theory (the corresponding one for quantum theory is Eq. (2.5)). Suppose that the measurement configuration is chosen randomly at each location and the outcomes are detected at A and B – for the two spin-1/2 particle case, this corresponds to randomly selecting the measurement direction and performing a spin readout process. If such complete measurement processes at A and B happen space-like separated, then by locality, the measurement outcome at individual locations depends only on the shared hidden variable and the local measurement setting. Therefore in EPR's scenario, LHV theories become more restrictive and Eq. (2.14) factorises to

give

$$P_{\text{LHV}}(a, b | \mathcal{A}, \mathcal{B}; W) = \sum_{\lambda} P(a | \mathcal{A}, \lambda) P(b | \mathcal{B}, \lambda) p_{\lambda}, \quad (2.15)$$

which is illustrated in Fig. 2.3(b). Note that for LHV models there are no non-commuting properties, such that outcome probability may be an arbitrary function as long as it is non-negative ($P(m | \mathcal{M}, \lambda) \geq 0$) and sums to unity ($\sum_m P(m | \mathcal{M}, \lambda) = 1$), for all measurements \mathcal{M} and hidden variable λ . Although it may appear to give no further insight, the formalisation of LHV theories shown in Eq. (2.15) is all that is needed to prove the celebrated Bell's theorem: “predictions of quantum theory are incompatible with those of any physical theory satisfying a natural notion of [local realism]” [1].

The correlation function for an arbitrary LHV model of two qubits is given by

$$E(\mathcal{A}, \mathcal{B}) = \sum_{a,b=\pm 1} \sum_{\lambda} ab P(a, b | \mathcal{A}, \mathcal{B}; \lambda) p_{\lambda}. \quad (2.16)$$

Then for any four different measurement configurations created by each observer switching between any two choices (see Fig. 2.4 for a schematic of two spin-1/2 Bell test), for example $\{\mathcal{A}, \mathcal{A}'\}$ for A and $\{\mathcal{B}, \mathcal{B}'\}$ for B, the Bell inequality [38] holds for all LHV theories (see Section C.2 for a proof)

$$\mathcal{S}_{\text{CHSH}} \equiv |E(\mathcal{A}, \mathcal{B}) + E(\mathcal{A}, \mathcal{B}') + E(\mathcal{A}', \mathcal{B}) - E(\mathcal{A}', \mathcal{B}')| \leq 2. \quad (2.17)$$

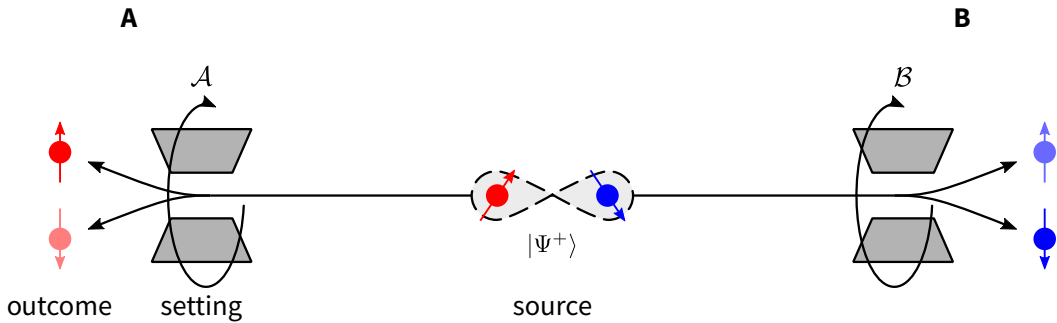


Figure 2.4: Schematic of CHSH Bell test. A pair of spin-1/2 particles are entangled as $|\Psi^+\rangle$ (source), and each particle is sent to spatially separated locations A and B, equipped with a detector to measure the spin along an arbitrary direction \mathcal{A} and \mathcal{B} (setting), respectively.

The Bell inequalities, Eq. (2.17) being in particular the most famous one called the CHSH inequality, are the no-go theorem of local realism. Crucially, there exist QM states which violate Bell inequalities and therefore exhibit strikingly nonlocal correlations, called *Bell nonlocality* (see Fig. 2.2). Similar to our treatment for separability criterion in Eqs. (2.12) and (2.13), let us parameterise the measurement setting at A and B by the polar angle of the spin projection in the zx -plane, such that $\mathcal{A} \equiv \theta$

and, $\mathcal{B} \equiv \phi$. For the Bell triplet state $|\Psi^+\rangle$ the correlation function is explicitly given by $E(\theta, \phi) = -\cos(\theta + \phi)$. The maximal violation of CHSH Bell inequality is achieved for $|\Psi^+\rangle$ (similar results holds for the other Bell states) when the set of measurement angles are $(\theta, \theta', \phi, \phi') = (0, \pi/2, -\pi/4, \pi/4)$, giving the CHSH parameter $S_{\text{CHSH}} = 2\sqrt{2}$ by QM⁶.

Observe that for a localised system LHV describes the most general measurement-outcome behaviour, which can indeed imitate the more restrained quantum theory of measurement (i.e. obeys the uncertainty principle). Therefore any correlation arising from a separable quantum state as in Eq. (2.11) can always be explained by a LHV model in Eq. (2.15). However the converse is not true – there exists quantum states which can be completely explained by a LHV model, called *Bell local*, which are entangled. The strict hierarchy of entanglement under Bell nonlocality can be illustrated by the $\hat{\rho}_+$ states. However, it turns out to be extremely challenging to decide whether a given state is Bell nonlocal [1], even in the case of a two qubit system. The range of two-qubit Werner states, and by extension the $\hat{\rho}_+$ states, which are Bell nonlocal yields the cutoff $p > 1/K_G(3) \approx 1/1.5$ [42], as shown in Fig. 2.2. Suffice to say K_G (the Grothendieck constant) is a mathematical constant that is fundamentally linked to quantum nonlocality (first observed in [43]).

EPR-steering: the hybrid

A hybrid hidden variable model of those used to define entanglement and Bell nonlocality naturally arises by assigning a LHS model on one side, and a LHV model on the other [16]. The joint probability distribution of a *LHS/LHV* model is then explicitly given by

$$P_{\text{hyb}}(a, b | \mathcal{A}, \mathcal{B}; W) = \sum_{\lambda} P_Q(a | \mathcal{A}, \hat{\rho}_{\lambda}) P(b | \mathcal{B}; \lambda) p_{\lambda}, \quad (2.18)$$

choosing a LHV model for B, and shown schematically in Fig. 2.3(c). The asymmetry in the hybrid model, where LHV model could have been chosen for A above, is itself a unique and fascinating feature currently being explored [17], but a proper discussion is outside the scope of this thesis. Briefly, the hybrid formalism exposes an asymmetry in QM which allow for a LHS/LHV description in only one-way [44], and was recently experimentally demonstrated in the simplest case of just two-qubits [45].

Observe that Eq. (2.18) respects locality and captures the possibility of hidden variable theories, as well as a QM state description for an observer. Wiseman, Jones, and Doherty [16, 46] showed that this hybrid description formalises EPR's delocalised system [2], whereby a violation of it would be a simultaneous demonstration of the nonlocality in the EPR paradox, and, by extension Schrödinger's steering [3].

⁶As a nonlocality criterion, note that the QM limit of Bell inequalities, called the Tsirelson bound [39], is still far from the algebraic limit $S_{\text{CHSH}} \leq 4$. In a similar vein to revealing the discrepancy between the axiom of local realism and QM, extensive theoretical research has gone into distilling new fundamental axioms of physics. Surprisingly, QM turns out to be just one particular theory from those that obey locality but not realism [40], such that there exists such super-quantum models that may violate the Tsirelson bound [41].

States exhibiting nonlocal correlations which are incompatible with the LHS/LHV model are thus called EPR-steering (see Fig. 2.2). Following the definition of the Bell inequality and separability criterion with respect to local realism and separable states, a no-go theorem of the hybrid model is called an EPR-steering inequality. The reader interested in the historical development and foundation of EPR-steering should refer to the seminal works in Refs. [16, 46, 33] and review articles on the topic in Refs. [47, 17].

The particular EPR-steering inequality relevant for our two-qubit state of interest $\hat{\rho}_+$ is given by (see Chapter 4 for a proof)

$$\mathcal{S}_{\text{EPR}} \equiv |E(\theta, \theta) - E(\theta + \pi/2, \theta + \pi/2)| \leq \sqrt{2}. \quad (2.19)$$

$\hat{\rho}_+$ is EPR-steering iff $p > 1/2$, from an extension of the two-qubit Werner state [16], and is illustrated in Fig. 2.2. This means that although our EPR-steering inequality is maximally violated by $|\Psi^+\rangle$ ($\max \mathcal{S}_{\text{EPR}} = 2$ achieved for $\theta = 0$), it is not optimal since it saturates at $p = 1/\sqrt{2} > 1/2$.

Curiously, note the similarity in the form of the above EPR-steering inequality to the separability criterion Eq. (2.12): both inequalities place a bound on the maximum variation in the correlation that can be observed when the measurement angles are uniformly rotated between the two parties. The EPR-steering inequality (2.19) is *weaker* than the separability criterion (2.12) – the latter clearly implies the former, a restricted subset of orthogonal measurements, by a greater bound; but not the other way around.

The hierarchy of nonlocality is clear from the definitions of LHS and LHV probabilistic models. Indeed since a localised quantum system can always be explained by some arbitrary hidden variable model, but not conversely, nonlocal correlations from (the invalidity of) LHS/LHV models (2.18) lie intermediate between those of LHS (2.11) and LHV (2.15): Bell nonlocality implies EPR-steering, and EPR-steering implies entanglement. We have already demonstrated that the hierarchy is strict by completely characterising the nonlocality the two-qubit $\hat{\rho}_+$ states (see Fig. 2.2).

2.1.3 Role of quantum nonlocality in quantum technology

Quantum nonlocality is not only interesting for purely fundamental research. In fact, such peculiarities of QM allow radical improvements and novelties to a diverse range of classical technologies, that this idea is coined the second quantum revolution. Among the useful QM *resource* to technologies, nonlocality plays the central role in some of the most prominent applications, namely in quantum communication (secret sharing and networking with untrusted parties), and more broadly in quantum metrology (precision sensing), and quantum computing. Surprisingly in many of these applications, the hierarchy of quantum nonlocality directly relates to how useful a given quantum state will be.

Bell nonlocality, for instance, allows one to test the security of a completely untrusted quantum network, in general called a device independent protocol [48]. Here,

if and only if a Bell nonlocal state can be efficiently distributed and manipulated coherently, then the system can demonstrate its security/correctness claim by the demonstration of a Bell inequality violation. Additionally Bell correlation serves as an essential resource for quantum teleportation [14], certified random number generation [49], and improved communication efficiency [50, 26].

In practice, however, a loophole-free test of a Bell inequality to rigorously verify Bell nonlocality is extremely challenging [7]. When one can trust a part of the network to be QM, for example their own system, then a similar argument to the previous paragraph can be made to show that EPR-steering cannot be faked by a classical adversary without a nonlocal resource. Therefore a simpler demonstration of EPR-steering is sufficient to gain physically guaranteed trust in communication over the QM network [18]. The concept of EPR-steering opens up a way for unique applications in quantum communication protocols concerning asymmetry in the trust or resources in the network, which is explicitly present in the definition of the LHS model. EPR-steering states therefore allow realistic applications in one-sided device independent protocols [18].

Entanglement is almost ubiquitous in quantum technology, since hardly any utilise uncorrelated or isolated qubits. Besides from having a central role in quantum nonlocality, entanglement finds applications in various quantum technologies, such as in sensors [51, 27, 52], information processing [53], and quantum computing [54]. Entanglement mostly appears in these applications in a localised composite system. Strictly speaking therefore, it is rather inappropriate to describe the central resource here as nonlocality, although the definition of separability in Eq. (2.11) still holds for spatially overlapping subsystems.

2.1.4 Experimental demonstrations

Historical demonstrations of the quantum nature of light has paved the way to a better understanding of quantum mechanics by providing a variety of non-classical sources of light such as entangled pairs, also called bi-photons, or squeezed states of light, as well as macroscopic quantum states such as the Schrödinger cat state. Recently, atomic counterparts to these non-classical states of light have been realised in labs, relying on atom-atom or atom-light interactions as the entangling mechanism. Of these, pair source of atoms have been studied less and correlation properties investigated so far have been limited to large population measurements, without a direct evidence for their quantumness. The pair source is a major technology powering quantum information and computing technologies based on the photonic platform, since it is the basis for heralded single photon sources used in discrete variable (DV) architectures, as well as allowing distant parties to share entanglement. This section provides a review of experimental demonstrations of quantum nonlocality, especially highlighting the achievements and gaps from cold atom platforms.

Here I provide an overview of experimental demonstrations of quantum nonlocality. A brief history of Bell tests and EPR-steering experiments are given to introduce the readers to the progress made over diverse range of quantum platforms.

We identify a clear gap in the literature for demonstrations of quantum nonlocality with massive particles, due to the particular experimental challenges involved, and discuss some unique aspects the strong gravitational coupling it may bring.

A short history of quantum nonlocality

Between the birth of quantum nonlocality in EPR's 1935 paper to the time of writing this thesis in 2020, has seen an incredible progress in the manipulation of quantum systems, and equally enormous amounts of research dedicated to quantum nonlocality. The works I have highlighted below made significant breakthroughs which clarify immense practical challenges for a conclusive demonstration of quantum nonlocality. The seminal works have eliminated previous untested assumptions in the experimental tests of nonlocality, called *loopholes* [7], and verified the universality of QM in all the interrogated physical platforms.

The early experiments to realise the Bell test faced the quintessential problem of reliably generating pairs of particles entangled in some observable degrees of freedom (DOF). Pair sources of photons were of great interest in quantum optics, and the polarisation entanglement in photon pairs from a radiative cascade decay in an atom was used in the first experimental demonstration of the Bell test in 1972 by Freedman and Clauser [5]. The first photonic Bell test however was undertaken in a localised environment with predetermined polarisation settings on both photons, and therefore open to the challenge that parties could influence each other called the *locality loophole*. In this scenario, since the outcome of each particle is influenced not only by its measurement setting, but also by its counterpart's, the nonlocal measurement assumption in constructing the Bell inequality are falsified. After this conceptual demonstration, significant milestones in Bell tests were achieved on the photonic system by Aspect and coworkers in 1982 who first addressed the locality loophole by periodically switching the measurement settings [6], and Rarity and Tapster (1990) who demonstrated Bell correlations in the motional DOF of parametric downconverted pair source [55]. Using fibre optics the photonic Bell test was realised over 10.9 km separation by the Gisin group [56], and was able to address the locality assumption in the same year by the Zeilinger group [57].

Contemporary to the early photonic Bell tests, nuclear physics experiments also observed the violation of a Bell inequality from pairs of protons in scattering experiments [58]. More recently, a pair of protons yielded from the decay of ^2He was used in a proof-of-principle demonstration in 2004 [59] and Bell correlations were consequently observed in 2006 [60].

Although photons have been running the Bell test for the longest time, other physical platforms overtook photonic systems in addressing the problem of the *detection loophole*, where the notably poor efficiency of single-photon detectors (prior to transition-edge sensors [61]) invalidates the Bell inequality violation [62]. Here, briefly speaking, the loophole lies in the open possibility that the violation was caused by an unfair sample of all actually LHV realisations [7]. The detection loophole was first closed in Bell tests with trapped ions in 2001 by the Wineland

group [63], and with superconducting circuits in 2009 by the Martinis group [64], where almost ideal detection efficiency is possible since the methods effectively rely on a state-dependent emission of many photons/microwaves. Led by the recent breakthrough in the efficiency of single photon detectors by the superconducting transition edge sensors [61], photonic Bell tests relaxed the fair sampling assumption in 2013 [65, 66].

Loophole-free Bell tests are few but have utmost significance to fundamental physics, since the experimental violation of a Bell inequality means that nature is not both local and deterministic. These include photon pairs prepared by parametric down-conversion [9, 10], nitrogen vacancy centres in diamond [8], and trapped neutral atoms [11]. Even in the latter solid-state and atomic systems, single-photon techniques are key to the entangling operation. Here the two independent photon emitters, each entangled to its emitted photon, are subsequently entangled by entangling the photons, called entanglement swapping [67].

References [47, 17] include an extensive review covering both theoretical and experimental sides of EPR-steering in both continuous and discrete variable.

The massive gap

One may reasonably grant quantum mechanics to hold quite universally. In reality however, decoherence limits quantum phenomena to be confined to highly isolated conditions largely for laboratories, and within very specific subspace of physical systems. As such, tests of nonlocality with massive particles in the motional DOF (position and momentum) have been previously proposed [68, 69, 70], but without an accompanying experimental realisation due to the practical difficulties. However, the gap in tests of quantum nonlocality with massive systems is an important one to explore for the fundamental questions over the interplay between QM and gravity.

Massive systems allow one to explore the interaction between quantum mechanics and gravity, which currently lacks a complete description. Indeed it is not known whether a massive object in a spatial superposition would cause the gravitational field to be in a quantum superposition as well. Based on this profound idea, Penrose noted such a scenario causes an ambiguous (superposition) direction of time based on general relativity, and suggested a decoherence theory to destabilise such a gravitational superposition [71]. More broadly, massive quantum mechanical systems are of interest to the test of gravitational decoherence theories which explain why quantum mechanical phenomena are unobserved in macroscopic systems [72]. It has therefore been suggested that the effect of gravitational decoherence could be detectable in tests of quantum nonlocality with massive particles, and especially in their motional DOFs [70].

A source of entangled masses is among the foreseeable range of experimental tools that will be gained in the effort, and it has a variety of unique applications elsewhere. A pair of entangled atomic isotopes, for instance, was noted as a unique proof mass for the test of the weak equivalence principle [73], one of the central axioms in general relativity which states that gravitational acceleration is independent of an ob-

ject's mass. This allows the exploration of general relativity at the microscopic regime and when the system is a *quantum proof mass*. Unfortunately general relativity has evaded a quantum description, so gravitational effects cannot be consistently incorporated into quantum dynamics of these systems. But it has been recently shown that a reasonable quantum formulation of the equivalence principle would produce an observable effect in such an atomic quantum proof mass [74]. This piece of technology developed for nonlocality tests additionally provides a quantum proof mass for exploring general relativity, and integrates well to the established gravimeters based on atom interferometry [75].

The current lack of experimental demonstrations of quantum nonlocality with massive particles, especially in their motional DOF, is due mostly to experimental challenges in preparing and manipulating their quantum states. Consider the problems for neutral atoms which is the focus of this thesis. Since atoms interact very strongly with the environment, in order to preserve coherence they must be isolated in a vacuum chamber and localised by optical or magnetic trapping. The manipulation and measurement of a single atom requires more complex atom optic equivalent procedures than bulk electro-optic elements such as waveplates and detectors used for photons. Lastly, the atomic pair source is much more difficult to generate than for photons, as evidenced by the Weinfurter group's method on entanglement swapping via fluorescent photons [76], a process already relying on quantum optics and single photon detection. The method we used for addressing the above points and realising the EPR paradox with atoms are discussed in Section 2.3.

2.2 Entanglement via atomic collisions

In the classical description of gases, atoms interact ballistically such that they collide like hard spheres and propagate freely between collisions. This classical picture is appropriate so long as the individual atom's de Broglie wavelength, which characterises the quantum coherence length of a particle, is unresolved. However, when gases are cooled to temperatures near absolute zero (e.g. sub-microkelvin) the atomic de Broglie wavelength can become comparable to the average inter-atomic spacing, or even the ensemble itself (order micrometers). The so-called ultracold (or quantum-) gases exhibit distinctly QM properties that can persist over macroscopic scales, and requires a fully QM description. An iconic phenomenon observed in ultracold gases is the quantum phase transition called Bose-Einstein condensation [77], wherein all particles condense into the same ground state wavefunction, thus behaving collectively as a matter-wave. On the other hand, waves are the classical description of light, but due to the quantal, particle-like photons which constitute it, and QM correlations possible among them, there exists so-called *nonclassical light* which cannot be described by classical wave statistics [78].

Ultracold atoms have been a simple yet versatile platform for quantum physicists. Unlike photons which require a nonlinear medium to mediate their interactions [79], and still do so quite weakly, atomic collisions are always present and highly tun-

able [80]. As we show in this section, it turns out that a simple collision entangles a pair of ultracold atoms. The types of *nonclassical atomic ensembles* that are realised this way broadly fit into two categories: the atomic pairs and the squeezed states, with close photonic analogues to photon pairs and squeezed light [79], respectively. This platform has opened up a wide range of research into quantum correlations with ultracold atoms, from multipartite entanglement in many-body systems [81], quantum-enhanced metrology [82, 83], to nonlocality [84] (see Ref. [25] for an excellent review of nonclassical atomic ensembles).

This section provides a background on nonclassical states of matter realisable in ultracold atomic systems, and illustrates that quantum nonlocality is present at the basic level of atomic collisions. We first give an overview of the common types of nonclassical atomic ensembles listed above, and distil the types of quantum correlations and ultimately nonlocal aspects so far investigated. Then we give a conceptual explanation for the basic entangling process, namely how a collision induces a Bell state entanglement for a pair of particles in the quantum regime. This atomic pair source is the starting point for our investigation into the experimental demonstration of quantum nonlocality.

2.2.1 Types of nonclassical atomic ensembles

We first define what is meant by a *nonclassical* atomic ensemble. For simplicity, let us treat an individual atom as a spin-1/2 particle and consider a system made of N atoms. A simple N -atom ensemble is $|\uparrow\rangle^{\otimes N}$, where all atoms are prepared $|\uparrow\rangle$ spin-polarised, and the collectively rotated state $|\uparrow; \hat{n}\rangle^{\otimes N}$ could be readily prepared by a single-qubit rotation [25]. Generally such an ensemble of two level systems where every qubit's Bloch vector is identically \hat{n} is called the *coherent spin state* [85, 25], in an analogy to the coherent state (classical harmonic oscillator) in quantum optics. Since every atom in such an ensemble has a definite state, we say the ensemble is *classically correlated*. Note that based on this definition, clearly a classically correlated ensemble does not need to be completely classical, since individual atoms are pure, and not completely mixed states. However without the risk of confusion, we define the *nonclassical atomic ensemble* to mean an entangled state of atoms. To prepare a nonclassical state of atoms, experiments must begin with a separable state, such as $|\uparrow\rangle^{\otimes N}$, and implement an entangling procedure, usually based on atomic collisions which we will focus on. The nature of undergoing interatomic collisions governs the outcome, but broadly either the entangled atomic pair or the so-called spin squeezed state are produced [86], which we describe below. For the sake of keeping this overview brief, we do not discuss other types of entangled states, such as the Schrödinger cat and two-mode Fock states, and less common entangling mechanisms, based on atom-light interactions and interaction-free measurements. Interested readers however should seek Ref. [25].

The atomic pair

Entangled pairs of atoms are the simplest kind of nonclassical atomic ensemble in existence. However as exemplified by the nonlocality of Bell states, due to the unique research avenues provided by the atom's mass, and the key role photon pair sources currently play in quantum information technology, the atomic pair source promises fascinating research. In practice however, creating an isolated pair of entangled atoms is not a trivial task, and two distinctly varied approaches have been demonstrated so far.

The first method exploits interatomic interactions in an atomic ensemble, a Bose-Einstein condensate (BEC; see next section for details), which cause it to spontaneously emit entangled pairs in easily distinguishable modes from the reservoir. Mechanisms for the pair emission which have been experimentally demonstrated include the de-excitation of an unstable condensate in a 1D trap [87], the spontaneous four-wave mixing in a periodic potential [88], and lastly pairwise scattering from a collision of BECs [89]. Some theoretical proposals have suggested that counter-propagating, entangled atom pairs could be sourced from the dissociation of dimer molecules in BEC [90]. The above mechanisms all rely on atom-atom interaction at their core, with conceptual analogy to the quantum optics of spontaneous four-wave mixing (SFWM) in a nonlinear medium. In SFWM, two incoming photons from a single mode laser are converted into two entangled photons of new and different frequencies [79]. When the rate of SFWM increases and multiple pairs emit into the same mode, squeezed light is produced. Later we analyse the collision of BECs from the quantum field description of identical bosons. There the role of the BECs and the collisional interaction turns out to correspond to that of the laser and the nonlinear medium of SFWM, respectively. The collision is therefore said to be a SFWM of matter-waves, and is of interest for the generation of entangled pairs and squeezed states of atoms [86].

The second method initially prepares an isolated system of two atoms and then entangles them, by a measurement-induced projection of the pair onto one of the Bell states [67]. This is the entanglement swapping scheme used by the Weinfurter group [11], highlighted in Section 2.1 for the loophole-free violation of a Bell inequality. Unlike the first method, entanglement swapping relies crucially on the atom-photon interaction, specifically the Bell state entanglement between each isolated atom with its emitted photon. This method allows for deterministic entanglement of two specific atoms based on communication of photons, and simultaneously the control of an individual atom, which makes it a favourable building block for a quantum network. However since this method works on a particular pair of isolated atoms, its yield is limited (Weinfurter group measured 1–2 entangled pairs per minute in Ref. [91]), compared to the first method (later we see in our experiment over 1000 pairs may easily be scattered into mostly separate modes in a single collision of BECs cycling every ≈ 30 s).

Spin squeezed state

The spin squeezed state is a many-body entangled state of qubits, and is the most prevalent type of nonclassical atomic ensemble due to its desirable properties for atomic sensing applications. In general atoms act as oscillating dipoles even classically, which forms the current state-of-the-art technique for measuring magnetic fields [92]. For the classical spin coherent state however, there is a quantum mechanical uncertainty in the measurement of the oscillation phase (the angle of the mean dipole/spin), arising fundamentally from random and independent projections of the qubits, called the standard quantum limit (SQL). Indeed just as in squeezed light, where uncertainties in phase quadratures can be redistributed, atoms in spin coherent states can be entangled with each other to reduce the measured phase uncertainty below the SQL, at the expense of uncertainty in the perpendicular quadrature. In general, any spin ensemble with a *mean moment* having sub-SQL uncertainty along any direction is defined as *spin squeezed*, and thus allows quantum enhanced measurement sensitivities [25].

Spin squeezing an atomic ensemble, first proposed by Kitagawa and Ueda [93], has been experimentally realised in both thermal vapour cells [94] and BECs [95]. The underlying physics of spin squeezing closely resembles the nonlinear collisional interaction between atoms for the atomic pair source, with the difference that scattered pairs remain indistinguishable from the reservoir (the macroscopic input ensemble), so that the ensemble builds up with correlated pairs. When the collisional interactions can be tuned between different spin configurations, many atoms' spins become entangled and the reservoir will no longer be a coherent spin state. The interaction is realised by the nonlinear Hamiltonian $\hat{H}_{\text{OAT}} = \chi \hat{j}_z^2$ (called one-axis twisting), where $\hat{j} = \sum \hat{S}_i$ is the total angular momentum of the ensemble and χ is the interatomic coupling strength. This system resembles $\Omega \hat{j}_z$ which describes a precession of the Bloch vector around the z -axis, except that the rotation frequency Ω is dependent on the z -component of the vector itself. Thus a localised region on the equator of the Bloch sphere is stationary, while regions away from it rotate around the z -axis at faster rates, and in opposite direction for the two hemisphere where the sign of \hat{j}_z flips. The resulting dynamics for an initially coherent spin state $|\uparrow; \hat{x}\rangle^{\otimes N}$, which has a circular uncertainty region around the $+x$ -axis on the Bloch sphere, is approximately a twisting of the Bloch sphere around the z -axis, and a combination of squeezing and anti-squeezing of the elliptical uncertainty region.

2.2.2 Theory of pairwise entanglement by collision

The physics of correlated atomic pairs scattered from a collision of Bose-Einstein condensates are analogous to the production of photon pairs by SFWM [96], where the atoms are treated using bosonic field theory in the fully quantum mechanical description. When the entangling atomic collisions scatter back into the condensate mode, this leads to the spin squeezing dynamics analogous to squeezed light in quantum optics [23], and furthermore promises the generation of macroscopically entangled, Schrödinger cat states. When relatively low numbers of pairs are generated and has

negligible effect on the source, the many-body scattered state can even be solved analytically.

Before delving into the physics of colliding BECs, we first consider an entangling collision of just two quantum mechanical objects. This simple picture gives a powerful intuition to treat the many-body system as multiple independent, discrete pairwise collisions. This is indeed adequate in the spontaneous scattering regime studied in this thesis, where the number of scattered atoms and bosonic stimulation effects are small.

A cold collision of two atoms

Two particles that interact purely based on their relative position $\mathbf{r}_1 - \mathbf{r}_2 = \mathbf{r}$, correspond to the scattering of a wavefunction (describing their relative motion \mathbf{r}) from the potential $V(\mathbf{r})$, as shown in Fig. 2.5. In this system, the Schrödinger equation describes the relative motion of the two-body system, with an effective mass $m = (1/m_1 + 1/m_2)^{-1}$ and relative momentum/wavevector $\mathbf{k} = \mathbf{k}_1 - \mathbf{k}_2$, where the subscripts denote the respective particle.

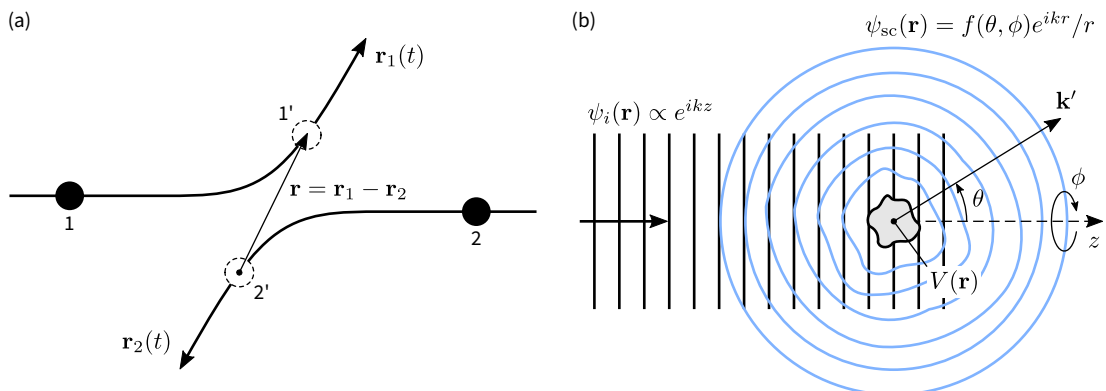


Figure 2.5: (a) A schematic of a collision of two incoming particles ($1, 2 \rightarrow 1', 2'$), which scatter along a single classical trajectory (arrowed curves). (b) A QM picture of the collision (in the relative coordinate \mathbf{r}). The incoming plane wavefunction ψ_i (black) scatters off the interatomic potential V as spherical waves ψ_{sc} (blue), when viewed from far away. The result is a superposition of all classical trajectories described by the scattering function $f(\theta, \phi)$. The scattering angles, θ and ϕ , are defined relative to the incoming wavevector $k\hat{z}$.

The system is most commonly initialised such that the two particles approach from far away with definite momenta and relative (collision) wavevector pointing along z , such that the corresponding incoming wavefunction approaching $V(\mathbf{r})$ is a planewave (see Fig. 2.5(b))

$$\psi_i = e^{ikz} / (2\pi)^{3/2}. \quad (2.20)$$

Scattering theory is concerned with solving the Schrödinger equation to find the

complete wavefunction (far away from the potential) given by a sum of this incoming plane wave and scattered product. Indeed the plane wave solution is complete, since by linearity it can be extended to, for example, scattering from localised wavepackets. By experimentally tuning the collision energy and measuring the resulting products/flux from the collision, physicists most commonly use scattering theory to determine the underlying interactions between particles. Here we are interested in knowing how the particles are entangled from a collision, and therefore require the knowledge of the complex amplitudes in scattering, rather than the more commonly reported flux of scattered particles (differential cross section).

After the wavefunction interacts with the potential and propagates far away, the potential vanishes and the outgoing wave becomes spherical $\propto e^{ik'r}/r$ (propagates radially; $1/r$ decay from probability conservation) with scattered wavenumber k' (see Fig. 2.5(b)). For simplicity, we restrict ourselves to elastic collisions for which the kinetic energy $E = \hbar^2 k^2 / 2m$ is conserved and the internal states do not change, such that $k' = k$. This outgoing wave is exactly the scattered part of the wavefunction, and the complete spatial wavefunction (after collision) is formally expressed as a sum of incoming and outgoing parts according to [97]

$$\psi(\mathbf{r}) \xrightarrow{\mathbf{r} \rightarrow \infty} \frac{1}{(2\pi)^{3/2}} \left[e^{ikz} + f(\theta, \phi) \frac{e^{ikr}}{r} \right]. \quad (2.21)$$

In the above expression the scattering amplitude $f(\theta, \phi)$ corresponds to the probability amplitude for scattering with wavevector \mathbf{k}' (at $r \rightarrow \infty$), where θ and ϕ denote its polar and azimuthal angles, respectively, relative to \mathbf{k} (recall the incoming plane wave propagates along z).

The scattering problem simplifies enormously when there is spherical symmetry, since we can use the well-known result that the Schrödinger equation separates into a radial and an angular part of wavefunction $\psi(\mathbf{r}) = R(r)Y(\theta, \phi)$.⁷ Crucially, the spherical harmonics $-Y_l^m(\theta, \phi)$ with angular momentum number $l = 0, 1, \dots$ and projection $m = -l, -l+1, \dots, l$ along the z -axis⁸ (see Fig. 2.6) – then diagonalises the

⁷Note the simplifying assumptions we have made so far: (1) elasticity, including the claim that internal structures of objects are unaffected by the collision, and (2) the interaction between objects depends only on their centre of mass (c.m.) separation r . The validity of these assumptions are, of course, closely tied to the internal structure of the individual objects. Even in atomic collisions, each of these assumptions may be violated, such as in the inelastic processes of spin exchange [98], and the orientation-dependent dipole-dipole interaction [99]. Later we shall see that these assumptions turn out to be valid for the binary collision of metastable helium atoms in the cold temperature regime of our experiment.

⁸Spherical harmonics are given by

$$Y_l^m(\theta, \phi) = \sqrt{\frac{(2l+1)}{4\pi} \frac{(l-m)!}{(l+m)!}} P_l^m(\cos \theta) e^{im\phi},$$

where $P_l^m(x)$ is the associated Legendre function of degree l and order m [100]. They form an orthonormal basis over the spherical polar angles, such that integrating over all solid angle Ω on the sphere

$$\int d\Omega Y_l^m * Y_{l'}^{m'} = \delta_{m,m'} \delta_{l,l'}.$$

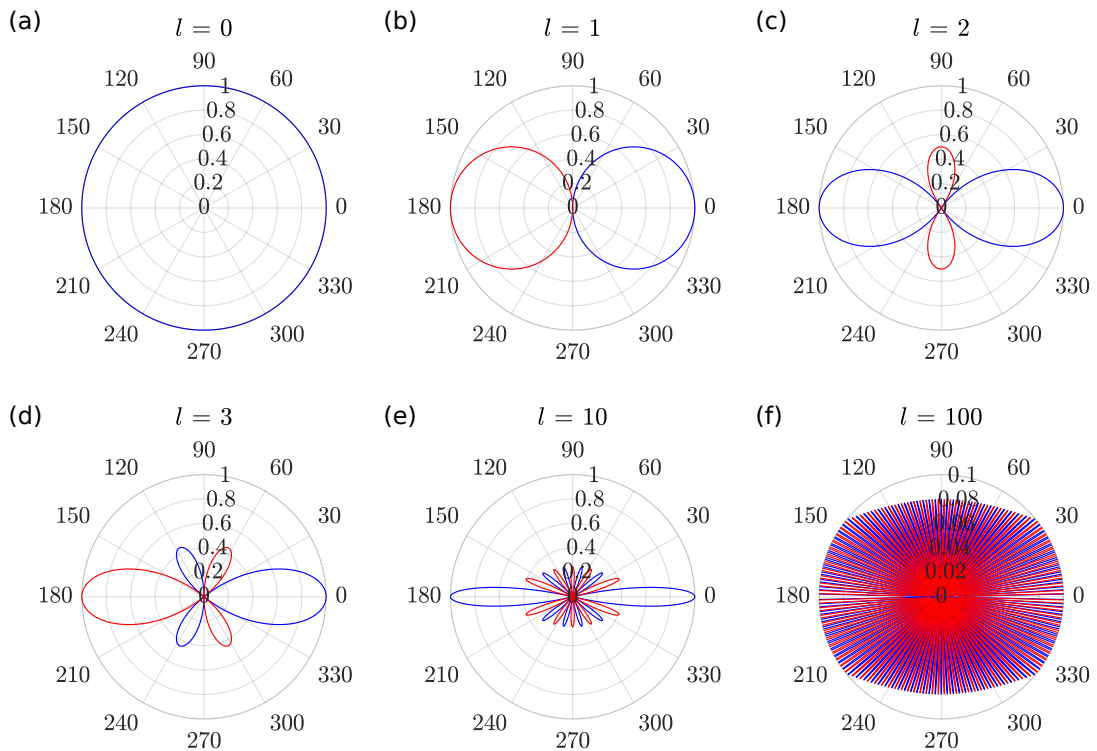


Figure 2.6: Spherical harmonics $Y_l^m(\theta, \phi)$ of indices $m = 0$ for various angular momentum number l . Shown are the polar plots in θ , since $m = 0$ indices have azimuthal symmetry. The magnitude has been normalised so that the maximum is scaled to unity, and the colour (blue/red) indicates the sign (positive/negative) of the (real-valued) function. (f) is zoomed-in to show the typical finely-spaced fringes from a high- l partial wave.

Hamiltonian.

The scattering amplitude then takes the following form when expressed as a sum of spherical harmonics

$$f(\theta) = \frac{\sqrt{4\pi}}{k} \sum_{l=0}^{\infty} \sqrt{2l+1} Y_l^0(\theta, \phi) e^{i\delta_l} \sin \delta_l, \quad (2.22)$$

where $\delta_l \in \mathbb{R}$ is called the phase shift corresponding to l -wave. As we expect from the rotational symmetry of the system around the z -axis, the scattering amplitude in the above equation contains spherical harmonics with only $m = 0$ index,⁹ and is therefore independent of the azimuthal angle.

Let us summarise why spherical harmonics give such a simple result in Eq. 2.22 and give a physical picture of the phase shifts (a rigorous derivation is found in Ref. [97]). First consider the expansion of the incoming plane wave in spherical harmonics

$$e^{ikz} = \sqrt{4\pi} \sum_{l=0}^{\infty} i^l \sqrt{2l+1} j_l(kr) Y_l^0(\theta, \phi), \quad (2.23)$$

where j_l is a spherical Bessel function of first kind with index l [100]. Now due to the spherical symmetry of the scattering potential angular momentum is conserved, such that each *partial wave* (term in Eq. 2.23 of definite angular momentum l , which is referred to as l -wave) can be solved independently. The problem therefore reduces to solving a 1D Schrödinger equation in the radial coordinate, where the angular momentum of each partial wave introduces a repulsive centrifugal barrier $\sim l^2/r^2$ that screens the interaction potential, given explicitly as [97]

$$-\frac{\hbar^2}{2m} \frac{d^2}{dr^2} u_l + \left[V(r) + \frac{\hbar^2 l(l+1)}{2mr^2} \right] u_l = \frac{\hbar^2 k^2}{2m} u_l, \quad (2.24)$$

where $ru_l(r)$ is the actual radial wavefunction. Rather than probing into the wavefunction in the interaction region, it is much more instructive to observe the behaviour far away. Indeed, since the asymptotic radial behaviour of each partial wave is given by [100]

$$j_l(kr) \xrightarrow[r \rightarrow \infty]{} \frac{1}{2ikr} \left[e^{i(kr-l\pi/2)} - e^{-i(kr-l\pi/2)} \right], \quad (2.25)$$

we can neatly describe the plane wave as a sum of incoming and outgoing spherical waves ($\propto e^{\mp ikr}/r$). It turns out that an interaction with $V(r)$ can only shift the phase of the outgoing wave relative to that of the plane wave solution (a result due to

For an eigenstate of angular momentum operators \hat{L} and \hat{L}_z denoted with respective quantum numbers by the ket $|l, m\rangle$, $Y_l^m(\theta, \phi)$ describe the angular part of the position and momentum-space wavefunctions [97], namely $\langle \mathbf{r}|l, m\rangle \propto Y_l^m(\hat{\mathbf{r}})$ and $\langle \mathbf{k}|l, m\rangle \propto Y_l^m(\hat{\mathbf{k}})$.

⁹Note the spherical harmonics with zero angular momentum along the principal z -axis is given explicitly as

$$Y_l^0(\theta, \phi) = Y_l^0(\theta) = \frac{1}{\sqrt{4\pi}} \sqrt{2l+1} P_l^0(\cos \theta).$$

unitarity of scattering wherein the total particle flux is conserved [97]), by an amount equal to δ_l in Eq. 2.22 for each partial wave. The phase shift therefore encodes all the information about the collision, such that it depends on the collision energy (hence k and m), l and $V(r)$, and is therefore the variable one solves from Eq. 2.24 for a given scattering problem.

Let us build an intuitive picture of two-body collision without explicitly solving the 1D Schrödinger equation to obtain the phase shifts quantitatively. First, notice from Eq. 2.22 that the phase shifts δ_l determine the contribution of each partial wave to the scattering amplitude. For example, consider the case when the potential is absent or negligible $V(r) = 0$. This then gives the trivial plane wave solution in Eq. 2.23, such that by definition the phase shifts completely vanish $\delta_l = 0$, and thus a vanishing scattering amplitude $f(\theta, \phi) = 0$ as expected. Not all phase shifts vanish in general, and the contributions from $l = 0, 1, 2, 3, \dots$ spherical harmonics (called s, p, d, f, ...-waves respectively) must be summed coherently as in Eq. 2.22 to produce the measurable scattering probability/intensity $|f(\theta, \phi)|^2$, known as the differential cross-section. Now from a classical picture of scattering, we expect higher partial waves ($l \gg 1$) to correspond to large angular momentum $L = d \times p$ collisions with a large separation d from the scatterer (p is the given linear collision momentum), and thus be little affected by the scattering potential. Equation 2.24 exhibits an identical result in which for large l the scattering potential $V(r)$ becomes shielded from the approaching wavefunction by the (typically longer-ranged) centrifugal barrier.¹⁰ Therefore we observe that s-wave ($l = 0$) scattering should dominate at low collision energies since there is no centrifugal barrier for $l = 0$ in Eq. 2.24, giving rise to a spherically uniform scattering amplitude since $Y_0^0(\theta, \phi) = 1/\sqrt{4\pi}$. On the other hand, at high collision energies, a large number of spherical harmonics will contribute such that the phase of scattering amplitude (see Eq. (2.22)) becomes effectively incoherent over the scattering angle. These are the two key results needed to understand how a pair of particles entangle from a collision.

Let us consider a back-to-back (BB) scattering event along $\hat{\mathbf{k}}$, which captures the collision product with scattered momenta about $\pm \mathbf{k}$. When the collision is in the s-wave regime, the scattering amplitude is spherically symmetric $f(\hat{\mathbf{k}}) = f(-\hat{\mathbf{k}})$, such that the pair's state is given by

$$\begin{aligned} |\hat{\mathbf{k}}\rangle_{\text{BB}} &\propto f(\hat{\mathbf{k}}) |\mathbf{k}\rangle + f(-\hat{\mathbf{k}}) |-\mathbf{k}\rangle \\ &\propto |\mathbf{k}\rangle + |-\mathbf{k}\rangle. \end{aligned} \tag{2.26}$$

We can readily express kets describing the relative motion of the two particles as corresponding tensor products of individual particles, namely $|\mathbf{k}\rangle \mapsto |\mathbf{k}/2\rangle_1 |-\mathbf{k}/2\rangle_2$,

¹⁰At long atomic separations the centrifugal potential $\sim r^{-2}$ clearly dominates over the interatomic van der Waals or covalent bonding potentials of leading order $\sim r^{-6}$. In general for a given collision energy, there is a threshold of angular momentum l beyond which partial waves are effectively shielded, and accrue negligible phase shift [97].

so that Eq. 2.26 becomes (after normalisation)

$$|\hat{\mathbf{k}}\rangle_{BB} = \frac{1}{\sqrt{2}} (|+\mathbf{k}/2\rangle_1 |-\mathbf{k}/2\rangle_2 + |-\mathbf{k}/2\rangle_1 |+\mathbf{k}/2\rangle_2). \quad (2.27)$$

This state is particle entangled, since it cannot be factorised as a definite state of particle 1 and 2, such that $|\hat{\mathbf{k}}\rangle_{BB} \neq |\psi\rangle_1 |\phi\rangle_2$. It is instructive to switch the labelling of subsystems from particles (1,2) to the BB spatially distant regions (denoting $\pm\mathbf{k}/2$ as \pm), namely by $|\pm\mathbf{k}/2\rangle_i \mapsto |i\rangle_\pm$ for $i = 1, 2$, since this clarifies the use of this state to the EPR paradox and tests of quantum nonlocality. In this form the ket of the state at \pm describes the internal state of the particle (that we have so far used to distinguish each particle as 1 and 2), which rearranges to give the archetypal Bell triplet state, since

$$\begin{aligned} |\hat{\mathbf{k}}\rangle_{BB} &= \frac{1}{\sqrt{2}} (|1\rangle_+ |2\rangle_- + |2\rangle_+ |1\rangle_-) \\ &= |\Psi^+\rangle. \end{aligned} \quad (2.28)$$

Therefore, an s-wave collision of different atomic spin states (denoted \uparrow / \downarrow), produces a counter-propagating atom pair which is spin-entangled, which was experimentally demonstrated in Ref. [101].

The above discussion considered the ideal capture of a BB scattering events along $\hat{\mathbf{k}}$. In practice however, no such ideal pinhole detector is available, such that we need to consider the effect of some finite uncertainty to $\pm\mathbf{k}$ by a solid angle $\delta\Omega$ in defining the \pm regions. Observe that for the s-wave collision, since the scattered state is independent of the scattering angle since $f(\theta, \phi) = f$, introducing any uncertainty in the scattering angle does not change the pair's state from the ideal Bell triplet state in Eq. 2.28. In contrast, when many partial waves contribute, the scattered pair state will show a strong dependence on the scattering angle, such that a small uncertainty can lead to a mixed ensemble with negligible coherence. Below we illustrate this phenomenon with a simple toy model.

The quantum mechanical analogy to the classical billiard ball collision is made by a simple interaction which vanishes outside a spherical particle of radius a , but infinitely repulsive inside it. In a two-body collision, the so-called hard sphere model is then defined by a spherically symmetric potential in the relative coordinate, according to

$$V(r) = \begin{cases} 0, & r \leq a \\ \infty, & r > a. \end{cases} \quad (2.29)$$

The hard sphere scattering has a simple analytic solution (see Ref. [97] for a derivation) summarised by the partial wave phase shifts (see Fig. 2.7)

$$\tan \delta_l(k) = \frac{j_l(ka)}{y_l(ka)}, \quad (2.30)$$

where j_l and y_l are the spherical Bessel functions of first and second kinds [100].

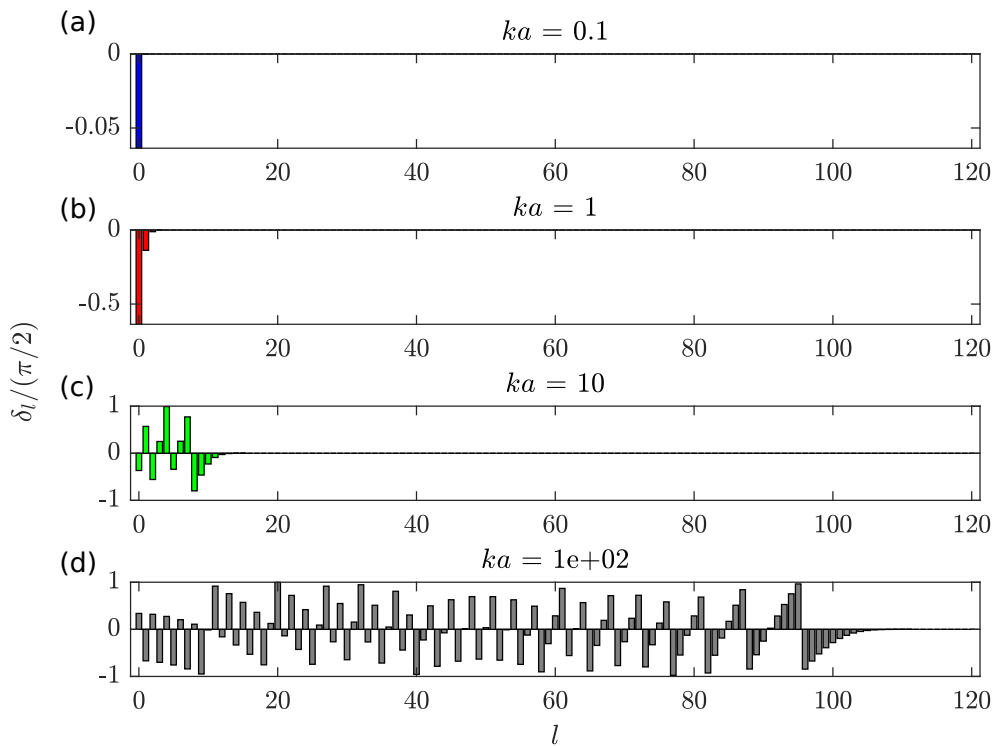


Figure 2.7: The partial wave phase shifts δ_l from a hard sphere scattering model (2.29), shown for $l \leq 120$ terms over a range of collision parameters ka (see Eq. (2.30)). Approximately ka number of partial waves contribute in scattering. Note that the limits of y-axis in (a,b) are zoomed-in to reveal the dominant s-wave scattering phase shift (i.e. $\delta_l \approx 0$ for $l > 0$).

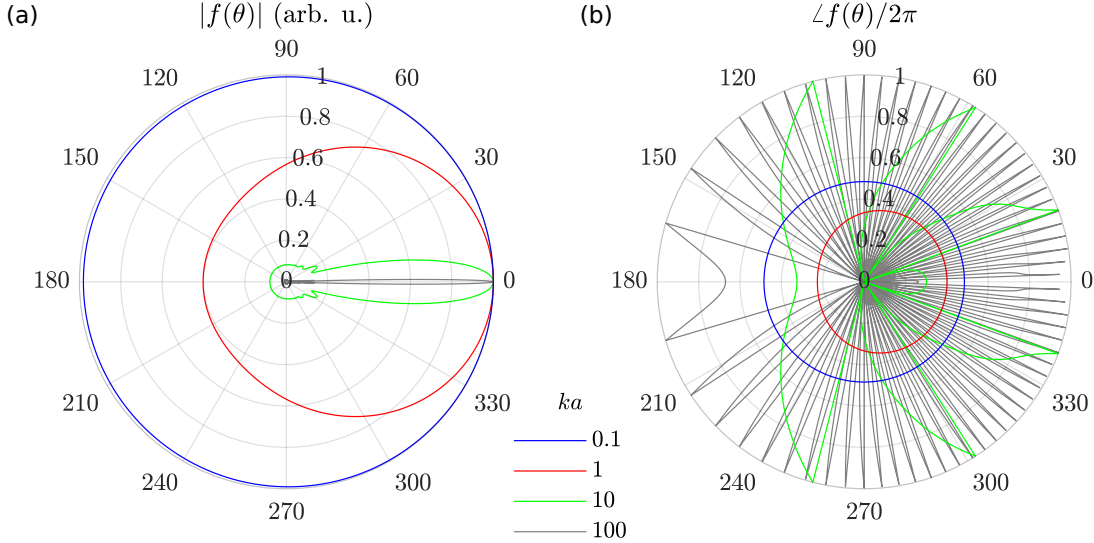


Figure 2.8: Angular distribution of the hard sphere scattering amplitude. (a) Magnitude of $f(\theta)$ normalised so that the maximum is unity. (b) Complex phase of $f(\theta)$.

Then the scattering amplitude can be evaluated by substituting the phase shifts into Eq. 2.22 to give the result in Fig. 2.8. As discussed previously, at low collision energies $ka \ll 1$, s-wave scattering dominates since $\delta_l \approx 0$ for all higher order partial waves $l > 0$ (see Fig. 2.7), and the scattering amplitude is spherically symmetric (see Fig. 2.8) in agreement with our previous result in Eq. 2.26. However as seen in Fig. 2.7, more partial waves begin to contribute as the scattering energy increases (in fact up to $l \lesssim ka$), such that when $ka \gg 1$ a large number of spherical harmonics interfere to produce a scattering amplitude which fluctuates rapidly over θ (see Fig. 2.8). Observe from Fig. 2.8(b) that the phase between the scattered pair undergoes a full 2π sweep roughly ka times over the polar angle. Remarkably, this simple model of scattering exhibits the importance of low energy collisions to observe quantum mechanical phenomena. Since at higher collision energies, the detection of scattering angle must become proportionally more precise to observe the pair's coherence, for instance in the applications/tests of quantum nonlocality.

By using the density matrix formalism, we can make the above argument for quantum-to-classical transition more rigorous. Following our previous definition of the two systems \pm in Eq. 2.28, describing a quantum state localised at the respective spatially separated region, we must now account for a general momentum subspace in each system. Since the detector cannot discern the momentum of the state in each region, the reduced density matrix ρ' that describes this system is given by taking a partial trace of the momentum variable in each system, separately. Without explicitly writing out the algebraic manipulations, the effective density matrix turns out to be an ensemble

$$\rho' = \int_{\delta\Omega} d\Omega p(\hat{\mathbf{k}}) |\hat{\mathbf{k}}\rangle\langle\hat{\mathbf{k}}|_{\text{BB}} \quad (2.31)$$

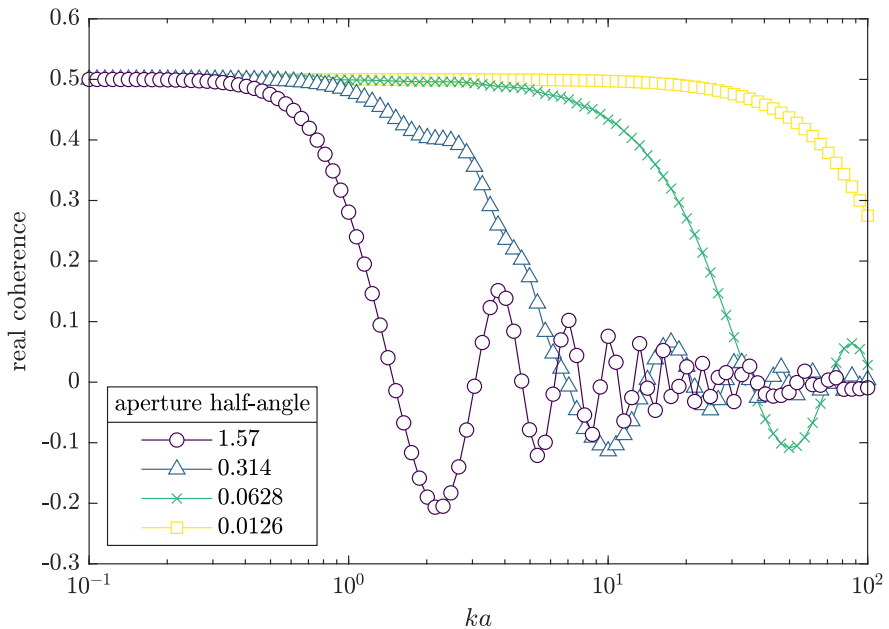


Figure 2.9: Loss of coherence $\langle 1, 2 | \rho' | 2, 1 \rangle$ between back-to-back scattered particles vs. collision parameter ka . The data shows the real part of coherence from a numerical integration (2.31) of the cross terms in Eq. 2.32, over a conical aperture centred at $\theta = \pi/2$. Aperture sizes have a half-angle of $\pi/2$ (hemisphere), $\pi/10$, $\pi/50$, and $\pi/250$. The imaginary part of coherence is negligible. f was approximated with partial waves truncated to $l \leq 200$; integration over the solid angle was approximated with a Riemann summation over 1000 equal-sized partitions in θ .

of generalised BB scattered states (see Eqs. 2.26 and 2.28)

$$|\hat{\mathbf{k}}\rangle_{\text{BB}} = \frac{1}{\sqrt{|f(\hat{\mathbf{k}})|^2 + |f(-\hat{\mathbf{k}})|^2}} (f(\hat{\mathbf{k}}) |1,2\rangle + f(-\hat{\mathbf{k}}) |2,1\rangle), \quad (2.32)$$

with corresponding probabilities $p(\hat{\mathbf{k}}) = (|f(\hat{\mathbf{k}})|^2 + |f(-\hat{\mathbf{k}})|^2)/[\int_{\delta\Omega} d\Omega (|f(\hat{\mathbf{k}})|^2 + |f(-\hat{\mathbf{k}})|^2)]$. This is consistent with an intuitive picture that for every detection event, the pair has a probability to be found in the pure entangled state $|\hat{\mathbf{k}}\rangle_{\text{BB}}$. Indeed, this probability is proportional to the sum of scattering events along $\pm\hat{\mathbf{k}}$. From Eq. 2.32 it is clear that the coherence of the pair, namely the reduced density matrix elements for $|1,2\rangle\langle 2,1|$ (and its conjugate), is given by the ensemble average of $f(\hat{\mathbf{k}})f^*(-\hat{\mathbf{k}})/(|f(\hat{\mathbf{k}})|^2 + |f(-\hat{\mathbf{k}})|^2)$, and shown in Fig. 2.9 for a few configurations of aperture sizes. Since this cross term fluctuates rapidly when a large number of partial waves contribute to scattering (as seen in Fig. 2.8(b)), the coherence reduces when integrated over a larger solid angle or at higher collision energies as evident from Fig. 2.9. On the other hand, due to the azimuthal symmetry of the hard sphere collision, scattering is equally likely to occur into opposite directions when the apertures are placed around $\theta = \pi/2$, thus giving a uniform *population* of

$$\langle 1,2|\rho'|1,2\rangle = \langle 2,1|\rho'|2,1\rangle = 1/2,$$

independent of ka . In other words, when two apertures are placed symmetrically on the opposite sides of the equatorial ring ($\theta = \pi/2$), each particle has a 50:50 chance of scattering into each region, regardless of collision energy. Observe that another extreme case exists when apertures are placed at $\theta \approx 0$ and π (i.e. on both sides of the collision axis). Since the scattering occurs predominantly over small-angles for high energies (see Fig. 2.8(a)), particle 1 (2) scatters into the $\theta \approx 0$ (π) region.

In summary, the maximum pairwise coherence of 1/2 is reached when $ka \rightarrow 0$ (see Fig. 2.9), which corresponds the Bell triplet state $|\Psi^+\rangle$. At large collision energies $ka \rightarrow \infty$ coherence reduces to zero, arising in the mixed state $\rho' \rightarrow (|1,2\rangle\langle 1,2| + |2,1\rangle\langle 2,1|)/2$, and the loss of entanglement between the BB scattered pair.¹¹ The hard sphere model is therefore a surprisingly insightful model. In particular, a collision is characterised by the so-called (s-wave) scattering length a , which corresponds to the hard sphere radius that captures the universal behaviour at low collision energies [97]. For the collision of 2^3S_1 helium between $m_J = 0$ and 1 that we investigate in this thesis, the s-wave scattering length is $a_{1,0} \approx 7.5$ nm $\approx 120a_0$ [102], where a_0 is the Bohr radius. The experiment begins with an ultracold quantum gas of helium from which the pairwise collision is initiated by accelerating half of the gas with a laser induced coherent 2-photon recoil process (detailed in Sec-

¹¹This state $\rho'(C) = 1/2 |1,2\rangle\langle 1,2| + C |1,2\rangle\langle 2,1| + C |2,1\rangle\langle 1,2| + 1/2 |2,1\rangle\langle 2,1|$, parametrised by the coherence $-1/2 \leq C \leq 1/2$ (see Fig. 2.9), turns out to be particle entangled for all C , except trivially at $C = 0$. This is readily seen from computing the negativity (an entanglement witness that vanishes for all separable states [32]) of the density matrix which gives $\mathcal{N}(\rho'(C)) = |C|$. Suffice to say, reduced coherence leads to the state having, still a useful, but lesser value as a resource for quantum information tasks, such as an imperfect quantum teleportation [53].

tion 2.3). This indeed corresponds to the s-wave scattering regime, since the collision momentum from $\lambda \approx 1083\text{ nm}$ photons results in the collision parameter $ka = \sqrt{2}(2\pi/\lambda)a_{1,0} \approx 0.06 \ll 1$ (by conservation of momentum $\hbar k_{\text{atom}} = \hbar k_{\text{photon}}$; the factor of $\sqrt{2}$ comes from geometric considerations in the sum of 2-photon recoils, as discussed in Section 2.3).

A collision of Bose-Einstein condensates

A collision of two atoms in isolation, discussed above, is however an impractical method as an entangled atomic pair source due to its extremely low yield.¹² The problem is two-fold since the scattering length of atoms are generally on the order of nanometres, and even if a collision is deterministic only a single pair is created.

A simple way forward to increase the rate of pair generation is by colliding many atoms simultaneously, which we picture as the collision of counter-propagating, high intensity atomic beams. However, since every scattered atom is identical there must be a clear way to distinguish individual entangled atomic pairs. Ideally every scattered atom must be distinguishable from the beam, and its entangled counterpart easily identifiable. This requirement is met when the atomic beams have minimal uncertainty in their position and velocity profile at the point of collision, reminiscent of the laser beam in optics. These properties are exhibited by the coherent matter-wave analog of lasers called Bose-Einstein condensates (BEC), discussed in further detail in Section 2.3.2. An archetypal feature of a BEC is the macroscopic occupation of the ground state by the constituent bosonic particles (integer spin).¹³ Throughout this thesis, we utilise BECs as a means for the generation of entangled atomic pairs, and refrain from discussing many of their other fascinating properties that is central to the vibrant field of quantum gases.¹⁴

Here we treat a collision of Bose-Einstein condensates in the identical boson picture. The quantum field formalism is required over the particle picture to capture both number fluctuations arising from spontaneous processes, and quantum statistical effects from particle indistinguishability, in a natural manner. Let us denote the field operator of the many-body atomic system by $\hat{\Psi}(\mathbf{r}, t)$, obeying the bosonic commutation relation $[\hat{\Psi}(\mathbf{r}, t), \hat{\Psi}^\dagger(\mathbf{r}', t)] = \delta(\mathbf{r} - \mathbf{r}')$. For dilute gases at ultracold temperatures, the only interatomic interaction is due to binary collisions, and at such low energies these are s-wave collisions for most common atomic species. The Hamilton-

¹²One of the holy grails for fundamental chemistry is the experimental control of isolated molecular interactions [103]. By configuring individual atoms with tightly confining optical tweezers, the experimentalist have recently been able to achieve both a cooling of thermal motions to quantum regime, and a high probability for a collision, and a subsequent molecular formation, to happen [104].

¹³A weakly interacting Bose gas, such as a dilute atomic gas, undergoes a quantum phase transition across a critical temperature (typically around $1\text{ }\mu\text{K}$), roughly when the individual atomic wavepackets begin to overlap (i.e. thermal Broglie wavelength is comparable to the mean interatomic distance).

¹⁴Interested readers should refer to Refs. [77, 105].

nian of the many-body system can then be given by

$$\hat{H} = \int d\mathbf{r} \hat{\Psi}^\dagger \left(-\frac{\hbar^2 \nabla^2}{2m} \right) \hat{\Psi} + \frac{g}{2} \int d\mathbf{r} \hat{\Psi}^\dagger \hat{\Psi}^\dagger \hat{\Psi} \hat{\Psi} + \int d\mathbf{r} \hat{\Psi}^\dagger V(\mathbf{r}) \hat{\Psi}, \quad (2.33)$$

where the terms correspond to the total kinetic energy, the effective contact interaction¹⁵ ($g = 4\pi\hbar^2 a/m$, where a is the s-wave scattering length and m the mass of an atom), and the external potential $V(\mathbf{r})$, respectively.

Recall that a macroscopic number of atoms normally occupy the same single particle wavefunction $\psi(\mathbf{r}, t)$ (the condensate) in a BEC, normalised such that $\int d\mathbf{r} |\psi(\mathbf{r}, t)|^2 = N$ where N is the number of condensed atoms. In the field theoretical analysis of BECs, the many-body field operator may be treated as the complex-valued condensate wavefunction (since any action of creation/annihilation scales the macroscopic state simply by a complex number; see Ref. [77]), which can be solved by a non-linear Schrödinger equation (called the Gross-Pitaevskii equation) that we will soon encounter. Such a mean-field description of the BECs provides a powerful understanding of the macroscopic quantum gas, such as its density profile, and thermodynamic functions including the phase transition [107], for instance. Beyond mean-field theory is required, however, to capture many other wonders of BECs, most notably their collective excitations which lead to pair correlations and superfluidity [108].

A fruitful step going beyond the mean-field theory is to consider a small correction to the classical condensate wavefunction by a quantum field fluctuation $\hat{\delta}(\mathbf{r}, t)$. This is explicitly a bosonic field operator satisfying the commutation relation

$$[\hat{\delta}(\mathbf{r}, t), \hat{\delta}^\dagger(\mathbf{r}', t)] = \delta(\mathbf{r} - \mathbf{r}'),$$

with negligible occupation compared to the condensate ($\int d\mathbf{r} \langle \hat{\delta}^\dagger(\mathbf{r}, t) \hat{\delta}(\mathbf{r}, t) \rangle \ll N$), which gives rise to particle-like phenomena and correlations, absent in the macroscopic condensate description [108]. In fact, sometimes quantum field theory alone captures the most prominent aspects of interactions in BECs. This is indeed the case for the scattering halo generated in a collision of BECs as we show below (see Fig. 2.10), which has received much research interest.¹⁶

Following our discussion above, we may describe the two colliding BECs by the mean-field wavefunction $\psi(\mathbf{r}, t) = \psi_{+Q}(\mathbf{r}, t) + \psi_{-Q}(\mathbf{r}, t)$, where $\pm\hbar\mathbf{Q}$ is the mean momentum of each condensate. Then as long as the macroscopic BEC wavefunction remains negligibly affected by the scattered product, the many-body field operator will be given by

$$\hat{\Psi}(\mathbf{r}, t) = \psi_{+Q}(\mathbf{r}, t) + \psi_{-Q}(\mathbf{r}, t) + \hat{\delta}(\mathbf{r}, t), \quad (2.34)$$

called the Bogoliubov approximation [105]. As we show below, the dynamics of

¹⁵A two-body contact pseudo-potential $V_{\text{int}}(\mathbf{r}, \mathbf{r}') = (g/2)\delta(\mathbf{r} - \mathbf{r}')$ arises in the field operator formulation for the many-body system of bosons with hard-sphere interaction [106], which is appropriate in the s-wave scattering regime.

¹⁶Among many investigations, a few notable works investigating correlations in the scattering halo are experimental works in Refs. [89, 109, 110, 111, 112, 22, 112], and theoretical works in Refs. [113, 114, 115, 116, 117, 118].

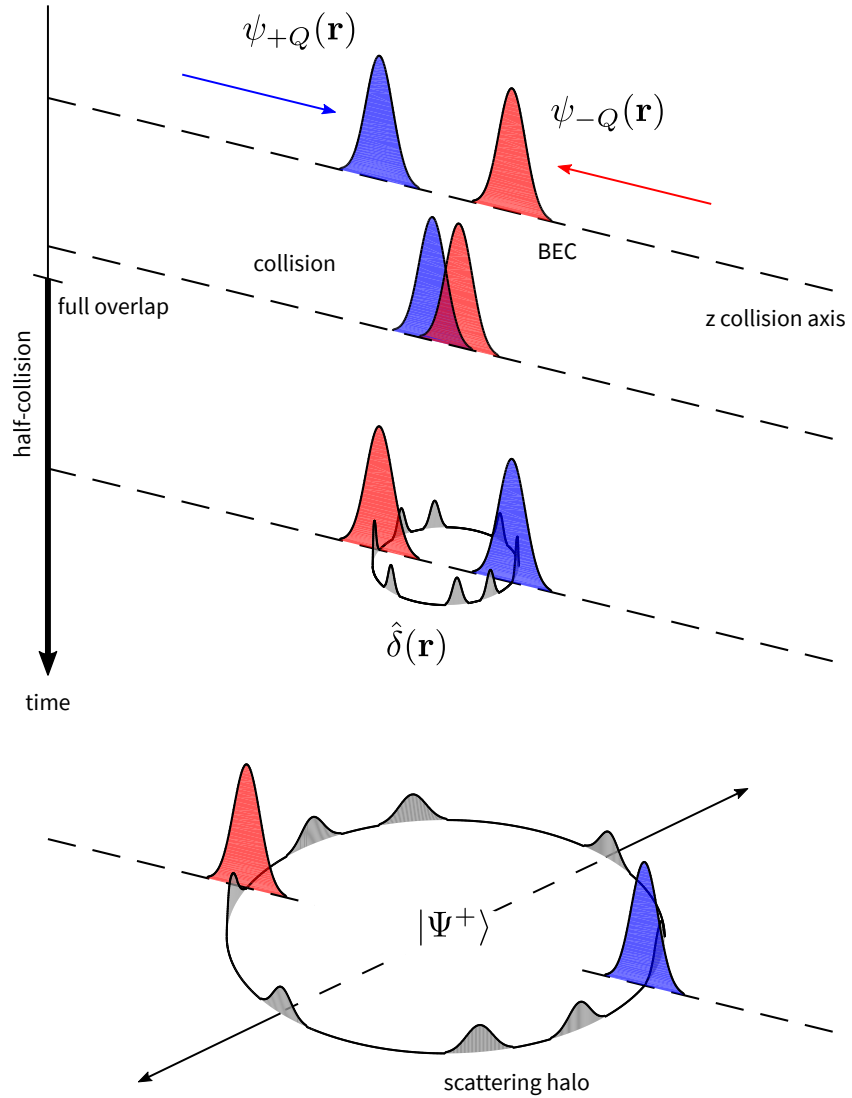


Figure 2.10: A schematic of a collision between two BECs (colours indicate spin state of BECs). The spontaneous scattering halo $\hat{\delta}(\mathbf{r})$ is composed of BB scattered atom pairs entangled as $|\Psi^+\rangle$. A half-collision begins with the two condensates separating from a complete spatial overlap, rather than approaching from an initial separation.

condensate and quantum fluctuation may be separated in the Heisenberg equation of motion for the field operator given by

$$\begin{aligned} i\hbar \frac{\partial}{\partial t} \hat{\Psi}(\mathbf{r}, t) &= [\hat{\Psi}(\mathbf{r}, t), \hat{H}] \\ &= \left(-\frac{\hbar^2 \nabla^2}{2m} + g \hat{\Psi}^\dagger(\mathbf{r}, t) \hat{\Psi}(\mathbf{r}, t) + V(\mathbf{r}) \right) \hat{\Psi}(\mathbf{r}, t). \end{aligned} \quad (2.35)$$

We require the number of scattered pairs to be small for their distinguishability, therefore the scattering product will be a small fraction of the condensate as will later be verified experimentally. We may therefore assume that the BEC wavefunctions are not affected by the small quantum fluctuations, and solve Eq. (2.33) in the mean field approximation called the Gross-Pitaevskii equation (GPE) $i\hbar \partial_t \psi(\mathbf{r}, t) = \left(-\hbar^2 \nabla^2 / 2m + g|\psi(\mathbf{r}, t)|^2 + V(\mathbf{r}) \right) \psi(\mathbf{r}, t)$ [119]. In most situations the condensate wavefunction resembles an inverted parabola, since experiments typically prepare BEC in the ground state of a harmonic trapping potential $V(\mathbf{r}) = (m/2)(\omega_x^2 x^2 + \omega_y^2 y^2 + \omega_z^2 z^2)$ [120]. As the condensates collide and separate, we assume for simplicity that their shapes are identical and symmetric, and propagate freely without expansion, so that their wavepackets are

$$\psi_{\pm Q}(\mathbf{r}, t) = \sqrt{n(\pm \mathbf{r}')} e^{\mp i \mathbf{Q} \cdot \mathbf{r}'} e^{-i(\hbar Q^2 / 2m)t}, \quad (2.36)$$

where n is the condensate density distribution containing a large number of atoms $N = \int d\mathbf{r} n(\mathbf{r})$ in each $\psi_{\pm Q}$, \mathbf{r} the collision c.m. coordinate, $\pm \mathbf{r}'(t) = \pm(\mathbf{r} - [(\hbar \mathbf{Q}/m)t + \mathbf{r}_0])$ the relative coordinate from each condensate's c.m., and $\pm \mathbf{r}_0$ the origin of condensates at $t = 0$.

The dynamics of the quantum fluctuation can now be determined by substituting the Bogoliubov approximation of the field operator Eq. (2.34) into the Heisenberg equation of motion Eq. (2.35). If the collision energy dominates over the condensate mean field interaction energy $\hbar^2 Q^2 / 2m \gg gn$, and we keep terms up to first order in $\hat{\delta}$, then the equation simplifies to

$$i\hbar \frac{\partial}{\partial t} \hat{\delta}(\mathbf{r}, t) = -\frac{\hbar^2 \nabla^2}{2m} \hat{\delta}(\mathbf{r}, t) + 2g \psi_{+Q}(\mathbf{r}, t) \psi_{-Q}(\mathbf{r}, t) \hat{\delta}^\dagger(\mathbf{r}, t). \quad (2.37)$$

Since the scattered many-body state should consist of counter-propagating pairs, we decompose the quantum field fluctuation into the plane wave modes $\hat{\delta}(\mathbf{r}, t) = (2\pi)^{-3/2} \int d\mathbf{k} \hat{a}_{\mathbf{k}}(t) e^{i\mathbf{k} \cdot \mathbf{r}}$, where $\hat{a}_{\mathbf{k}}$ is the annihilation operator for the momentum mode \mathbf{k} , satisfying the bosonic commutation relation $[\hat{a}_{\mathbf{k}}(t), \hat{a}_{\mathbf{k}'}^\dagger(t)] = \delta_{\mathbf{k}, \mathbf{k}'}$. By also applying the plane wave decomposition for the condensate wavepackets, and collecting all terms for a given \mathbf{k} -mode, we arrive at the equation of motion in the rotating frame of the collision energy $e^{-i(\hbar Q^2 / 2m)t} \hat{a}_{\mathbf{k}} \rightarrow \hat{a}_{\mathbf{k}}$

$$i\hbar \frac{d}{dt} \hat{a}_{\mathbf{k}}(t) = \hbar \Delta_k \hat{a}_{\mathbf{k}}(t) + \frac{1}{(2\pi)^{3/2}} \int d\mathbf{q} \hbar \tilde{\chi}(\mathbf{q}, t) \hat{a}_{-\mathbf{k}+\mathbf{q}}^\dagger(t), \quad (2.38)$$

where $\Delta_k = \hbar(k^2 - Q^2)/2m$ is the detuning between scattered and colliding atoms, and

$$\tilde{\chi}(\mathbf{q}, t) = \frac{2g}{(2\pi)^{3/2}} \int d\mathbf{r} \sqrt{n(\mathbf{r}'(t))n(-\mathbf{r}'(t))} e^{-i\mathbf{q}\cdot\mathbf{r}} \quad (2.39)$$

is the effective coupling between momentum modes, given by the Fourier transform of the interaction between the colliding condensates $2g\psi_{+Q}\psi_{-Q}e^{2i(\hbar Q^2/2m)t}$ in the rotating frame.

We can illustrate the physics by making a few more simplifications. Let us assume that scattering predominantly occurs when the condensates are fully overlapped, and that the momentum distribution of the condensates are sharply peaked around $\pm\mathbf{Q}$ like a macroscopic plane wave, such that n is uniform. From Eq. (2.39) the effective coupling is then simply a delta function $\tilde{\chi}(\mathbf{q}) = 2gn/\hbar\delta(\mathbf{q}) \equiv \chi\delta(\mathbf{q})$ during the overlap. Equation (2.38) then simplifies dramatically, since each momentum mode $\hat{a}_{\mathbf{k}}$ couples only to its directly oppositely scattered mode $\hat{a}_{-\mathbf{k}}$, given by the pairwise coupled equations

$$\frac{d}{dt} \hat{a}_{\mathbf{k}}(t) = -i\Delta_k \hat{a}_{\mathbf{k}}(t) - i\chi \hat{a}_{-\mathbf{k}}^\dagger(t). \quad (2.40)$$

The Hamiltonian expressed in the momentum mode creation/annihilation operators, giving rise to Eq. (2.40) then clearly must be (momentum modes are discretised for simplicity)

$$\hat{H} = \sum_{\mathbf{k}} \hbar \left(\Delta_k \hat{a}_{\mathbf{k}}^\dagger \hat{a}_{\mathbf{k}} + \Delta_k \hat{a}_{-\mathbf{k}}^\dagger \hat{a}_{-\mathbf{k}} + \chi \hat{a}_{\mathbf{k}}^\dagger \hat{a}_{-\mathbf{k}}^\dagger + \chi \hat{a}_{\mathbf{k}} \hat{a}_{-\mathbf{k}} \right), \quad (2.41)$$

which is the well known Hamiltonian describing parametric amplification in quantum optics [79]. The solution of Eq. (2.40) and Eq. (2.41) is given by

$$\hat{a}_{\mathbf{k}}(t) = \alpha_{\mathbf{k}}(t) \hat{a}_{\mathbf{k}}(0) + \beta_{\mathbf{k}}(t) \hat{a}_{-\mathbf{k}}^\dagger(0), \quad (2.42)$$

where the coefficients are

$$\alpha_{\mathbf{k}}(t) = \left[\cosh\left(\sqrt{\chi^2 - \Delta_k^2}t\right) - \frac{i\Delta_k}{\sqrt{\chi^2 - \Delta_k^2}} \sinh\left(\sqrt{\chi^2 - \Delta_k^2}t\right) \right] \quad (2.43)$$

$$\beta_{\mathbf{k}}(t) = -\frac{i\chi}{\sqrt{\chi^2 - \Delta_k^2}} \sinh\left(\sqrt{\chi^2 - \Delta_k^2}t\right). \quad (2.44)$$

Let us now determine the many-body state of the scattering halo. For simplicity we consider only the resonant s-wave scattering modes $\Delta_k = 0$ ($|\mathbf{k}| = Q$), which are far away from the condensates so that initially they are unoccupied. We denote the Fock states $\otimes_{\mathbf{k}} |n_{\mathbf{k}}\rangle_{\mathbf{k}}$ where each momentum mode \mathbf{k} is occupied by exactly $n_{\mathbf{k}}$ atoms. Then the scattering halo evolves from the initial multimode vacuum state $|0\rangle$

to

$$|\delta(t)\rangle = \prod_{\mathbf{k}} \exp\left(\chi t (\hat{a}_{\mathbf{k}}^\dagger \hat{a}_{-\mathbf{k}}^\dagger - \hat{a}_{\mathbf{k}} \hat{a}_{-\mathbf{k}})\right) |0\rangle \quad (2.45)$$

$$= \bigotimes_{\mathbf{k}} \left(\sqrt{1 - (\tanh \chi t)^2} \sum_{n=0}^{\infty} (\tanh \chi t)^n |n\rangle_{\mathbf{k}} |n\rangle_{-\mathbf{k}} \right) \quad (2.46)$$

$$= \bigotimes_{\mathbf{k}} |\tanh \chi t\rangle_{(\mathbf{k}, -\mathbf{k})}, \quad (2.47)$$

where in the first line the mode operators were shifted by a constant phase to express the Hamiltonian in a familiar form. This is expanded into Fock states in Eq. (2.46) where the multimode state is clearly factorised into pairs of opposite momentum modes $(\mathbf{k}, -\mathbf{k})$ (see Ref. [78]). Notice that each mode-pair is occupied by the name number of atoms, at a probability that decreases exponentially with the atom number. This two-mode state is denoted in Eq. (2.47) by

$$|\zeta\rangle_{(\mathbf{k}, -\mathbf{k})} = \sqrt{1 - \zeta^2} \sum_{n=0}^{\infty} \zeta^n |n\rangle_{\mathbf{k}} |n\rangle_{-\mathbf{k}}, \quad (2.48)$$

which is called the two-mode squeezed vacuum (TMSV) and ζ the squeezing parameter ($|\zeta| \leq 1$). Each unitary operator in the operator product in Eq. (2.45) is a particular instance of the two-mode squeezing operator $S(G) = \exp(G \hat{a}_1^\dagger \hat{a}_2^\dagger - G^* \hat{a}_1 \hat{a}_2)$ acting on a unique pair of BB-modes $(\mathbf{k}, -\mathbf{k})$ [79]. The descriptor ‘squeezing’ originates from the effect this operator has on a coherent state, whereby uncertainties in the field quadratures¹⁷ are reduced and increased with respect to vacuum fluctuations [121]. Indeed the generation of squeezed light and spin squeezed atomic ensemble relies on the realisation of the squeezing operator. As we have shown above for the atomic case, this is produced by collisions. However spin squeezed states require squeezing of an initially coherent state (BEC), and therefore happens when scattered pairs are indistinguishable from the condensate mode – this becomes more obvious later when we consider atomic spin.

There are a few useful features of the TMSV that we illustrate below. The first is the single-mode atom number statistics, where the unobserved mode is traced over, giving the thermal (exponential decay) number distribution

$$p_n = (1 - \zeta^2) \zeta^{2n} = \bar{n}^n / (1 + \bar{n})^{n+1}, \quad (2.49)$$

characterised by the mean (single-)mode occupancy $\bar{n} = (\zeta^{-2} - 1)^{-1}$, and the super-Poissonian atom number fluctuation $(\Delta n)^2 = \bar{n}^2 + \bar{n}$. Next are the correlations that can inform us of structure in fluctuations. An obvious one is that two modes are per-

¹⁷For a boson annihilation operator \hat{a} , we can define the phase operator

$$\hat{X}(\theta) = \hat{a}_i e^{-i\theta} + \hat{a}_i^\dagger e^{i\theta}.$$

This obeys the canonical commutation relation between conjugate phases (quadratures) $[\hat{X}(\theta), \hat{X}(\theta + \pi/2)] = -2i$ [79], and provides an oscillator picture of the system useful in quantum optics.

fectly correlated in atom number each realisation, such that $n_{\mathbf{k}} = n_{-\mathbf{k}}$, which is an extreme demonstration of *number squeezing* $\Delta n < \bar{n}$ (i.e. sub-Poissonian fluctuation), since the *number difference* $\delta n = n_{\mathbf{k}} - n_{-\mathbf{k}}$ for TMSV $\Delta(\delta n) = 0$. An ideal pair source would require an on-demand, deterministic generation of a single perfectly correlated pair. However a spontaneous scattering halo can emit multiple pairs into the same mode with exponentially decreasing but finite probability, as we state above. Such a distribution of particle number is analogous to the photon number statistics of thermal light, and exhibits a peculiar correlation between particles in the same mode, called bosonic bunching [122]. Suffice to say, indistinguishable bosons tend to bunch into an identical mode, hence multiple scattered atomic pairs are not independent. Indeed, the bunching effect is rather small in the spontaneous scattering regime, where less than one particle is created per mode.

In quantum field theory these effects are described by the second-order, number/intensity correlation function developed by Glauber [123]

$$g^{(2)}(\mathbf{k}_1, t_1; \mathbf{k}_2, t_2) = \frac{\langle : \hat{n}(\mathbf{k}_1, t_1) \hat{n}(\mathbf{k}_2, t_2) : \rangle}{\langle \hat{n}(\mathbf{k}_1, t_1) \rangle \langle \hat{n}(\mathbf{k}_2, t_2) \rangle}, \quad (2.50)$$

where $: O :$ corresponds to the normal ordering of the creation and annihilation operators in expressing O (\hat{a} located right-side of \hat{a}^\dagger). Thus the numerator of Eq. (2.50) is given explicitly as $\langle \hat{a}_{\mathbf{k}_1}^\dagger(t_1) \hat{a}_{\mathbf{k}_2}^\dagger(t_2) \hat{a}_{\mathbf{k}_2}(t_2) \hat{a}_{\mathbf{k}_1}(t_1) \rangle$, and measures a particular two-body correlation in the many-body system. One can interpret $g^{(2)}$ roughly as *the relative likelihood of observing the second event conditioned on the first, versus the marginal likelihood of the second event without any prior knowledge about the first*. Indeed we observe Bose enhancement for two different atoms to bunch into a single, *collinear* (CL; $\mathbf{k}_1 = \mathbf{k}_2$) mode $g^{(2)}(\mathbf{k}, t; \mathbf{k} + \delta\mathbf{k}, t) = 2$. In a complementary manner, the conservation of momentum in pairwise scattering gives a much stronger bunching into *back-to-back* (BB; $\mathbf{k}_1 = -\mathbf{k}_2$) modes $g^{(2)}(\mathbf{k}, t; -\mathbf{k}, t) = 2 + 1/\bar{n}$. The super-bunching of BB-correlated pairs, namely $g^{(2)} > 2$, observed at low mode occupancy characterises the purity of the pair source, namely its resemblance to an ideal single pair source.

Let us now consider what happens if the atoms have internal states α , so that the original many-body Hamiltonian Eq. (2.33) must be generalised to a spinor field that describes interactions between these spin components Ψ_α (in our case, $\alpha \in \{-1, 0, 1\}$ is the Zeeman sublevels of He^*). Assuming again only a two-body contact interaction to describe collisions in and between ultracold gases, the system is given by (using the Einstein summation convention)

$$\begin{aligned} \hat{H} = \int d\mathbf{r} \Psi_\alpha^\dagger \left(-\frac{\hbar^2 \nabla^2}{2m} \right) \Psi_\alpha + \frac{1}{2} \int d\mathbf{r} \Psi_\alpha^\dagger \Psi_\beta^\dagger (g_{\alpha,\beta} \delta_{\alpha,\alpha'} \delta_{\beta,\beta'} + g'_{\alpha,\alpha',\beta,\beta'}) \Psi_{\beta'} \Psi_{\alpha'} \\ + \int d\mathbf{r} \Psi_\alpha^\dagger V(\mathbf{r}) \Psi_\alpha. \end{aligned} \quad (2.51)$$

Note that g and g' denote the interaction strengths (tensors) for the particular elastic and spin-changing collisions, respectively. Let us consider the situation we wish

to realise experimentally to create spin entangled atom pairs: a collision of two oppositely spin-polarised BECs. We may ignore spin-changing collisions, since an appropriate choice of the two atomic states (denoted by \uparrow and \downarrow) may be decoupled from any near-resonant inelastic channels by the conservation of angular momentum. Indeed, a collision between $m_J = 0$ and 1 states of the He* has no inelastic channel within the $\hat{J} = 1$ triplet that conserves angular momentum. The Bogoliubov approximated spinor field generalised from Eq. (2.34) then takes the form $\Psi(\mathbf{r}, t) = \psi_{\uparrow,+Q}(\mathbf{r}, t) + \psi_{\downarrow,-Q}(\mathbf{r}, t) + \hat{\delta}(\mathbf{r}, t)$. Subsequent steps follow similarly as before, and we again arrive at the central result for the quadratic Hamiltonian in the plane wave amplitudes (evaluated at resonance for simplicity)

$$\hat{H} = \sum_{\mathbf{k}} \hbar \chi \left(\hat{a}_{\uparrow}^{\dagger}(\mathbf{k}) \hat{a}_{\downarrow}^{\dagger}(-\mathbf{k}) + \hat{a}_{\downarrow}^{\dagger}(\mathbf{k}) \hat{a}_{\uparrow}^{\dagger}(-\mathbf{k}) \right) + \text{h.c.}, \quad (2.52)$$

where $\chi = 2gn/\hbar$ is the interaction strength, defined as before. A crucial distinction to this spinor Hamiltonian from Eq. 2.41 is that every scattered atom is now perfectly correlated with a twin that is oppositely polarised in spin, as well as BB scattered in momentum. Since creation and annihilation operators between different spins commute, the time evolution factorises once again into two-mode squeezing operators acting on opposite momentum-spin pairs $((\mathbf{k}, \uparrow), (-\mathbf{k}, \downarrow))$ and $((\mathbf{k}, \downarrow), (-\mathbf{k}, \uparrow))$. A particular pair of counter-propagating modes $(\mathbf{k}, -\mathbf{k})$ in the scattering halo therefore evolves according to

$$|\delta(t)\rangle_{(\mathbf{k}, -\mathbf{k})} = \exp\left(\hbar\chi\hat{a}_{\uparrow}^{\dagger}(\mathbf{k})\hat{a}_{\downarrow}^{\dagger}(-\mathbf{k}) - \text{h.c.}\right) \exp\left(\hbar\chi\hat{a}_{\downarrow}^{\dagger}(\mathbf{k})\hat{a}_{\uparrow}^{\dagger}(-\mathbf{k}) - \text{h.c.}\right) |0\rangle \quad (2.53)$$

$$= (1 - (\tanh \chi t)^2) \sum_{n,m=0}^{\infty} (\tanh \chi t)^{n+m} |n\rangle_{\mathbf{k}\uparrow} |m\rangle_{\mathbf{k}\downarrow} |m\rangle_{-\mathbf{k}\uparrow} |n\rangle_{-\mathbf{k}\downarrow} \quad (2.54)$$

$$= |0\rangle + \chi t \underbrace{(|\uparrow\rangle_{\mathbf{k}} |\downarrow\rangle_{-\mathbf{k}} + |\downarrow\rangle_{\mathbf{k}} |\uparrow\rangle_{-\mathbf{k}})}_{|\Psi^+\rangle} + \mathcal{O}((\chi t)^2), \quad (2.55)$$

where in the last line we used a particle state notation to emphasize the generation of $|\Psi^+\rangle$ Bell state. Notice from Eq. (2.55), if the total number of particles in the \mathbf{k} -mode can be verified to be 1, without measuring its spin, this heralds the generation of $|\Psi^+\rangle$ into $\pm\mathbf{k}$. Although such heralding scheme requires efficient detection that is out of reach in our experiment, we are still able to treat the scattering halo as a pair source, since the likelihood of multiple pair occupation in a single mode is negligible at the low mode occupancies $\bar{n} \approx \chi t \approx 0.1$ we can operate.

Although the pair generation is still probabilistic, the advantage of utilising a collision of atomic beams is clearly in the highly parallel generation of entangled pairs per pulse. Indeed for M near-resonant and distinguishable \mathbf{k} -spin scattering modes, a single BEC collision generates on average as many as $\bar{n}M$ individual $|\Psi^+\rangle$ pairs, where at a reasonable mode occupation $\bar{n} \approx 0.1$ already gives $\approx 90\%$ chance for every non-empty mode (a detection) to be individually occupied (see Eq. 2.49). Let us now consider the case when more than one pair is detected in the same scattering mode. Here the indistinguishability of each atom pair prevents us from post-processing

which two atoms are entangled, even in principle. One may picture this uncertainty as if initially distinguishable pairs with two nearby BB momenta are coarse binned into the same momentum mode. Fortunately the physics of finite mode size is clear without needing to solve Eq. (2.38) to allow for multimode coupling¹⁸, since its origin can be explained by the finite size of the colliding condensates. A localised wavepacket of condensate imposes a finite volume to the \mathbf{k} -scattering mode

$$\delta\tilde{V} \approx (2\pi)^{3/2}\tilde{\sigma}^3 \quad (2.56)$$

called the mode volume (tilde indicates momentum space) matched to the coherence volume of the source in momentum, where $\tilde{\sigma}$ is the (geometric mean) Gaussian width of the condensate's momentum profile [124]. Detectors can easily resolve individual atom's momentum to a precision better than an order of magnitude below the condensate width (see Section 2.3 for details). Still, indistinguishability cannot be resolved by better detection. Consider an ideal \mathbf{k} -detection (i.e. it does not measure spin or otherwise destroy the atom) of two BB pairs which simultaneously lie within a single correlation volume, corresponding to terms in Eq. (2.54) satisfying $n + m = 2$. Such an event heralds the four-particle mode-entangled state $1/\sqrt{3}(|2,0,0,2\rangle + |1,1,1,1\rangle + |0,2,2,0\rangle)$ (where $|a,b,c,d\rangle = |a\rangle_{\mathbf{k}\uparrow}|b\rangle_{\mathbf{k}\downarrow}|c\rangle_{-\mathbf{k}\uparrow}|d\rangle_{-\mathbf{k}\downarrow}$), which cannot be separated into two Bell states. Since the collision velocity determines the radius of the scattering halo $p = \hbar Q$, which has a finite shell thickness $\delta p \approx \tilde{\sigma}$ reflecting the uncertainty of source, the total number of modes in a scattering halo is given by

$$M = \tilde{V}/\delta\tilde{V}, \quad (2.57)$$

where

$$\tilde{V} \approx 4\pi\sqrt{2\pi}(\hbar Q)^2\delta p \quad (2.58)$$

is the total volume of the scattering halo. Of course an additional factor of 2 should come from spin for the system considered in Eq. (2.55). In our experiment, M of the order of 10^3 has been realised at modest collision velocities by reducing BEC widths to $\tilde{\sigma}/\hbar Q \sim 0.03$ using low trapping frequencies. In another work not contained in this thesis, a multiple parallel collision of BEC was realised to increase pair generation additionally by around ten-fold, and was used to demonstrate atomic ghost imaging [22].

In summary, our theoretical analysis of colliding BECs yields a consistent picture with that of two atoms. Atoms are scattered in pairs into the initially empty, opposite momentum modes ($\mathbf{k}, -\mathbf{k}$) in all directions forming the scattering halo. From the elasticity of the collision, the scattered pair has approximately the same momentum before and after $|\mathbf{k}| \approx Q$, such that the scattering halo is a sphere of radius Q in momentum space.

¹⁸See Ref. [118] for the most sophisticated analysis to date, which includes the finite spatio-temporal broadening effects and condensate expansion during the collision.

2.2.3 Quantum correlations and nonlocality observed in atomic ensembles

Here we highlight a few quantum mechanical phenomena, ranging from number squeezing, to tests of nonlocality, that has been so-far observed in atomic pairs and spin squeezed ensembles.

Soon after atomic gas could be Bose condensed by evaporative cooling in magnetic traps, various experimental tools were developed to control and manipulate the ultracold atoms coherently. Among these techniques the simultaneous control of a condensate's momentum and spin was achieved by a precisely tuned pulse from two laser beams, called a two-photon stimulated *Raman transition* (see Section 2.3 for details). A collision of BECs is therefore realised by putting the condensate into an equal superposition of stationary and travelling wavepackets [89], as illustrated in Fig. 2.10. Strictly speaking, this method realises a half-collision, in which the collision begins fully overlapped (see Fig. 2.10), rather than separated [115]. Note that only a few other experimental techniques have demonstrated atomic pair generation, namely from a dynamical instability in an optical lattice [88], and collisional de-excitation in a 1D degenerate gas [87]. Compared to the highly multimode scattering halo ($M \sim 10^3$) these mechanisms have a significantly restricted number of resonant scattering modes since the trapping potential strongly affects the dispersion relation in FWM, and thus can produce twin atomic beams.

In 2002, the Ketterle group investigated BEC collisions for a wide range of scattered atom numbers to observe the spontaneous regime of FWM and the coherent amplification of matter-waves by Bosonic enhancement [125]. Interestingly, the first direct observation of pairwise scattering from colliding BECs [89] came a few years later by the Westbrook group using metastable helium. This is because of the extreme difficulty in resolving individual atoms in cold atom experiments, since most atomic species used in labs are either in their ground or low lying excited states, and are thus most commonly optically imaged at high densities. Helium is somewhat of an exception to other atomic species, since it can be cooled to BEC in a highly excited and metastable state, which allows single particle detection at a significantly higher efficiency (see Section 2.3 for details).

The ability to obtain atom number statistics around the scattering halo quickly led to demonstrating a correspondence between SFWM in quantum optics and the atomic scattering halo. Two notable results are the observation of relative number squeezing between opposite momentum modes [109], and the violation of the classical Cauchy-Schwarz inequality for number fluctuations [111]. Historic quantum optic experiments demonstrated from two beams of intensity $I_{1,2}(t)$ intensity squeezing from the sub-shot-noise fluctuation of the difference signal $[\Delta(I_1 - I_2)]^2 < \langle I_1 \rangle + \langle I_2 \rangle$ [126], and the violation of the classical Cauchy-Schwarz inequality $\langle I_1 I_2 \rangle^2 \leq \langle I_1^2 \rangle \langle I_2^2 \rangle$ [37]. These correlations are strictly forbidden in the classical field description of physical objects [127], such as Maxwell's theory of the electromagnetic field. The matter-wave on the other hand is a quantum description of atomic gases, where the classical particle description explains the above nonclassical correlation with little effort. The atomic pair source continues to be a fruitful system for fundamental interest in

quantum atom optics, enabling the recent demonstrations of the atomic Hong-Ou-Mandel effect [128] and atomic ghost imaging [22, 129]. Furthermore, recent efforts have shown promise towards a motional Bell test [130], in an analogy with the original photonic experiment by Rarity and Tapster [55]. Until now [101] however, none of these atomic pair sources verified quantum entanglement or nonlocality, where the latter admit no classical explanation whether it be framed in a particle or wave description [127].

A few proposals for realising the EPR paradox and Bell test with atomic pairs have interested experimentalists, and the technical challenges of these experiments are currently being addressed by some groups around the world (e.g. the Westbrook [130], and the Zeilinger group [69]). Such proposals approximate the original schema of the EPR paradox faithfully, such as in the position-momentum entangled state [131]. A motional Bell test as proposed in [70] (schematically identical to the seminal work by Rarity and Tapster [55]) is extremely challenging technically but will be significant since motional entanglement in massive systems has never been realised. Other outstanding proposals in this field (see Refs. [68] and [69]) also await experimental realisations, which reflects the practical complexities involved.

In experiments investigating spin squeezed ensembles, multipartite entanglement has received much interest recently. A many-body Bell correlation was detected in a spin squeezed BEC [84]. In that experiment, a multipartite Bell inequality was violated, but it relied on some prior assumptions for QM to hold for using collective measurements, since the detection system cannot resolve atoms individually. By an extension, observing genuine nonlocal correlations presents some challenges in that it becomes extremely challenging to spatially separate the subsystems. The current aim for such experiments is to demonstrate Bell correlations between spatially separated regions of the BEC, and even to create spatially separated Schrödinger cat states to observe quantum nonlocality in a massive mesoscopic system. Recently, experiments with an ultracold atomic ensemble have demonstrated EPR-steering within an ensemble [132], as well as verifying spatially separated entanglement [133] and EPR-steering [134, 135] between different parts of the condensate. A matter-wave homodyne technique was used to detect continuous variable EPR-steering first in Ref. [132] and then across a spatial separation in Ref. [135].

2.3 Experimental apparatus

A Bose-Einstein condensate of a dilute gas of metastable helium-4 (He^*) atoms is reproducibly achieved by a series of cooling techniques in a magnetic trap at ultra-high vacuum. Details of the He^* BEC apparatus along with some important physical mechanisms will be presented. The details of the Raman laser system will be presented, including details to the set-up of the optics and control system. This apparatus is responsible for the coherent control of momentum and internal state of He^* atoms in this thesis. Single atom detection by an MCP-DLD system resolves both individual He^* atoms' momentum vector and internal state. This is a crucial exper-

imental tool for the determination of pairwise generation of atoms, and the higher order coherence properties of the ensemble.

2.3.1 Metastable helium

The helium atom has unique atomic properties that distinguishes it from other atomic species studied in ultracold gases. Here we discuss the properties of its long-lived first excited state 2^3S_1 , called metastable helium (He^*), in relation to the generation of BEC, and quantum atom optic experiments. We show that the high internal energy stored in the He^* atom enables an unparalleled single particle detection and particle counting capabilities required to reveal quantum statistics and the demonstration of nonlocality. The unique detection capability has also been of much interest in exploring many-body physics with quantum gases [136], where a direct detection of individual atoms can reveal correlations hidden by a collective measurement. Furthermore the simple atomic structure of helium is well complemented by extremely precise theoretical predictions, and therefore precision spectroscopy of ultracold He^* provides a test of quantum electrodynamics for many different measurements.

Atomic structure

The key distinguishing feature of noble gases is the extremely large energy gap between the ground and first excited state (ranging from 8.8 eV for Xe^* to 19.8 eV for He^*). As such, there are no practical lasers at such short wavelengths ($\sim 100\text{ nm}$) which could optically manipulate noble gases in their ground state. When excited, however, noble gas atoms resemble the hydrogen atom in structure and energy levels, dictated by the single valence electron which is readily addressed optically. Thus unlike other atomic species in ultracold gases, the noble gases must first be prepared in an excited state for various laser cooling and control processes. Although the energy gap between the outer closed shell of a noble gas atom and the lowest unfilled s-shell can be extremely high, the first excited spin-triplet (total spin $S = 1$) state has a long lifetime, hence giving the term “metastable”.

For the helium-4 atom, which is the only isotope of helium discussed in this thesis and thus going forward we will simply refer to as He^* , the excitation energy of $1s2s\ ^3S_1$ is $E^* \approx 19.8\text{ eV}$, and the relevant few lower lying energy levels are shown in Fig. 2.11. A direct de-excitation to the ground state $\text{He}^* \rightarrow 1s^2\ ^1S_0$ is doubly forbidden, since the transition violates two separate electric dipole selection rules [137, 138]: 1. a spin-flip or other change in spin angular momentum is forbidden ($S = 1 \nrightarrow 0$) since spin does not couple to the dipole electric field, and 2. the orbital angular momentum L of the atom must change by 1 ($L = 0 \nrightarrow 0$) to account for the angular momentum of the emitted/absorbed photon. This gives rise to an extremely long lifetime of He^* by $7870(510)\text{ s}$ [137], which effectively allows He^* to be treated as a ground state in ultracold gas experiments, which are typically $\approx 30\text{ s}$ long (see Section 2.3.2 for details).

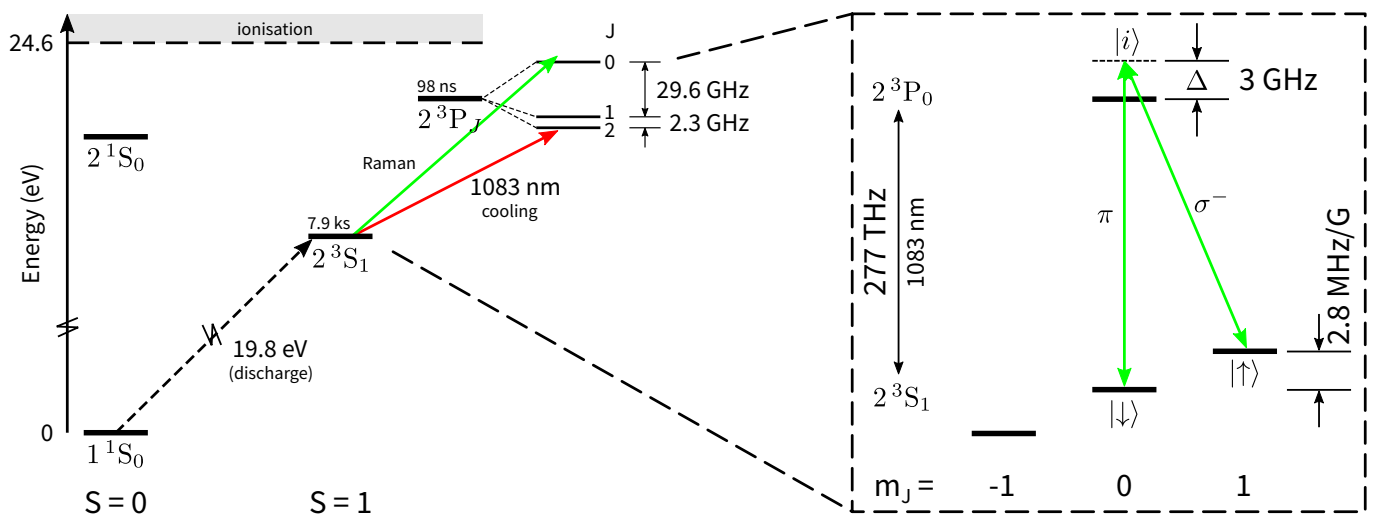


Figure 2.11: Helium level diagram for ground and first few excited states relevant for ultracold gas experiments. (left) The long-lived metastable helium 2^3S_1 is excited by HV discharge from ground state. Laser cooling is implemented by using the 1083 nm cycling transition 2^3P_2 (red arrow indicates the cooling laser transition). The three-fold degeneracy of He^* ($J = 1$) is split in a magnetic field by the Zeeman effect. $m_J = 1$ states are confined in a magnetic trap and evaporatively cooled to Bose-Einstein condensation with RF radiation. (right) A two-photon stimulated Raman transition (green arrow indicates the transitions driven by the Raman laser) is used to couple $m_J = 0$ and 1 , in a Λ scheme via an intermediate state detuned from the 2^3P_0 transition. Note for the atomic levels, the vertical axis is not to scale, but their ordering is correct, and the colours of arrows do not correspond to the actual wavelength of the transition.

Laser cooling

Bose-Einstein condensation in dilute gas of He* was first demonstrated by the Aspect and Leduc groups in 2001 [139, 140], and achieved at the ANU in 2007 [141]. Laser cooling and trapping techniques are essential tools for preparing an atomic ensemble around μK from room temperature. For He* the 1083.33 nm fast cycling transition $2^3\text{S}_1 \longleftrightarrow 2^3\text{P}_J$ with an upper state lifetime of $\tau \approx 98\text{ ns}$, and corresponding natural, full width at half maximum (FWHM) linewidth $\Gamma \equiv 1/\tau = 2\pi \times 1.6\text{ MHz}$, is used for laser cooling. The very short lifetime and closed cycle transition are clearly ideal atomic properties for ultracold gas experiments, since laser cooling relies on the effective radiative pressure emerging from a repetition of directed absorption and random emission process. Each photon absorption-scattering process from a near-resonant laser with wavevector \mathbf{k} imparts a change in atom's momentum by $\hbar(\mathbf{k} - \mathbf{k}_{\text{em}})$, where the recoil from the fluorescence $-\hbar\mathbf{k}_{\text{em}}$ averages to zero over many cycles. The time-averaged effective force on an atom is therefore [21]

$$\bar{\mathbf{F}} = \left\langle \frac{\Delta\mathbf{p}}{\Delta t} \right\rangle_t = \hbar\mathbf{k}\gamma, \quad (2.59)$$

where γ is the Lorentzian absorption rate of a photon for an atom with energy splitting $\hbar\omega_a$ moving at a velocity \mathbf{v} , given explicitly by

$$\gamma = \frac{s\Gamma/2}{1 + s + (2\Delta/\Gamma)^2}, \quad (2.60)$$

where $\omega = kc$ is the laser frequency, $\Delta = \omega - \omega_a - \mathbf{k} \cdot \mathbf{v}$ is the effective detuning from atomic resonance including the Doppler shift of light by the atom's motion, $s = I/I_{\text{sat}}$ is the saturation parameter of the laser intensity I , and $I_{\text{sat}} = \hbar\Gamma\omega^3/(12\pi c^2)$ is the saturation intensity of the atomic transition [21]. A monochromatic laser therefore imposes a velocity-dependent force on the atoms, and will be effective for the group of velocities which are Doppler shifted to near resonance $|\Delta| \lesssim (1 + s)\gamma/2$. In particular, the photon absorption rate of atoms increases with respect to light intensity, and eventually saturates at a maximum acceleration ($s \rightarrow \infty$)

$$\mathbf{a}_{\text{max}} = \hbar\mathbf{k}\Gamma/2m, \quad (2.61)$$

where m is the mass of the atom. In our experiment I is delivered by an external-cavity laser, where its design and characterisation is detailed in Chapter 3. This seed laser system was developed as a first part of my thesis, which led to an upgrade of the laser system for the lab.

Ionising collision

Although a single metastable helium atom in isolation is long-lived, it will readily decay to the ground state upon contact with other atoms or molecules M by Penning

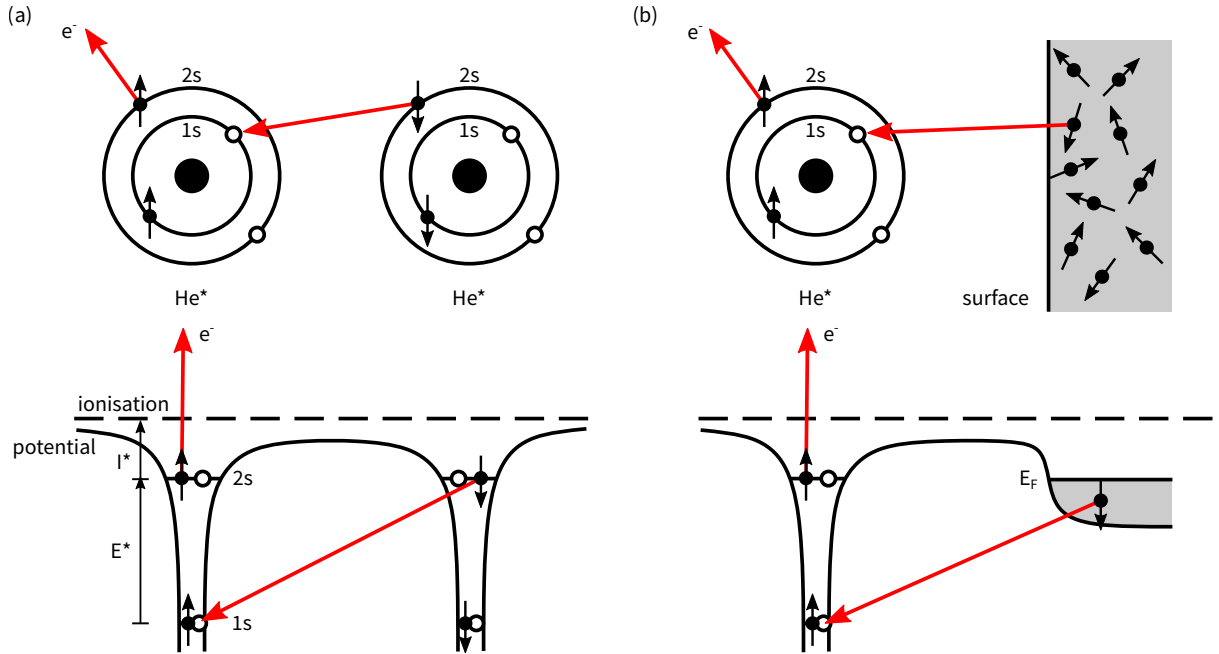
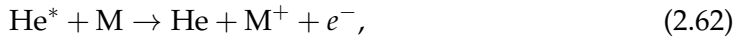


Figure 2.12: (a) Penning ionisation between two unpolarised He^* atoms. (b) Surface Penning ionisation.

ionisation



where an electron from atom M is captured by the 1s orbital, M^+ is the ion, and the release energy goes to eject the valence electron, no longer bound to the He atom. This decay process is highly favourable and covers general electronic matter M, since the most energetic electrons in atoms and solids are bound by $\lesssim 10\text{ eV}$ (except noble gases) [142]. This ionising property of He^* has two key impacts on our experiments, as discussed below.

First, confining the cold atom sample in an ultrahigh vacuum (UHV) chamber eliminates the lossy, inelastic collisions with the background thermal gas, which can in addition heat the sample by elastic collisions. Such environmental isolation does not address the inelastic collisions within the He^* sample, which would ultimately prevent it from reaching phase-space densities required for Bose-Einstein condensation. Notice that since Penning ionisation between two He^* is a capture of the other's valence 2s electron into a particular 1s orbital (see Fig. 2.12(a)), the scattering rate must depend on the relative spin states of the atoms, and thus the total spin. Consider an ionising collision of two spin-polarised He^* each in the $m_J = 1$ state: $\text{He}^* + \text{He}^* \rightarrow \text{He} + \text{He}^+ + e^-$. This process is forbidden since it cannot conserve spin angular momentum: the initial system has total spin of $S_i = 2$, whereas the scattered product is at most $S_f = 1$. Indeed the Penning ionisation rate of He^* is suppressed by 4 orders of magnitude in such spin-polarised collisions relative to the

unpolarised collisions which contain $S = 0, 1$ scattering channels [143]. At the final cooling stage, He^* is transferred to a non-dissipative trap in which an evaporative cooling technique [21] is used to achieve BEC, which I explain later. A magnetic trap, for instance a static quadrupole magnetic field, confines only the weak-field seeking Zeeman sublevel $m_J = 1$ (magnetic dipole is anti-parallel to field) near its centre, and therefore simultaneously provides a trapped and spin-polarised ensemble (see Section 2.3.2 for a discussion on the magnetic trap in our apparatus).

On the other hand, this ability to ionise material in a collision (2.62) enables a unique detection capability for He^* (and other metastable noble gases [143]) over other atomic species. This is the efficient operation of a single particle detector, which relies on the high probability of an electron being ejected from a surface upon an impact from He^* , as illustrated in Fig. 2.12(b). It is precisely the high excitation energy of He^* that is freed by surface de-excitation, which overcomes any typical work function (~ 5 eV) binding the surface electrons and thus causes the emission [144]. In particular, the ejected electron can be amplified into a well-localised electron cascade preserving information about the impact location and electronically detected [145]. Ultimately the electrical pulse position and timing information are coupled, such that the full 3D momentum of individual He^* atoms can be reconstructed, in a geometry where the atoms expand freely onto the detector located far from trap (see Section 2.3.4 for a discussion on the single atom detector in our apparatus).

Zeeman sublevels

Finally, consider the three-fold degeneracy in the $J = 1$ He^* with angular momentum projection number $m_J \in \{-1, 0, 1\}$, which we refer to as atomic spin. Since the total angular momentum of He^* consists entirely of electron spins aligned in parallel, the gyromagnetic relationship is simply that from an electron spin: namely the atom's magnetic moment is $\hat{\mu} = -g_L\mu_B\hat{j}$, where $g_L = 2$ is the Landé g-factor of He^* , and μ_B the Bohr magneton. Therefore m_J energy levels split in a static magnetic field $\mathbf{B} = B\hat{\mathbf{z}}$, according to the Zeeman interaction $U_B = -\hat{\mu} \cdot \mathbf{B}$, given explicitly by

$$\Delta U_B(m_J) = g_L\mu_B m_J B \equiv \hbar\gamma m_J B, \quad (2.63)$$

where $\gamma \approx 2\pi \times 2.80 \text{ MHz G}^{-1}$ is the gyromagnetic ratio (see Fig. 2.11).

Observe that in an inhomogeneous magnetic field $m_J = \pm 1$ are forced towards the direction of weaker (stronger) magnetic field, whereas $m_J = 0$ atoms are completely magnetically insensitive. This is the basis for magnetic trapping of neutral atoms, and inherent spin-polarisation of the He^* ensembles in particular to eliminate lossy, ionising collisions. By extension, the magnetic sensitivity allows one to perform an atomic spin-resolved detection via the Stern-Gerlach effect.

The internal state m_J of a He^* atom, the total angular momentum projection along the magnetic field, can be coherently controlled by radio frequency (RF) pulses by the Zeeman effect [146], as well as by two-photon processes as seen in Fig. 2.11 called the stimulated Raman transition. Although high-fidelity RF pulses are readily implemented, in practice they offer limited qubit control for He^* . In particular, RF

pulses manipulate only internal states, and furthermore couple all three m_J -states because the triplet is equally split in energy, and coupling $\Delta m_J = 2$ is forbidden by the magnetic dipole transition. On the other hand, Raman transitions allow for both coherent control of an atom's motional degrees of freedom, as well as a selective two-state m_J -coupling of He^* . In Section 2.3.3 we discuss the theory behind Raman transitions and the experimental setup of the Raman laser system.

2.3.2 He^* BEC machine

This section describes the experimental apparatus at ANU for creating BECs of He^* , shown schematically in Figure 2.13. The He^* BEC machine generates a BEC of approximately 10^6 He^* atoms at $\approx 100\text{nK}$ at a duty cycle of $\approx 20\text{s}$. The complete procedure with this apparatus, starting from a room temperature helium-4 gas, is implemented in three major stages. The first stage creates a beam of He^* , where the metastable excitation occurs by high voltage discharge through the nozzle of gas injection into the vacuum chamber, after which the atomic beam is collimated, filtered, and slowed by radiative pressure [147]. The second stage captures this beam and cools the gas further to create an intense and cold He^* beam at sub-mK temperature [148]. The third stage captures and cools atoms from the second stage beam under higher vacuum conditions, followed by evaporative cooling the He^* gas in a magnetic trap that creates the BEC [141]. Below we provide a further explanation for each key stage with relevant concepts and methods for completeness.

Metastable excitation and first atomic beam

Our apparatus uses a dc discharge source [147], cooled by a liquid nitrogen (LN2) cryostat, to create a beam of excited mixtures of helium (see inset in Fig. 2.13). In its operation, a continuous flow of helium-4 gas fills the liquid nitrogen-cooled source chamber (cathode), from which the gas supersonically expands through an exit nozzle and cools. A counter-propagating jet of electrons emits from the anode needles, located downstream of the nozzle, and bombards into the exiting helium beam, and onto the inner walls of the source block. Only about 1 out of 10^5 atoms in the ejected atomic beam is excited to the He^* state this way. Furthermore the beam is initially too divergent and fast, with a peak velocity of $\approx 1000\text{m s}^{-1}$ [147], to be efficiently captured by available trapping techniques.

First, an aperture placed in between differentially pumped vacuum chambers, called a skimmer, crops the highly divergent atomic beam. Then a series of laser cooling techniques collimate, filter, and slow the beam, in succession, to produce a He^* beam with a mean velocity of $\approx 70\text{m s}^{-1}$.

The essential mechanism underlying the focussing and cooling of atomic beams or trapped gas by laser techniques is the manipulation of the ensemble's momentum distribution. In fact, an extension of the Doppler selective radiative force, from a single laser with wavevector \mathbf{k} in Eqs. (2.59) and (2.60) to a counter-propagating pair

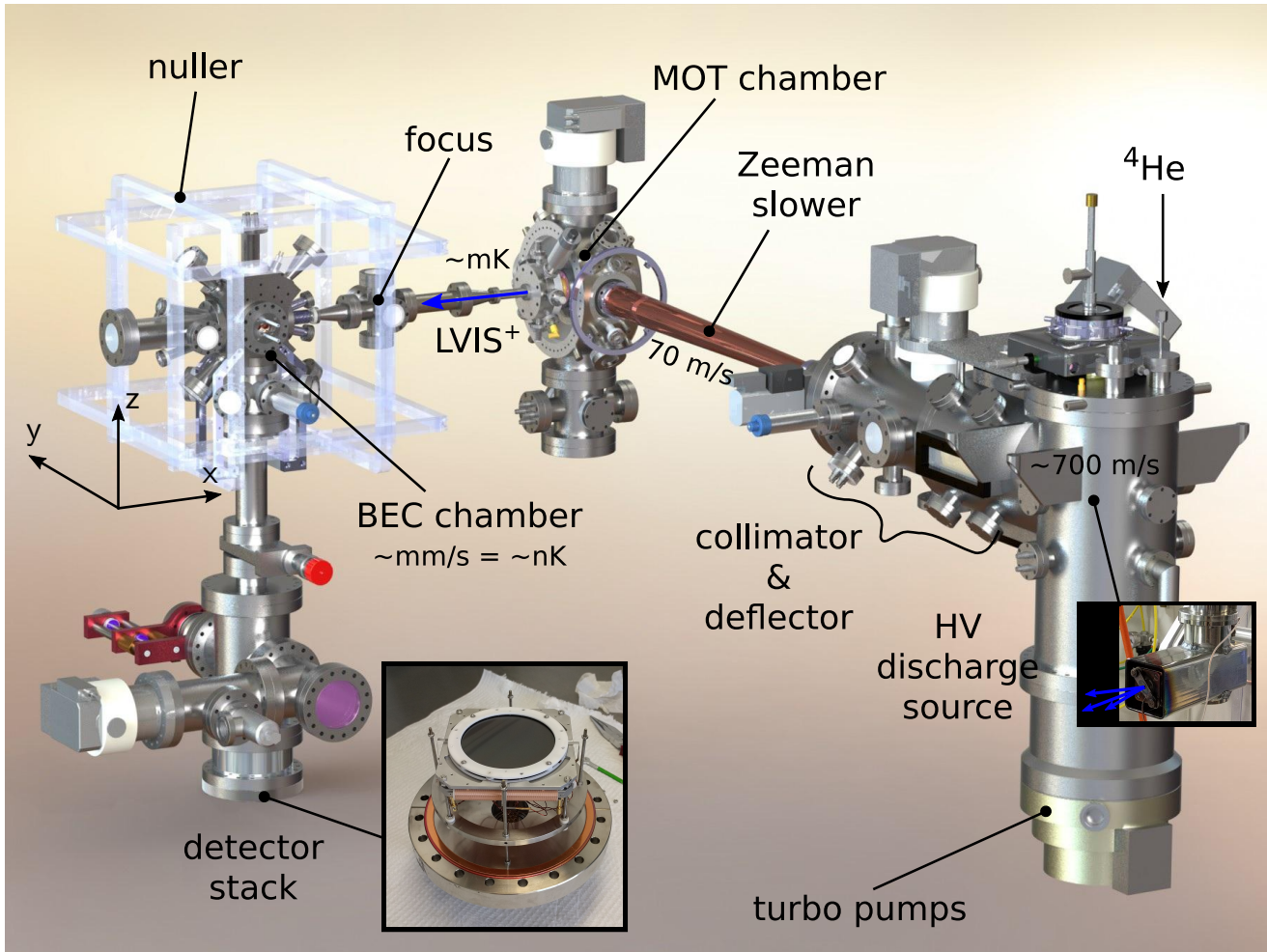


Figure 2.13: Simplified schematic of the He^* BEC apparatus. The right inset shows a photo of the HV discharge source attached to the cryostat. The left inset shows a photo of the MCP-DLD detector stack. The laser optics, electronics, vacuum system, and other subsystems are not shown for simplicity.

$\pm \mathbf{k}$, produces a damping force acting on the atom's velocity parallel to the laser \mathbf{v}_{\parallel}

$$\mathbf{F}_{\text{OM},1\text{D}} = \bar{\mathbf{F}}_{+\mathbf{k}} + \bar{\mathbf{F}}_{-\mathbf{k}} \approx \frac{8\hbar k^2 \delta s}{\Gamma[1 + s + (2\delta/\Gamma)^2]^2} \mathbf{v}_{\parallel} \equiv -\beta \mathbf{v}_{\parallel}, \quad (2.64)$$

where $\delta = \omega - \omega_a$, and the friction parameter β is positive for red-detuned light ($\delta < 0$), and approximately constant over a small range of velocities around zero [21]. This friction force can readily be set up in two or three dimensions, by applying additional pairs of counter-propagating laser beams along the desired damping axes. However such radiative pressure, called optical molasses, is purely frictional and has no spatially-dependent restoring force, which is necessary to trap atoms.

The collimator stage involves a 2D optical molasses from a recirculating mirror array, and compresses the transverse velocity distribution of the He^* beam exiting the skimmer. Next, the atomic beam is passed through the deflector stage similar to that of the 2D optical molasses as in the collimator using in-vacuo mirror array, but slightly tilted with respect to the collimator. The He^* beam is effectively bent off-axis by $\approx 1.7^\circ$ and filtered from the background gas load through an aperture formed by a narrow tube, which also acts as a differential pumping stage to reduce the pressure from the high-background source chamber. Finally the atomic beam significantly decelerates through a Zeeman slower, from which its longitudinal velocity is reduced by more than an order of magnitude [149]. As a beam slows by radiative pressure from the oncoming light, the atomic resonance is shifted in the lab frame due to the Doppler effect, such that the rate of deceleration of the beam decreases along its propagation. The basic concept of the Zeeman slower is to sustain a constant maximum deceleration of the beam throughout its propagation, by compensating the velocity dependent Doppler shift with Zeeman effect from a spatially varying magnetic field [21].

First stage magneto-optical trap loading and sub-mK atomic beam

Located at the outlet of the Zeeman slower, a magneto-optical trap (MOT) captures the slow He^* beam and prepares a cold reservoir of trapped He^* at a temperature of $\sim \text{mK}$ (see Fig. 2.13). A second He^* beam, significantly colder and more intense than the Zeeman slowed discharge beam, is then continuously out-coupled from this reservoir [148] for loading the final stage of cooling to Bose-Einstein condensation.

MOTs trap atoms with high capture velocities, while at the same time cooling the trapped gas [21], such that they are workhorses of ultracold gas experiments. Our MOT consists of 3D optical molasses set up in a quadrupole magnetic potential from anti-Helmholtz coils. Crucial to the operation of the MOT, each pair of counter-propagating laser beams of the optical molasses are oppositely circularly polarised to σ^{\pm} , and red-detuned from resonance in zero magnetic field. The magnetic field lifts the three-fold degeneracy in the $J = 1$ ground state of He^* , and the $J = 2$ five-fold degenerate excited state 2^3P_2 . Since the magnetic field is spatially varying, the resonance (energy gap) of the σ^{\pm} -transitions also depends on the atom's location and split oppositely in sign, such that $\omega_a \mapsto \omega_a \pm \Delta\omega(\mathbf{r})$, respectively. For simplicity, consider

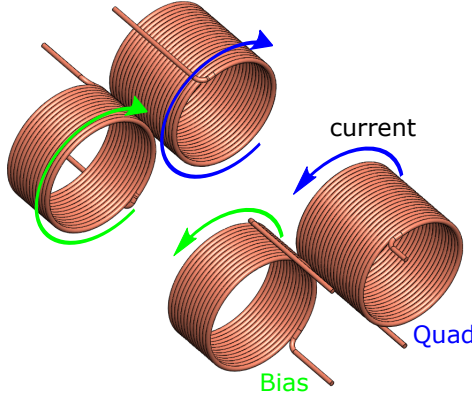


Figure 2.14: A schematic of the BiQUIC magnetic trap.

for stationary atoms in 1D the σ^\pm -transition rates in a region where the magnetic field varies linearly in space $B(r) = B'r$. Indeed a straight-forward incorporation of the Zeeman effect into Δ (as above) in Eq. (2.60) generates a spatially restoring force proportional to $-\mathbf{r}$ (sign is determined by the choice of beam polarisation), and a damping force from the optical molasses (see Ref. [21] for details). By summing the interaction in each dimension independently, the force on an atom in a 3D MOT is then a combination of cooling and confinement, as explicitly given by

$$\mathbf{F}_{\text{MOT}} = -\beta \mathbf{v} - \kappa \mathbf{r}, \quad (2.65)$$

where β is the friction parameter defined in (2.64), $\kappa = \Delta\mu B'/\hbar k$ is the spring constant, and $\Delta\mu$ is the difference in magnetic moments between the σ_\pm -transitions in the MOT ($2\mu_B$ for He^*) [21].

A low-velocity intense source (LVIS $^+$) beam is out-coupled from the MOT and transferred through a differentially pumped aperture to the BEC chamber with the lowest background pressure in our apparatus (see Fig. 2.13). Here a weak, blue-detuned laser beam pushes the atoms out of the MOT, and through a small aperture in a in-vacuo retro-reflecting mirror of MOT that separates the MOT- and BEC chambers [148]. After passing through this aperture, the LVIS $^+$ beam is focussed through a 2D MOT stage before reaching the centre of the BEC chamber.

Bose-Einstein condensation in magnetic trap

After the LVIS $^+$ beam loads a secondary MOT in a significantly higher vacuum condition, the atom trap is transformed to a pure magnetic confinement. Ultimately, by a forced evaporative cooling process in the magnetic trap, the Bose-Einstein condensation of $m_J = 1$ spin-polarised, dilute gas of He^* is realised.

The geometry of our atom trap in the BEC chamber consists of two sets of anti-Helmholtz coils, denoted Quad (Q) and Bias (B), in the *bi-planar quadrupole Ioffe configuration* (BiQUIC) (see Fig. 2.14), and for the MOT formation three orthogonal

pairs of counter-propagating laser beams (see Ref. [141] for a detailed discussion of BiQUIC and the experimental sequence summarised here). The unique coil geometry of BiQUIC achieves two key goals in magnetic traps: a wide optical access to atoms (although pure optical dipole traps eliminating obstructive coils now exist), and a versatile manipulation of the trapping potential. In our apparatus, optical access to the atoms is completely unobstructed in the radial plane of BiQUIC, at the cost of restricted view around the axis of coils. The unobstructed plane simplifies the optical set up of Raman lasers used to coherently control atoms, as well as in the MOT arrangement.

A diverse range of trapping parameters can be realised by controlling the currents through the Q and B coils independently [141]. In the MOT configuration, the Q coil is activated alone and produces a quadrupole magnetic field on the atoms. The ensemble is first cooled in the MOT to $\approx 1\text{ mK}$, then compressed and 1D Doppler cooled to $\approx 100\text{ }\mu\text{K}$, before loading the magnetic trap, and switch-off of the 3D optical molasses.

The magnetic trap is formed by simultaneously activating the B coil along with the Q coil [141]. This magnetic field around the new trap centre (slightly displaced) forms an approximately harmonic oscillator potential in 3D on the $m_J = 1$ states. Since $m_J = 0$ and -1 states are unaffected and repelled, respectively, the magnetic trap polarises the trapped ensemble in $m_J = 1$. A non-zero (bias) field lifts the degeneracy between m_J at the trap centre (magnetic field minimum can be zero), thereby eliminating the loss of $m_J = 1$ atoms via Majorana spin-flipping [21]. Furthermore, a wide range of trap configurations, characterised by the ratio and magnitude of Cartesian trapping frequencies, are possible by gradually tuning the currents through Q and B coils appropriately [141, 150].

In the magnetic trap, a $\approx 17\text{ s}$ RF sweep achieves evaporative cooling to go beyond temperatures achievable in laser cooling towards Bose-Einstein condensation, where the critical temperature for our experiment is $T_c \approx 1\text{ }\mu\text{K}$. The principle of evaporative cooling is the selective removal of high energy atoms from an ensemble which quickly re-thermalise by elastic collisions to a distribution of lower mean energy. Atoms with higher energies experience larger Zeeman splitting in the magnetic trap than the rest, since this is essentially the conservative trapping potential. A forced evaporation is thereby achieved by a selective rf radiation (a rf knife), that out-couples the atoms via a spin-flip $m_J = +1 \rightarrow 0$, resonant on a high energy fraction of the atomic ensemble, but detuned for low energy particles. The final temperature of the atomic ensemble is determined by the lowest evaporation cut-off in energy, and therefore tunable via the minimum RF out-coupling frequency applied at the end of the evaporation ramp. With a trade-off between total atom number and temperature, we can reproducibly achieve temperatures down to a few nK with $\sim 10^4$ atoms. Therefore the apparatus can produce a diverse range of ultracold He^{*} ensemble in temperature ranging from a classical regime $T \gg T_c$ called a thermal/classical gas satisfying Maxwell-Boltzmann distribution, near transition $T \lesssim T_c$ where a macroscopic occupation of the ground state suddenly appears among the thermal fraction, to a fully quantum gas $T \ll T_c$ where almost all atoms are Bose condensed.

The stable production of BECs is an utmost desirable feature of our apparatus, which goes hand in hand with the control and stabilisation of the magnetic field seen by the atoms. Such magnetic disturbances range from dc sources such as geomagnetism, to noisy electronic equipment. A few passive methods first reduce the penetration of external fields into the vacuum chamber, such as the usage of materials (titanium) with low magnetic permeability for the BEC chamber, and the magnetic shielding with mu-metal of nearby noisy equipments (e.g. turbomolecular pumps). In addition, our apparatus features an active control system to stabilise the magnetic field around the trap centre, called the nollerometer. It consists of three orthogonal sets of Helmholtz coils, in which each coil is independently feedback controlled, based on the uniform bias and the first order gradient of the magnetic field predicted from an array of six fluxgate and pickup coil magnetometers positioned around the BEC chamber [151]. This achieves magnetic field noise at the centre of the trap to $\approx 30 \mu\text{G}$ in a bandwidth below 3 kHz. In addition, the nollerometer set-points can be tuned in our experiment to realise a range of stable magnetic field conditions around the centre of BEC chamber. In particular, a uniform field with a controllable pointing (atomic spin quantisation axis) turns out to be crucial for implementing a coherent control of spin and momentum of atoms by Raman transitions, as explained below.

2.3.3 Coherent manipulation of momentum and spin of single He^{*} atoms

The coherent control of a single He^{*} atom, namely its internal and momentum state, is a necessary tool for almost any application of its quantum properties, and in particular forms the basis of quantum information protocols such as tests of nonlocality. With Raman transitions we realise the collision of BECs, and the manipulation of individual spins of the atomic pairs for the experimental demonstration of nonlocal correlations, and their applications to quantum metrology.

Consider the problem of controlling the m_J atomic spin states of He^{*}. Although a resonant RF field is the simplest way to couple different m_J states by Zeeman effect, a few difficulties exist towards realising qubit operations on He^{*}. Observe that it is not possible to couple just two neighbouring m_J states in this way, without additionally coupling to the third state. Indeed, an RF field can in principle be used to couple only the $m_J = \pm 1$ qubit states by driving at the double frequency, and thus eliminate coupling to $m_J = 0$ by the large detuning. However this is not a practical solution for two reasons. First, the $\Delta m_J = 2$ transition occurs by a higher order magnetic interaction and is therefore very weak. Second, in our experiment the $m_J = -1$ state is undesirable since its velocity is deleteriously affected by any stray magnetic field in its propagation to the detector, such that a significant fraction with moderate velocities are undetected. A discussion of this problem of magnetic lensing for $m_J = 1$ states is given in the data analysis section in Chapter 4, for which no atoms are lost and their undistorted velocities can be reconstructed.

Fortunately, Raman transitions can realise the desired coupling between a He^{*} atom's internal states (e.g. $m_J = 0 \leftrightarrow 1$), in addition to the manipulation of its momentum. Here I summarise the physics of stimulated Raman transitions (a more

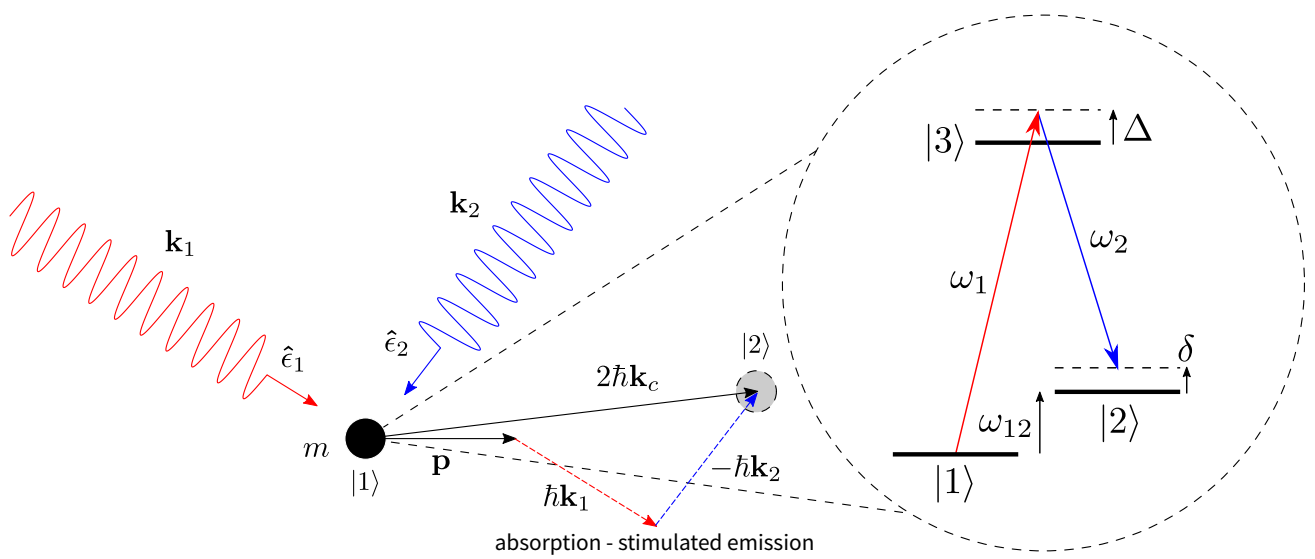


Figure 2.15: The Raman transition of an atom. (left) A schematic of an atom (black circle) driven by two lasers L_1 (red) and L_2 (blue) in the lab frame. (right) Energy level diagram for the two-photon stimulated Raman transition. The atom is abstracted as a three-level system in Λ configuration, where each driving field with frequency ω_1 and ω_2 couples only the lower lying state $|1\rangle$ and $|2\rangle$, respectively, to the excited (intermediate) state $|3\rangle$. A stimulated Raman transition occurs when individual fields are highly detuned but the combination of the two processes is nearly resonant to the lower states.

detailed theoretical treatment is found in the Appendix Appendix A), and describe the Raman laser system further developed in this thesis.

Theory of stimulated Raman transitions

The stimulated Raman transition is typically how atoms, ions, and spins in a solid state systems are controlled in laboratories while preserving their quantum coherence, using a highly coherent source of electromagnetic radiation, most commonly found in lasers, microwave and RF sources. The essential physics of Raman transitions is based on a three-level system's response (such as the electronic states of an atom) to two oscillating driving fields which individually couple a pair of levels [152]. Figure 2.15 shows a schematic of a Raman transition forming a Λ -shaped coupling, which can be realised in He^* as shown in Fig. 2.11.

Consider an atom with mass m and momentum \mathbf{p} in the lab frame that is illuminated with two monochromatic laser beams L_1 and L_2 as shown in Fig. 2.15. The internal state of the atom is abstracted as a three-level Λ system, with two lower lying states $|1\rangle$, $|2\rangle$, and an excited state $|3\rangle$ (such as electronic or hyperfine states),

with energies¹⁹ ω_i^a for $i = 1, 2, 3$, respectively. Denoting the difference in atomic energy levels by $\omega_{ij} \equiv \omega_j^a - \omega_i^a$, the lower lying energy gap is then given by ω_{12} (see Fig. 2.15).

The two lasers L_l ($l = 1, 2$) set up an electric field at the atom given by

$$\mathbf{E}(\mathbf{r}, t) = \frac{1}{2} (\mathcal{E}_1 \hat{\mathbf{e}}_1 \exp [i(\mathbf{k}_1 \cdot \mathbf{r} - \omega_1 t + \phi_1)] + \mathcal{E}_2 \hat{\mathbf{e}}_2 \exp [i(\mathbf{k}_2 \cdot \mathbf{r} - \omega_2 t + \phi_2)]) + \text{c.c.} \quad (2.66)$$

with respective frequency ω_l , wavevector \mathbf{k}_l , polarisation $\hat{\mathbf{e}}_l$, field amplitude \mathcal{E}_l , and phase ϕ_l , which are all controllable parameters in the experiment, and c.c. denotes the complex conjugate of the preceding expression.

The atom interacts with light in this scenario via the induced dipole moment of the atom $\hat{H}_{\text{dip}} = -\hat{\mathbf{d}} \cdot \mathbf{E}$. The *single-photon Rabi frequency* characterises the coupling between $|l\rangle$ to $|3\rangle$ according to [153]

$$\Omega_l \equiv -\mathcal{E}_l \langle 3 | \hat{\mathbf{d}} | l \rangle \cdot \hat{\mathbf{e}}_l / 2\hbar. \quad (2.67)$$

As the name suggests (roughly speaking) this is the rate at which a particle would oscillate between two quantum states. For an electric dipole driven by an oscillating field, we see from Eq. (2.67) that this frequency is proportional to the (electric) field amplitude \mathcal{E} , and therefore proportional to the square root of the light intensity $I = c\epsilon_0 n \mathcal{E}^2 / 2$, where c is the speed of light in vacuum, ϵ_0 is the vacuum permittivity, and n is the refractive index. If the two ground states have different angular momenta (such as for the Raman transition in He^* in Fig. 2.11), then clearly L_1 can be decoupled from the $|2\rangle \leftrightarrow |3\rangle$ transition based on photon polarisation by selection rules, and vice versa for L_2 . On the other hand, the ground state transition $|1\rangle \leftrightarrow |2\rangle$ is decoupled from the individual lasers due to the large detuning in energy.

The system Hamiltonian for the stimulated Raman transition for the Λ system is then given by

$$\hat{H} = \hat{\mathbf{p}}^2 / 2m + \hbar\omega_i^a |i\rangle\langle i| + [\hbar\Omega_l \exp(i(\mathbf{k}_l \cdot \hat{\mathbf{r}} - \omega_l t + \phi_l)) |3\rangle\langle l| + \text{h.c.}], \quad (2.68)$$

where the Einstein summation convention is implied over $i = 1, 2, 3$ and $l = 1, 2$.

For an atom with momentum \mathbf{p} and internal state $|1\rangle$, we expect it to absorb a resonant photon from L_1 such that it excites into $|3\rangle$ as well as receiving a recoil from the absorbed photon's momentum $\hbar\mathbf{k}_1$. Now the physics of the Raman process concerns the coherent transition from this excited state into the $|2\rangle$ ground state, by a stimulated emission of a photon into L_2 which accompanies an opposite momentum recoil $-\hbar\mathbf{k}_2$. By the conservation of momentum the atom is scattered with momentum $\mathbf{p} + \hbar(\mathbf{k}_1 - \mathbf{k}_2) \equiv \mathbf{p} + 2\hbar\mathbf{k}_c$. This choice of expression for the recoil momentum $2\hbar\mathbf{k}_c$ simplifies the two momentum states coupled by Raman transition to $\pm\hbar\mathbf{k}_c$ in the centre of mass frame, which corresponds to the collision momentum discussed in Section 2.2. Subsequently the two-photon process happens in reverse back to the

¹⁹For notational simplicity, we frequently refer to the wavevector \mathbf{k} and frequency ω as momentum and energy, respectively, without the risk of confusion for the missing factor of \hbar in the standard unit.

original state, such that the atom undergoes a coherent oscillation between the three states. In fact, the population of the excited state can be adiabatically eliminated throughout the process, when the two-photon Λ transition (detuning δ) is near resonant, but each single-photon transition (detuning Δ) to the intermediate state is sufficiently far detuned, namely when $|\Delta| \gg |\Omega_1|, |\Omega_2|, |\delta|$ (see Appendix A for a detailed discussion). In this case the intermediate state never becomes populated, and the dynamics reduces to two discrete states $|1; \mathbf{p}\rangle$ and $|2; \mathbf{p} + \hbar(\mathbf{k}_1 - \mathbf{k}_2) = \mathbf{p} + 2\hbar\mathbf{k}_c\rangle$, which is precisely the desired stimulated Raman transition. Indeed this regime is easily realised in atomic systems. For our experiment on He^* , the corresponding ground states are $m_J = 0, 1$ Zeeman sublevels, and the intermediate state is the 2^3P_0 singlet, as seen in Fig. 2.11.

The system Hamiltonian in Eq. (2.68) effectively reduces, under the adiabatic elimination conditions specified above, to the two-state subspace (see Appendix A for details), given by

$$\begin{aligned}\hat{H}_{\text{eff}} &= \hbar (-\Omega_0 \cos \phi', \Omega_0 \sin \phi', \Delta_{\text{eff}}) \cdot \vec{\sigma} \\ &= \hbar \boldsymbol{\Omega} \cdot \vec{\sigma},\end{aligned}\tag{2.69}$$

where the conventional $\hat{\sigma}_z$ basis states are $|\uparrow\rangle \propto |1; \mathbf{p}\rangle$ and $|\downarrow\rangle \propto |2; \mathbf{p} + 2\hbar\mathbf{k}_c\rangle$, in a particular choice of rotating frame to express the system in a time-independent form²⁰. Before we relate the components of $\boldsymbol{\Omega}$ back to atom-light properties, it will be more illuminating to first discuss the two-level system Eq. (2.69) in general. The atom's dynamics is most simply captured in the Bloch vector representation²¹, where the state precesses around the torque-like vector $\boldsymbol{\Omega}$ as illustrated in Fig. 2.16(a). First, observe that the azimuthal angle of the torque is summarised by ϕ' , which turns out to be controllable by the relative phase between the driving fields, according to $\phi' = (\phi_2 - \phi_1) + \arg(\Omega_1^* \Omega_2)$. As we see below, the resonance of the Raman transition corresponds to when the torque vector lies on the xy -plane.

The time-evolution of the system initially prepared $|\downarrow\rangle$ is shown in Fig. 2.16(b) for a range of $\boldsymbol{\Omega}$. The polarisation of the atom undergoes a Rabi oscillation $\langle \hat{\sigma}_z \rangle_t = -1 + A(1 - \cos \Omega' t)$ at the generalised Rabi frequency Ω' , and amplitude A , given

²⁰Reversing the rotating frame effectively causes the original basis states (lab frame) $|1; \mathbf{p}\rangle$ and $|2; \mathbf{p} + 2\hbar\mathbf{k}_c\rangle$ to accrue a relative phase, at the sum of their free-particle energies and the two-photon detuning frequencies. This frame conversion therefore corresponds to a spinning of the Bloch sphere around the z -axis.

²¹The Bloch vector of a two-state system $\hat{\rho}$ is defined as a real 3D vector $\text{Tr}[\vec{\sigma}\hat{\rho}]$ [154]. When the system corresponds to angular momentum (i.e. spin-1/2) the Bloch vector corresponds to a picture of a particle's angular momentum. The time evolution of state is given by the unitary operator $U = \exp \times (-i\hat{H}t/\hbar) \equiv \exp(-i\boldsymbol{\Omega} \cdot \vec{\sigma}t)$, equivalent to a rotation operation of the Bloch vector by angular momentum algebra.

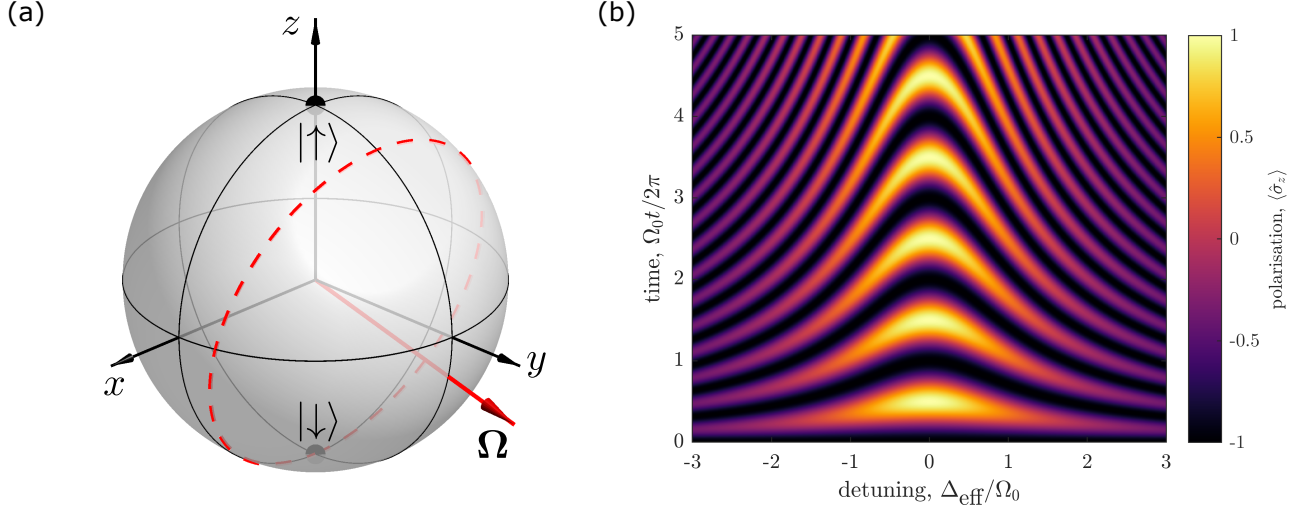


Figure 2.16: (a) Bloch sphere representation of a time-independent two-state system. (b) Rabi oscillation of a two-state system initialised as $|↓\rangle$ under a generalised time-independent Hamiltonian.

by

$$\Omega' = |\boldsymbol{\Omega}| = \sqrt{\Omega_0^2 + \Delta_{\text{eff}}^2} \quad (2.70)$$

$$A = \sqrt{1 - \frac{(\boldsymbol{\Omega} \cdot \hat{\mathbf{z}})^2}{|\boldsymbol{\Omega}|^2}} = \frac{|\Omega_0|}{\sqrt{\Omega_0^2 + \Delta_{\text{eff}}^2}}. \quad (2.71)$$

Now we can fully appreciate how the atom-light properties characterise the stimulated Raman transition, namely to the resonant Rabi frequency Ω_0 , and effective detuning Δ_{eff} , which are given explicitly according to

$$\Omega_0 = \frac{|\Omega_1^* \Omega_2|}{\Delta} \quad (2.72)$$

$$\Delta_{\text{eff}} = \frac{|\Omega_1|^2 - |\Omega_2|^2}{2\Delta} - \frac{\delta}{2}, \quad (2.73)$$

where the single- and two-photon detunings are, respectively,

$$\Delta \approx \omega_1 - \omega_3^a + \omega_1^a \quad (2.74)$$

$$\delta = (\omega_1 - \omega_2 - \omega_{21}) + \frac{\mathbf{p} \cdot (\mathbf{k}_1 - \mathbf{k}_2)}{m} + \frac{\hbar(\mathbf{k}_1 - \mathbf{k}_2)^2}{2m}. \quad (2.75)$$

Notice that the effective detuning Δ_{eff} from Raman transition involves two key contributions: the ac Stark shift from individual driving fields (light intensity dependent shift from terms proportional to $|\Omega_l|^2$), and the two-photon detuning δ . The first term in Eq. (2.75) is the detuning between the energy of photons and the atom (the

$ \Omega_1 , \Omega_2 $	Δ	Ω_0	ω_1	$\omega_1 - \omega_2$	$(\hbar\mathbf{k}_1)^2/2m\hbar$	$ \Delta v /c$	ω_{12}	Γ_{sc}
~ 10 MHz	3 GHz	≈ 50 kHz	276.7 THz	≈ 1.5 MHz	42 kHz	$\leq 3.3 \times 10^{-9}$	≈ 1.5 MHz	~ 1 kHz

Table 2.1: Experimental parameters used for spin rotation (co-propagating Raman beams). Δv is the spread in atom's velocity, c speed of light, and Γ_{sc} is the rate of spontaneous emission from the excited state of He^* .

qubit states), the second term is the Doppler shift due to the atom's motion in the lab frame, and the third term is the change in kinetic energy from photon recoil. On the other hand for the single-photon transition, ac Stark and Doppler shifts are, by design, negligible fractions of the large frequency difference between light and atom, giving Eq. (2.74).

A notable advantage of the two-photon Raman transition, over a single-photon transition, is that it is insensitive to the laser's phase noise. Indeed near the resonance condition, the Raman transition has an equivalent picture to a two-state system driven with a single field at the difference frequency $\omega_{\text{mod}}(t) = \omega_1(t) - \omega_2(t)$. Consequently when two Raman beams are prepared by frequency modulating a single laser at $\omega_{\text{mod}}(t)$, for instance by an acousto- or electro-optic modulator [155]), the frequency noise in the reference laser itself is inherently eliminated by common-mode rejection. The Raman transition is however clearly sensitive to the stability of the optical modulator, and the laser intensity $\propto |\mathcal{E}_i|^2$, which effectively broaden the transition by coupling through recoil ($\omega_{\text{mod}} \propto |\mathbf{k}_1 - \mathbf{k}_2|$) and ac Stark shifts (see Eqs. (2.72) and (2.73)), respectively.

In the following section, we discuss the Raman laser system employed in our experiment. Briefly, a pair of perpendicularly-crossed laser beams L_1 and L_2 (see Figs. 2.17 and 2.18(b)) achieve the momentum-spin control to realise BEC collisions. In addition, we modulate a single laser beam L_3 to achieve two *co-propagating* driving fields for an effectively recoil- and Doppler-free control (insensitive to velocity) of the atom's internal state. A summary of the experimental parameters is shown in Table 2.1.

Raman laser system

The Raman laser system (see Fig. 2.17 for a schematic) is based on a single Ytterbium-doped fibre laser (IRE-Polus YDL-1BC). This laser is tunable around 1083 nm, so that we can achieve a Λ level system by engineering the single-photon detuning with respect to the 2^3P manifold. The laser wavelength is computer controlled with a proportional-integral (PI) algorithm (see Fig. 2.17), using a wavemeter (Burleigh WA-1100) as the wavelength monitor and feedback is applied directly to the fibre laser system. Simultaneously, the intensity of the laser is stabilised by a noise eater, where the optical power of a particular diffraction order from an acousto-optic modulator (AOM) is stabilised by controlling the power of the RF input. This laser serves as the common source for all Raman beams in our experiment, each with an independently controlled AOM and polarisers. A clear advantage is gained from having

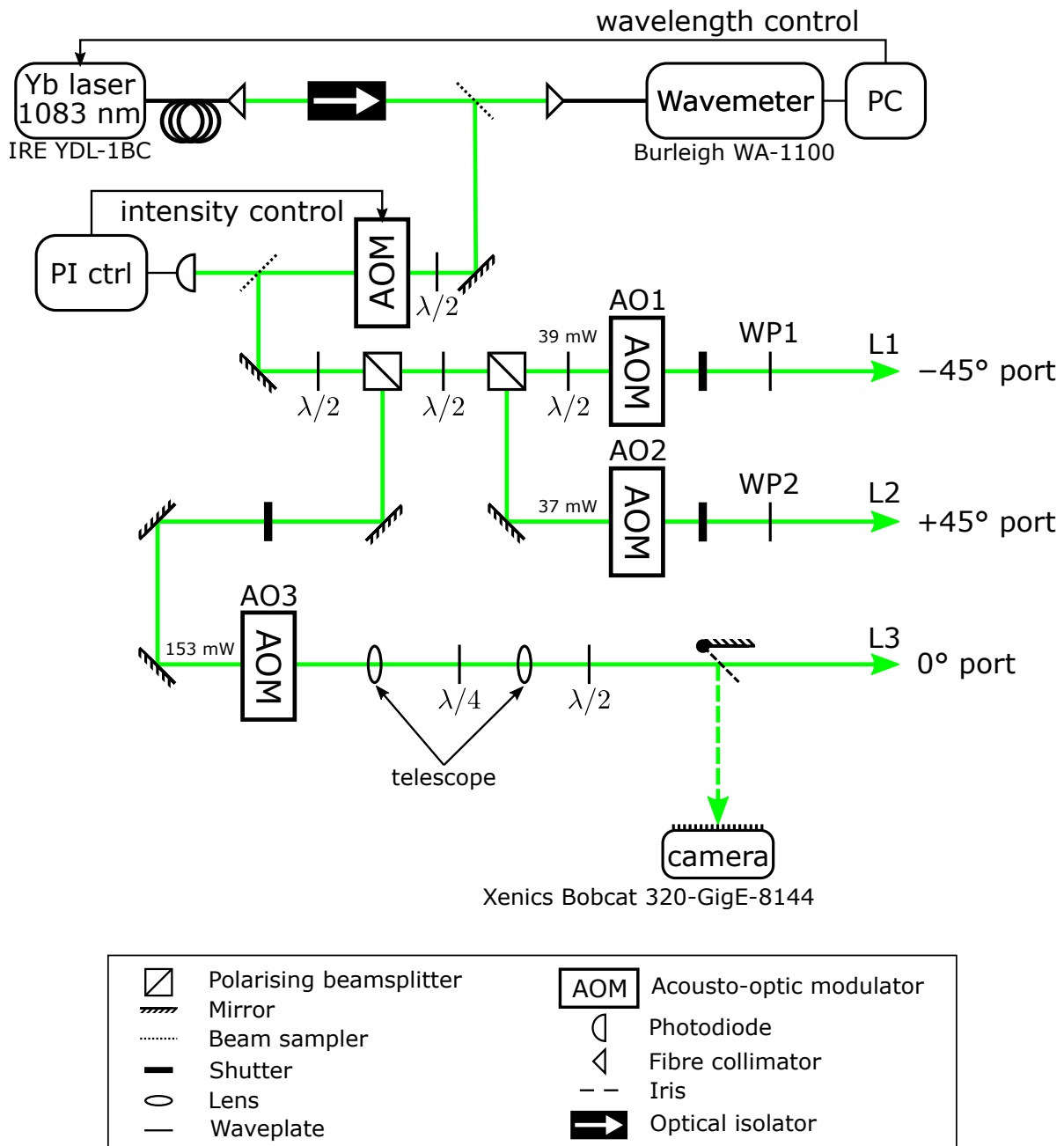


Figure 2.17: Simplified schematic of the Raman laser system. A single wavelength and intensity stabilised fibre laser provides all the Raman beams. The polarisation of each Raman beam is tuned using the waveplates after the relevant AOM, and is particular to the transition involved. The camera to image the beam profile is positioned equidistant to the location of the atoms, and used as a reference for precise alignment. The schematic shows the nominal setup where the L3 beam is imaged.

such a common laser source for all the Raman beams, since it inherently eliminates relative optical phase noise between different Raman beams, and is therefore largely insensitive to the coherence of the laser.

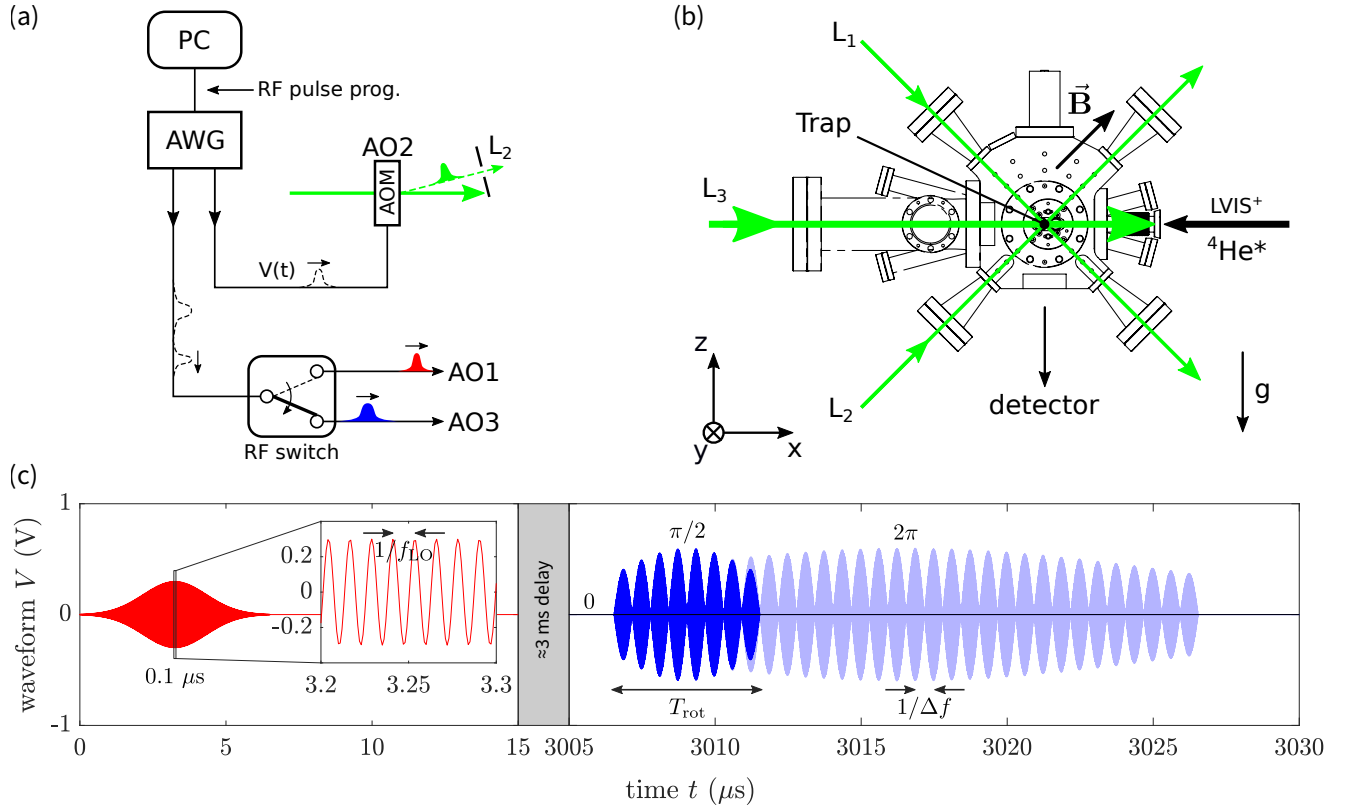


Figure 2.18: (a) Schematic of the RF modulation for Raman beams. A computer-generated RF waveform is loaded into an arbitrary waveform generator and drives the individual AOMs. An RF switch sends delayed pulses to AO1 and AO3 using a single output channel of the AWG. (b) Schematic of the Raman beam geometry. The geometry of Raman beams, aligned approximately to the centre of the magnetic trap, are shown with respect to the science chamber, and the atoms' quantisation axis defined by the magnetic field. The magnetic field shown here is the nominal setup stabilised by the nullder system (not shown). (c) RF waveform to AOMs. The RF switch passes the first part of the pulse to AO1 (red), which is a Gaussian enveloped sine wave. The inset shows a zoomed-in 100 ns segment of the waveform. The RF switch is then flipped to pass the rest of the pulse to AO3 (blue), where the beat note from the two-tone modulation gives rise to the interference pattern. The dark (zero signal), normal, and light blue waveforms represent $0, \pi/2$, and 2π spin-rotation pulses, respectively.

As shown in Fig. 2.18, the Raman beam geometry at the science chamber is composed of 3 independently modulated beams L₁, L₂, and L₃ at $\lambda \approx 1083 \text{ nm}$, which propagate along $([\hat{x} - \hat{z}] / \sqrt{2}, [\hat{x} + \hat{z}] / \sqrt{2}, \hat{x})$, respectively, aligned to the centre of the

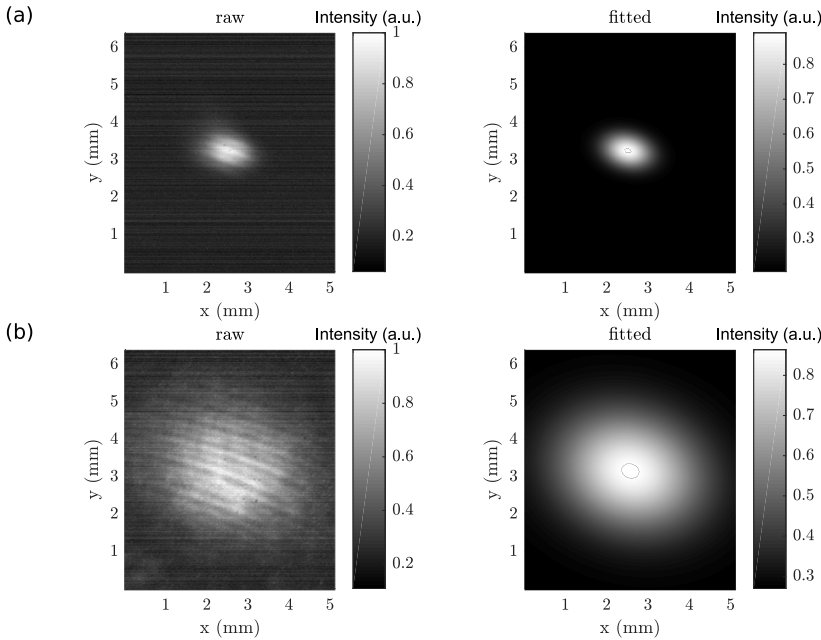


Figure 2.19: Raman laser beam profiles. (a) Intensity profile of the L1 beam taken by a camera (left) located approximately equidistant to the trap centre, and a fitted 2D Gaussian profile (right). The slanted fringes seen in the raw camera images are due to the interference from the glass window in front of the sensor, and do not reflect the true spatial feature of the beam. L2 has a similar beam profile to L1 and is not shown. (b) Same as (a) for the L3 beam.

trap. More precisely speaking, each beam is aligned to the location of the atoms they need to target at the desired moment of the experimental sequence, which is within a few ms after the trap switch-off to allow for both the background magnetic field to stabilise, and more importantly, to allow the atomic pairs to separate. Each set of Raman beams are tuned closely to 2^3P_0 ($\Delta = 3\text{ GHz}$) to realise a single level intermediate state, since couplings to the next nearest excited states $2^3P_{1,2}$ become negligible by an order of magnitude in detuning ($\approx 30\text{ GHz}$), as can be seen from the level diagram in Fig. 2.11. This setup allows for both a coherent momentum transfer and recoil-free spin control of atoms.

First, two-photon stimulated Raman transitions based on the perpendicularly-crossed pair of L₁ and L₂ generate a two-photon momentum recoil of $2\hbar\mathbf{k}_c = \pm\sqrt{2}\hbar\mathbf{k}\hat{\mathbf{z}}$. These beams are Gaussian in transverse intensity profile and collimated to a $1/e^2$ radius of $\approx 0.7\text{ mm}$, which provides a uniform intensity, within a $\approx 100\text{ }\mu\text{m}$ range, for diffracting BECs near trap switch-off (see Fig. 2.19(a)). Indeed, beam parameters such as polarisation and detuning can be tuned to couple any pair of m_J -states, even the same state. Second, I demonstrate a recoil-free coherent control of atomic spin by modulating the single L₃ beam. Here I realise two co-propagating fields which drive a Raman transition with negligible two-photon recoil. This beam is also Gaussian and approximately collimated, with a measured $1/e^2$ radius of $\approx 2.3\text{ mm}$ at

the corresponding position of the trap (see Fig. 2.19(a)). The reason for using such a wide beam is to ensure that a stimulated Raman transition is applied uniformly to all atoms after the collision products have separated, at which time the atoms spanned as much as ≈ 0.4 mm. Note that having a spatially uniform intensity and phase profile only partly addresses the challenge to achieve a uniform Raman process on the atoms, since the velocity distribution of the atoms also introduces a Doppler shift. Fortunately, the Doppler effect on a Raman transition is effectively eliminated in the co-propagating beam geometry that we use.

The magnetic field near the trap was uniformly stabilised to $\mathbf{B} \approx 0.5[(\hat{\mathbf{x}} + \hat{\mathbf{z}})/\sqrt{2}]$ G for the majority of the experimental results presented in this thesis, which is verified by atom interferometry in Chapter 5. In this stabilised field the atomic quantisation axis is adequately defined such that the polarisation of the crossed beam pair $L_{1,2}$ is set to π and σ^- , respectively. This setup is used to resonantly drive the two states $|\uparrow; \hbar\mathbf{k}_0\rangle$ and $|\downarrow; \hbar(\mathbf{k}_0 + 2\mathbf{k}_c)\rangle$, where a preparation of a 50:50 superposition state effectively splits a BEC into two counter-propagating condensates (in CM) of opposite spin-polarisation, and thus realise the entangling collision.

The exception to this setup is used to implement *Bragg diffraction* of atoms [19], which allows for both the testing of spin control techniques on scattering halos, and atom interferometry schemes discussed later in this thesis. The Bragg diffraction is essentially the elastic scattering case of stimulated Raman transition, in other words the atoms' internal states do not change (i.e. a two-photon Bragg diffraction couples $|\uparrow; \hbar\mathbf{k}_0\rangle \leftrightarrow |\uparrow; \hbar(\mathbf{k}_0 + \mathbf{k}_1 - \mathbf{k}_2)\rangle$, and similarly for other internal states). When the magnetic trap is activated, the BiQUIC provides a dominant bias field at the trap centre, which points approximately along the $\hat{\mathbf{x}}$ -axis. The Zeeman sublevels are therefore split further which reduces the coupling between different internal states, and both the collision Raman lasers can be polarised to drive the σ^- transition. To let the atoms propagate freely after the collision, the magnetic trap is switched-off 50 μ s after the Bragg pulse ($T_\pi \approx 10 \mu$ s), and no effect on the momentum distribution from the trap and its switch-off was observed. Since the Bragg diffraction can reproduce the same momentum superposition for the atoms as the Raman method, but leave the internal state unchanged, it can realise a collision between atoms of same spin. This turns out to be a crucial tool for characterising the spin rotation pulses, since the Bragg pulse creates a $|\uparrow\rangle$ -polarised initial state that undergoes a simple Rabi oscillation seen in Fig. 2.16.

The atomic spins of He* are independently controlled as a two-state system without recoil, implemented by using a single co-propagating beam, the L_3 , in another stimulated Raman transition. The diagonally pointing magnetic field with respect to the laser wavevector is crucial, since it allows the light to be composed of a combination of σ^- and π (i.e. elliptically polarised), with no component in σ^+ , with respect to the atoms' quantisation axis. This phenomenon has a rather straightforward explanation when one decomposes each component of the polarisation vector $\hat{\mathbf{f}}$ in the light propagation frame \mathbf{k} ($\hat{\mathbf{f}} \perp \mathbf{k}$), for instance vertical (v) and horizontal (h) polar-

isation, into that of the quantisation axis \mathbf{q} , composed of σ^\pm and π .²² Observe that for all configurations, except when \mathbf{k} is either perpendicular or parallel to \mathbf{q} , both \mathbf{v} and \mathbf{h} , individually decomposes into all components of σ^\pm and π . Therefore, one can always adjust the relative amplitude and phase between \mathbf{v} and \mathbf{h} (using a standard $\lambda/2$ - and $\lambda/4$ -waveplate arrangement), to eliminate at least one polarisation component in the quantisation axis. The need to eliminate σ^+ will become apparent in the description for two-tone modulation, but suffice to summarise at this point that this component couples the unwanted $m_J = -1$ state by stimulated emission from the 2^3P_0 $m_J = 0$ state.

The RF waveform to modulate each Raman beam L_i ($i \in \{1, 2, 3\}$) is designed in software and implemented by an arbitrary waveform generator (AWG) to drive the corresponding AOM, denoted AO_i (see Fig. 2.18(a)). We use a 2-channel arbitrary waveform generator, with an RF switch to split one of the channels to switch between driving AO_1 and AO_3 , since they need not be simultaneously driven in this work.

For the crossed pair L_1 and L_2 , each waveform was a pulse of Gaussian enveloped sine wave (see Fig. 2.18(c)). The Gaussian envelope to the finite pulse reduces the spectral leakage which couples undesirable states in the Raman process, especially significant for Bragg diffraction where velocity sensitivity can be crucial. The absolute modulation frequency is restricted to the bandwidth of the AOM to around the nominal carrier frequency (80 MHz for the device used here), but note that what matters in stimulated Raman transitions is the relative difference in frequency between individual fields. In this work, each pair of RF modulations were designed to lie symmetric about the AOM's centre frequency, and were well within the operational bandwidth, since the Raman detunings investigated here were $\lesssim 2$ MHz.

For the L_3 co-propagating Raman beam for implementing spin rotation, a two-tone RF waveform is modulated onto the beam by a single AOM. This waveform is also Gaussian enveloped, although it required much less smoothing since coupling to the most nearby $m_J = -1$ state was already eliminated with electric field polarisation (see Fig. 2.18(c)). The RF pulse design for the spin rotation beam involves setting the two sine waves' difference frequency (note the characteristic beat interference pattern in the RF waveform), relative phase offset, pulse duration, and amplitude. Since this beam is modulated by a single RF waveform and AOM, phase noise that could be present between the two optical fields is further eliminated.

The electric field from L_3 in the atom's frame can then be decomposed into 4 components from a permutation of two polarisations $\{\sigma^-, \pi\}$, and two frequencies $\{\omega_{13}, \omega_{23}\}$. This complexity seems far from the ideal theoretical model of two-mode optical fields Eq. (2.66), since each mode could potential couple a pair of atomic levels. However at the desired Raman resonance condition, when the (ω_{13}, σ^-) and (ω_{23}, π) fields couple $m_J = 0$ and 1 with zero detuning, all other transitions become negligible since their detunings ($\approx \omega_{12}$) are much greater than their corresponding resonant Rabi frequencies in the weak-coupling regime. It is now clear to see why it was necessary to minimise σ^+ polarisation. Otherwise there will be the two fields

²²Note π -component is parallel to the quantisation axis \mathbf{q} , and σ^\pm -components are right/left-handed circularly-polarised along \mathbf{q} , respectively [138].

(ω_{13}, π) and (ω_{23}, σ^+) which inevitably couple $m_J = 0$ and -1 .

2.3.4 Single atom detection

A crucial requirement for many foundational experiments in quantum atom optics is the ability to detect and count individual atoms, in an analogy to the importance of single photon detectors and photon counters in quantum optics. Thanks to the high internal energy of He^* , particle detector technologies developed for ionising particles are directly used to resolve an ultracold gas of He^* with the single atom resolution.

Our detector system is a combination of the microchannel plate and delay line detector (MCP-DLD, see Fig. 2.20), that offers a unique tool for probing single-atom resolution in the far-field, due to the high internal energy of metastable noble gases. The MCP first converts a He^* atom that hits it to a narrow shower of electrons through the corresponding active microchannel by a cascade of charge multiplication. When this spatially localised electron shower is incident on the delay line, it causes a spike in electric voltage which then propagates as two pulses travelling in opposite directions along the winding. The time of arrivals of these pulses that finally arrive at the ends of the delay line are measured. A reconstruction algorithm then takes a list of such pulse timings as inputs and determines the generation time of the initial spike (i.e. the trigger He^* atom) as well as its location along the winding. Our detector is composed of an orthogonal pair of delay lines to allow a self-consistent reconstruction of the atom's striking position on the detector fully on the 2D plane, as well as the time of arrival.

Some notable characteristics of our MCP-DLD system is that the total detection efficiency, referred to as quantum efficiency, is $\eta_{QE} \approx 0.1$, and the spatial (temporal) resolution is $\approx 120 \mu\text{m}$ ($\approx 3 \mu\text{s}$). The detection efficiency is limited by the MCP due to a fraction of non-active region over the front surface, and the probability of triggering a downward electron cascade upon an impact from He^* . The geometry of the MCP and the pulse timing electronics limits the reconstructed spatio-temporal information of the atoms' impact, due to the finite size of the individual microchannels which effectively blurs the event (see supplementary materials in [156]). Note that this detector system is located inside the vacuum chamber $\approx 848 \text{ mm}$ below the trap where BECs are created, close to where all external controls and interesting physics take place. It turns out that a far-field, velocity distribution of atoms are measured this way since the trapped atoms are initially localised to $\sim 0.1 \text{ mm}$ at the source, as we explain in the following section. Furthermore, each atom's internal state m_J can be determined by splitting the time-of-arrival for each m_J with an adiabatically ramped inhomogeneous magnetic field, which we refer to as the Stern-Gerlach (SG) sequence.

3D velocity and spin reconstruction

Here we describe the method to reconstruct the 3D velocity and spin of the atoms in our experiment. We denote $t = 0$ to be the time at which the magnetic trap is

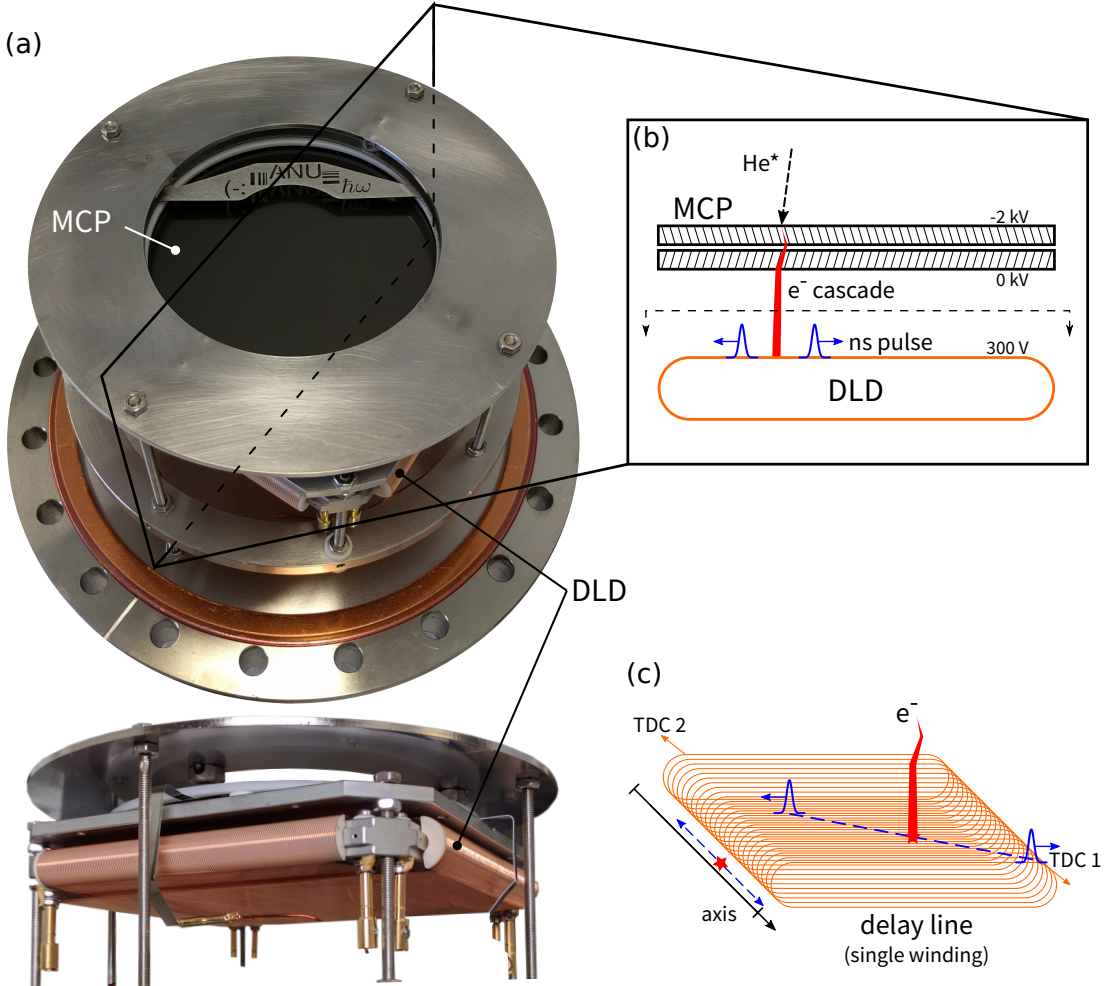


Figure 2.20: The microchannel plate – delay line detector. (a) Photo of the MCP-DLD stack assembly with a stencil mask (ANU pattern) placed over the MCP for a ghost imaging experiment [22]. The mask was removed from the detector for all results reported in this thesis. (b) A schematic side view of the detector stack. A cascade of electrons is triggered by an impact of He^* with the wall of the MCP, and the narrow shower of electrons impinges on the DLD. (c) A schematic view of a single winding of the delay line. The counter-propagating pulses are recorded by their time of arrival, from which the position and time of arrival of a single He^* atom can be reconstructed. The DLD used in this work is composed of 2 perpendicular windings, which allows the full 3D reconstruction of an individual atom's arrival time and position.

switched off, and $t = t^*$ the detection time at which an atom impacts the MCP-DLD detector. The impact position on the detector is then given by the coordinates $x(t^*), y(t^*)$. The 3D velocity of atoms at trap switch-off \mathbf{v} is then readily reconstructed from (t^*, x, y) -events, under the free-fall assumption of the atoms' trajectories. First, observe that the x, y -components are given by $v_x = (x - x(0))/t^*$, $v_y = (y - y(0))/t^*$. The vertical component includes the acceleration due to gravity by $v_z = gt^*/2 - (d - z(0))/t^*$, where z is measured relative to the centre of the trap.

In our experiment, the scale of displacement at the detector is set by a single-photon recoil $t_0 \hbar k_{\text{photon}}/m \approx 38.3 \text{ mm}$, where m is the mass of a helium-4 atom, $k_{\text{photon}} = 2\pi/1.083 \mu\text{m}^{-1}$ is the wavevector of a Raman laser, and $t_0 = \sqrt{2d/g} \approx 416 \text{ ms}$ the time-of-flight of a stationary atom. With typical trapping frequencies used in our experiment, the spatial extent of the source is less than $100 \mu\text{m}$, and therefore can be safely ignored (i.e. $x_0, y_0, z_0 \approx 0$) in comparison to the displacement due to the free-expansion after a photon scattering or an interatomic collision event.

A Taylor's expansion of v_z about an initially stationary state ($\mathbf{v} \approx 0$) yields $v_z = gt_0\tau - \frac{d}{t_0}\tau^2 + O(\tau^3)$, where $\tau = (t^* - t_0)/t_0$ is the normalised relative time of arrival. In our experiment, the collision geometry from the two-photon Raman process restricts τ to less than 0.03, such that even the first order approximation $v_z \approx gt_0\tau$ is accurate to 1%.

Figure 2.21 shows a typical reconstructed scatter plot of atoms from a single shot of our experiment. The time of arrival of each atom has been transformed to the relative vertical location by $z^* = v_z t^*$ for each atom. From the raw scatter data in Fig. 2.21, we observe the collision BECs (six dense balls) and the scattering halos (faint spheres), distinguished by their m_J states by the SG separation along the z -axis.

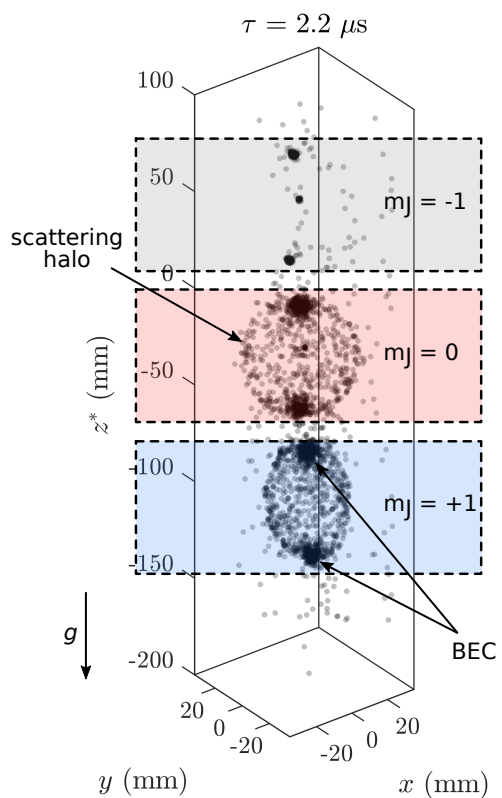


Figure 2.21: A typical 3D scatter plot from a single shot of BEC a collision experiment, where m_J states are discriminated by the Stern-Gerlach effect.

Master laser system for cooling and trapping metastable helium

Lasers are ubiquitous in modern technologies, where its diverse applications range from telecommunication over optical fibres, and non-invasive imaging and surgery in medicine, to the nano-fabrication of modern electronic gadgets. The technological impact of the laser has also undoubtedly shaped much of scientific discovery, among which is the modern physics of matter. Atomic, molecular and optical (AMO) physics took historic leaps thanks to the narrow linewidth and intense light offered by lasers, such as in precision spectroscopy and time-keeping, as well as in the unprecedented control of atoms and molecules to utilise their quantum properties. In the latter case, coherent light from lasers are an essential tool used to isolate and cool particles to temperatures where quantum mechanical effects can be observed. Such milestone achievement of laser cooling and trapping of atoms is the experimental realisation of Bose-Einstein condensation (BEC) of atomic gases – a degenerate quantum gas at the macroscopic scale [107] – which has become an extremely fruitful system for studying diverse aspects of many-body quantum systems, such as entanglement and thermalisation.

In the experiments investigated in this thesis, lasers play an essential role in the key stages of preparation of BECs of He^* , entangling of two atoms by inducing a collision, and coherent manipulation of individual atoms to realise spin measurement along an arbitrary axis. This chapter discusses the design and characterisation of the master laser of the He^* BEC machine responsible for the laser cooling and trapping of metastable helium, which was published in Ref. [157].

Laser cooling of He^* addresses the rapidly cycling $2^3\text{S}_1 - 2^3\text{P}_2$ transition at 1083.331 nm (276.73 THz) with a natural linewidth $\Gamma \approx 1.6 \text{ MHz}$ [143]. An important advantage for the laser cooling He^* is that only a single laser is required¹.

¹For the general laser cooling and trapping of helium, since the optically excited state 2^3P_2 cannot decay to other states than 2^3S_1 He^* , a simple closed loop cycle is maintained. Multi-electron atoms generally have a richer structure that allows multiple decay paths from the relevant excited level. A significant proportion of atoms then de-excite to a long-lived level which is no longer resonant with the cooling light. In such cases additional frequency shifted beams and even additional lasers, for much more complex systems such as dipolar atoms, trapped ions, and molecules, are required to optically pump the off-resonant dark states to re-populate the bright ground state [21].

Unfortunately there is a scarcity in commercially available lasers at this region of the infrared spectrum [158], with the added condition that they should be widely tunable (a continuously tunable range of wavelength, between 1–10% of the operating point) and of high spectral purity (laser linewidth is negligible compared to the linewidth of atomic transition) for a diverse range of experiments in atomic physics. The requirement of a narrow linewidth laser at this wavelength region in order to achieve BEC of He* has therefore led the community to typically adopt Ytterbium-doped fibre lasers. Although such specialised fibre lasers are commercially available, they tend to be expensive, whilst offering limited wavelength tunability and ability for end-user modifications and repairs. This has motivated us to develop a so-called external-cavity laser (ECL) using a single-angled-facet gain chip around 1083 nm for ultracold He* experiments, as a low-cost, high-performance candidate for the master laser. We demonstrate the ECL as an excellent low-cost laser system offering a narrow linewidth of a few kHz and widely tunable around $\sim 1.0 - 1.1 \mu\text{m}$. Indeed, all BECs created and collided in this thesis were slowed/cooled from an 880 m s^{-1} He* beam from a liquid-nitrogen cooled dc discharge source at 77 K, down to 1 mK in a MOT (average thermal velocity of 2 m s^{-1}), by amplifying the master laser developed in this thesis (see section on experimental apparatus for more details). This laser operates 24/7 in our lab and maintains a stable lock to an atomic reference (helium vapour cell) for well over a month. The output from the master laser is distributed to two different labs and easily scalable.

3.1 Design and operation of the master laser

ECLs are the workhorse of AMO physics labs due to their wide wavelength tunability, narrow spectral linewidth, low-cost and simple design [159]. This last feature has allowed end-user design and development, especially from laboratories that ultimately utilise the lasers for applications requiring wavelength tunability and low spectral noise [159, 160]. For completeness, a brief introduction of ECLs is given here. A modern review of ECLs is given in [161], while an encyclopedic reference to ECLs can be found in [162].

3.1.1 External-cavity laser

A common semiconductor laser such as a diode laser relies on the semiconductor as the gain medium, as well as the two end facets of the chip serving as reflectors to form the laser cavity, called Fabry-Pérot (FP) laser diodes. Notable features of semiconductor optical gain media are their low cost, flexibility in design parameters, and broadband spectrum. Nonetheless, the geometrically fixed cavity modes and relatively high cavity losses in laser diodes limit their wavelength tunability, give rise to broad linewidths, and multiple longitudinal modes. Laser diodes are therefore rarely used in atomic physics experiments without additional spectral elements. Fortunately, when a separate optical cavity is formed outside of a semiconductor gain

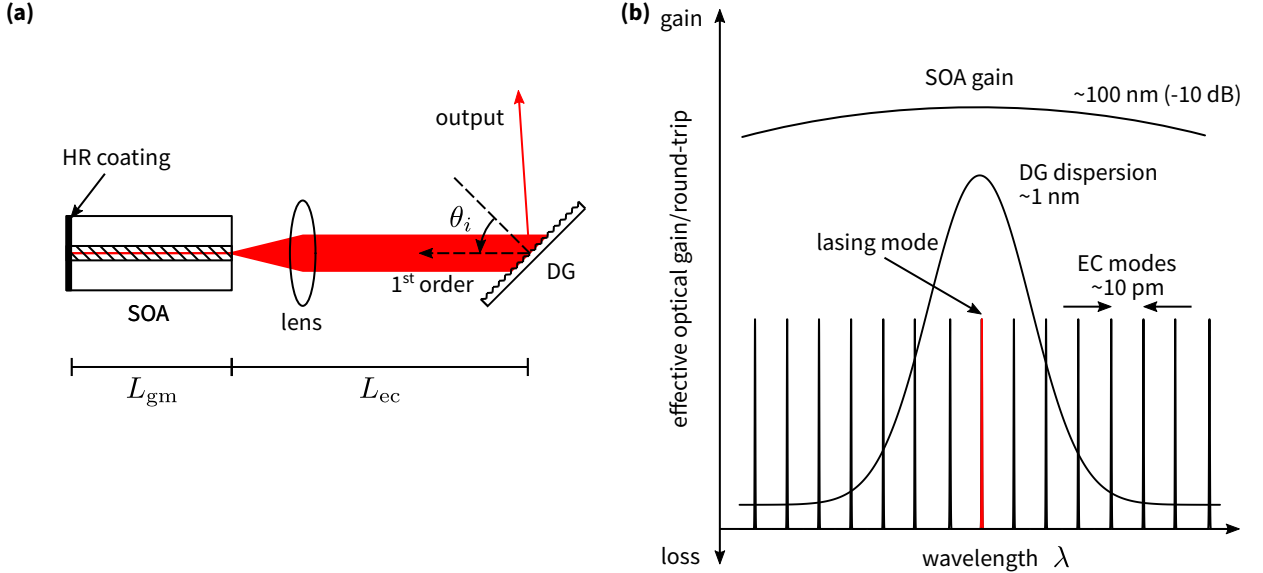


Figure 3.1: (a) A simplified schematic of an external-cavity semiconductor laser in the Littrow configuration (SOA: semiconductor optical amplifier, DG: diffraction grating). (b) Effective optical gain function around a lasing wavelength ($\sim 1 \mu\text{m}$) for the key elements of a Littrow-ECL. The vertical axis indicates a contribution to the round-trip efficiency by an optical element. Spectral shapes and scales are for illustrative purposes only, and not exact. The laser operates at the dominant external-cavity mode marked red.

medium, the total system can suppress all but one lasing mode of the bare laser diode, giving rise to an external-cavity laser [161].

A common type of an external-cavity (EC), termed the Littrow configuration [161], is created by a high reflectivity (HR) mirror to define one end of the cavity, while a diffraction grating forms an out-coupler, as shown in Fig. 3.1(a). The Littrow configuration operates by orienting the diffraction grating to the Littrow angle where the 1st diffraction order is back-reflected into the gain medium (see Fig. 3.1(b) for the gain spectrum), while the specular reflected light (zeroth order) normally serves as the output of the laser. The grating equation is given by $a(\sin \theta_i + \sin \phi_m) = m\lambda$, where a is the grating pitch, θ_i the incidence angle, ϕ_m the diffraction angle of m -th order, and λ is the wavelength of light. Therefore the Littrow condition for lasing of an ECL at λ is $\theta_i = \phi_1$, which gives

$$\lambda = 2a \sin \theta_i, \quad (3.1)$$

and provides wavelength tunability via small adjustments of the grating orientation [161]. The key feature of this configuration is that the diffraction grating directly acts as a wavelength selective mirror, by the angular dispersion of back-reflected beam at

the Littrow condition

$$\frac{d\lambda}{d\phi_1} = 2a \cos \phi_1, \quad (3.2)$$

so that only wavelengths near the desired central λ are well coupled to the cavity (see Fig. 3.1(b)). Lastly, the EC supports resonant longitudinal modes at frequencies

$$\nu_{ec,q} = qc/2(L_{ec} + n_{gm}L_{gm}), \quad (3.3)$$

where q is the integer labelling a longitudinal mode, c the speed of light, L_{ec} the total path length of the EC, and n_{gm} and L_{gm} are the refractive index and length of the gain medium, respectively. The EC modes provide the periodic comb function as seen in Fig. 3.1(b), from which it is intuitively clear that a single EC mode becomes the preferential lasing mode of an ECL, after accounting for other major gain and loss processes during mode competition. As a consequence, laser wavelength can be finely and continuously controlled by tuning the cavity length as seen from equation (3.3), and more coarsely but widely tuned by adjusting the grating orientation from equation (3.2).

3.1.2 Laser design

A variety of ECL designs exist in the literature that trade-off design parameters to yield the required performance characteristics of the laser [161]. For applications in laser cooling atomic gases, the desired attributes are single spectral and spatial mode operation, fast wavelength modulation to allow high bandwidth frequency stabilisation, narrow spectral linewidth, and stable mode-hop free operation. A moderate optical power of a few mW is sufficient since the output can be used to seed a fibre amplifier.

Single-angled-facet (SAF) gain chips are the ideal gain media for external-cavity configurations due to their broadband gain spectrum and intrinsically extremely low facet reflectivity (< -40 dB), even without an anti-reflection (AR) coating [163]. Thus, a significantly wider wavelength tunability and narrower spectral linewidth have been demonstrated for ECLs using SAF gain chips compared to conventional FP laser diodes [164, 160], for which AR coating is only effective around the design wavelength. In addition, SAF gain chips are usually constructed with extended active ridge lengths spanning a few millimetres, an order of magnitude longer than FP laser diodes, allowing reductions in injection current induced frequency noise. However, the increased semiconductor device capacitance reduces the modulation bandwidth of the ECL.

Another notable advantage of SAF gain chips in a Littrow-configured ECL is the intrinsic output beam pointing stability from the normal facet of the gain chip, enabling a robust fibre-coupled operation unaffected by adjustments on the grating orientation, which is problematic for designs using the output beam from specular reflection. For conventional ECLs utilising FP gain chips for which only the free-space output beam is available, an additional fold-mirror component can be used to

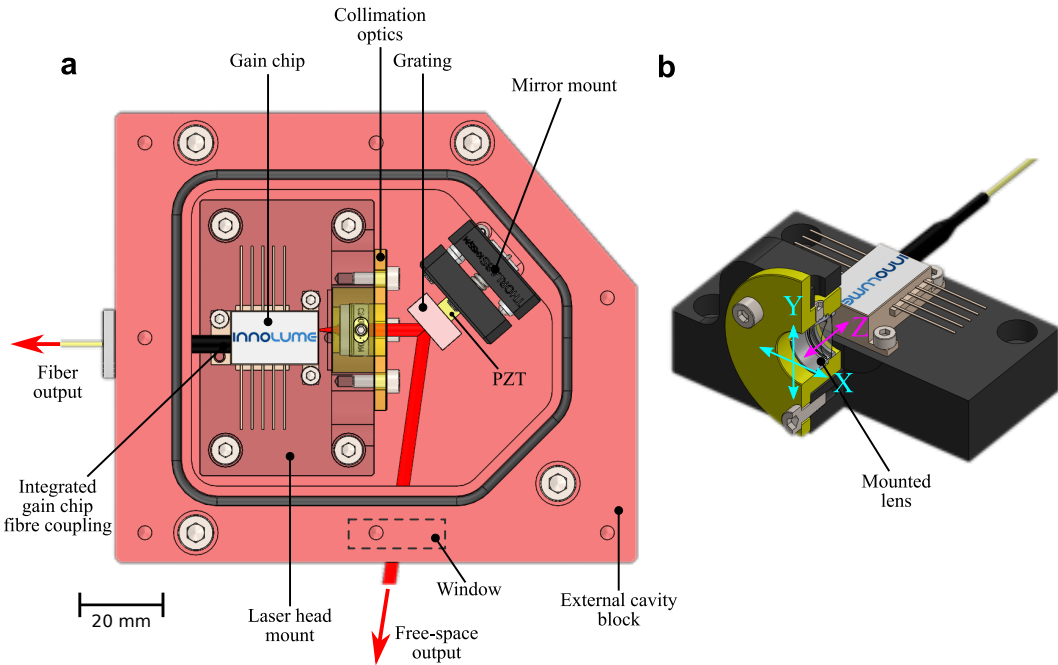


Figure 3.2: Design of the external-cavity gain chip laser. (a) The schematic shows the mechanical design of the Littrow configured ECL with a fibre-coupled gain chip. Components not shown in the schematics include the cavity temperature monitoring thermistor, cavity TEC (under the external-cavity block), and the integrated TEC inside the gain chip module. See Section B.2 for a list of components used in the design. (b) An isolated section view of the laser head consisting of the fibre-coupled gain chip and collimation optics. The arrows indicate the degrees of freedom in the lens alignment provided by the custom lens mount.

reduce the displacement of the beam [165]. Even then, significant beam steering will occur for tuning ranges over $\sim 10\text{ nm}$.

Here we provide a brief discussion on our design of the ECL system where the basic schematic is shown in Fig. 3.2. For completeness, we have collated the list of parts used in the design of the ECL and instruments for the complete laser system in Section B.2. We used a commercial, integrated SAF gain module with a built-in fibre-coupled output at the chip's normal facet. The SAF gain chip of 3 mm active length had a specified back reflectivity of approximately 10% at the normal facet for output coupling, while the reflectivity at the angled facet was specified to be less than 0.001%. The gain module had a built-in precision thermistor and thermoelectric cooler to allow independent temperature control of the gain chip from the cavity. Last but not least, the fibre-coupled output simplified the laser housing design for isolation from the environment. This allowed us to construct a hermetically sealed housing and achieve sufficient vibration, acoustic and thermal isolation of the laser (Fig. 3.2(a)).

The Littrow configuration clearly benefits from the simplicity in its design, as the low number of components helps to minimise disturbances from mechanical vibrations, and minimises complexity in optical alignment and maintenance by the end-user. The EC length was designed to be $L_{\text{ec}} = 25$ mm for a compact size of the laser and moderate EC free spectral range (FSR) of $\text{FSR}_{\text{ec}} \simeq c/2L_{\text{ec}} \simeq 6$ GHz. This approximately corresponds to the comb spacing between longitudinal modes from (3.3) such that $|\nu_{\text{ec},q\pm 1} - \nu_{\text{ec},q}| \approx \text{FSR}_{\text{ec}}$, since the length of gain chip is an order of magnitude smaller compared to the EC. Therefore this approximately sets the continuous tuning range achievable by changing the cavity length.

In order to collimate the free-space output beam from the gain chip, which has a manufacturer specified full width at half maximum (FWHM) divergence angle of 16 deg, we used a 0.5 NA lens with 8 mm focal length at 1083 nm. A customised mount for the collimation lens provided the translational degrees of freedom required to optimise the laser's performance (see Fig. 3.2(b)). The custom lens mount allows relatively precise adjustments of ≈ 50 μm in the axial position (Z axis) via the finely pitched thread on the lens tube (see Fig. 3.2(b)). In contrast, the transverse (XY plane) adjustments of the lens were relatively coarse by design and found to be less critical for the laser operation. A more detailed description of the alignment procedure can be found in Section B.1.

A blazed diffraction grating at 1200 lines/mm with 80% efficiency at 1083 nm was selected as the coarse wavelength-selective element to form the EC. To allow for a wide tuning of the wavelength and alignment of the back-reflected beam, the grating was fixed onto a kinematic mirror mount. With careful manual operation, the grating orientation can be manually tuned to below 20 mrad which corresponds to a change in back-reflected laser frequency of 50 GHz, as seen from Eq. (3.2). For a continuous and moderate bandwidth (~ 1 kHz) control of the laser frequency, we installed a piezoelectric transducer (PZT) chip between the grating and the mirror mount to precisely modulate the cavity length, since a nanometre displacement is sufficient to shift the EC mode by 12 MHz given by Eq. (3.3) at 1083 nm.

Independent temperature control of the gain chip and the cavity block was achieved from separately located thermoelectric coolers (TECs) and thermistors: the integrated TEC in the gain module and a TEC module installed under the EC block. The dual-stage temperature control decouples two major temperature-dependent behaviours of the ECL, in addition to allowing optimised control for stabilising two systems of extremely different thermal masses. As a result we achieve a fast temperature control of the gain chip, which affects its length as well as electro-optic properties, independently from the temperature stabilisation of the EC block which must be shielded against temperature drifts in the environment, since the EC modes are sensitive to the thermal expansion of the cavity to approximately -8 MHz mK^{-1} at 1083 nm.

The laser housing – to which the gain chip, collimation optics and kinematic grating body were mounted – was machined from a single block of aluminium, providing a rigid structure that attenuates environmental noise. The laser was enclosed in an acoustically insulated box built on an optics table and vibrationally isolated from the tabletop via viscoelastic dampers. The box also provided thermal insula-

tion from significant diurnal room temperature fluctuations caused by the laboratory air conditioning system.

3.1.3 Laser system setup

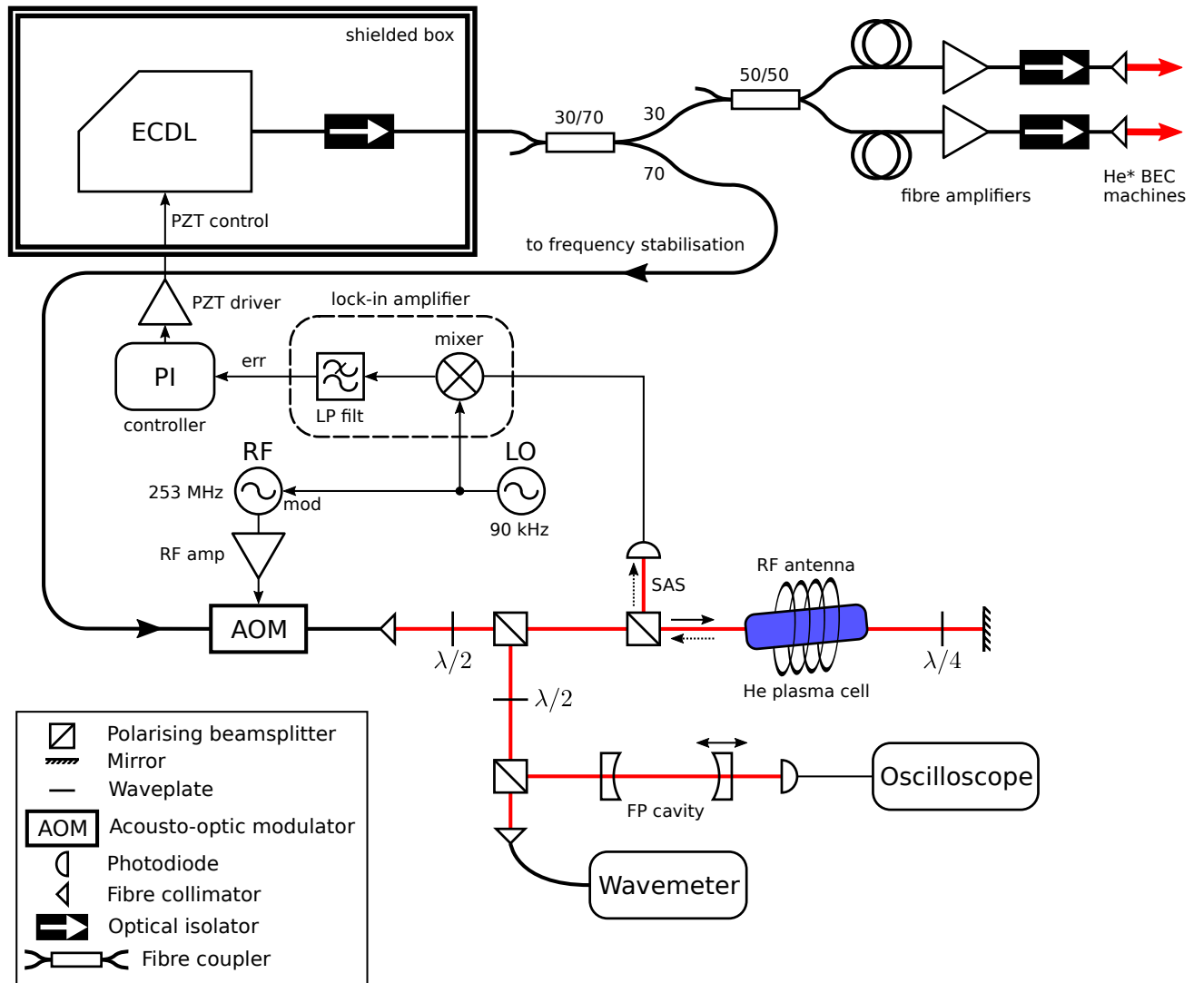


Figure 3.3: Experimental schematic of the master laser system set-up. The laser is offset locked to the laser cooling transition of He^* via dither-locking to the saturated absorption spectroscopy (SAS) signal. The fibre-coupled output seeds two identical fibre amplifiers for two different ultracold He^* experiments. See Section B.2 for a list of instruments.

The output light from the ECL is amplified by a 5W, polarisation and narrow linewidth maintaining fibre amplifier at each He^* experimental apparatus at ANU,

since it cannot directly provide enough power of ≈ 3 W required. Operating as the seed-laser for the laser cooling system reduces the power requirement for the ECL, to only ≈ 5 mW, which should significantly improve the system's lifetime even under continuous use. The setup of the master laser system is shown in Fig. 3.3. Since the output of the master laser is already fibre-coupled, power distribution and coupling to the amplifiers at each experiment does not drift significantly. The experimental setups for frequency stabilisation and performing laser diagnostics are shown in the lower part of Fig. 3.3.

To diagnose the operation of the laser, a scanning FP interferometer with a free spectral range of ~ 1.5 GHz was used to ensure that the laser was operating single-mode during the alignment procedure and the measurements discussed in this work. Operating in single-mode, the measured light output power versus injection current curve is shown in Fig. 3.4(a). The threshold current and the slope efficiency were 50(1) mA and 0.57(1) mW/mA, respectively at the laser cooling transition wavelength of 1083.33(1) nm, monitored by the wavemeter. The laser diode current driver used in this experiment limited the maximum injection current to 195 mA, from which the laser's maximum output power was 83(1) mW (Fig. 3.4(a)). Around 300 mW of output power through the fibre should be achievable by increasing the current to the manufacturer's nominal value of ~ 600 mA. In order to extend its lifetime, the master laser for our ultracold He * apparatus runs continuously at a quarter of the gain chip manufacturer's recommended operating current.

3.2 Wavelength tunability

This section characterises the ability to adjust the wavelength of our laser, which is generally a crucial feature to laser applications enabling spectroscopy and frequency stabilisation. First, we discuss the range of wavelengths our ECL can operate in single-mode, distinguishing a continuously tunable range from a much wider spectrum scanned through discrete hops. Then we characterise the dynamical controls we can implement on the laser, and finally the sensitivity of our system to temperature variations.

3.2.1 Tuning range

The tunable range of a single-mode laser can be broadly categorised by its mode-hop free (MHF) and coarse tuning ranges. For our ECL, we define these tunability measures by adjusting only the degrees of freedom in the Littrow grating. As such, the MHF tuning range refers to the continuous range of wavelengths, achieved by scanning the length of EC with the PZT, over which the laser remains single-mode. In contrast, a manual adjustment of the grating angle, via the mirror mount, covers a much wider but discontinuous spectrum.

An illustrative scan over the MHF tuning range can be given by an absorption profile centred around the 1083.331(1) nm laser cooling transition of He * . Figure 3.6 shows the saturated absorption spectroscopy (SAS) signal over the $2^3S_1 - 2^3P_{1,2}$

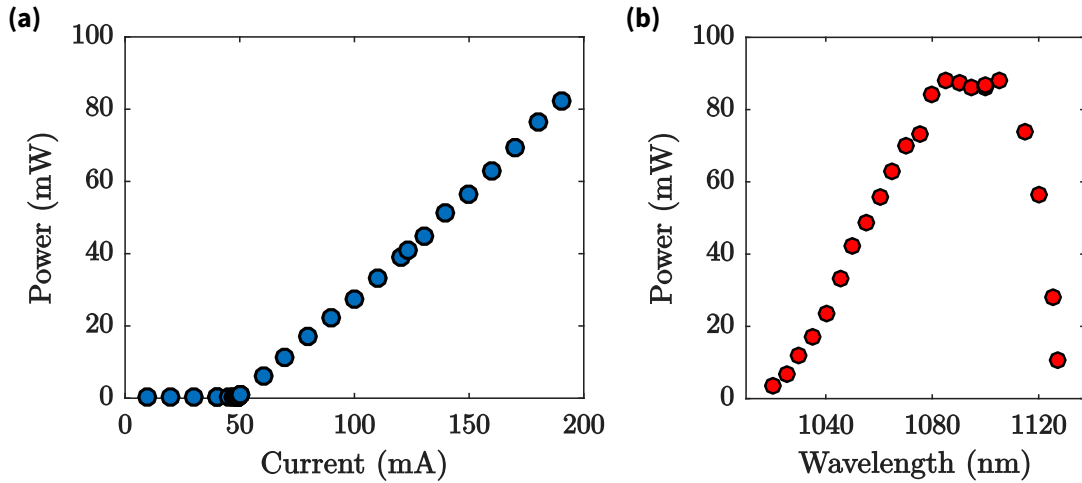


Figure 3.4: Laser power and wavelength tunability. (a) Injection current versus laser power measured at the fibre-coupled output, operating at 1083.33(1) nm. The threshold current and slope efficiency were measured to be 50(1) mA and 0.57(1) mW/mA, respectively. (b) The plot shows the laser output power over the coarse wavelength tuning range when the injection current was at 195 mA. The laser was single-mode at each data point after adjustments. The tuning ranges at FWHM (-3 dB) and FWTM (-10 dB) were determined to be 70(3) nm and 100(3) nm, respectively, with the centre wavelength at 1080(3) nm.

transitions in helium (see Fig. 3.3 for a schematic) obtained by continuously scanning the ECL. Before we explain SAS in detail, suffice to say the obtained spectrum resembles what one expects from a simple absorption spectroscopy through an atomic vapour cell. In a separate measurement, MHF tuning ranges of 30(1) pm ($7.8\text{ GHz} \simeq 1.3 \cdot \text{FSR}_{\text{ec}}$) were observed, which is clearly limited by the mode competition between longitudinal EC modes at a comb spacing FSR_{ec} . Indeed, synchronous tuning of the grating angle and the PZT displacement could be used to further increase the MHF tuning range [166], however this was not necessary for our application.

Figure 3.4(b) shows the coarse tunability curve obtained from our ECL, demonstrating a FWHM (-3 dB) and full width at tenth maximum (FWTM; -10 dB) coarse wavelength tunability of 70(3) nm and 100(3) nm, respectively, around the centre wavelength of 1080(3) nm. The laser operated within 10% of its maximum power when tuned between 1080 nm and 1115 nm, away from which the power decayed asymmetrically, reflecting the amplifier's gain asymmetry.

3.2.2 Fast modulation

A number of critical factors influencing the ECL's wavelength were characterised. These include changes in the EC length induced by the PZT, thermal expansion, the

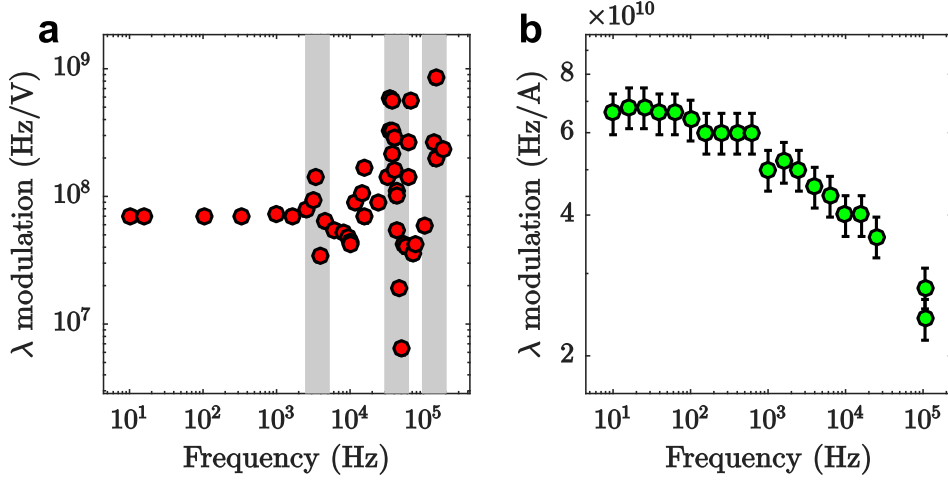


Figure 3.5: Laser wavelength modulation response. (a) The frequency response of the laser frequency to modulations of PZT voltage. A flat response of $71(1)$ kHz/mV was observed below the resonance feature at 3.6 kHz, indicated by the leftmost grey band. The second band located at 40 kHz indicates the predicted mechanical resonance of the grating loaded PZT. The resonance at 140 kHz is most likely an electrical resonance. (b) A similar plot is shown for the modulation of injection current. A flat response of $-67(3)$ kHz/ μ A (sign determined from DC adjustments) was observed below 100 Hz and a slow roll-off to the -6 dB point at $37(3)$ kHz was measured.

laser diode injection current and the temperature of the gain chip. For each parameter, the laser's sensitivity (i.e. the rate of change in lasing frequency, as determined by heterodyne detection, with respect to small changes in the measured parameter) and frequency response were determined and summarised in Table 3.1.

The wavelength sensitivity to the PZT voltage measured for our ECL was determined to be $71(3)$ kHz/mV (Fig. 3.5(a)). A resonance was observed around 3.6 kHz, most likely from the coupling between the grating loaded PZT and the mirror mount. The usable bandwidth of the PZT was thus limited to the flat-gain region below 3 kHz.

The wavelength modulation transfer function for the injection current is shown in Fig. 3.5(b) and displays no resonance below 100 kHz. The wavelength sensitivity was measured to be $-67(3)$ kHz/ μ A, with a -6 dB bandwidth of $37(3)$ kHz. The measured wavelength sensitivity of the ECL to injection current is around a factor of 50 less than that for conventional FP diode ECLs [159]. The relative insensitivity to current may be due to the large differences in gain stripe lengths between SAF (3 mm) and FP (typically ~ 300 μ m) chips, resulting in reduced changes in charge carrier density in affecting the refractive index to Eq. (3.3). The slow response to injection current for our ECL as seen from the low modulation bandwidth, compared to FP diode lasers which can be modulated up to a few gigahertz [159], was most likely due to the larger electrical capacitance from the extended size of the gain chip's

Table 3.1: Laser frequency modulation sensitivity. The bandwidth is calculated at the -6 dB gain point (*limited by a mechanical resonance).

Parameter	Sensitivity	Units	Bandwidth
Intra-cavity PZT	71(3)	kHz/mV	3* kHz
Injection current	-67(3)	kHz/ μ A	37(3) kHz
Gain chip temperature	-5.4(4)	MHz/mK	-
Cavity temperature	-6.5(5)	MHz/mK	-

active region.

It follows that broadband noise in the injection current should contribute less to the broadening of laser linewidth due to both the relatively insensitive effect on laser wavelength and low modulation cut-off bandwidth. As a consequence, a less stringent noise performance of laser current controllers is required for our ECL to achieve a narrow linewidth compared to conventional ECLs, for which a root mean squared (rms) current noise over only a few hundred nA is typically sufficient to broaden linewidths over 100 kHz [167]. For our ECL to achieve a sub-100 kHz linewidth δf , the maximum allowable PZT voltage δV_{PZT} and injection current noise is given by $\delta f / (\delta V_{\text{PZT}} / \text{df/d}V_{\text{PZT}}) \approx 1.4 \text{ mV rms}$ and $\approx 1.5 \mu\text{A rms}$, integrated over their corresponding bandwidths, respectively.

3.2.3 Thermal sensitivity

The sensitivity of the laser wavelength to thermal effects was measured directly with a wavemeter. From incremental temperature changes applied over a range of 200 mK to the gain chip, the laser's wavelength sensitivity with respect to the gain chip temperature was measured to be $-5.4(4)$ MHz/mK.

In order to determine the laser's sensitivity to its EC temperature, the laser wavelength and the cavity temperature were monitored over several hours while all other parameters were stabilised. The sensitivity of the laser wavelength on the cavity temperature was then estimated to be $-6.5(5)$ MHz/mK, based on the time-correlated traces, which agrees well with the prediction from Eq. (3.3) based on the thermal expansion of the aluminium cavity.

3.3 Stabilisation to an atomic reference

The frequency stability of a laser is an essential requirement for laser cooling and trapping experiments. Since laser cooling and trapping techniques rely on a precise detuning of the beams with respect to a specific atomic transition, having access to an error signal of the laser's frequency against an absolute frequency reference is generally desired for feedback control. In our setup, spectroscopy of the helium atom itself provides the desired absolute frequency reference, obtained via a Doppler-free spectroscopy technique.

In addition to improvements in the laser's long-term frequency drifts, a frequency stabilisation scheme with high-bandwidth feedback can provide a significant linewidth narrowing over a free-running laser [168, 169]. In our experiment, we adopt an acousto-optic frequency modulation technique discussed in [170] to frequency stabilise the laser to the atomic reference of interest, namely the $2^3S_1 - 2^3P_2$ laser cooling transition of He*.

3.3.1 Saturated absorption spectroscopy of He*

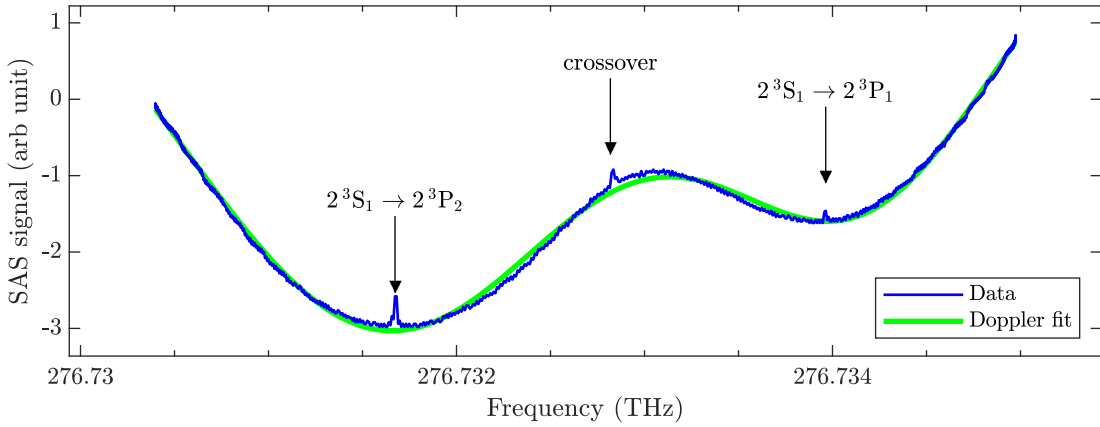


Figure 3.6: Saturated absorption spectroscopy of metastable helium obtained from a continuous mode-hop free scan of the laser wavelength over 4.6 GHz (15 pm). The green curve is a bimodal Gaussian fit to the observed spectrum as expected from two discrete Doppler broadened lines.

A vapour cell filled with the atomic species of interest commonly serves as an absolute frequency reference for stabilising lasers in AMO applications, since resonances are tied to the fundamental atomic structure. For cooling and coherent control of atoms, a crucial advantage given by a reference cell of the same atomic species is the ability to control the absolute detuning of the laser with respect to a target transition. The atomic resonances of the thermal ensemble however suffer from a significant amount of broadening due to thermal motion, exhibiting orders of magnitude broader spectral response than the natural linewidth of the atom. Here we introduce a Doppler-free spectroscopic technique which eliminates effects from thermal broadening to resolve the laser cooling transition of He* close to its natural linewidth with a vapour cell.

Recall that an atom moving at a velocity \mathbf{v} (non-relativistic) in the lab frame experiences a Doppler shift $\delta f_{\text{Doppler}} = -\mathbf{k} \cdot \mathbf{v}/2\pi$, given by the atom's relative motion with respect to the light's wavevector \mathbf{k} . For a gaseous ensemble of atoms at room temperature $T \approx 300$ K, its rms velocity along $\hat{\mathbf{k}}$ (from the equipartition theorem $\langle mv_{\hat{\mathbf{k}}}^2/2 \rangle = k_B T/2$) therefore induces the Doppler-broadening of a resonance f_0 by a

FWHM of $\Delta f_{\text{Doppler}} = 2\sqrt{2 \ln 2} \sqrt{k_B T / mc^2} f_0$. For the laser cooling transition of He^* this evaluates to $\Delta f_{\text{Doppler}} \approx 6.2 \times 10^{-6} f_0 \approx 1.7 \text{ GHz}$, approximately three orders of magnitude broader than natural linewidth of the transition $\Gamma \approx 1.6 \text{ MHz}$.

The bottom right part of Fig. 3.3 shows the experimental setup for Doppler-free spectroscopy of He^* with a vapour cell filled with helium. First, excited states of helium including the He^* state of interest are created in the cell by RF discharge. The laser is retro-reflected through this vapour cell, in which the counter-propagating pump (first pass through vapour) and probe (retro-reflected) beams are overlapped. We use a polarising beam splitter at the pump input and place a quarter-wave plate in the retro-reflective path to orthogonally polarise the probe beam with respect to the pump, which allows us to measure the probe beam after it has passed through the vapour.

Figure 3.6 shows the absorption signal obtained across the 2^3P_1 and 2^3P_2 transitions, taken in a single MHF scan with the PZT. The atomic transitions are clearly resolved as sharp peaks (a few MHz wide) far below the Doppler broadened line-shape, which are indeed Gaussian and a few GHz in width as predicted. Below we briefly explain this phenomenon behind saturated absorption spectroscopy (SAS).

Observe that the absorption of an off-resonant light through the thermal ensemble are due to atoms with particular v_z that Doppler-shifts the light into resonance (suppose the natural linewidth is negligible). Since the probe beam is retro-reflected and propagates at $-\mathbf{k}$, it is absorbed by atoms with opposite velocity $-v_z$, which are equally populated as v_z . Therefore when the laser is off-resonant to a transition, SAS is essentially identical to the normal single-pass absorption spectroscopy in which the scattering medium's length can be algebraically summed over the retro-reflected paths. Indeed, we observe the expected Doppler broadened absorption features of the atomic transitions in Fig. 3.6. When the laser is on resonance with the transition, however, the pump and probe beams are now both absorbed by the same set of atoms $v_z \approx 0$ that are stationary along the beam. In this case, the population of ground state (here He^*) is depleted (equivalently the population of the excited state is saturated) by the passage of the pump beam, which significantly enhances the transmission of the probe light through the ensemble. Since the probe beam therefore does not scatter at resonance, the effective beam path through the scattering medium becomes roughly half that of off-resonance. This ultimately gives rise to the Doppler-free SAS peak with an ideal linewidth corresponding to the natural linewidth of the atomic transition. In summary, SAS is therefore a Doppler-free spectroscopic technique relying on the nonlinearity in saturating the excited state population of the ensemble, at which point no more absorption is possible as seen by the enhanced transmission of the probe beam.

Figure 3.7(a) shows a zoomed-in profile of the Doppler-free resolved laser cooling transition from the SAS that was taken with our master laser setup. We clearly observe a Doppler-free linewidth around $13 \text{ MHz} \approx 8\Gamma$, noting the uncertainties arising from the sparsity of the sample and quantisation noise in the measuring instrument due to the small SAS signal. In this demonstration the observed linewidth is indeed expected to be greater than the natural linewidth, since the laser linewidth

is effectively broadened by a few MHz from the AOM to enable the dither-frequency locking technique as explained in the next section.

The third SAS peak mid-way between the atomic transitions (see Fig. 3.6) is an artefact called a crossover – a saturated absorption phenomena at the mid-frequency between two transition which is resonant for atoms which are exactly oppositely Doppler detuned with respect to the pump and probe beams.

3.3.2 Frequency stabilisation by acousto-optic modulation

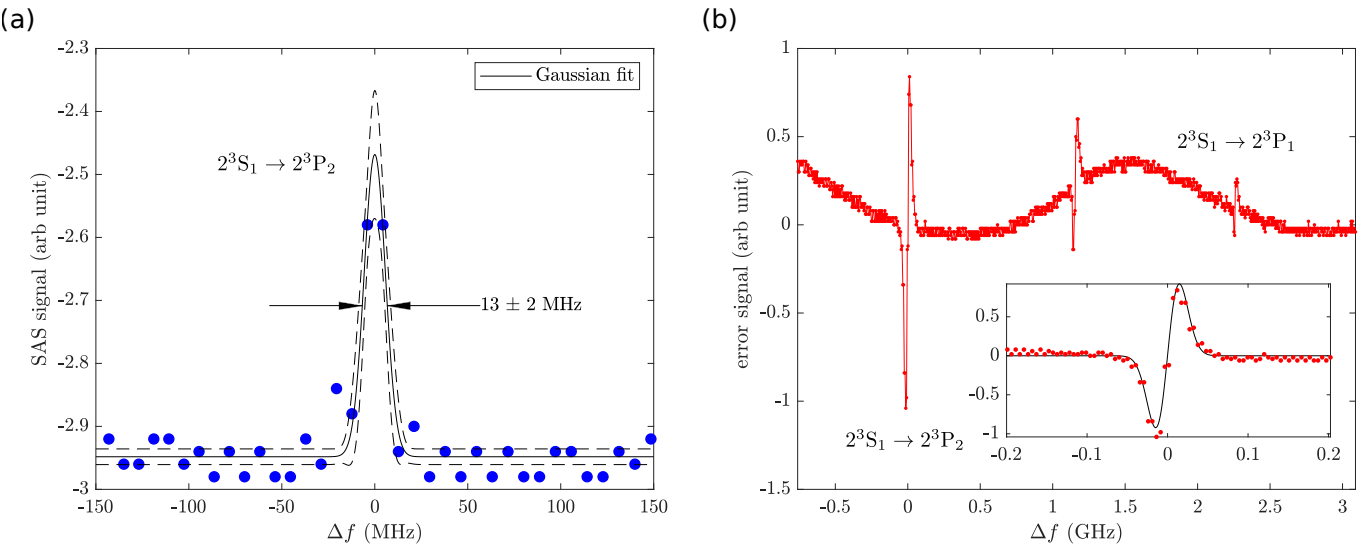


Figure 3.7: SAS signal for frequency stabilisation. (a) Doppler-free absorption spectrum of the ${}^4\text{He}^*$ laser cooling transition, zoomed-in from Fig. 3.6. Solid line is a Gaussian lineshape fit to data. (b) Measured error signal from the lock-in amplifier over the MFH scanning range. Inset shows the dispersive error signal zoomed-in at the laser cooling transition which is stabilised to the zero-crossing point by a PI control of the PZT. The solid line is a fit of the first order derivative of the Gaussian lineshape to data.

In order to stabilise or lock the laser's frequency to an atomic reference such as Fig. 3.7(a), a dispersive error signal, proportional to the error in frequency from the transition $\Delta f = f - f_0$, is required. We utilise a dither-lock technique to obtain a dispersive error signal based on the first order derivative of the SAS profile to feedback control the laser frequency by the PZT.

Indeed for the approximately Gaussian SAS peak a gradient signal with respect to the laser frequency suffices as the error signal, since the first order derivative of a Gaussian profile is approximately linear around the peak, which corresponds to the zero-crossing (see inset of Fig. 3.7(b)). Derivative signals with respect to a drive can generally be obtained by dithering/modulating the drive by a small range at a precise local oscillator frequency f_{LO} , and demodulating the oscillatory output of

the signal at the modulation frequency to determine the excursion of the signal with respect to the change in drive.

Our experimental setup of the dither–demodulation technique is shown in Fig. 3.3. In particular, an in-fibre acousto-optic modulator (AOM) provided the fast dither (modulation) in laser wavelength at $f_{\text{LO}} = 90 \text{ kHz}$ (limited by the frequency range of the demodulator), as well as setting a constant offset of 253 MHz to the transition. Figure 3.7(b) shows the dispersive error signal obtained from a phase-locked demodulation of the SAS signal by a lock-in amplifier (LIA). The inset shows a zoomed-in section of the LIA error signal at the laser cooling transition, where the narrow region centred at the transition is indeed a linear function of the true frequency error Δf . To stabilise the laser frequency on the AOM dither error signal, a proportional-integral (PI) controller was used to feedback control the intra-cavity PZT. The system bandwidth of our stabilisation scheme was limited to $\approx 1 \text{ kHz}$ due to the LIA with a maximum demodulation and output-filter bandwidths of 100 kHz and 1 kHz, respectively.

Disturbances to the laser wavelength (e.g. change in cavity length by mechanical vibration) greater than a width of this feature can however destabilise and unlock a simple control system such as the PI controller, since the output of the LIA (demodulated error signal) will no longer be in the linear regime of the true frequency error. Due to passive environmental isolation design features such as the acoustically shielded box and rubber dampers as supports, disturbances including striking the optics table and loud acoustic noises are unable to destabilise the laser. In our system, the laser can be easily re-locked and typically maintains the lock for months. Finally this stabilised output is distributed to two different fibre amplifiers located at each ultracold He^{*} experimental apparatus, as shown in Fig. 3.3.

3.4 Frequency stability

The unsurpassable stability of the monotonically oscillating electric field is the key property of lasers for state-of-the-art applications, other than their high power output. For example in AMO and quantum physics, the stability at short time scales is relevant in the precision spectroscopy and the coherent manipulation of atoms and molecules. However characterising the spectral linewidth of a stable laser can prove to be nontrivial, since typical optical spectrum analysers have resolutions much broader than the lasers themselves. On the other hand, since all lasers are inherently sensitive to the environment, without an appropriate frequency stabilisation scheme a free-running laser can fluctuate and drift out of application range over long time-scales. In this section, we characterise (1) the linewidth of the ECL based on heterodyne interferometry and (2) the long-term frequency stability, for both its free-running and SAS-locked operating modes.

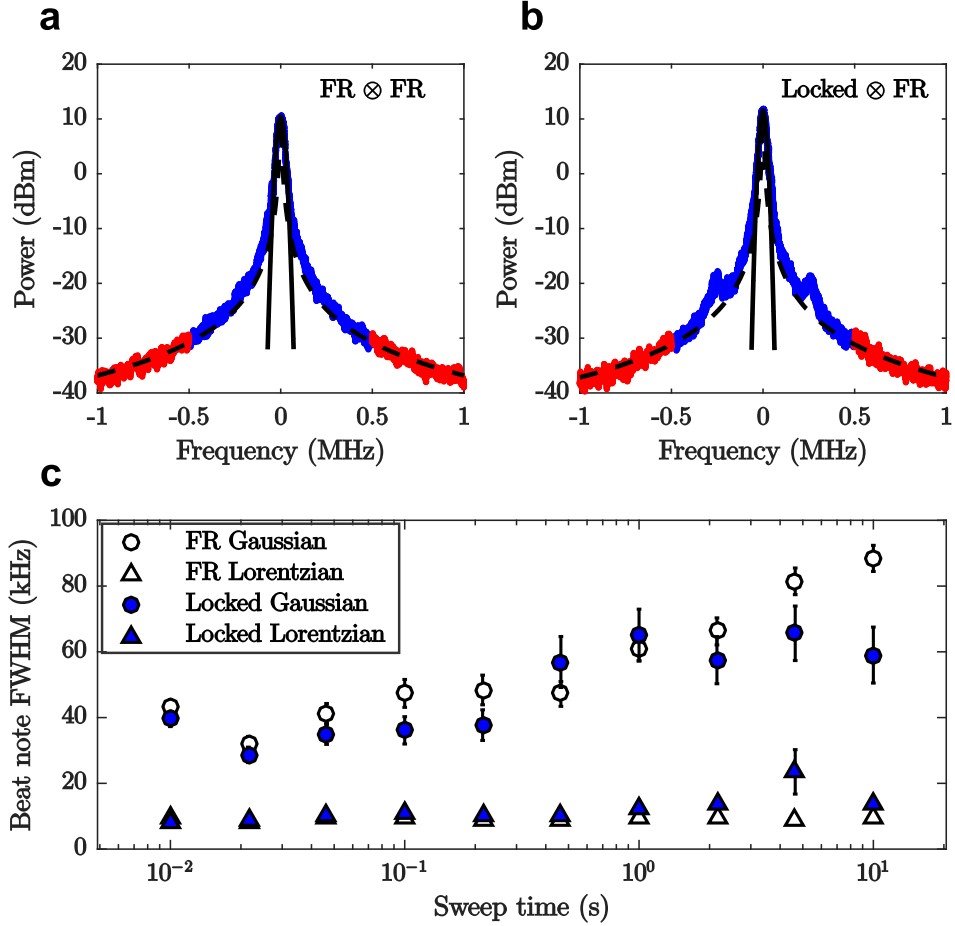


Figure 3.8: Heterodyne laser linewidth measurement. (a) Averaged beat note spectrum, taken at 10 ms sweep time, from a heterodyne detection of two identically constructed free-running lasers ($\text{FR} \otimes \text{FR}$). The beat note is divided into the central 1 MHz region (blue) and remaining tails (red) and separately fitted by a Gaussian (solid curve) and a Lorentzian (dashed curve) profile, respectively. (b) A heterodyne beat note from a free-running and a locked laser ($\text{Locked} \otimes \text{FR}$) taken over 10 ms sweep time. The sidebands at ~ 260 kHz were due to the switching noise of the PZT driver used in the locking scheme. (c) The behaviour of heterodyne beat note FWHM when the sweep time of the spectrum analyser is varied between 10 ms to 10 s for the $\text{FR} \otimes \text{FR}$ (unfilled) and $\text{Locked} \otimes \text{FR}$ (filled) cases. The Gaussian peak (circle) was observed to broaden in sweep time in contrast to the Lorentzian tail (triangle) which was almost constant even from three orders of magnitude increase in sweep time. Each data point is an average of fits to 50 individual traces.

3.4.1 Laser linewidth

The spectral linewidth of the ECL was determined from a heterodyne detection technique, where the interference of beams from two identically constructed lasers are used to infer the short timescale frequency stability of an individual laser. In our experiment we mixed the light from two independent ECLs operating identically at 1083 nm on a 50:50 beam splitter and detected the output on a fast photodetector with 12 GHz bandwidth. The heterodyne technique produces an intensity signal (square of the electric field amplitude) at the difference frequency between the two mixed sources called the beat note (as well as sum- and double-frequency signals which are undetected/filtered). As such, optical frequencies can be down-shifted into the radio and microwave domain (MHz – GHz) which offer mature spectral analysis techniques, such as with RF spectrum analysers. More importantly, the heterodyne technique is conceptually ideal for the characterisation of noise, since the beat note exactly corresponds to the convolution of the two individual laser lineshapes.

Since the two ECLs are identical in design and operating condition, we may assume the fluctuations in their output lights to be identical in process and uncorrelated. The resulting beat note can then be fitted with Gaussian and Lorentzian profiles, from which an individual laser's linewidth can be estimated to lie between the estimations from Gaussian $w_G/\sqrt{2}$ and Lorentzian $w_L/2$, first demonstrated in Ref. [171], where $w_{G,L}$ denotes each profile's FWHM². Following the methods of Thompson and Scholten [172], each beat note spectrum was divided into the central (1 MHz wide) and tail band for the Gaussian and Lorentzian fits, respectively (see Figs. 3.8(a) and 3.8(b)).

Linewidth broadening due to technical noise was minimised for the free-running ECL by driving the PZT with a low-noise DC voltage supply with a measured noise of $\approx 300 \text{ nV rms}$ over 0.2 Hz – 100 kHz (bandwidth of the measuring instrument), using a precision multimeter with a 100 nV resolution (Tektronix DMM4040). In addition, identical low-noise current controllers (custom-built based on the circuitry described in [167]), with noise measured to be less than 20 nA rms over the same bandwidth, were used to supply a constant injection current for both lasers. Lastly, environmental disturbances to the laser frequency noise were minimised by placing the lasers in a well-protected enclosure.

Figure 3.8(c) shows the beat note FWHM from two different setups: 1. two free-running lasers, and 2. a free-running and a locked laser. We measured the beat note spectra at various integration times, set by the sweep times (SWTs) of a spectrum analyser. The minimum linewidth for the free-running laser was observed with a fitted Gaussian and Lorentzian linewidths of 22(2) kHz and 4.2(3) kHz, respectively, at 22.5 ms SWT (Fig. 3.8(c)). No significant changes to the beat note linewidth were seen when one of the ECLs was locked (see Fig. 3.8(c)). However, small sidebands

²This result follows from the convolution theorem, which states that the convolution operation is equivalent to the multiplication operation in the Fourier conjugate domain. Note that the Fourier transform of Lorentzian (Gaussian) is an exponential (Gaussian) function, where the width parameter exists only inside the exponent in its first (second) power. Therefore a Lorentzian (Gaussian) linewidth adds algebraically (in quadrature).

at 260 kHz were present in the heterodyne spectra with a locked laser (compare Figs. 3.8(a) and 3.8(b)). The sidebands correspond to narrow-band noise from the PZT driver, required only when locking the laser.

The free-running laser linewidth increases with sweep time as seen by the trend in the Gaussian fits, due to increasing contribution from frequency drift to the laser linewidth at longer observation times. In contrast, no such behaviour is seen for the Lorentzian counterpart for which the linewidth was independent of observation time since it is less sensitive to slow drifts [173]. In addition, the stationary Lorentzian lineshape is consistent with the qualities of intrinsic laser line broadening mechanisms including amplified spontaneous emission of the gain chip and lossy output-coupling of the EC [174].

In order to precisely determine the locked laser linewidth, a delayed self-heterodyne technique as demonstrated in [160] or locking of two ECLs is required for the heterodyne detection method discussed here. These steps were not undertaken in our study since the locking scheme did not obviously degrade the spectral linewidth.

We note that an investigation into the laser frequency noise spectrum and noise in the feedback chain is required to better understand the noise sources and their relative contributions to the measured integrated linewidth [175]. In principle, the spectral linewidth of our ECL could be further narrowed from a high-bandwidth feedback scheme, such as locking to polarisation spectroscopy signal [169], or by improving the current set-up to increase modulation and feedback bandwidth, reduce noise in the feedback chain, and increase the dynamic range of error signal.

3.4.2 Long-term stability

The long-term frequency drift of the ECL was measured by monitoring the beat note frequency against an independent stabilised reference laser (the 1083.331 nm fibre laser with ~ 1 MHz linewidth that so far served as our experiment's master laser). The beat note was acquired at a sampling rate of ~ 1.5 Hz from a spectrum analyser and monitored for over 24 hours (see Fig. 3.9(a)). The measured frequency drifts, namely its deviation from an initial time point, from both a free-running and a locked laser in the time-domain are shown in Fig. 3.9(a).

We observe as expected in Fig. 3.9(a) that locking the laser significantly improves its long-term frequency stability. The free-running laser exhibited fluctuations of ~ 100 MHz compared to ~ 0.1 MHz of the locked laser over long timescales (see inset of Fig. 3.9(a)). The fluctuations seen around ~ 0.1 MHz in the beat note frequency measurement are accountable by the statistical uncertainty caused by the reference laser's broad linewidth. Thus we note that the drift measurement in the locked laser was an overestimate limited by the measurement noise and its true frequency stability will be better.

It is more illustrative to characterise the long-term stability of lasers [176], and in general oscillators, by analysing the frequency jumps observed over various timescales. One such measure is Allan deviation $\sigma_y(\tau)$ [177] of the instantaneous oscillator fre-

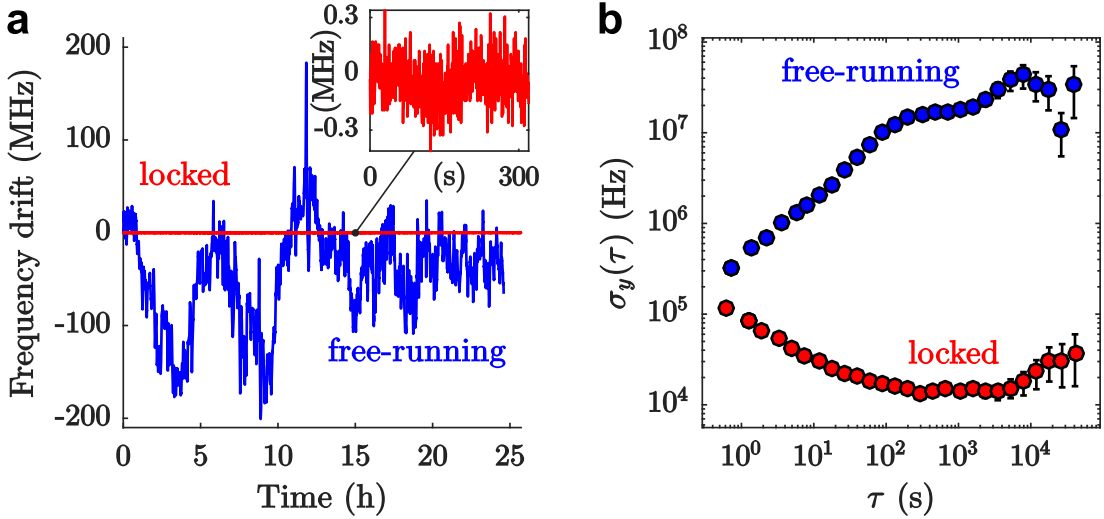


Figure 3.9: Long-term laser frequency stability. (a) The frequency drift of the free-running (blue) and the locked (red) laser monitored over a day, sampled at ~ 1.5 Hz. (b) Allan deviation of the laser frequency. Allan deviations calculated over an observation time of 11 hours for the free-running and locked laser were 30(20) MHz and 40(20) kHz, respectively.

frequency $f(t)$, defined by

$$\sigma_y^2(\tau) \equiv \frac{1}{2} \langle (f(t) - f(t + \tau))^2 \rangle, \quad (3.4)$$

where the expectation value is taken over the observation time t . From its similarity to the standard definition of variance, the Allan deviation quantifies the rms variation in the oscillator frequency over a time period τ .

Figure 3.9(b) shows Allan deviation evaluated from the time series measurement in Figure 3.9(a). We observe qualitatively different Allan deviation characteristics from the two modes of ECL, where it is seen to increase in time for the free-running mode, in contrast to the decreasing trend seen when locked to SAS. At timescales longer than 100 s, the frequency stability of the free-running laser was improved by around 3 orders of magnitude by locking to an atomic reference.

The Allan deviation for the free-running and locked laser frequencies is seen to approach a constant value at long timescales. The drift at the longest timescale we could measure were ~ 30 MHz and ~ 20 kHz for the free-running and locked laser, respectively. The drift measurement for the locked laser is likely an overestimate, as explained previously. The asymptotic behaviour in the Allan deviation is expected from the servo control of individual inputs to the laser which should suppress low frequency noise around DC. The calculated Allan deviation for the frequency drift implies a frequency instability in the free-running laser of $30(20)$ MHz $\equiv 19(13) \cdot \Gamma$ over 11 hours. Thus the ECL must be stabilised against a stationary reference for our

applications to ultracold He^{*} experiments where the resonance has width Γ . Indeed, the laser's frequency instability was reduced to 40(20) kHz $\equiv 0.025(13) \cdot \Gamma$ over the same time scale (an overestimate), upon locking to an atomic reference.

Nonlocal spin correlations across pairs of spatially separated atoms

4.1 Introduction

Nonlocality is a crucial signature of quantum mechanics, a feature which is incompatible with classical physics that rests on principles of determinism and locality [4]. Aside from its importance in fundamental physics, quantum nonlocality plays an important role in the rapidly growing quantum information technologies enabling absolutely secure communication and device verification [1].

Quantum nonlocality has so far only been definitively verified in a restricted set of physical systems, due to the stringent requirements in the entanglement distribution between separated particles, the coherent control, and efficient detection [7]. Most notably the observed nonlocal correlations have been predominantly realised between massless particles in their internal degree of freedom, such as from photon polarisation [9, 10] and electron spin [8] entanglement. Indeed, as our understanding and capability of manipulating physical systems in the quantum regime grows, fundamental interests in the motional superposition of massive systems for the interaction of quantum mechanics and gravity may become relevant [72]. This gap has sparked some renewed interest in the Bell test with motion-entangled massive systems [68, 70, 130].

This chapter reports on the demonstration of quantum nonlocality from spatially separated pairs of helium atoms scattered from a collision of Bose-Einstein condensates. The experiment consists of the three essential components necessary to realise a Bell test: a correlated atomic pair source, a rotation of the spins of both atoms, and the momentum and spin resolved single-particle detection necessary for evaluating pair correlations. The pairwise correlation as the spins are rotated exhibits EPR-steering, and directly verifies that s-wave collisions produce the Bell triplet state.

4.2 Theory of nonlocal correlations in a scattering halo

Let us revisit the theory of colliding BECs for a test of quantum nonlocality, which were separately discussed in the background chapter Section 2.2.2. When two oppo-

sitely spin-polarised BECs collide at low energies and the total number of scattered atoms remain few, pairs of atoms, entangled in a Bell state, are emitted back-to-back in momentum [178]. Since the atomic pairs spatially separate after emission, the scattering halo is an obvious candidate for a test of quantum nonlocality. In practice, as we show, this emission is a random process and the number of pairs fluctuate about the average such that an entangled pair cannot always be distinguished, ultimately reducing the observable correlation. It turns out that only when the average scattering mode occupation is below a critical threshold, will the back-to-back scattered atoms exhibit nonlocal spin correlations.

4.2.1 Collision of oppositely spin-polarised BECs

Let us allow atoms to have discrete internal states α , so that the original many-body Hamiltonian Eq. (2.33) must be upgraded to describe the interaction of all different spin components $\hat{\Psi}_\alpha$. We will briefly summarise this system which was discussed in Section 2.2.2. Assuming only a two-body contact interaction to describe collisions between two ultracold gases, the system Hamiltonian was given in Eq. (2.51) according to

$$\hat{H} = \int d\mathbf{r} \hat{\Psi}_\alpha^\dagger \left(-\frac{\hbar^2 \nabla^2}{2m} \right) \hat{\Psi}_\alpha + \frac{1}{2} \int d\mathbf{r} \hat{\Psi}_\alpha^\dagger \hat{\Psi}_\beta^\dagger (c_0 \delta_{\alpha\alpha'} \delta_{\beta\beta'} + c_1^{\alpha\alpha' \beta\beta'}) \hat{\Psi}_{\beta'} \hat{\Psi}_{\alpha'} + \int d\mathbf{r} \hat{\Psi}_\alpha^\dagger V(\mathbf{r}) \hat{\Psi}_\alpha, \quad (4.1)$$

where we used Einstein summation convention. Here c_0 and c_1 are the interaction strengths for the elastic and spin-changing collision $\alpha\beta \rightarrow \alpha'\beta'$, respectively. For the $J = 1$ spinor such as He*, these are related to the s -wave scattering lengths $a_{0/2}$ of the interaction channels of total angular momentum $J = 0, 2$, according to $c_0 = \frac{4\pi\hbar^2}{m} \frac{a_0+2a_2}{3}$, and $c_1^{\alpha\alpha' \beta\beta'} = \frac{4\pi\hbar^2}{m} \frac{a_2-a_0}{3} (\mathbf{F}_{\alpha\alpha'} \cdot \mathbf{F}_{\beta\beta'})$, where $\mathbf{F} = (F_x, F_y, F_z)$ is a vector of spin-1 matrices.

Our experiment implements a collision of two oppositely spin-polarised BECs in order to create spin entangled atom pairs. We investigate the $m_J = 1$ and 0 collision of He*, denoted \uparrow and \downarrow respectively, in which spin-changing collisions (terms proportional to c_1) are forbidden by the conservation of angular momentum ($|J=1, m_J=1\rangle + |J=1, m_J=0\rangle \rightarrow |1, m_1\rangle + |1, m_2\rangle$), and can be safely neglected.

When a negligible fraction of atoms collide, the majority of atoms are unscattered and remain in the BECs, and the many-body state may be represented in by the Bogoliubov approximation

$$\hat{\Psi}(\mathbf{r}, t) = \psi_{\uparrow,+Q}(\mathbf{r}, t) + \psi_{\downarrow,-Q}(\mathbf{r}, t) + \hat{\delta}(\mathbf{r}, t), \quad (4.2)$$

where $\psi_{\alpha,q}(\mathbf{r}, t)$ are the condensate wavefunction polarised in internal state $\alpha \in \{\uparrow, \downarrow\}$, and mean momenta $q = \pm Q$, and $\hat{\delta}(\mathbf{r}, t)$ is the quantum fluctuation describing the scattered product. In the experiment, the momentum (rms) width of the condensate σ_k is negligible compared to the collision momentum Q ($\sigma_k/Q \approx 0.03$). The Hamiltonian (4.1) simplifies considerably in such a case, such that the condensates may be

approximated as plane waves, and the nonlinear contact interaction (*s*-wave scattering) causes spontaneous four-wave mixing (see Section 2.2.2 where we discussed the collision of BECs in detail). A familiar quadratic Hamiltonian appears in the plane wave basis (for resonant scattering \mathbf{k} -modes conserving energy and momentum), given by

$$\hat{H} = \sum_{\mathbf{k}} \hbar \chi \left(\hat{a}_{\uparrow}^{\dagger}(\mathbf{k}) \hat{a}_{\downarrow}^{\dagger}(-\mathbf{k}) + \hat{a}_{\downarrow}^{\dagger}(\mathbf{k}) \hat{a}_{\uparrow}^{\dagger}(-\mathbf{k}) \right) + \text{h.c.} \quad (4.3)$$

The above system is a generalisation of the two mode squeezed vacuum to include internal states in each plane wave mode. As expected, every scattered atom is perfectly correlated with an oppositely scattered twin, that is also oppositely polarised in spin. Since creation and annihilation operators between different spins commute, the time evolution factorises into two-mode squeezing operators acting on opposite momentum-spin pairs $\{(\mathbf{k}, \uparrow), (-\mathbf{k}, \downarrow)\}$ and $\{(\mathbf{k}, \downarrow), (-\mathbf{k}, \uparrow)\}$.

An initially empty pair of counter-propagating modes $(\mathbf{k}, -\mathbf{k})$ in the scattering halo therefore evolves according to

$$|\delta(t)\rangle_{(\mathbf{k}, -\mathbf{k})} = \exp\left(\hbar \chi \hat{a}_{\uparrow}^{\dagger}(\mathbf{k}) \hat{a}_{\downarrow}^{\dagger}(-\mathbf{k}) - \text{h.c.}\right) \exp\left(\hbar \chi \hat{a}_{\downarrow}^{\dagger}(\mathbf{k}) \hat{a}_{\uparrow}^{\dagger}(-\mathbf{k}) - \text{h.c.}\right) |\text{vac}\rangle \quad (4.4)$$

$$= (1 - (\tanh \chi t)^2) \sum_{n,m=0}^{\infty} (\tanh \chi t)^{n+m} |n\rangle_{\mathbf{k}\uparrow} |m\rangle_{\mathbf{k}\downarrow} |m\rangle_{-\mathbf{k}\uparrow} |n\rangle_{-\mathbf{k}\downarrow} \quad (4.5)$$

$$= |0\rangle + \chi t \underbrace{(|\uparrow\rangle_{\mathbf{k}} |\downarrow\rangle_{-\mathbf{k}} + |\downarrow\rangle_{\mathbf{k}} |\uparrow\rangle_{-\mathbf{k}})}_{|\Psi^+\rangle} + \mathcal{O}((\chi t)^2), \quad (4.6)$$

where in the last line we used a particle state notation to emphasize the generation of $|\Psi^+\rangle$ Bell state. Notice that if the total number of particles in the \mathbf{k} -mode (regardless of spins) can be verified to be 1, this heralds the generation of $|\Psi^+\rangle$ into $\pm \mathbf{k}$, which is useful for the test of nonlocality. Since Eq. (4.5) arises in an exponentially decaying probability distribution of atom number occupation, the purity of such pair source is improved by reducing its average emission rate. Below we discuss how the purity of such pair source relates to the test of quantum nonlocality.

4.2.2 Nonlocal correlations in the *s*-wave scattering halo

Here we derive the entanglement and EPR-steering witnesses tailored for violation by the Bell triplet state created in an *s*-wave collision experiment. Compared to Bell inequalities for two qubit systems, entanglement and EPR-steering may be verified with a restricted set of measurements, such as when the spin readout angles coincide for both subsystems.

Sufficient condition for the demonstration of Bell nonlocality

Although the two qubit system has been studied extensively for its simplicity as a building block for large-scale interacting systems, its properties for quantum nonlocality are not yet fully understood [179]. Namely there is not yet a simple way to

determine whether an arbitrary two qubit density matrix can exhibit a violation of a Bell inequality [179] (not even for the seemingly simple family of Werner states introduced in Section 2.1). On the other hand, any two qubit state can be tested for whether it is entangled or separable by a relatively simple calculation from its density matrix [32], for example by a measure called entanglement of formation [180]. As we saw in Section 2.1 however, entanglement is only a necessary condition for performing nonlocal tasks such as EPR-steering and violation of a Bell inequality. Indeed, so far there is no such necessary and sufficient criteria to distinguish whether even a general two qubit state is EPR-steering or Bell nonlocal, with significant progress being made [181, 182].

As such, various Bell inequalities have been found for the bipartite LHV models where each system, denoted A and B, yields a binary measurement outcome [1]. The most widely tested no-go theorem for LHV models of two qubits is the CHSH inequality [38]

$$B_{\text{CHSH}} = |E(\theta, \phi) + E(\theta', \phi') + E(\theta', \phi) - E(\theta, \phi')| \leq 2, \quad (4.7)$$

where $E(\theta, \phi)$ is the correlation coefficient of the outcomes of A and B, defined

$$E(\theta, \phi) = P_{\uparrow\uparrow}(\theta, \phi) - P_{\uparrow\downarrow}(\theta, \phi) - P_{\downarrow\uparrow}(\theta, \phi) + P_{\downarrow\downarrow}(\theta, \phi), \quad (4.8)$$

where P_{ij} is the joint detection probability for the outcome i and $j \in \{\uparrow, \downarrow\}$, when the measurement settings are configured θ and ϕ , respectively. In practice, A and B share an entangled pair of spin-1/2 particles and the measurement settings correspond to a rotation angle of the respective particle's spin, prior to its readout in the $\hat{\sigma}_z$ basis. In other words, the spin measurement is fixed (denoted as $\hat{\sigma}_z$ basis by convention), but the atomic spins themselves are rotated prior to measurement, so that the outcome is a readout of the spin component rotated at an angle relative to $\hat{\sigma}_z$. In QM formalism, the correlation coefficient is then clearly

$$E(\theta, \phi) = \left\langle \hat{\sigma}_z^{(A)} \hat{\sigma}_z^{(B)} \right\rangle_{\theta, \phi}, \quad (4.9)$$

where subscripts on the expectation value indicate that the average is to be taken on the rotated state $|\theta, \phi\rangle = \hat{R}_y^{(A)}(\theta) \hat{R}_y^{(B)}(\phi) |\psi\rangle$, such that

$$\hat{R}_y^{(l)}(\theta) = \exp(-i\theta \hat{\sigma}_y^{(l)}/2) = \cos(\theta/2) \mathbb{1} - i \sin(\theta/2) \hat{\sigma}_y \quad (4.10)$$

is the unitary rotation operation for the qubit $l = A, B$, and $|\psi\rangle$ is initial state of the two-qubit system. Some examples of the correlations exhibited by simple two-qubit states are shown in Fig. 4.1.

Let us consider the CHSH-Bell nonlocality witness for the back-to-back scattered modes in the scattering halo in (4.6). The Bell test starts with the mixing of the two spin components independently in two opposite regions of the halo, A and B, by the angles ϕ and θ over the y -axis. The many-body angular momentum \vec{J} and atom

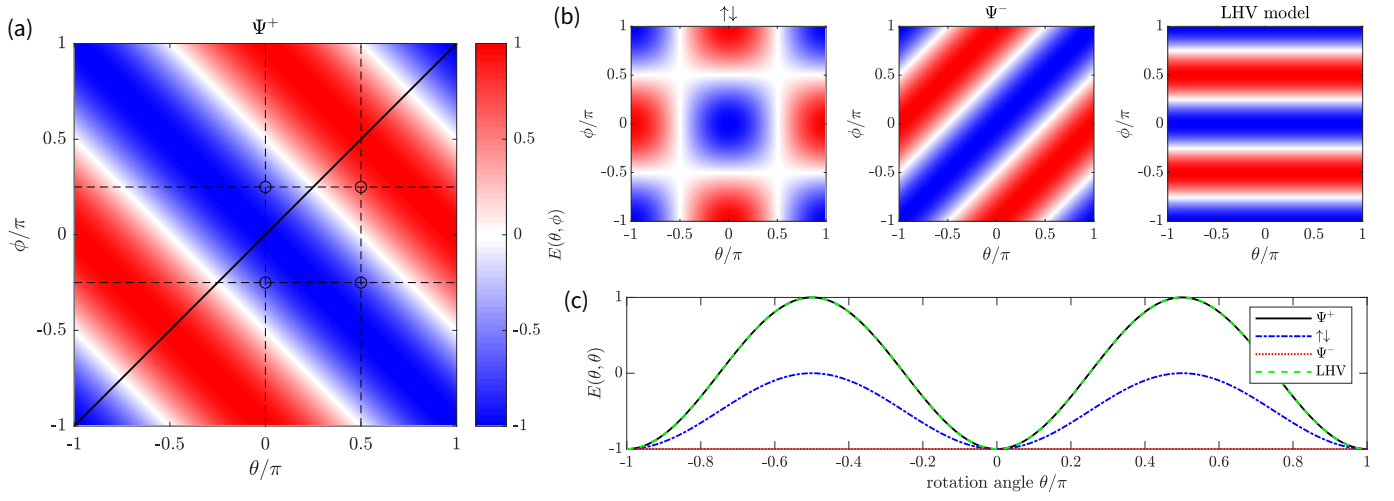


Figure 4.1: Correlations in two-qubit systems. (a) Pairwise correlation $E(\theta, \phi)$ for $|\Psi^+\rangle$. Solid line indicates the restricted set of symmetrically rotated measurement settings $\theta = \phi$ accessible in our experiment. Dashed vertical/horizontal lines and their intersection (markers) indicate (one of) the optimal measurement settings for θ/ϕ that maximise the CHSH parameter. (b) Correlation coefficient evaluated for separable state $|\uparrow\rangle|\downarrow\rangle$, Bell singlet $|\Psi^-\rangle$, and a particular adversarial LHV model (from left to right), which produces identical outcomes to $|\Psi^+\rangle$ under symmetrically rotated measurement settings. (c) A comparison of the pairwise correlation under symmetric rotation.

number operators \hat{N} can then be constructed from creation/annihilation operators (Jordan-Schwinger map [183]) according to

$$\hat{J}_x^\alpha = \frac{1}{2} \int_{\alpha} \frac{d\mathbf{k}}{2\pi} \left(\hat{a}_\uparrow^\dagger(\mathbf{k}) \hat{a}_\downarrow(\mathbf{k}) + \hat{a}_\downarrow^\dagger(\mathbf{k}) \hat{a}_\uparrow(\mathbf{k}) \right), \quad (4.11)$$

$$\hat{J}_y^\alpha = \frac{1}{2i} \int_{\alpha} \frac{d\mathbf{k}}{2\pi} \left(\hat{a}_\uparrow^\dagger(\mathbf{k}) \hat{a}_\downarrow(\mathbf{k}) - \hat{a}_\downarrow^\dagger(\mathbf{k}) \hat{a}_\uparrow(\mathbf{k}) \right), \quad (4.12)$$

$$\hat{J}_z^\alpha = \frac{1}{2} \int_{\alpha} \frac{d\mathbf{k}}{2\pi} \left(\hat{a}_\uparrow^\dagger(\mathbf{k}) \hat{a}_\uparrow(\mathbf{k}) - \hat{a}_\downarrow^\dagger(\mathbf{k}) \hat{a}_\downarrow(\mathbf{k}) \right), \quad (4.13)$$

$$\hat{N}^\alpha = \frac{1}{2} \int_{\alpha} \frac{d\mathbf{k}}{2\pi} \left(\hat{a}_\uparrow^\dagger(\mathbf{k}) \hat{a}_\uparrow(\mathbf{k}) + \hat{a}_\downarrow^\dagger(\mathbf{k}) \hat{a}_\downarrow(\mathbf{k}) \right), \quad (4.14)$$

with $\alpha = A, B$ indicating the two subsystems. The atom number-normalised correlation coefficient is readily constructed and evaluated analytically from (4.5) (see Appendix), given explicitly as

$$E(\theta, \phi) = \frac{\langle \hat{J}_z^{(A)} \hat{J}_z^{(B)} \rangle_{\theta, \phi}}{\langle \hat{N}^{(A)} \hat{N}^{(B)} \rangle_{\theta, \phi}} \quad (4.15)$$

$$= -\mathcal{E} \cos(\theta + \phi). \quad (4.16)$$

Before we specify the amplitude term \mathcal{E} in the previous expression, let us introduce the second order correlation function after a (θ, ϕ) -rotation sequence (at back-to-back \mathbf{k} -regions A, B respectively)

$$g_{ij}^{(2)}(\theta, \phi) = \frac{\iint_{AB} d\mathbf{k} d\mathbf{k}' \left\langle \hat{a}_i^\dagger(\mathbf{k}) \hat{a}_j^\dagger(\mathbf{k}') \hat{a}_j(\mathbf{k}') \hat{a}_i(\mathbf{k}) \right\rangle_{\theta, \phi}}{\iint_{AB} d\mathbf{k} d\mathbf{k}' \langle \hat{a}_i^\dagger(\mathbf{k}) \hat{a}_i(\mathbf{k}) \rangle_{\theta, \phi} \langle \hat{a}_j^\dagger(\mathbf{k}') \hat{a}_j(\mathbf{k}') \rangle_{\theta, \phi}}, \quad (4.17)$$

where $i, j \in \{\uparrow, \downarrow\}$ denote spin modes in $\hat{\sigma}_z$ -basis. The amplitude coefficient in Eq. (4.16) is then given by

$$\mathcal{E} = \frac{g_{\uparrow\downarrow}^{(2)}(0, 0) - 1}{g_{\uparrow\downarrow}^{(2)}(0, 0) + 1}, \quad (4.18)$$

where the $g^{(2)}$ amplitude of the pair source is related to the average mode occupancy $\bar{n} \equiv \langle \hat{a}_i^\dagger(\mathbf{k}) \hat{a}_i(\mathbf{k}) \rangle$ (uniform over the scattering halo) by [112]

$$g_{\uparrow\downarrow}^{(2)}(0, 0) = 2 + \frac{1}{\bar{n}}. \quad (4.19)$$

The result in (4.16) is therefore simply that of an ideal Bell triplet with a reduced amplitude \mathcal{E} , and equivalent to the effective mixed pair state $\hat{\rho}_+$ introduced in Section 2.1.

The correlation coefficient $E(\theta, \phi)$ for a generalised many-body state (see Eq. (4.15)) indeed exhibits a clear correspondence to the ideal two particle scenario in terms of

joint detection probabilities as in Eq. (4.8), given explicitly in terms of $g^{(2)}$ functions by (see Appendix)

$$P_{ij}(\theta, \phi) = \frac{g_{ij}^{(2)}}{g_{\uparrow\uparrow}^{(2)} + g_{\downarrow\downarrow}^{(2)} + g_{\uparrow\downarrow}^{(2)} + g_{\downarrow\uparrow}^{(2)}} \quad (4.20)$$

(arguments specifying the measurement settings are omitted from $g_{ij}^{(2)}(\theta, \phi)$ without the risk of ambiguity), satisfying $P_{ij} \in [0, 1]$ and $\sum_{i,j} P_{ij} = 1$.

From the similarity of the correlation coefficient in (4.16) to that of the Bell state, the CHSH parameter in (4.7) takes the maximum QM value $\max_{\theta, \phi}(B_{\text{CHSH}}) = 2\sqrt{2}\mathcal{E}$ [39], optimised over all measurement strategies (i.e. the set of angles in (4.7)). Under ideal experimental conditions in a CHSH-Bell test, the scattering halo therefore exhibits Bell nonlocality when $\mathcal{E} > 1/\sqrt{2}$. This QM signalled Bell nonlocality condition is equivalently expressed in terms of the correlation function from Eq. (4.18)

$$g_{\uparrow\downarrow}^{(2)}_{\text{Bell}} > 2\sqrt{2} + 3 \approx 5.8, \quad (4.21)$$

and therefore places a critical threshold average mode occupancy from (4.19)

$$\bar{n}_{\text{Bell}} < (1 + 2\sqrt{2})^{-1} \approx 0.26, \quad (4.22)$$

below which the CHSH-Bell inequality is violated (this result was proved in [178]).

In our current experimental apparatus, spin rotation beams are much larger than the scattering halo and operate identically on all atoms. Therefore we are restricted to correlation measurements where the rotation angle is symmetric, namely $\theta = \phi$, and have access to only the diagonal part of the 2D function E . An extension to implement independent rotations to each atom of the pair, so that θ, ϕ may be arbitrary, would be experimentally possible and a discussion is found in Chapter 6. It turns out that there is no Bell inequality that can be constructed as a function of the diagonal elements of $E(\theta, \phi)$ (see Appendix for details). After some thought, LHV models supporting any $E(\theta, \theta)$ profile can be constructed rather trivially, since every pair can be locally programmed at the source to return any desired set of correlation along all common axes. Surprisingly, the diagonally restricted measurement denoted $\mathcal{B}(\theta) \equiv E(\theta, \theta)$ of the bipartite system turns out to be sufficient information for the verification of entanglement and EPR-steering (see Eq. 14 in Ref. [184]), as discussed below.

The separability criterion

Here we consider what form the diagonal correlator $\mathcal{B}(\theta)$ may take for a general separable two qubit system, and construct the separability criterion on their maximum range. Note that in QM, a rotation $\hat{R}_y(\theta)$ of the target state prior to performing $\hat{\sigma}_z$ measurement is equivalent to a rotated axis readout on the original target state, given by a unitary transformation of the observable $\hat{R}_y^\dagger(\theta)\hat{\sigma}_z\hat{R}_y(\theta) = \cos\theta\hat{\sigma}_z + i\sin\theta\hat{\sigma}_x$ (here we assume the rotation is about the y -axis without loss of generality). We can therefore express the symmetrically y -rotated correlator 4.9 in the orthogonal basis on the

original state denoted $C_{ij} \equiv \langle \hat{\sigma}_i^{(A)} \hat{\sigma}_j^{(B)} \rangle$ where $i, j \in \{x, z\}$, written as follows

$$\mathcal{B}(\theta) = \frac{1}{2}[C_{xx} + C_{zz} + (C_{xx} - C_{zz}) \cos 2\theta + (C_{xz} + C_{zx}) \sin 2\theta]. \quad (4.23)$$

The difference between the minimum and maximum values of $\mathcal{B}(\theta)$ over θ yields the range \mathcal{A} (note that it is the peak-to-peak amplitude), given explicitly by

$$\mathcal{A} \equiv \max \mathcal{B}(\theta) - \min \mathcal{B}(\theta) = \sqrt{(C_{xx} - C_{zz})^2 + (C_{xz} + C_{zx})^2}. \quad (4.24)$$

Let us now consider a general separable state, expressed as a convex combination (i.e. a linear combination with non-negative coefficients that sum to unity) of product states by definition

$$\hat{\rho}_{\text{sep}} = \int d\lambda p(\lambda) \hat{\rho}_{\lambda}^{(A)} \otimes \hat{\rho}_{\lambda}^{(B)}, \quad (4.25)$$

where $p(\lambda)$ is the probability distribution of a hidden variable λ and $\hat{\rho}^{(i)}(\lambda)$ is the hidden state of the subsystem $i = A, B$. Since we are interested in two level systems, we can express each hidden state of the subsystem (a single-qubit density matrix) in the Bloch vector representation, namely

$$\begin{aligned} \hat{\rho}_{\lambda}^{(A)} &= \frac{1}{2}(\mathbb{1} + \mathbf{a}(\lambda) \cdot \vec{\sigma}^{(A)}), \\ \hat{\rho}_{\lambda}^{(B)} &= \frac{1}{2}(\mathbb{1} + \mathbf{b}(\lambda) \cdot \vec{\sigma}^{(B)}), \end{aligned} \quad (4.26)$$

such that the Bloch vectors $\mathbf{a}(\lambda), \mathbf{b}(\lambda) \in \mathbb{R}^3$ have a maximum length of unity. The correlators are then given explicitly for a general two-qubit state (4.25) by the distribution of such hidden Bloch vectors according to

$$C_{ij} = \text{tr}[\hat{\rho}_{\text{sep}} \hat{\sigma}_i^{(A)} \hat{\sigma}_j^{(B)}] = \int d\lambda p(\lambda) a_i(\lambda) b_j(\lambda), \quad (4.27)$$

thus the symmetrically y -rotated correlation in Eq. (4.23) is independent of the y -component of Bloch vectors. Let us therefore parameterise the Bloch vectors' projections on the zx -plane as follows

$$\mathbf{a}'(\lambda) = \alpha(\lambda) \begin{pmatrix} \cos \phi_A(\lambda) \\ \sin \phi_A(\lambda) \end{pmatrix}, \quad \mathbf{b}'(\lambda) = \beta(\lambda) \begin{pmatrix} \cos \phi_B(\lambda) \\ \sin \phi_B(\lambda) \end{pmatrix}, \quad (4.28)$$

where the prime notation indicates the projection $\mathbf{r}' \equiv \mathbf{r} - (\mathbf{r} \cdot \hat{\mathbf{y}})\hat{\mathbf{y}}$, $0 \leq \alpha, \beta \leq 1$, and the y -coordinate has been dropped. The range of the diagonal correlator \mathcal{A} from

(4.24) is then given by

$$\begin{aligned}\mathcal{A}^2 &= (C_{zz} - C_{xx})^2 + (C_{zx} + C_{xz})^2 \\ &= \langle \alpha\beta(\sin\phi_A \sin\phi_B - \cos\phi_A \cos\phi_B) \rangle^2 \\ &\quad + \langle \alpha\beta(\cos\phi_A \sin\phi_B + \sin\phi_A \cos\phi_B) \rangle^2 \\ &= \langle \alpha\beta \cos(\phi_A + \phi_B) \rangle^2 + \langle \alpha\beta \sin(\phi_A + \phi_B) \rangle^2,\end{aligned}\tag{4.29}$$

where the expectation value is taken over λ . The Cauchy-Schwarz inequality¹ can be applied on each term in the last line, namely

$$\begin{aligned}\langle \alpha\beta \cos(\phi_a + \phi_b) \rangle^2 &\leq \langle (\alpha\beta)^2 \rangle \langle \cos^2(\phi_A + \phi_B) \rangle, \\ \langle \alpha\beta \sin(\phi_a + \phi_b) \rangle^2 &\leq \langle (\alpha\beta)^2 \rangle \langle \sin^2(\phi_A + \phi_B) \rangle,\end{aligned}\tag{4.30}$$

to arrive at the desired separability criterion based on the maximum range of diagonal correlator as follows

$$\mathcal{A}^2 \leq \langle (\alpha\beta)^2 \rangle [\langle \cos^2(\phi_A + \phi_B) \rangle + \langle \sin^2(\phi_A + \phi_B) \rangle]\tag{4.31}$$

$$= \langle (\alpha\beta)^2 \rangle \leq 1.\tag{4.32}$$

To summarise, since all separable two-qubit states have a maximum variation in the symmetrically rotated correlator at unity (the inequality is tight, since it can be saturated for example by $|\uparrow\rangle|\downarrow\rangle$ as in Fig. 4.1(c)), a state which shows $\mathcal{A} > 1$ is therefore necessarily entangled. This is indeed a suitable entanglement witness for our experiment, since $|\Psi^+\rangle$ shows the maximum variation in correlation of 2 when symmetrically rotated, in particular flipping between completely anti-correlated and correlated outcomes along z and x , respectively (see Fig. 4.1(c)).

EPR-steering criterion

The EPR-steering criterion based solely on symmetrically rotated measurements on two qubit systems can be derived in a similar argument as to the separability criterion. Recall from the definition that EPR-steering is the violation of LHV-LHS model description of a spatially delocalised system [16]. We therefore consider a general LHV-LHS model for a bipartite system as a combination of a black box subsystem, on which one can perform dichotomic measurements (two possible outcomes), and a qubit. Without loss of generality, let the subsystem A be the qubit, whereas B an object governed by a LHV model (its outcome need not obey a quantum description).

The measurement outcomes $a, b = \pm 1$ from A and B, respectively, can then be

¹In probability theory, random variables X, Y satisfy the Cauchy-Schwarz inequality [100]

$$\langle XY \rangle^2 \leq \langle X^2 \rangle \langle Y^2 \rangle.$$

described by the explicit probability distribution

$$P(a, b; \theta, \phi) = \int d\lambda p(\lambda) P_Q(a|\lambda, \theta) P(b|\lambda, \phi), \quad (4.33)$$

where θ (ϕ) is the measurement setting, and $P_Q(a|\lambda, \theta)$ ($P(b|\lambda, \phi)$) the probability for observing a (b) at A (B), for the hidden variable λ arising from a probability distribution $p(\lambda)$. Here the probability model for A follows quantum theory, completely determined by the hidden state of the qubit $\hat{\rho}(\lambda)$ and the corresponding POVM element \mathcal{M}_a^θ giving the outcome a upon the measurement θ , such that

$$P_Q(a|\lambda, \theta) \equiv \text{Tr}[\mathcal{M}_a^\theta \hat{\rho}(\lambda)]. \quad (4.34)$$

Similar to our previous derivation for the separability criterion, let $\mathbf{a}(\lambda)$ be the Bloch vector of hidden quantum state at A, interrogated with the rotated measurement $\hat{\mathbf{n}}(\theta) \cdot \vec{\sigma}$ where $\hat{\mathbf{n}}(\theta) = (\sin \theta \ 0 \ \cos \theta) \hat{\sigma}_z$.

The diagonal correlator is then given explicitly by

$$E(\theta, \theta) = \sum_{a,b=\pm 1} \int d\lambda p(\lambda) ab P_Q(a|\lambda, \theta) P(b|\lambda, \theta) \quad (4.35)$$

$$= \int d\lambda p(\lambda) \sum_{a,b=\pm 1} ab P_Q(a|\lambda, \theta) P(b|\lambda, \theta) \quad (4.36)$$

$$= \int d\lambda p(\lambda) \left[\sum_{a=\pm 1} a P_Q(a|\lambda, \theta) \right] \left[\sum_{b=\pm 1} b P(b|\lambda, \theta) \right] \quad (4.37)$$

$$= \int d\lambda p(\lambda) (\hat{\mathbf{n}}(\theta) \cdot \mathbf{a}(\lambda)) \bar{b}(\lambda, \theta), \quad (4.38)$$

where $\bar{b}(\lambda, \theta) = \sum_b b P(b|\lambda, \theta)$ is the mean outcome of B from the LHV model for a hidden variable λ and measurement setting θ (note $|\bar{b}(\lambda, \theta)| \leq 1$, and inequality saturates for all λ, θ iff LHV model is deterministic). Now let us explicitly determine the possible range of the diagonal correlator for all LHV-LHS models by considering the difference

$$E(\theta', \theta') - E(\theta, \theta) = \int d\lambda p(\lambda) (\hat{\mathbf{n}}(\theta') \cdot \mathbf{a}(\lambda)) \bar{b}(\lambda, \theta') - \int d\lambda p(\lambda) (\hat{\mathbf{n}}(\theta) \cdot \mathbf{a}(\lambda)) \bar{b}(\lambda, \theta) \quad (4.39)$$

$$= \int d\lambda p(\lambda) \mathbf{a}(\lambda) \cdot [\bar{b}(\lambda, \theta') \hat{\mathbf{n}}(\theta') - \bar{b}(\lambda, \theta) \hat{\mathbf{n}}(\theta)] \quad (4.40)$$

$$\leq \int d\lambda p(\lambda) \|\bar{b}(\lambda, \theta') \hat{\mathbf{n}}(\theta') - \bar{b}(\lambda, \theta) \hat{\mathbf{n}}(\theta)\|, \quad (4.41)$$

where the inequality in the last line follows from $\|\mathbf{a}\| \leq 1$.

Unlike the separability criterion, the range of the diagonal correlator itself serves no useful purpose to the test of EPR-steering, as we explain below. Such useful non-locality criterion would place a limit on all possible ranges from LHV-LHS models, that can nonetheless be violated by QM. As it stands from the general property of

LHV-LHS models, however, the upper bound derived in Eq. (4.41) approaches 2, the algebraic maximum range, when the two vectors $\bar{b}(\lambda, \theta')\mathbf{n}(\theta')$ and $\bar{b}(\lambda, \theta)\mathbf{n}(\theta)$ are unit length and nearly oppositely pointing as $\theta - \theta' \rightarrow 0$. This explicitly corresponds to the LHV subsystem's mean outcome flipping between ± 1 as the measurement configurations approach each other. Indeed the following simple LHV-LHS system saturates this limit: A is a qubit $|\uparrow\rangle$, and B returns λ -independent outcomes $b(\lambda, \theta) = b(\theta)$ such that for $\theta \in (-\pi, \pi]$

$$b(\theta) = \begin{cases} 1 & \text{if } \theta \geq 0 \\ -1 & \text{if } \theta < 0, \end{cases}$$

which gives $\lim_{\theta \rightarrow 0^\pm} E(\theta, \theta) = \pm 1$, and a full range that can approach 2 in principle.

Let us utilise the relative measurement angle dependence on the bound of the difference in correlator in Eq. (4.41), which we refer to as the steering parameter $S(\theta, \theta') \equiv |E(\theta, \theta) - E(\theta', \theta')|$. In particular, when the correlation is interrogated along two orthogonal directions ($\theta' = \theta \pm \pi/2$), the norm in (4.41) adds in quadrature and the bound takes on the minimum, given by $\sqrt{\bar{b}(\lambda, \theta')^2 + \bar{b}(\lambda, \theta)^2} \leq \sqrt{2}$. Therefore, we arrive at the EPR-steering inequality based on a orthogonal pair of diagonal correlator measurements, given by

$$\mathcal{S}(\theta, \theta + \pi/2) = |\mathcal{B}(\theta + \pi/2) - \mathcal{B}(\theta)| \underset{\text{EPR-local}}{\leq} \sqrt{2}. \quad (4.42)$$

It can be shown that the essence of our argument arriving at (4.41) holds generally for any orthogonal measurements, not necessarily in zx -plane.

Finally, let us express the correlator in QM formalism, so that the above EPR-steering inequality becomes

$$\left| \left\langle \hat{\sigma}_{\mathbf{n}}^{(A)} \hat{\sigma}_{\mathbf{n}}^{(B)} \right\rangle - \left\langle \hat{\sigma}_{\perp}^{(A)} \hat{\sigma}_{\perp}^{(B)} \right\rangle \right| \underset{\text{EPR-local}}{\leq} \sqrt{2} \quad (4.43)$$

where \mathbf{n} and \perp indicate the orthogonal measurement directions. This correlation can indeed be obtained in our experiment, since we can apply any arbitrarily rotation common to both particles. Furthermore the EPR-steering inequality (4.43) is violated for $|\Psi^+\rangle$ since the maximum variation in correlation is observed exactly between the orthogonal measurements $\theta = 0$ and $\pi/2$ where $E(\theta, \theta) = \mp 1$, respectively. Indeed, we now discuss below how to experimentally realise $|\Psi^+\rangle$ state from an s-wave collision of atoms, and demonstrate the nonlocal spin correlation between the scattered pairs of atoms.

4.3 Experimental methods

Here we give details on the experimental methodology on the test of quantum nonlocality with pairs of atoms scattered in a collision. The experimental sequence closely follows Bohm's version of the EPR paradox [28] with freely propagating pairs of

atoms. For completeness, we also give details on the data analysis to discriminate every atom's internal state and reconstruct its momentum in the collision frame.

4.3.1 Experimental sequence

The experimental sequence is composed of three key phases like the Bell test, as illustrated in Fig. 4.2: the generation of entangled pair of atoms, the rotation of atomic spins by an arbitrarily chosen angle, and the single atom-resolved readout of spin and momentum. Below we explain the general experimental sequence, and give details to each experimental phase listed above.

[t]

Preparation of the condensate

Our experiment starts with a magnetically trapped BEC of helium-4 atoms in the long-lived metastable state 2^3S_1 , in the bi-planar quadrupole Ioffe configuration magnetic trap discussed in the background Section 2.3 at harmonic frequencies of $(\omega_x, \omega_y, \omega_z)/2\pi \approx (15, 25, 25)$ Hz. The initially prepared condensate corresponds to the state illustrated in Fig. 4.2(d) as a filled circle. The atomic ensemble is almost purely Bose condensed with a negligible thermal fraction. The number of atoms in the condensate, and hence the number of scattered pairs from the collision, can controllably be reduced by outcoupling a variable amount by rf, in a similar manner as evaporative cooling but on a BEC.

The magnetic trap is switched-off, henceforth denoted by time $t = 0$, from which it takes ≈ 2 ms for the magnetic field to stabilise to a uniform field set up by the nullerometer at $\mathbf{B}_0 \approx 0.5 \left[(\hat{\mathbf{e}}_x + \hat{\mathbf{e}}_z) / \sqrt{2} \right] \text{G}$. This field is desirable for realising the Raman transitions illustrated in Fig. 4.2(d), and is actively stabilised until the detection phase. In our experiment, the Zeeman sub-levels of He^* are denoted $|J = 1, m_J = 1\rangle = |\uparrow\rangle$ and $|J = 1, m_J = 0\rangle = |\downarrow\rangle$, and form the relevant qubit subspace of the EPR-Bohm scenario (see level diagram in Fig. 4.2(b)). The Zeeman splitting gives a Larmor precession frequency $\Omega_L = g\mu_0 B_0 \approx 2\pi \cdot 1.4 \text{ MHz}$ in the stabilised magnetic field.

Collision of BECs

At $t = 3$ ms when the magnetic field is well stabilised (recall $t = 0$ is trap switch-off), a $\pi/2$ -pulse (*collision pulse*) from a two-photon stimulated Raman process (via the $\lambda = 1083 \text{ nm}$ $2^3S_1 \rightarrow 2^3P_0$ transition; see Fig. 4.2(b) and background Section 2.3.3) prepares all N condensed atoms in the 50/50 superposition of spin and momentum

$$|\mathbf{k} = 0, \uparrow\rangle^{\otimes N} \mapsto \left[\frac{1}{\sqrt{2}} (|0, \uparrow\rangle + |2\hbar\mathbf{Q}, \downarrow\rangle) \right]^{\otimes N}, \quad (4.44)$$

where the recoil velocity is $2v_r = 2\hbar\mathbf{Q}/m \approx (120 \text{ mm s}^{-1})\hat{\mathbf{z}}$ in the lab frame (see Fig. 4.2(a,d,e); \mathbf{Q} is given by the transferred photon momenta). In the centre of

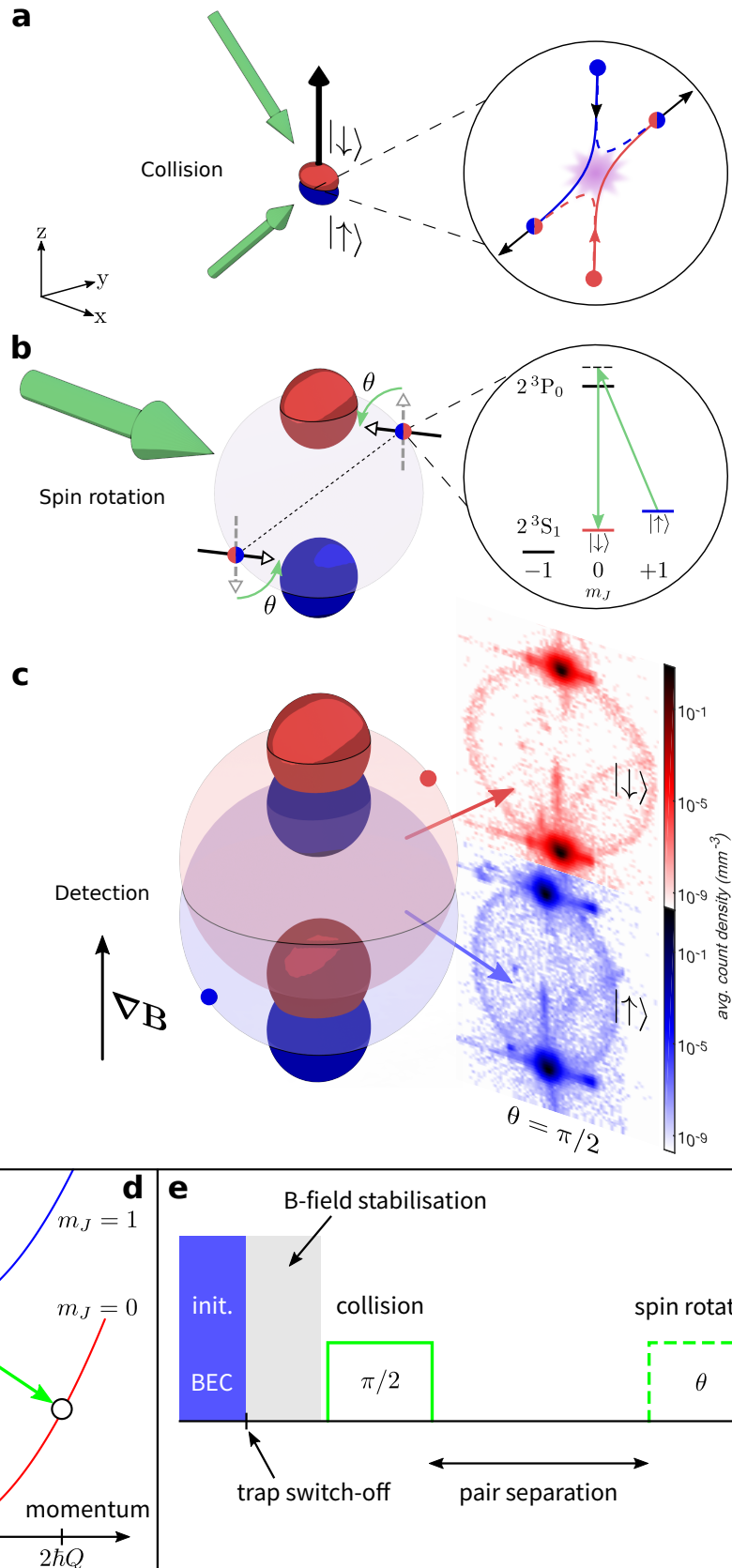


Figure 4.2: Experimental schematic. (Continued on the following page.)

Figure 4.2: Experimental schematic. (Continued.) (a) Raman lasers (two green arrows) initiate the collision of oppositely spin-polarised BECs (coloured ellipsoids), from which the pairs s-wave scatter into $|\Psi^+\rangle$ (see right inset). Spin- \uparrow (\downarrow) is labelled blue (red), denoting $m_J = 1$ (0) He*. (b) The scattering halo forms as an expanding spherical shell, in which the entangled pairs are located oppositely in momentum and spatially separate. A pair of co-propagating Raman beams (green arrow) rotates individual atom's spin (hollow-headed arrows) by an arbitrary angle θ . (c) Stern-Gerlach magnetic field gradient spatially separates atoms by their spin components, after which individual atoms' momentum and spin are detected. The images on the right show the atom count density (averaged over 1000 shots) in the zx -plane when the spins were rotated uniformly by $\theta = \pi/2$. Spin correlations between the back-to-back scattered pairs exhibit quantum nonlocality. (d) Level diagram and simplified Raman transitions. The effective couplings for the collision and spin rotating Raman transitions are indicated by the solid and dashed arrows, respectively. (e) The experimental sequence.

mass frame of this state (4.44), henceforth called the *collision frame*, the superposition resembles two condensates counter-propagating at velocities $v_r \approx \pm 60 \text{ mm s}^{-1}$ (momenta $\pm \mathbf{Q}$). Therefore while the condensates are spatially overlapped, atoms spontaneously scatter into correlated pairs of opposite momentum and spin by binary *s*-wave collisions, forming a uniformly distributed spherical halo in momentum space with radius $k_r = Q$ [89].

In an analogy to hyperentangled photon pairs (entangled in both polarisation and momentum) generated by SPDC [185], the oppositely spin-polarised collision of BECs entangles the atom pairs in spin (see inset of Fig. 4.2(a)) as well as in momentum, from the conservation of total angular (m_J) and linear momentum. By selecting a particular scattering direction we can label the momentum of each atom by $\pm \mathbf{k} = A, B$. The state of a single atom pair is anti-correlated both in their spin as well as in momentum, giving the archetypal Bell triplet

$$|\Psi^+\rangle = (|\uparrow\rangle_A \otimes |\downarrow\rangle_B + |\downarrow\rangle_A \otimes |\uparrow\rangle_B) / \sqrt{2}, \quad (4.45)$$

where the exact phase between the two kets (here just +1) comes from the spherical symmetry in *s*-wave scattering (see Section 2.2.2).

Following the collision pulse the scattering halo evolves freely in the stabilised and uniform magnetic field. During this period the halo expands spherically at a constant rate of change in its diameter $\dot{d}_{\text{sep}} \approx 120 \text{ mm s}^{-1}$, identical to the separating velocity of the condensates. The entangled pairs also spatially separate at this speed, and can be identified by their diametrically opposite locations in the halo after expansion.

Spin rotation

At $t = 3.8 \text{ ms}$ a pair of co-propagating Raman beams (see Fig. 4.2(b)) uniformly illuminate the scattering halo to provide a spin rotation on each atom pair corresponding

to

$$\hat{R}_y(\theta) = \exp\left(-i\frac{\theta}{2}\hat{\sigma}_y^{(A)}\right) \otimes \exp\left(-i\frac{\theta}{2}\hat{\sigma}_y^{(B)}\right), \quad (4.46)$$

where the rotation angle θ is controlled by the pulse duration (see Section 2.3.3 for details). Crucially the atoms' net momenta are unaffected by this Raman transition, since the absorption-stimulated emission of a photon happen between co-propagating beams of similar optical frequencies (difference frequency is in rf range and negligible).

In the results reported in this chapter of the thesis, the atomic spins are measured when the pairs are separated by $d_{\text{sep}} \approx 96 \mu\text{m}$, corresponding to the free expansion time between the collision and rotation pulse of $t_{\text{sep}} = 0.8 \text{ ms}$. Note that larger separations are readily achieved by letting the halo expand further at readout, however the entangled atomic pairs are sensitive to spatial variations in the magnetic field, which becomes more noticeable when the halo is larger. The time evolution of the scattering halo is the subject of investigation for the last chapter of this thesis which led to novel applications in magnetic field sensing.

Single atom-resolved readout

After the rotation pulse, a spatially uniform magnetic field gradient is applied along the z -direction (see Fig. 4.2(c)) using a large coil surrounding the vacuum chamber (see Section 2.3 for details). This projects the atoms into the $\hat{\sigma}_z$ eigenstates $\{|\uparrow\rangle, |\downarrow\rangle\}$ upon measuring their displacement via the Stern-Gerlach (SG) effect ². Since only $m_J = \pm 1$ states have a non-zero magnetic moment, they are each deflected along and away with respect to the magnetic field gradient, respectively, causing the triplets to spatially separate at the detector for spin-resolved detection. We achieved a spatially uniform SG force around the halo, corresponding to an approximately uniform magnetic field gradient near the trap centre, such that the $|\uparrow\rangle$ atoms' velocities are shifted by a constant amount, and no distortion was observed due to the SG sequence.

The atoms then fall under gravity onto a microchannel plate – delay-line detector (MCP-DLD) located 0.848 m below the trap centre, which allows the crucial part of this experiment, discussed in Section 2.3: single-atom detection with full 3D resolution [143]. Let us briefly recall that the 3D momentum \mathbf{k} of each atom is reconstructed from the 2D spatial positions on the plate, and arrival time as recorded by the MCP-DLD, while its m_J -state is distinguished from the large separation between the arrival time of the different spin states due to the SG effect (see Section 4.5).

²Note the difference between the two usages of z : One is used to label the spatial coordinate axis along gravity, and the other indicates the conventional spin axis (quantisation of m_J). When the SG splitting field ramps on gradually with respect to the atom's spin dynamics (Larmor frequency), the atomic magnetic moment (atomic spin in the Bloch sphere picture) tracks the changing magnetic field vector (quantisation axis) while maintaining its relative orientation throughout (same superposition after a change of basis). The field gradient induces the spin-dependent force, thereby enabling the displacement-based measurement of spin, equivalent to a projection onto the $\hat{\sigma}_z$ eigenstates. In our experiment the SG displacement was chosen in the z direction to identify the spins by the atoms' time-of-arrival, due to limited size of the MCP-DLD detector in the xy plane.

Figure 4.2(c) shows a typical image from an average of 1000 experimental shots, displaying two completely separated halos, when a $\pi/2$ -rotation pulse was applied. Atoms in the $|\uparrow\rangle$ state form the lower halo, arriving at the detector earlier, which is slightly non-spherical due to inhomogeneity in the magnetic field gradient causing a spatially dependent force around the halo (see Fig. 4.2(c)). Such distortion results in the misalignment of ideal back-to-back pairing in the halo and is removed by post-processing the data, as described in the following section. $m_J = 0$ states are unaffected by magnetic fields, the $|\downarrow\rangle$ -halo maintains the spherical shell shape at the detector (see the upper halo in Fig. 4.2(c)).

4.3.2 Data analysis

The detector is located far from the magnetic trap and the region where collisions and rotations occur. In such a far-field detection regime (see Section 2.3.4) the relevant physics may be assumed to occur at a point source, each atom's position at detector directly corresponds to its initial velocity multiplied by its time-of-flight (TOF) t in free-fall (without the risk of confusion with the time in experimental sequence). However in our experiment there are a few factors, namely the SG pulse and lensing by stray magnetic fields in the vacuum chamber, that cause the atoms to significantly deviate from the ideal free-fall trajectory, as seen in Fig. 4.4. Here we give details of the data analysis procedure followed to accurately determine scattered atoms' momenta \mathbf{k} , along with spin m_J .

The key stages in post-processing of the experimental data, illustrated in Fig. 4.3, are (a) the identification of each detected atom's internal state, (b) the data reduction to filter for scattered atoms in the collision, and (c) the elimination of magnetic lensing effect to reveal the momenta of the scattered atoms in the collision frame. We skip the pre-processing step to yield 3D position vectors $\{(x, y, z)\}$ reconstructed from a set of MCP-DLD detection events, which was already discussed in Section 2.3.4.

Discrimination of spin state

Figure 4.4 shows that different Zeeman sublevels of He^* are fully spatially separated at the detector coordinate with a SG sequence. The discrimination of spin state is implemented in software as shown in Fig. 4.4(c) by dividing the detected space into three z -bins, each corresponding to respective m_J .

The scattering halo in the collision frame

For each m_J species, composed of two BECs and a scattering halo, we transform the coordinates from the detector coordinate to the collision frame, as follows (see Fig. 4.3). The mid-point between the two condensates marks the centre of the scattering halo, and therefore the centre of mass of the colliding system. We transform the scatter data into relative positions from this reference point.

Next, we filter out background atoms other than the scattering halo, namely the BECs and thermal fraction. In this step we keep only counts lying inside a truncated

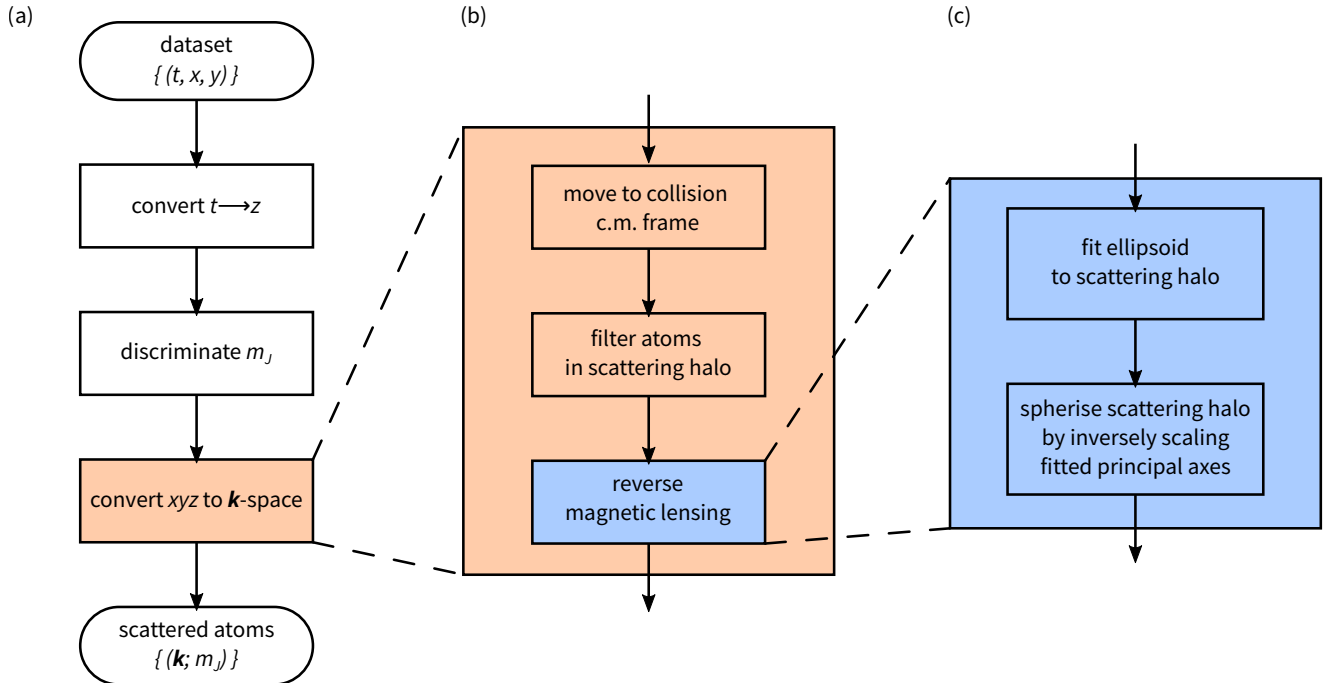


Figure 4.3: Data analysis flowchart. (a) An overview of the process from raw detector reconstruction data reduced to scattered atoms' momenta and spins. (b) Steps to convert atom's position from the spatial coordinates to momentum in the collision frame. (c) Steps to revert the magnetic lensing effect by post-processing.

spherical shell region centred in the origin of the collision frame, with typical inner and outer radius $0.6R$ and $1.2R$ (chosen to capture as much of the distorted scattering halo as possible, while removing undesirable background), respectively, and for collision z -coordinates typically in $|z/R| < 0.8$ (removing direct counts and detector saturation effects from BECs), where $R \approx 25$ mm is the radius of the scattering halo determined by half the separation of $m_J = 0$ BECs.

Magnetic lensing

The most crucial post-processing operation is the removal of the shape distortion in the $m_J = 1$ scattering halo, since without it we cannot identify the entangled pairs initially created back-to-back in momentum. Below we explain the physical source of this deformation, and describe the procedure for accurately reconstructing \mathbf{k} under such conditions (see Fig. 4.3(c)).

As seen from Fig. 4.4(a,b), the spatial distribution of scattered atoms at the detector is noticeably aspherical for $m_J = +1$ (bottom) while spherical for $m_J = 0$ states (middle), as expected from elastic scattering and free expansion. The cause for the discrepancy in the $m_J = +1$ states from the ideal spherical shell is due to inhomogeneous forces from the stray magnetic field (gradient) present in the vacuum chamber,

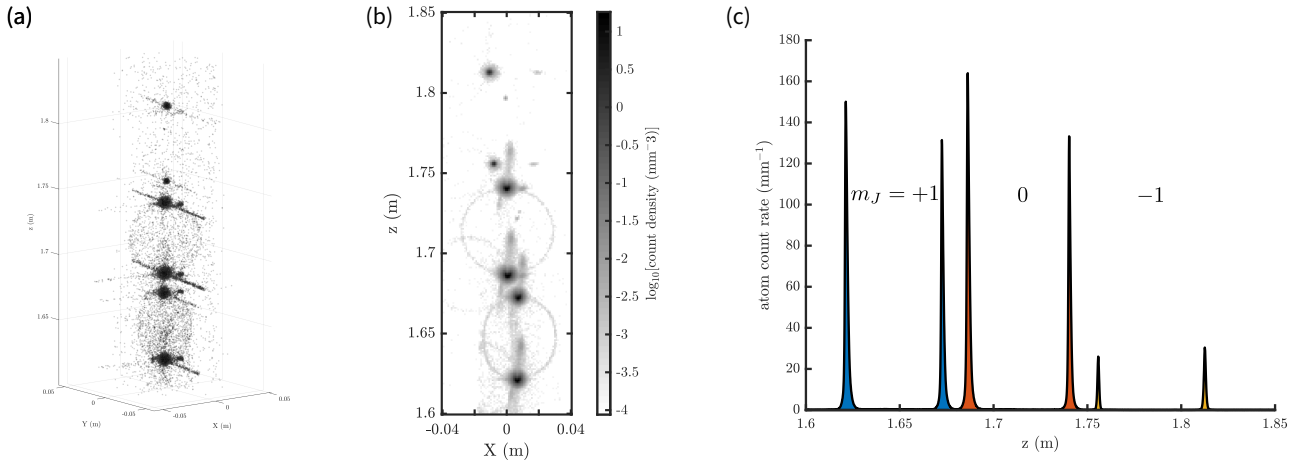


Figure 4.4: Pre-processed experimental data. (a) (x, y, z) scatter data from a total of 100 shots of a typical experiment illustrated in Fig. 4.2. (b) The average atom count density image in the $y = 0$ cross-section. (c) m_J -discriminated detector count rate along the z -axis. Note the small presence of $m_J = -1$ BECs are due to imperfection in the spin rotation stimulated Raman transition, and makes insignificant contributions to the discussion of our experiment.

which causes the atoms' TOF evolution to deviate from free-fall. The observed convergent (divergent) lensing phenomenon on the $m_J = \pm 1$ states along the falling axis z is consistent with the magnetic field expected from static magnetisation and eddy-currents induced around a narrow neck connecting the science and detection chambers (see Fig. 2.13).

Recall that m_J -dependent forces can arise from the gradient in dc magnetic field B from the Zeeman effect. Let us consider the gradient field $\nabla B(\mathbf{r})$ in terms of its Taylor expansion in the spatial coordinate \mathbf{r} . The zeroth-order gradient describes the spatially uniform component in $\nabla B(\mathbf{r})$ which acts as a homogeneous force over the ensemble. This is the ideal m_J -discriminating force utilised for the SG effect, since it simply shifts all \mathbf{k} by a well known amount so that \mathbf{k} is readily recovered. Lensing effects occur from first-order in $\nabla B(\mathbf{r})$, since these describe position dependent forces. Now if we assume the tubular vacuum chamber where magnetic lensing happens as an ideal finite solenoid, the non-uniform part of the induced field inside it will have a leading quadratic term in the radial plane (odd terms vanish by symmetry). Ignoring higher order non-uniformities, the harmonic potential describes a linearly-varying position dependent force (lowest Taylor order for lensing), which effectively transforms a spherical distribution into an ellipsoid (when the effect is weak as in our experiment), scaling vectors along each axis by a constant lensing factor. Indeed, since the initial distribution of atoms, regardless of m_J is known to be spherical from s-wave scattering, we can estimate and reverse the lensing effect in post-processing as described below.

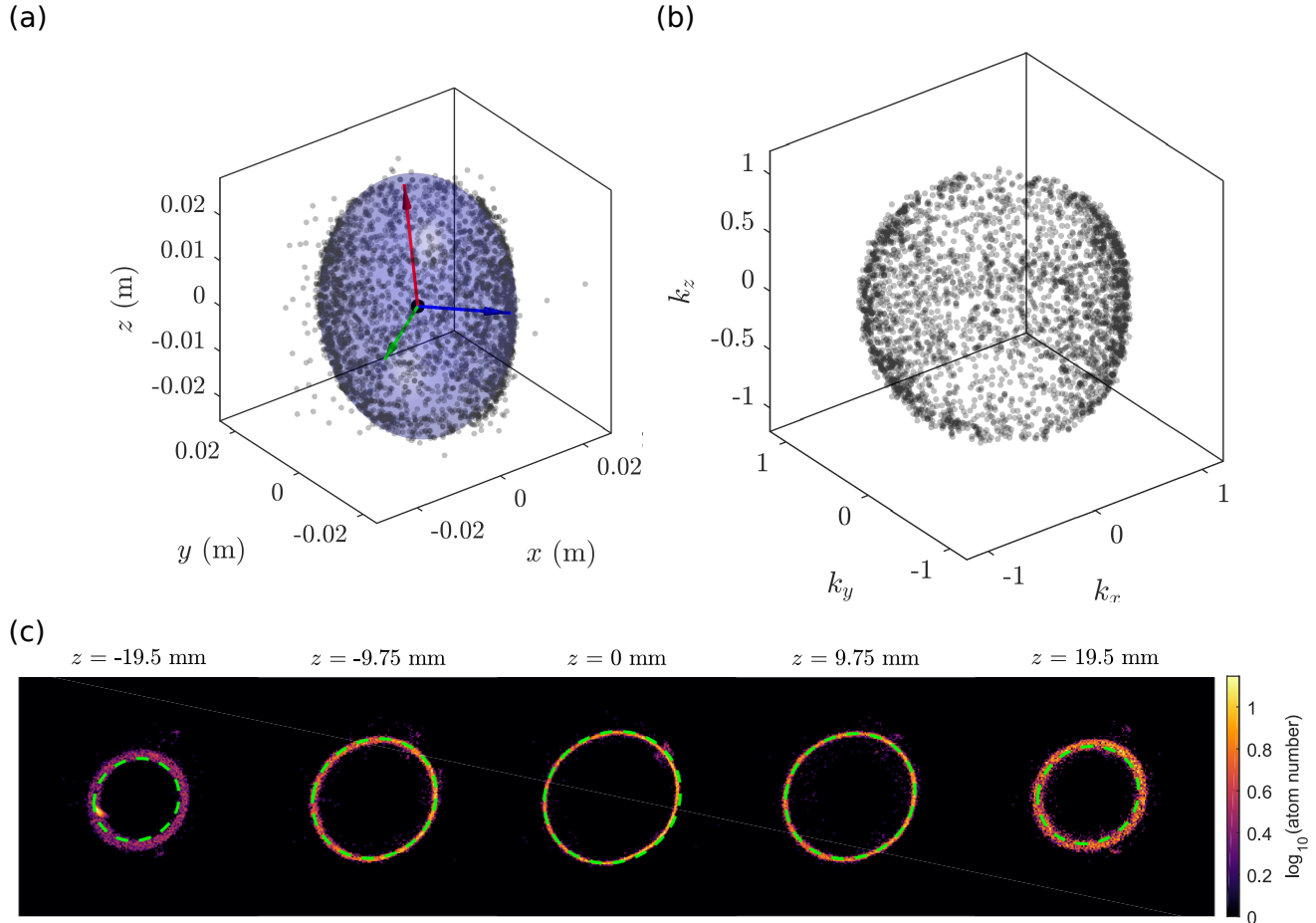


Figure 4.5: An illustration of the post-processing to remove magnetic lensing. (a) Ellipsoid fit (blue surface) to the $m_J = +1$ scattering halo in the c.m. frame of the collision (grey points). Black point: centre of fitted ellipsoid. Coloured arrows: the semi-axes. (b) Post-processed normalised momentum \mathbf{k} distribution. (c) A comparison between the fitted ellipsoid (green dashed line) and the observed density profile of an $m_J = +1$ scattering halo (in (a)), at various 2D slices taken perpendicular to the z -axis.

First we estimate the magnetic lensing effect by fitting a general ellipsoid³ to the 3D density distribution of the scattering halo obtained by collating over all shots in the same experimental sequence (see Fig 4.5). The fitted ellipsoid's semi-axes satisfactorily characterises the magnetic lensing effect from our simple model, as evident by the agreement of this fit illustrated in Fig. 4.5(c). Finally, the \mathbf{k} -distribution is recovered by inversely scaling the scatter data along each fitted semi-axes as seen in 4.5(b). Since this step transforms the modelled ellipsoid to a unit sphere, \mathbf{k} coordinates are automatically normalised with respect to the collision momentum Q .

4.4 The atomic pair source

The correlated pair source is the most basic system for tests of quantum nonlocality. This section characterises the scattering halo created from a collision of oppositely spin-polarised BECs, and identifies correlated atomic pairs, without the spin rotation pulse (see schematic in Fig. 4.2). The key characteristics of scattering halo, introduced in Section 2.2.2, can be broadly classified into (1) atom distribution around the scattering halo, and (2) atom number statistics, fully characterised by pairwise correlations.

4.4.1 The s-wave scattering halo

Figure 4.6 shows the average distribution of detected atom counts around the scattering halo for each spin state in \mathbf{k} -space. The atomic collision is readily verified to be elastic and s-wave, since scattered momenta are sharply peaked around the collision momentum (see Fig. 4.6(a)), and the scattering probability is radially symmetric (see Figs. 4.6(b–e)). There are imperfections in the k -space transformation by the ellipsoid fitting method described in Fig. 4.4, most noticeably in the small difference in the radii of the *spherised* scattering halos in Fig. 4.6(a). This reflects the fact that our distortion-cancelling method was too simplistic a model for more aberrant magnetic field distortions in the vacuum chamber, as well as the finite spread in the halo's thickness that is not modelled by an ellipsoid. The radial rms width of the scattering halos are $\delta k = 0.041(1), 0.029(1)$ for \uparrow, \downarrow , respectively, from the fitted Gaussian profiles. The difference in the radial distribution of the two halos are due to imperfections in the post-processing step to cancel magnetic lensing in the $m_J = 1$ halo,

³In general, an ellipsoid is a 2D surface composed of the roots of a quadratic polynomial in the coordinates of 3D vector \mathbf{x} , parametrised as

$$f(\mathbf{x}) = (\mathbf{x} - \mathbf{c})^\top \mathbf{A} (\mathbf{x} - \mathbf{c}) - 1,$$

where \mathbf{c} is the centre and \mathbf{A} is an invertible linear transformation [186]. Notably, eigenvectors and the corresponding eigenvalues of \mathbf{A} define the ellipsoid's principal axes and squared inverses of semi-axes. Observe that when the eigenvalues of \mathbf{A} are identical, the surface describes a 2D sphere. This multivariate polynomial has 9 degrees of freedom – 3 from the choice of centre, and 6 from the invertible linear transformation (3 scales and 3 orientation parameters) – which may be readily estimated from the scatter data by linear regression.

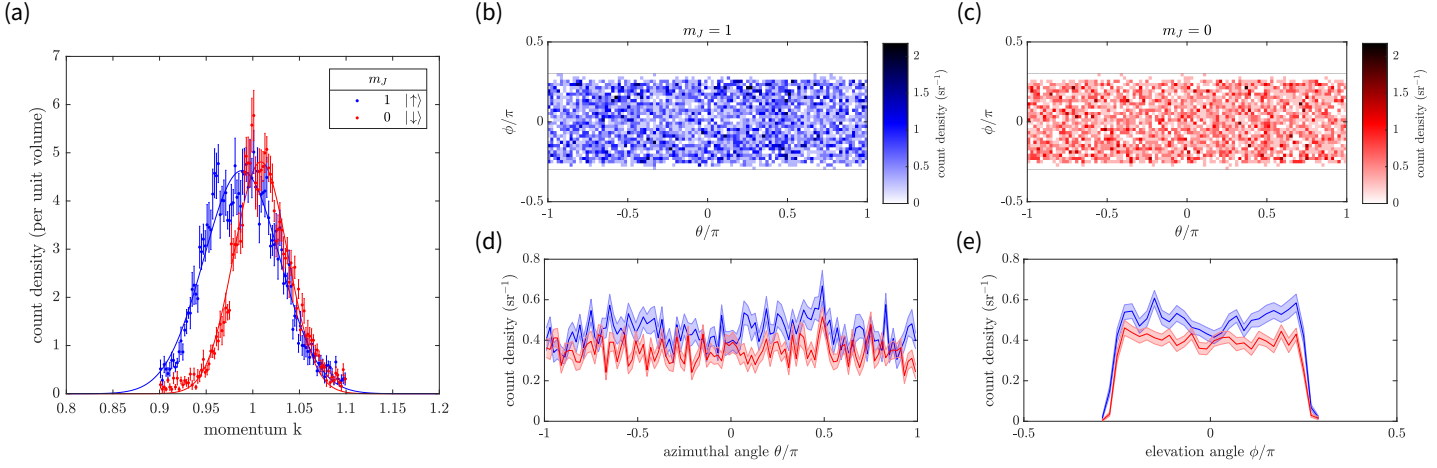


Figure 4.6: Distribution of atoms in the scattering halo. (a) Radial distribution (markers) and Gaussian fits (solid lines). Spherical distribution for (b) $m_J = 1$ and (c) 0. Average atom distribution along the (d) azimuthal and (e) elevation angles. Error bars in (a) indicate the statistical uncertainty estimated from bootstrapping [187], while error bars in (d) and (e) indicate standard error in the elevation and azimuthal angles, respectively. This illustrated data is from a total of approximately 1200 shots.

where we noticed local distortions of the halo that significantly deviate from an ellipsoid. The missing counts near the poles $|\phi| \approx \pi/2$ in Figs. 4.6(b,c,e) are an artefact of the data processing procedure, where the region overlapping with the tail of the condensates are removed to filter for only scattered atoms. For the data shown, the mean detected atom densities around the scattering halo are $0.44(1), 0.34(1)$ sr⁻¹ for \uparrow, \downarrow , respectively, which gives an estimate for a total of $49(1)$ pairs scattered in the collision on average, based on the detector efficiency of $\eta = 0.1$.

The ability to create distinguishable pairs is an essential requirement for the demonstration of nonlocal correlation across the back-to-back scattered modes. We showed previously that fluctuations in the number of scattered pairs give rise to a critical threshold in average mode occupation (4.22), above which pairwise correlations become indistinguishable from LHV models. In our experiment we tune the halo mode occupation by varying the number of atoms in the colliding BECs. This is achieved at the preparation stage of the condensate in the magnetic trap by adjusting the rf evaporation ramp. The population of the scattering halo is expected to scale quadratically with respect to the condensate number, since collision events arise from two-body processes, as seen from Section 2.2.2. As shown in Fig. 4.7, this simple method works effectively to achieve an approximately 50-fold variation in the scattered atom number, while the BEC production remains stable in a continuous operation.

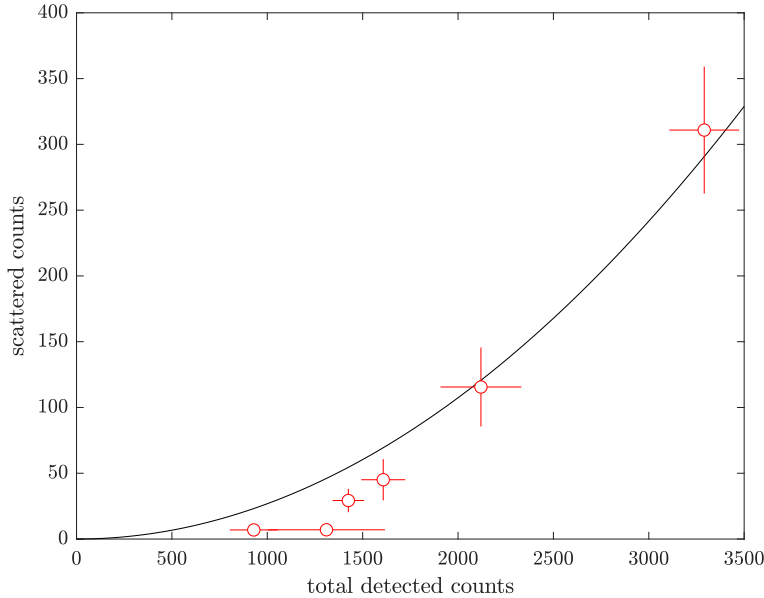


Figure 4.7: Tuning the number of scattered atoms by varying the condensate number. Total detected counts include the BECs which saturate the detector, and the scattered counts are total number detected in the truncated spherical shell filtering for only scattered atoms. Error bars indicate the standard deviation of the observed quantity. The solid line is a quadratic fit, passing through $(0,0)$, to data to guide the eye.

4.4.2 Correlated pairs

The key property of the scattering halo we wish to utilise here is the spin entanglement between counter-propagating pairs. In quantum theory correlated pairs can be conveniently formulated by the second-order correlation function [123]. Here we characterise the two-particle correlations in the scattering halo, and demonstrate the scattering halo is useful for the proposed test of quantum nonlocality.

For maximum clarity, let us consider the correlation between two scattering modes with a relative angle θ between their momenta (see Fig. 4.8(a) for a schematic). Due to the spherical symmetry of the scattering halo, we may sum over all possible mode configurations with identical θ .⁴ The correlation function is then explicitly given by

$$g_{ij}^{(2)}(\theta) = \frac{\sum_{\mathbf{k} \in V} \sum_{\mathbf{k}' \in \delta V(\mathbf{k}, \theta)} \langle : \hat{n}_{\mathbf{k},i} \hat{n}_{\mathbf{k}',j} : \rangle}{\sum_{\mathbf{k} \in V} \sum_{\mathbf{k}' \in \delta V(\mathbf{k}, \theta)} \langle \hat{n}_{\mathbf{k},i} \rangle \langle \hat{n}_{\mathbf{k}',j} \rangle}, \quad (4.47)$$

where $i, j \in \{\uparrow, \downarrow\}$ denote spin states, $\hat{n}_{\mathbf{q},m} = \hat{a}_m^\dagger(\mathbf{q}) \hat{a}_m(\mathbf{q})$ the number of atoms with momentum \mathbf{q} and spin m , $::$ the normal ordering of creation-annihilation operators, V the momentum space of the s -wave scattering halo, and $\delta V(\mathbf{k}, \theta)$ the subset of vectors in V with a relative angle θ with respect to \mathbf{k} .

⁴In our publication [101], we evaluated the $g^{(2)}$ function in Cartesian coordinate, where the sum of \mathbf{k} vectors parameterise the detuning. This method has the advantage in allowing effects of condensate anisotropy on the scattering to be studied [118].

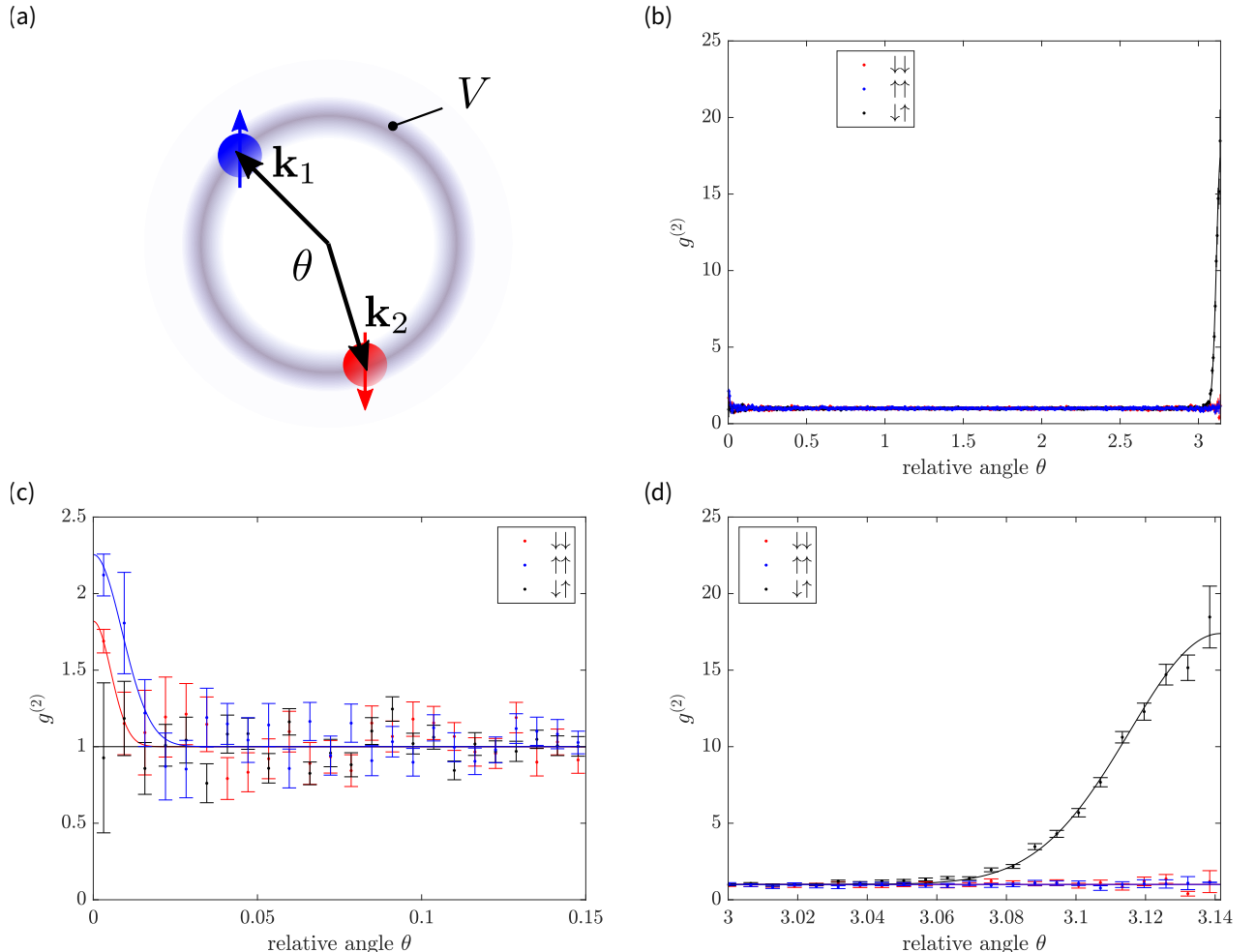


Figure 4.8: Second-order correlation functions of the atomic pair source. (a) Schematic of atoms with momentum and spin degrees of freedom in the scattering sphere. A 2D planar slice in momentum space is shown for simplicity. (b) Two-body cross-correlation function in momentum-spin $g_{\uparrow\downarrow}^{(2)}$ from approximately 2100 experimental shots of pair source with an average mode occupancy of $n = 0.045(6)$. Correlation functions zoomed near (c) co-linear, and (d) back-to-back scattering conditions. Error bars indicate the statistical uncertainty estimated by bootstrapping [187].

Figure 4.8(b) shows the characteristic $g_{ij}^{(2)}$ observed in the scattering halos created in our experiment, where the particular experimental collision for this result is indicated in Fig. 4.7. Aside from co-linear and back-to-back scattered configurations, with relative scattering angles $\theta = 0, \pi$ respectively, all other pairs are uncorrelated since $g_{ij}^{(2)} = 1$ elsewhere. As expected from the collision of oppositely spin-polarised atoms, strong correlation ($g^{(2)} > 2$) is seen between pairs with opposite \mathbf{k} , only when they are also opposite in spin (see Fig. 4.8(d)). On the contrary, bosonic enhancement ($g^{(2)} = 2$) is seen by the bunching of scattered pairs into identical \mathbf{k} and spin state (see Fig. 4.8(c)) predicted in [116].

The back-to-back correlation function $g_{\uparrow\downarrow}^{(2)}$ yields the correlation amplitude, as well as the rms correlation length σ_{BB} , from a 1D Gaussian fit as seen in Fig. 4.8(d). The single-mode scattering volume in momentum space $\delta\tilde{V}$ from Eq. (2.56) can then be determined, since the rms momentum width of condensate $\bar{\sigma}$ is related to σ_{BB} by $\bar{\sigma} \approx 1.1\sigma_{\text{BB}}$ [188]. With the total scattering volume \tilde{V} estimated from the spherical shell with Gaussian radial profile in Eq. (2.58), we obtain the number of scattering modes $M = \tilde{V}/\delta\tilde{V}$. Over the wide range of mean scattered counts \bar{N}_{sc} , M varied modestly between $2.9(2) \times 10^3$ and $6(2) \times 10^3$. Most crucially, this allows us to estimate the average number of atoms in a single scattering mode \bar{n} (mode occupancy) from the relation $\bar{n} = \bar{N}_{\text{sc}}/M$.

Figure 4.9 shows the observed relationship between correlation amplitude with respect to the mode occupancy of the scattering halo. This behaviour is in agreement with the theoretical prediction $g_{\uparrow\downarrow}^{(2)}(\pi) = 2 + 1/\bar{n}$ [89, 112], from a fully quantum mechanical treatment of the collision in the spontaneous scattering regime $\bar{n} \lesssim 1$. We can readily achieve correlation amplitudes in excess of the nonlocality threshold of 5.8 (4.21) for the violation of Bell inequality. Due to practical considerations in the duration of data acquisition to the signal to noise requirements, we balance the absolute magnitude of the violation signal against statistical uncertainty due to less acquired data at lower \bar{n} . For the actual test of quantum nonlocality discussed in Section 4.6, we utilise scattering halos with $g_{\uparrow\downarrow}^{(2)} \approx 30$. The corresponding average mode occupancy in the scattering halo of ≈ 0.03 means we are operating in the low-gain regime, where the dominant contribution to the halo comes from scattering of single pairs. To summarise pairwise coincidence rates, in a single run of the experiment which takes ≈ 30 s, this results in an average of ≈ 8.3 atoms detected in the scattering halos, and thus a joint detection rate ≈ 1.6 pairs/min at $\approx 10\%$ detection efficiency.

4.5 Coherent control of atomic spin

Atomic spin measurements can be made along any axes, not necessarily the quantisation axis from an adiabatic SG sequence, by rotating the spin appropriately prior to an adiabatic readout. This section discusses the spin rotation sequence realised in our experiment by a Raman transition, illustrated in Fig. 4.2.

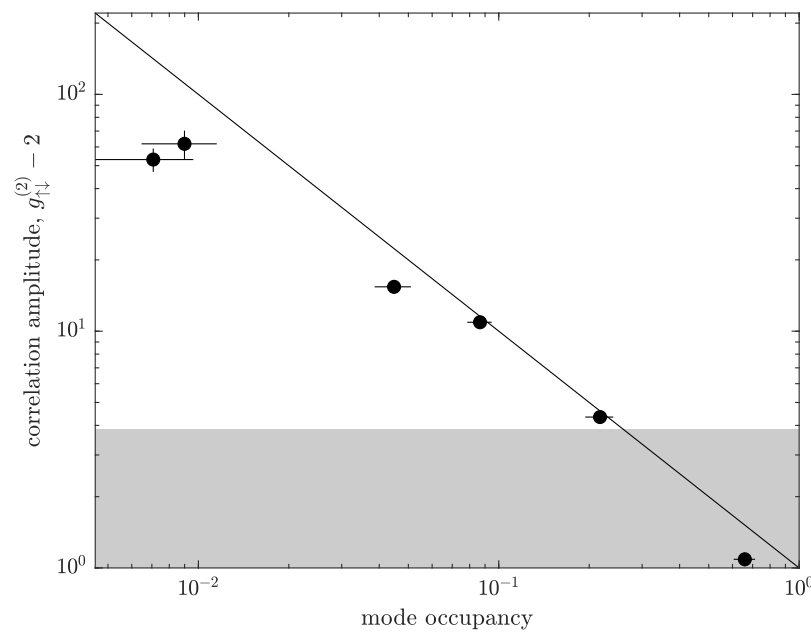


Figure 4.9: Tunable atomic pair source. The dependence of the degree of anti-correlation (amplitude of the corresponding second-order correlation function) is plotted against the average mode occupancy of the scattering halo. The solid line depicts the theoretical prediction. Demonstration of Bell nonlocality strictly requires $g_{\uparrow\downarrow}^{(2)} > 3 + 2\sqrt{2}$ (unshaded region), based on a fully QM prediction for the violation of CHSH inequality [178]. All error bars indicate the standard error in the mean.

Qubit operations by Raman pulse

The characterisation of spin rotation is essentially identical to the experimental sequence for the nonlocality test (see Fig. 4.2), except that only $m_J = +1$ states are initially prepared. Here the initial collision pulse splits an original $m_J = 1$ BEC into two condensates with different momenta, but without inducing a change in the internal state, by Bragg diffraction [189].⁵ This collision produces a $|\uparrow\rangle$ -polarised scattering halo (see Fig. 4.10(a)), in which we can characterise single-atom rotation processes. The Bragg pulse is applied approximately 50 μs before the trap switch-off, such that the magnetic field produced from trap bias points along the x -axis. This quantisation axis allows the Bragg collision to be driven with the same Raman beam geometry used for the spin-entangling collision (see Fig. 4.2(a)). The polarisations of the collision beams were re-tuned from the nonlocality test setup to contain σ^- -components, but cannot be completely σ^- -polarised in the given geometry. However, spin-changing Raman transitions are heavily suppressed by the detuning due to a large Zeeman splitting ($\sim 2 \text{ MHz}$) compared to Bragg splitting ($(2Q)^2\hbar/2m \approx 80 \text{ kHz}$), as seen in Fig. 4.2(d). The rotation pulse, described in Section 4.3.1, is then applied for a duration τ on the $|\uparrow\rangle$ -polarised ensemble at $t = 3.8 \text{ ms}$ (see Fig. 4.10(a)), when the magnetic field has stabilised to the condition to be used for the full sequence illustrated in Fig. 4.2(e). The $|\uparrow\rangle$ -scattering halo has a diameter of $d_{\text{sep}} \approx 0.46 \text{ mm}$, approximately five-fold larger than that of $|\Psi^+\rangle$ -halo, at the point of rotation. The spin rotation was observed to be uniform over the further expanded scattering halo (see Fig. 4.10(a)), since the Raman beam diameter is $\approx 4.6 \text{ mm}$ (see Section 2.3), such that it is an order of magnitude larger than that of the halo.

Figure 4.10(b) shows the total number of atoms detected in the truncated scattering halo N'_α for various rotation pulse durations applied on the $|\uparrow\rangle$ -halo ($\tau = 0$). The population fraction of each Zeeman sublevel $P(m_J) = N'_{m_J}/N'$, where $N' = \sum_\alpha N'_\alpha$ is the sum over the m_J -triplet, exhibits a Rabi oscillation between the qubit states $m_J = 1, 0$ shown in Fig. 4.11. The $m_J = -1$ state is negligibly populated in the Raman transition, as expected from the absence of σ^+ -polarisation of the beams to couple it via the 2^3P_0 intermediate state (see Section 2.3.3). We observed Rabi amplitude of 0.85(4) and effective Rabi frequency of $\Omega' = 2\pi \times 50.3(3) \text{ kHz}$. In order to verify that the Raman pulse acts uniformly over all atoms in the scattering halo, Rabi oscillation in localised \mathbf{k} regions over the scattering halo were determined. The rms spatial variation observed around the halo is represented as error bars in Fig. 4.11. Since the spatial inhomogeneity is at the level of statistical uncertainty, the Raman transition is uniform over the interrogated halo volume $\approx (0.46 \text{ mm})^3$ to better than $\approx 5\%$.

Figure 4.10(b) shows that the total number of detected atoms in the scatter-

⁵The Bragg scattering of atoms is a special case of stimulated Raman transition Section 2.3.3, in which the multi-photon scattering is elastic (internal state of atom remains unchanged). Its name derives from the Bragg diffraction of light and subatomic particles from a periodic potential in crystalline solids, since this regime of matterwave diffraction has an analogous semi-classical picture [19]. Here, the Raman beams impose an optical lattice (periodic potential from light) on the atomic wavepackets, from optical dipole interaction with the standing or moving wave.

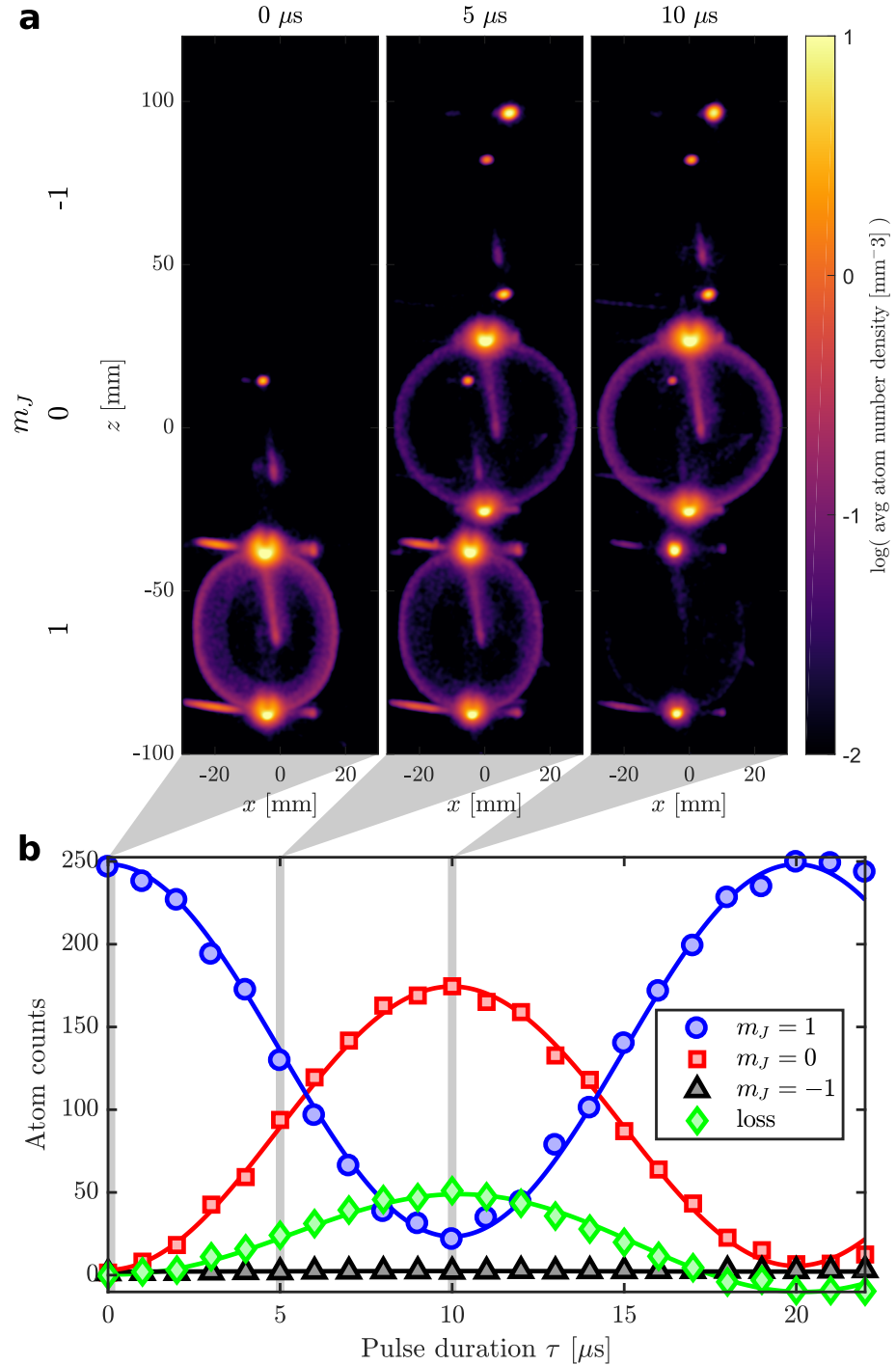


Figure 4.10: Characterisation of the rotation pulse. (a) Atom count density at the detector in the zx -plane, integrated over $-12 \text{ mm} < y < 15 \text{ mm}$, for different spin rotation pulse times applied to $|\uparrow\rangle$ -polarised scattering halo. (b) Number of atoms detected in each scattering halo labelled by the internal state m_J . Loss (green diamond) indicates the total number of atoms summed over all internal states with respect to when no rotation pulse is applied ($\tau = 0$). Solid lines are sine fits to data, and statistical uncertainties in the data are smaller than the graphical markers.

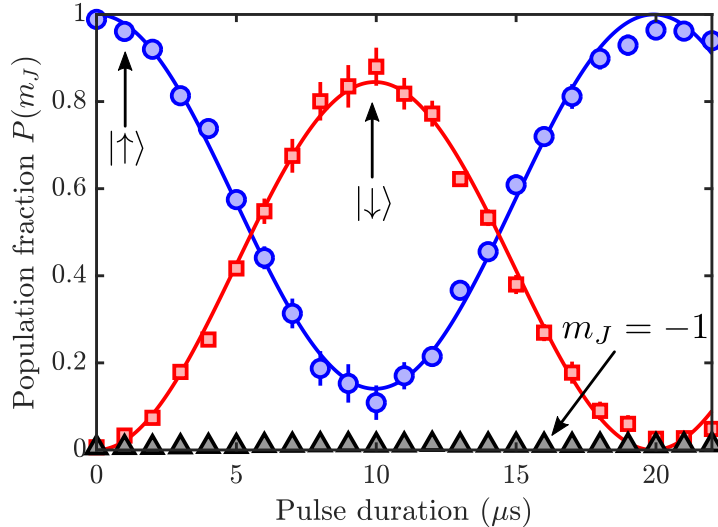


Figure 4.11: Rabi oscillation of the atomic spin over the scattering halo. Error bars indicate the standard deviation over the scattering halo divided into 8 equal-sized quadrants. Solid lines are sine fits to data.

ing halo was observed to be affected by the spin rotation sequence. Let us define this loss in the total number of atoms detected in the scattering volume by $N'_{\text{loss}}(\tau) \equiv N'(0) - N'(\tau)$. Observe the two key features evident in the behaviour of $N'_{\text{loss}}(\tau)$: its correlation with number in $m_J = 0$ states, and a steady, but much weaker decrease with pulse duration. Below we explain the mechanism responsible for this apparent atom loss during the spin rotation, and discuss its effect on the nonlocality experiment.

The significant decrease in the total atom number is observed to be at most 25% and correlated with the population in $m_J = 0$ (see Fig. 4.10(b)), which we attribute to the Penning ionisation of $m_J = 0$ atoms. Recall that Penning ionisation between pairs of He^* atoms is enhanced by 4 orders of magnitude in spin unpolarised pairs, compared to pairs of $m_J = +1$ atoms [143]. In our experiment, Penning ionisation would most strongly affect the entangled pairs at the earliest time following their production, since the local density of atoms is the highest during the spatial overlap of the pairs with the BECs, allowing for more frequent Penning ionising collisions. After the BEC and entangled pair wavefunctions have spatially separated, there should be a negligible fraction of atoms lost, since the $|\Psi^+\rangle$ pair source was prepared with very low numbers - an order of magnitude lower than the scattering halo used to characterise the Raman pulse in Fig. 4.10. In the presence of BECs in both spin-states, each atom from the $|\Psi^+\rangle$ pair is almost equally likely to be lost by Penning ionisation. The loss of an atom from any pair results in the detection of a single-hit event: a single-hit event will be detected in A with \uparrow or \downarrow , with no correlated hit in B . Such events are naturally treated by the correlation functions $g_{ij}^{(2)}$ as an uncorrelated background event (see Eq. (4.47)). Particle losses therefore reduce the observed correlator

asymptotically to the uncorrelated state $\mathcal{B} = 0$, such that in the extreme case where atom loss is definite, $g_{ij}^{(2)} = 1$ for all back-to-back correlations will be observed.

The small increase in total detected number of atoms for longer pulse durations, namely as in $N'_{\text{loss}} < 0$ for $\tau > 17 \mu\text{s}$, is due to the single-photon absorption of the Raman beams and subsequent de-excitation of atoms from the BECs. This process follows $2^3S_1 \rightarrow 2^3P_J \rightarrow 2^3S_1$ with each step accompanied by a single photon recoil, and therefore a small fraction scatters into *s*-wave scattering halo (see Fig. 4.4(b)). In our experiment, a large detuning of the Raman beams from resonance minimised the rate of the single-photon absorption, as demonstrated by the nearly absent scattering effects even from a large number of atoms in the BECs. The entangled atoms of interest originally occupying the halos are indeed equally subject to such loss process in principle, but it has a negligible effect overall, where the dominant loss process is the $\approx 10\%$ detector quantum efficiency.

Coherence

Here we verify that the Raman pulse does indeed induce a (coherent) rotation of the atomic spin, as in the Bloch sphere picture (see Section 2.3.3), by a simple two-pulse sequence shown in Fig. 4.12(a). This is the Ramsey interferometry from nuclear magnetic resonance [190], composed of two $\pi/2$ -pulses with a delay, reveals interference fringes when there is coherence between the two spin components, according to the transform

$$\begin{aligned} |\uparrow\rangle \mapsto \hat{R}_y(\pi/2) \underbrace{\exp(-i\theta(t)\hat{\sigma}_z/2)}_{\text{Larmor precession}} \hat{R}_y(\pi/2) |\uparrow\rangle &= -i \sin(\theta/2) |\uparrow\rangle + \cos(\theta/2) |\downarrow\rangle \\ &= |\uparrow; \mathbf{n}(\theta)\rangle, \end{aligned} \quad (4.48)$$

where θ is the Larmor phase accrued during delay, and $\mathbf{n}(\theta)$ lies on the yz -plane with polar angle $\pi - \theta$. To observe the Ramsey fringe, we scan the phase delay ϕ in the secondary $\pi/2$ -pulse over the range 0 to 2π , which corresponds to the azimuthal angle of the axis of spin rotation, with respect to the primary pulse (refer to Section 2.3.3 for the physical mechanism and experimental details). We applied a short delay between the two $\pi/2$ -pulses, approximately 10 Larmor precession periods, so that spins do not decohere during interrogation. Note that in the stabilised magnetic field we have been considering, the single Larmor period during the interrogation sequence is $T_L = 2\pi/\Omega_L \approx 0.66 \mu\text{s}$. Figure 4.12(b) shows the Ramsey fringe with a high visibility of 0.95(2), which provides a clear demonstration of the desired coherent control of the atomic spin $\hat{R}_\phi(\vartheta) = \exp[-i(\vartheta/2)(\cos\phi\hat{\sigma}_y + \sin\phi\hat{\sigma}_x)]$, where the rotation angle is set by the pulse duration $\vartheta = \Omega'\tau$.

In addition to the coherent control of an atom, the coherence in the superposition of the internal state must also be maintained throughout its evolution to exhibit quantum mechanical phenomena. Indeed, the loss of coherence from a Bell state ultimately leads to a completely mixed state and nonlocal correlations become unob-

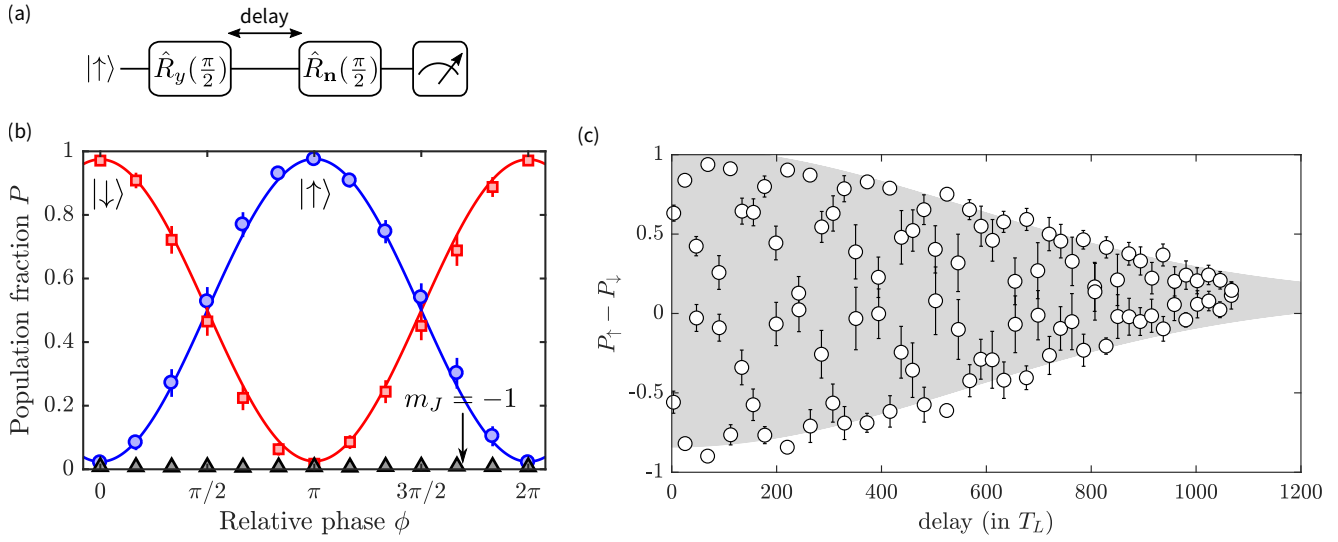


Figure 4.12: Ramsey interferometry. (a) Schematic of Ramsey interferometry sequence. Rotation axis of the second $\pi/2$ -pulse is controlled by the relative phase between Raman beams, according to $\mathbf{n} = (\sin\phi, \cos\phi, 0)$. (b) Ramsey signal in the population fraction of the scattering halo for a pulse delay of $\approx 10T_L$. Solid lines are sine-fits to data, giving a fitted fringe visibility of $0.95(2)$. (c) Decay of Ramsey signal (at $\phi = 0$) from varying the pulse delay t , shown for z -polarisation $\langle \hat{\sigma}_z \rangle = P_\uparrow - P_\downarrow$. Gray region is the function $A \exp[-(t/T)^2] \cos(\Omega_L t + \theta) + c$ fitted to data. Error bars indicate a standard deviation.

servable for sufficient decoherence (see Section 2.1). The key mechanism responsible for the spin decoherence in our experiment is the inhomogeneity of the magnetic field, wherein the collective coherence is lost since constituent atoms experience different Larmor precession frequencies, depending on their location. In Ramsey interferometry where we increase the delay between pulses while fixing $\phi = 0$ in the second pulse, for instance, the superposition $(|\uparrow\rangle + |\downarrow\rangle)/\sqrt{2}$ prepared by the first $\pi/2$ -pulse gradually decoheres to a 50/50 statistical mixture $|\uparrow\rangle$ and $|\downarrow\rangle$. Such mixed states do not interfere coherently at the second $\pi/2$ -pulse, and arise in the decay of fringe visibility as seen in Fig. 4.12(c) at a timescale $T = 800(30)T_L = 530(20)\mu\text{s}$.

Figure 4.13 shows a slightly modified pulse sequence to the Ramsey interferometry, where an additional π -pulse (spin-flip) is implemented mid-way between the $\pi/2$ -pulses. The π -pulse suppresses decoherence from inhomogeneous Larmor precession frequencies, by effectively inverting the sign of the phase accrued during the first evolution period τ , which is negated by the second period according to

$$\begin{aligned}
 |\uparrow\rangle &\mapsto \hat{R}_y(\pi/2) \underbrace{\exp(-i\theta_2 \hat{\sigma}_z/2)}_{\text{2nd}} \hat{R}_y(\pi) \underbrace{\exp(-i\theta_1 \hat{\sigma}_z/2)}_{\text{1st Larmor precession}} \hat{R}_y(\pi/2) |\uparrow\rangle \\
 &= |\uparrow; \mathbf{n}(\vartheta)\rangle,
 \end{aligned} \tag{4.49}$$

where θ_i is the Larmor phase accrued in segment- i ($i = 1, 2$), and \mathbf{n} lies in yz -plane with polar angle $\vartheta = \theta_1 - \theta_2$, clearly containing the difference in phase accrued between the two segments. The spin-echo signal from a spatially distributed ensemble is therefore ideally unity in an inhomogeneous, stationary potential. In practice, the initial spin-echo signal is ≈ 0.95 (see $\tau = 0$ in Fig. 4.13) since the spin rotation pulses are imperfect from a small detuning from Raman resonance, as seen in Fig. 4.11. We observe a coherence time of $T = 630(10)$ μs in the spin-echo signal, in a reasonable agreement with that from the decay of Ramsey fringe.

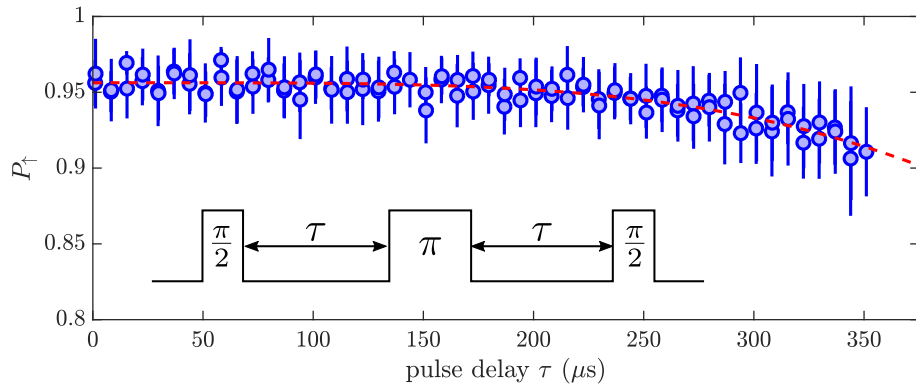


Figure 4.13: Spin-echo sequence. Inset shows the schematic of the spin-echo pulse sequence. The dashed red line is a fit to the decaying spin-echo signal according to $P_\uparrow = 1/2 + A \exp[-(\tau/T)^4]$. Error bars indicate a standard deviation.

We give a brief explanation for the observed decoherence of the scattering halo based on non-uniformities in the magnetic field. Note that the Larmor phase of He^* between $m_J = 0, 1$ states accrues in a magnetic field (magnitude $B(t)$) between times t_i and t_f according to $\theta(t_i, t_f) = \int_{t_i}^{t_f} \gamma B(t) dt$, where γ is the gyromagnetic ratio. Since the scattering halo is spatially distributed, the Larmor frequency $\omega = \gamma B$ will be distributed over the ensemble, assumed for simplicity by a normal distribution with a standard deviation $\Delta\omega$. The scattering halo is initially perfectly coherent with no phase uncertainty $\Delta\theta(t=0) = 0$, the ensemble's phase broadens also as a wrapped normal distribution $p_{\text{WN}}(\theta)$ given explicitly by integrating $\Delta\omega(t)$.⁶ Therefore at the output of the Ramsey interferometer (see Eq. (4.48)), the spin ensemble consists of

⁶A normal distribution with mean μ and standard deviation σ on $\theta \in (-\infty, \infty)$ wrapped onto the circle by $\theta \mapsto \theta (\bmod 2\pi)$ produces the wrapped normal (WN) distribution [191]. The probability density function for such WN distribution is

$$p_{\text{WN}}(\theta; \mu, \sigma) = \frac{1}{\sigma\sqrt{2\pi}} \sum_{k=-\infty}^{\infty} \exp\left[\frac{-(\theta - \mu + 2\pi k)^2}{2\sigma^2}\right],$$

for which the mean of complex coordinate $z \equiv e^{i\theta}$ (analogous to $\mathbf{n}(\theta)$ on yz -plane) is explicitly given by

$$\langle z \rangle = \int_0^{2\pi} d\theta e^{i\theta} p_{\text{WN}}(\theta; \mu, \sigma) = e^{i\mu - \sigma^2},$$

which gives Eq. (4.51).

Bloch vectors $\mathbf{n}(\theta)$ on yz -plane, which are no longer pointing together but fanned out, characterised with an angular width of $\Delta\theta(t) = t/T_1 + (t/T_2)^2 + O(t^3)$. Observe that the polynomial coefficients in the above expression of $\Delta\theta(t)$ are well determined by corresponding terms in the Taylor expansion of $B(t)$ distribution – for example the first order coefficient $1/T_1$ corresponds to the time-independent inhomogeneity (zeroth order in $\Delta B(t)$). An effective Bloch vector $\tilde{\mathbf{a}}$ characterising the halo arises from an ensemble average according to

$$\tilde{\mathbf{a}} \equiv \langle \mathbf{n}(\theta) \rangle = \int_0^{2\pi} d\theta \mathbf{n}(\theta) p_{WN}(\theta). \quad (4.50)$$

The Ramsey fringe visibility, corresponding to the length of Bloch vector, then decays according to the phase broadening dynamics by

$$|\tilde{\mathbf{a}}| = e^{-\Delta\theta^2} = e^{-(t/T_1)^2 - O(t^3)}, \quad (4.51)$$

as observed in the experiment (see Fig. 4.12(c)).

On the other hand, the phase encoded in a single atom by the spin-echo sequence ϑ (see Eq. (4.49)) is the difference in Larmor phases accrued on each side with τ -delay of the π -pulse (see Fig. 4.13), given explicitly by $\vartheta = \theta(0, \tau) - \theta(\tau, 2\tau) = \gamma \left(\int_0^\tau B(t) dt - \int_\tau^{2\tau} B(t) dt \right)$. Therefore by its insensitivity to static inhomogeneity over the ensemble (first order terms in τ from previous integral exactly cancel), the spin-echo signal ϑ contains negligible terms to both zeroth and first order in time, such that $\Delta\vartheta = (t/T)^2 + O(t^3)$. Following a similar argument to Eq. (4.50), the collective spin-echo signal then evolves according to $e^{-\Delta\vartheta^2} = e^{-(t/T)^4 - O(t^5)}$, as observed in Fig. 4.13.

Further discussion on the effect of magnetic field inhomogeneities on the scattering halo are found in Chapter 5, where the magnetic field is mapped in 3D, and the spatial gradient verified using the pairwise entanglement as a resource. The next section discusses the spin correlations measured across pairs separated by ≈ 0.1 mm, corresponding to the rotation pulse implemented 0.8 ms after the $|\Psi^+\rangle$ -entangling collision pulse. Suffice to say, at this point the atom pairs are still close to $|\Psi^+\rangle$, however for larger separations explored in Chapter 5, asymmetry in the magnetic potential traversed by the atoms cannot be ignored.

4.6 Experimental observation of quantum nonlocality

This section discusses the spin correlation observed from the entangling collision interrogated in single-atom detail, with the aid of a controlled rotation sequence. The pairwise spin correlations between freely counter-propagating atoms in the scattering halo are ultimately demonstrated to contradict the notion of locality held in the EPR paradox.

4.6.1 Symmetrically rotated spin correlation

Figure 4.14(a) shows the $g^{(2)}$ function of the $|\Psi^+\rangle$ -entangled scattering halo for a few symmetric rotation settings, selected from a total of 17 equispaced pulse durations (angles) between $0\ \mu\text{s}$ (no rotation) and $T_\pi \approx 10\ \mu\text{s}$ (spin-flip). Here we show the correlation function around back-to-back scattered modes $(\mathbf{k}, -\mathbf{k} + \Delta\mathbf{k})$ in the Cartesian coordinate system parameterised by the misalignment in momentum $\Delta\mathbf{k}$, explicitly given according to (compare with Eq. (4.47))

$$g_{ij}^{(2)}(\Delta\mathbf{k}) = \frac{\sum_{\mathbf{k} \in V} \langle : \hat{n}_{\mathbf{k},i} \hat{n}_{-\mathbf{k}+\Delta\mathbf{k},j} : \rangle}{\sum_{\mathbf{k} \in V} \langle \hat{n}_{\mathbf{k},i} \rangle \langle \hat{n}_{-\mathbf{k}+\Delta\mathbf{k},j} \rangle}, \quad (4.52)$$

where V is the volume of scattering halo in \mathbf{k} -space, and $\hat{n}_{\mathbf{k},i}$ is the atom number operator for the mode with momentum \mathbf{k} and spin $i, j \in \{\uparrow, \downarrow\}$.

The top row of Figure 4.14(a) shows the correlation function when there was no rotation ($\tau = 0\ \mu\text{s}$), where characteristics of the pair source prior to rotation was investigated earlier. The pair source, prior to any rotation, is of course almost perfectly anti-correlated in spin, and emits into counter-propagating \mathbf{k} -modes with a finite correlation length. The joint detection probability (defined in Eq. (4.20)) for this measurement setting is shown in Fig. 4.14(b). Here we take the $g^{(2)}$ value to be defined as amplitude at the back-to-back condition $g_{ij}^{(2)} \equiv g_{ij}^{(2)}(\Delta\mathbf{k} \approx 0)$, using a cubic bin in k -space (in units of collision momentum) of width 0.0138 as in Fig. 4.14(a).

As the spin measurement is rotated ($0\ \mu\text{s} < \tau \leq 5\ \mu\text{s} = T_{\pi/2}$) the atom pairs become gradually more positively correlated, until they become near-perfectly aligned with $\pi/2$ -rotation ($\tau = 5\ \mu\text{s}$), as expected for $|\Psi^+\rangle$ (see Fig. 4.1). Unlike the theoretical prediction however, the observed correlation profile is asymmetric about $\pi/2$ ($5\ \mu\text{s} < \tau \leq 10\ \mu\text{s} = T_\pi$), which is most striking where a spin-flip (π -pulse) does not return the degree of anti-correlation demonstrated originally ($\tau = 0\ \mu\text{s}$). This behaviour is due to the finite off-resonant effects in the Raman transition already observed in Fig. 4.11, that shifts the rotation axis away from the equator of Bloch sphere.

In Fig. 4.14(b), we also observe asymmetric outcomes between $\uparrow\uparrow$ and $\downarrow\downarrow$ configurations, where although their behaviour is similarly correlated as expected from the characteristic of $|\Psi^+\rangle$, but the former configuration occurs noticeably less. This can be caused by experimental imperfections, such as the asymmetric distortion of the correlation volumes by magnetic lensing of the $m_J = 1$ scattering halo, which means the alignment of BB-scattered pairs can be shifted quite strongly for $\uparrow\uparrow$ spin configurations.

4.6.2 Nonlocal spin correlations

The two-body correlator for the symmetrically rotated measurement settings we implemented are then given from Eq. (4.8) by

$$\mathcal{B}(\theta) = E(\theta, \theta) = P_{\uparrow\uparrow}(\theta, \theta) - P_{\uparrow\downarrow}(\theta, \theta) - P_{\downarrow\uparrow}(\theta, \theta) + P_{\downarrow\downarrow}(\theta, \theta),$$

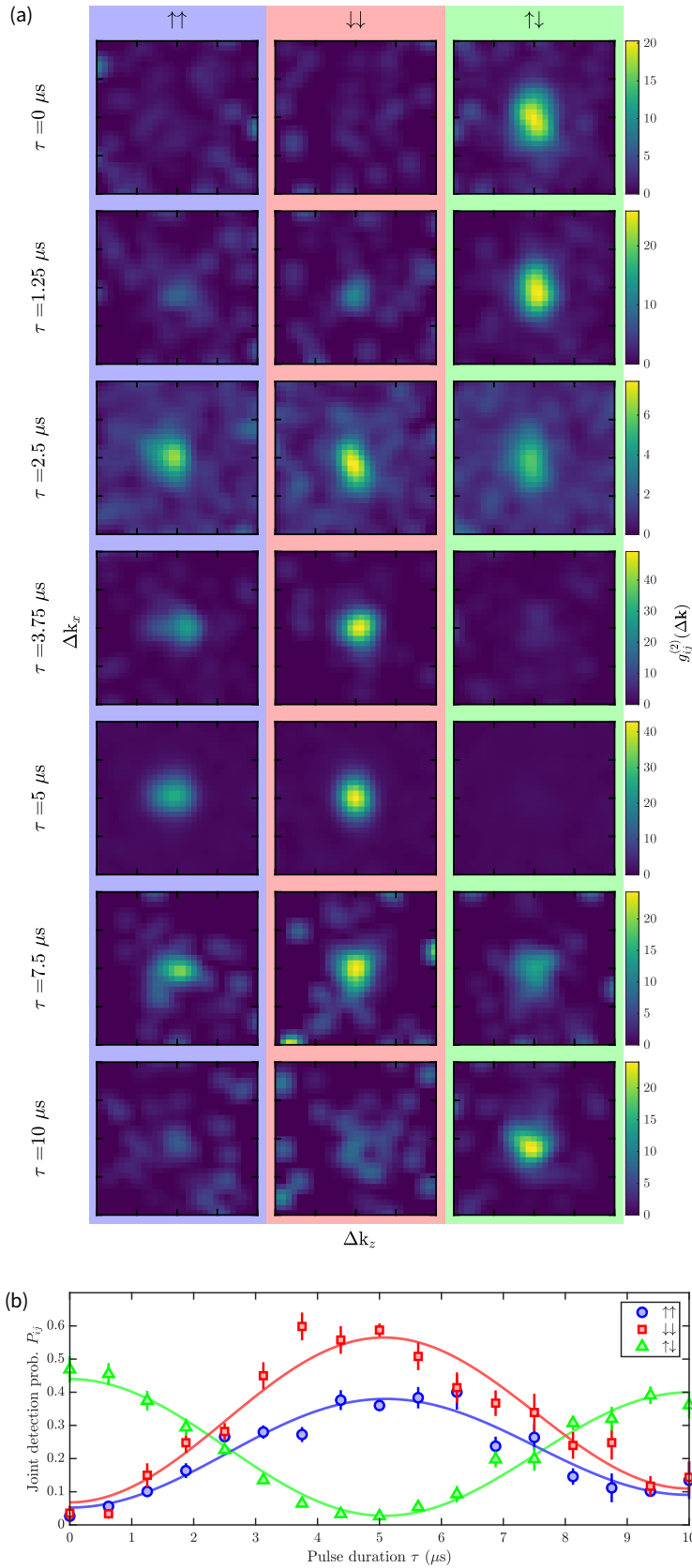


Figure 4.14: Second-order correlation functions after spin rotations. (Continued on the following page.)

Figure 4.14: Second-order correlation functions after spin rotations. (Continued.) (a) $\Delta k_y = 0$ slices of $g^{(2)}(\Delta \mathbf{k})$ for various spin rotation pulses (rows) and spin-pairing configurations (columns), shown for BB scattered regions around $\Delta k_x, \Delta k_z \in [-0.2, 0.2]$. k -space is normalised by the collision momentum (i.e. values are in units of the halo radius). (b) Joint detection probabilities for different spin configurations at the back-to-back condition ($\Delta \mathbf{k} = 0$). Error bars indicate statistical uncertainty estimated from bootstrapping [187]. Solid lines are fit to data.

and shown in Fig. 4.15(a).

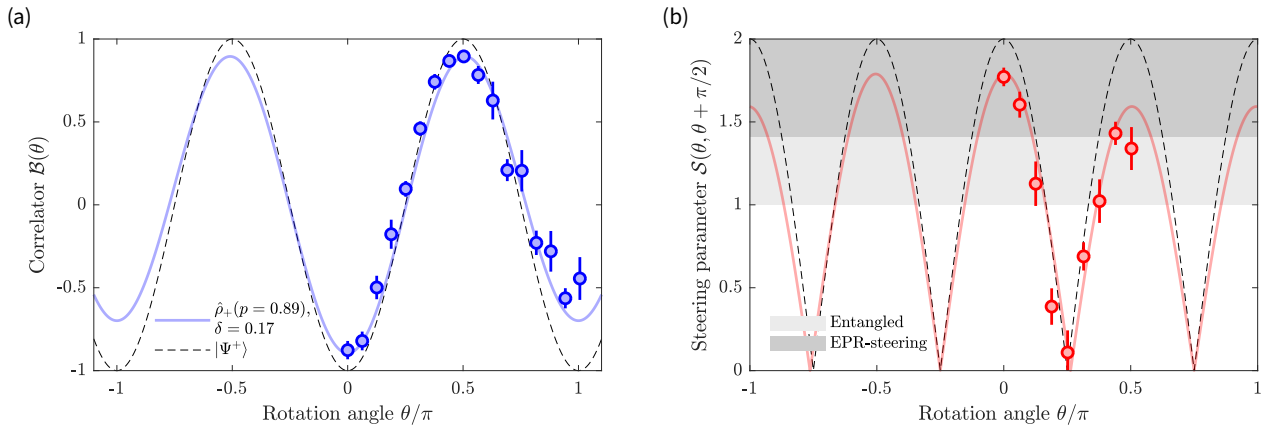


Figure 4.15: Nonlocal correlations in scattering halos. (a) Experimental determination of the symmetrically rotated correlation. In both figures, the dashed lines indicate prediction from $|\Psi^+\rangle$, whereas the solid lines are fits to data for a mixed state $\hat{\rho}_+$ under an off-resonant spin rotation from Eq. (4.53). (b) Experimental determination of the steering parameter, and the observation of quantum nonlocality. The light and dark shaded regions indicate the region outside of separability (4.32) and EPR-steering inequality (4.43), respectively. Error bars indicate statistical uncertainties estimated from bootstrapping [187].

The observed correlation deviates from that of the ideal Bell triplet state $|\Psi^+\rangle$, for which $B(\theta) = -\cos 2\theta$, in two aspects. First, the correlation amplitude is reduced from unity due to the spontaneous emission of pairs, as was already predicted from Eq. (4.16). Second, the correlation is significantly reduced near π -rotation and asymmetric about $\pi/2$. This is due to imperfections in the spin rotation process, where off-resonant Raman transition caused the Rabi amplitude to be less than unity (see Fig. 4.11). The above effects adequately account for the observed correlation (see fit in Fig. 4.15(a)), where we model the many-body entangled state as an effective pair $\hat{\rho}_+$, and detuning by a rotation vector off- xy plane by an elevation angle δ , explicitly

given by

$$\begin{aligned}\mathcal{B}(\theta|p, \delta) &= \text{Tr} \left[\hat{R}_\delta^{\dagger(A)}(\theta) \hat{R}_\delta^{\dagger(B)}(\theta) \hat{\sigma}_z^{(A)} \hat{\sigma}_z^{(B)} \hat{R}_\delta^{(A)}(\theta) \hat{R}_\delta^{(B)}(\theta) \hat{\rho}_+(p) \right] \\ &= -p(\sin^2 \delta + \cos^2 \delta \cos \theta)^2 + p(\sin \delta \cos \delta (1 - \cos \theta)^2 + (\cos \delta \sin \theta)^2),\end{aligned}\quad (4.53)$$

where $\hat{R}_\delta(\theta) = \exp[-i(\hat{\sigma}_y \cos \delta + \hat{\sigma}_z \sin \delta)\theta/2]$ applies a θ -rotation about the axis $(\cos \delta, 0, \sin \delta)$. The fit parameters are given by $p = 0.89(2)$ and $\delta = 0.17(3)$ (uncertainty is 1 standard error), which is in a reasonable agreement with the experimental conditions.

Violation of the entanglement inequality

Let us first show that the scattered atom pairs are entangled in spin, as this is the weakest form of quantum nonlocality. Recall from Eq. (4.32) that the maximum range of the correlator is bounded by unity for all separable states, such that

$$\mathcal{S}(\theta, \theta') \equiv |\mathcal{B}(\theta) - \mathcal{B}(\theta')| \underset{\text{sep}}{\leq} 1 \quad (4.54)$$

for all pairs of measurement settings θ, θ' . We detect a clear violation of the above separability criterion in Fig. 4.15(a), where the fitted amplitude is approximately p times the algebraic maximum 2, and we observe the maximum range between $\theta = 0, \pi/2$ of $\mathcal{S}(0, \pi/2) = 1.77(6)$ (see Fig. 4.15(b)). This establishes direct evidence of atomic entanglement by collision.

Violation of the EPR-steering inequality

Similarly, EPR nonlocality is signalled by the violation of local hidden quantum state-local hidden variable hybrid model. A particular EPR-steering inequality was earlier derived for the $|\Psi^+\rangle$ state (refer to Eq. (4.43)), based on the absolute difference in orthogonally measured correlations, given by

$$\mathcal{S}(\theta, \theta + \pi/2) \underset{\text{EPR-local}}{\leq} \sqrt{2}. \quad (4.55)$$

We observe a 6-sigma level violation of the above EPR-steering inequality between the z - and x -axis measurements (see Fig. 4.15(b)), where the steering parameter at $\theta = 0$ is $\mathcal{S}(0, \pi/2) = 1.77(6)$.

4.7 Conclusion

In conclusion, we have investigated quantum correlations in pairs of atoms after a collision. We interrogated individual atoms' spins after the pairs had separated by approximately 0.1 mm, and observed their correlation along symmetrically rotated measurement settings. Even such a restricted set of measurements on a two atom

system revealed that the collision pair is entangled. Most strikingly, the observed correlations reveal quantum nonlocality in the form of a 6-sigma violation of an EPR-steering inequality. Our results are in agreement with the theoretical prediction that a two-body *s*-wave collision entangles the particles in the maximally entangled Bell state, and therefore serve as a basic demonstration of entanglement by collision.

Rather than having to collide two atoms individually, here we collided two BECs and observed correlations across oppositely scattered regions in the halo. To obtain the pair correlation we could treat multiple scattered pairs in a single collision as parallel realisations of the same state in a single shot of the experiment (e.g. integration over all scattering \mathbf{k} -modes in Eqs. (4.47) and (4.52)). This embodies the inherent advantage in the rate of data acquisition by the large number of modes in the *s*-wave scattering halo used as a pair source. In the following chapter, we verify that the multiply scattered pairs are identical in the spin degree-of-freedom. Indeed we show that there is no scattering angle-dependence of the two-particle correlation functions localised in momentum for a limited duration after collision is induced. Longer evolutions disturb the initial $|\Psi^+\rangle$ pairs, since magnetic field becomes unequal across the atoms.

Entanglement-based 3D magnetic gradiometry with an ultracold atomic scattering halo

How precisely something can be known inevitably relies on the precision of the available yardstick. Nowadays details at subatomic length scales of materials are routinely imaged by microscopes measuring quantum tunneling electrical currents, while astrophysical events are detected via ripples in space-time using 4 km long laser interferometers. All physical measurements therefore ultimately face the inherent randomness of the yardstick at the quantum mechanical limit, such that even classical sensors employing coherent radio frequency waves and lasers to electrical currents and magnetisation of spin ensembles cannot evade the quantumness of their constituent particles. This notorious limit in measurement sensitivity, referred to as the shot-noise in electronics, can be surpassed by entangling a collection of the *sensor* particles to reduce quantum fluctuations and amplify the signal, as well as to enable nonclassical measurement tasks.

Quantum correlations such as entanglement or squeezing can enable measurement sensitivities that outperform that of classically correlated systems called the standard quantum limit [27, 51, 25], and even the realisations of classically-forbidden tasks [32]. In squeezing, the improvement in sensing is due to the suppression of quantum fluctuations of a variable below that of a classical state at the cost of amplified uncertainty in the complementary variable [23]. Striking nonclassical features such as nonlocality exist in other forms of strongly entangled systems such as the Bell states, which are central to quantum technologies like quantum computing and cryptography [32]. Utilising quantum correlations can therefore enable novel types of experimental techniques [192] and measurements [193, 194], as well as a metrological performance reaching the fundamental physical limit of precision known as the Heisenberg limit [27].

Here we report on a proof-of-principle demonstration of an entanglement-based 3D magnetic gradiometry using maximally entangled pairs of atoms created from a collision of Bose-Einstein condensates [101]. Measuring the phase evolution of entangled pairs as they oscillate between the symmetric and anti-symmetric Bell states

$|\Psi^\pm\rangle$, respectively, allows an intrinsically differential measurement of the magnetic field along the paths traversed by the atoms. In addition, we achieve a 3D tomography of the magnetic field gradient, as well as a measurement of the absolute magnetic field by Ramsey interferometry, with microscopic spatial resolution, limited in this demonstration by the size of the BECs to $\sim (35 \mu\text{m})^3$. This nonclassical scheme could be extended to robustly create freely propagating atomic Bell states entangled in masses such as for the quantum tests of general relativity [73].

5.1 Quantum metrology in a nutshell

Even though the time evolution of a wavefunction is deterministically governed by the Schrodinger equation, the post-measurement estimation processes must in general deal with a probability distribution of outcomes according to one of the fundamental postulates of quantum mechanics. This therefore places a fundamental limit on the accuracy of estimating the quantum state itself and in effect any property of the environment since any sensor is quantum mechanical, which has no analogy in classical physics where any property can be determined definitely. Although this result may seem at first detrimental to quantum sensing technologies, quantum sensors in fact offer powerful advantages over classical sensors, such as allowing a far superior sensitivity with the same amount of resources, and even measurement protocols which are classically impossible. Below, we give a brief overview of the field of quantum metrology, and show a way to go beyond classical noise limits and methods in sensing by harnessing quantum correlations that are found in the atomic Bell states.

5.1.1 Phase estimation of a single qubit and classically correlated ensembles

The central problem of parameter estimation in a quantum mechanical system can be illustrated with an ensemble of qubits, starting with a single qubit. The phase estimation of a quantum state is a key step to the operation of all quantum sensors which encode the parameter of interest x , a dimensionless phase, by a unitary transformation $\hat{U}(x) = \exp(-i\hat{G}x)$, although the generating physical interactions \hat{G} may vary depending on the sensor.

Suppose the phase θ encoded in the qubit $|\theta\rangle = (|\uparrow\rangle + e^{i\theta}|\downarrow\rangle)/\sqrt{2}$, prepared by rotating the input probe state $|\psi_0\rangle = (|\uparrow\rangle + |\downarrow\rangle)/\sqrt{2}$ around the z axis by the unknown angle θ (i.e. $\hat{G} = \hat{S}_z$), is to be determined experimentally.¹ One such method would be to rotate the state around the y axis by $-\pi/2$, giving $\cos\theta/2|\uparrow\rangle + \sin\theta/2|\downarrow\rangle$, and then by projecting it on the z axis to take directly the measurement $\hat{M} = \hat{\sigma}_z$. Since the phase is mapped to the polar angle of the Bloch vector, the average outcome of the measurement $\langle \hat{M} \rangle = \cos\theta$ can be used to give an estimate of the phase $\tilde{\theta} = \cos^{-1}\langle \hat{M} \rangle$. The catch is that the outcome takes discrete

¹Recall the Bloch sphere picture of qubits in Fig. 2.16 and the rotation operator defined in Eq. 4.10. In writing the phase-encoded state we ignore the global phase in the superposition as seen in Eq. 2.6.

values $\mu \in \{\pm 1\}$ corresponding to the two $\hat{\sigma}_z$ eigenstates the state becomes projected upon measurement, giving rise to the so-called projection noise of variance $(\Delta \hat{M})^2 \equiv \langle (\hat{M} - \langle \hat{M} \rangle)^2 \rangle = \langle \hat{\sigma}_z^2 \rangle - \langle \hat{\sigma}_z \rangle^2 = \sin^2 \theta$. The uncertainty in the estimated phase is therefore given by the sensitivity of the phase estimation function against the uncertainty in the measurement signal $\Delta \tilde{\theta} = \Delta \hat{M} / |\partial \langle \hat{M} \rangle / \partial \theta| = 1$.

The simplicity of the phase estimation protocol suggested above raises an important question: is it possible to do better? Such a task is classically formalised in the field of estimation theory.² For the known phase encoding operation $\exp(-i\hat{\sigma}_z \theta / 2)$ this problem requires searching for the optimal set of variables, specifically the initial state $|\psi_0\rangle$, the general set of measurements yielding outcomes $\tilde{\cdot}$, and the phase estimator $\tilde{\theta}(\tilde{\cdot})$, that ultimately minimise the phase uncertainty $(\Delta \tilde{\theta})^2 \equiv \langle (\theta - \tilde{\theta})^2 \rangle$ as well as being unbiased, such that $\langle \tilde{\theta} \rangle = \theta$ for all possible θ . Without delving into much detail, quantum metrology builds on solid foundations in parameter estimation theory in which there is the famous Cramér-Rao (CR) lower bound on the estimation uncertainty [196], such that $\Delta \theta \geq \Delta \theta_{\text{CR}}$, yielded for all locally unbiased estimators. This limit is given by $\Delta \theta_{\text{CR}} = 1 / \sqrt{F(\theta)}$, where F is the Fisher information defined according to [196]

$$F(\theta) \equiv \sum_{\mu} \frac{1}{p(\mu|\theta)} \left(\frac{\partial p(\mu|\theta)}{\partial \theta} \right)^2, \quad (5.1)$$

where the sum is taken over all possible measurement outcomes μ . Observe that Eq. (5.1) quantifies the statistical speed (squared) of the outcome probability distribution $p(\cdot|\theta)$ with respect to θ , where the statistical distance is related to the concept of distinguishability between the distributions [196]. Thus, the Fisher information captures the fundamental limit of how much information one can infer about changes in the parameter θ from observing probabilistic outcomes. Indeed analogous results can be derived when the parameter encoding and probability distribution is generalised to quantum states and measurements [197]. In quantum metrology, the quantum CR bound

$$\Delta \tilde{\theta} \geq \Delta \theta_{\text{QCR}} = 1 / \sqrt{F_Q} \quad (5.2)$$

places a fundamental lower limit to uncertainty in phase (or some other parameter characterising the quantum state) estimation [196]. Here the quantum Fisher information $F_Q[\psi_\theta]$ quantifies the statistical speed of the wavefunction ψ_θ in its trajectory along θ . It turns out that for pure states which transform as $|\psi_\theta\rangle = \exp(-i\hat{G}\theta) |\psi_0\rangle$, the quantum Fisher information is given by [197]

$$F_Q(\psi_\theta) = 4(\langle \hat{G}^2 \rangle - \langle \hat{G} \rangle^2), \quad (5.3)$$

where the expectation value is taken for the initial state $|\psi_0\rangle$. Recall that the simple qubit scheme illustrated above (initial state is $|\psi_0\rangle = (|\uparrow\rangle + |\downarrow\rangle) / \sqrt{2}$, and the generator is \hat{S}_z) gave unity phase uncertainty, which is in fact the optimal value we obtain

²An in-depth discussion of parameter estimation theory lies outside the scope of this thesis. Interested readers are referred to Ref. [195] for an insightful overview, and Ref. [196] for a comprehensive treatment of the mathematical foundations and applications to quantum metrology.

from Eqs. (5.2) and (5.3), since $F_Q = 1$.

Statistical uncertainties reduce with repeated sampling or equivalently by simultaneously measuring an ensemble of identically prepared random variables. Since both scenarios are independent sampling from a random distribution, the uncertainty in the mean scales exactly according to $N^{-1/2}$, where N is the number of repetitions or identically prepared systems. It should not be surprising that the same scaling should be seen when an ensemble of N uncorrelated qubits $|\theta^{(1)}\rangle \otimes |\theta^{(2)}\rangle \otimes \dots \otimes |\theta^{(N)}\rangle$ are used to estimate the same parameter, given that each qubit is transformed identically such that the phase is encoded by $\hat{U}^{(1)}(\theta) \otimes \hat{U}^{(2)}(\theta) \otimes \dots \otimes \hat{U}^{(N)}(\theta)$. Indeed when every qubit is prepared and measured identically as before but the outcome summed, we find that the signal scales linearly with N since $\langle \hat{M}_{\otimes N} \rangle = \sum \langle \hat{M} \rangle = N \cos \theta$, where the subscript distinguishes the separable ensemble from the single qubit case, as well as its variance since each random outcome from measuring individual qubits are independent such that $(\Delta \hat{M}_{\otimes N})^2 = N \sin^2 \theta$. The phase uncertainty from an uncorrelated ensemble of N qubits thus may achieve $\Delta \tilde{\theta}_{\otimes N} = \Delta \hat{M}_{\otimes N} / |\partial \langle \hat{M}_{\otimes N} \rangle / \partial \theta| = \sqrt{N} \sin \theta / N \sin \theta = 1 / \sqrt{N}$, which is also indeed the quantum CR limit for separable N qubits. Such uncorrelated and unentangled ensembles at arbitrarily large N idealise classically coherent systems. The standard quantum limit $\Delta \theta_{SQL} = 1 / \sqrt{N}$ is therefore the limit to the measurement precision of all classical sensors

5.1.2 Quantum enhancement in measurement sensitivity by entanglement

It turns out that entanglement is the necessary quantumness which must be exploited to surpass the SQL using the same number of particles.

Let us consider the same scenario for N sensor qubits prepared in a maximally entangled state consisting of equal superposition of all atoms in the spin up and all atoms in the spin down state, written $|\Psi(t=0)\rangle = (|\uparrow\uparrow\dots\uparrow\rangle + |\downarrow\downarrow\dots\downarrow\rangle) / \sqrt{2}$, referred to as the NOON or Schrodinger cat state. The name NOON originates from a two-mode bosonic field representation of the ensemble of identical qubits, which is given by $(|N,0\rangle + |0,N\rangle) / \sqrt{2}$. Observe that when each qubit evolves independently, namely by picking up a spin-dependent phase according to $|\uparrow\rangle \mapsto \exp(-i\theta/2) |\uparrow\rangle$ and $|\downarrow\rangle \mapsto \exp(+i\theta/2) |\downarrow\rangle$, the NOON state accrues a large phase as a sum of all individual qubit phases. The two stretched spin states comprising the NOON state accrue relative phase at N times the rate of a single qubit, such that it is transformed into $|\Psi(\theta)\rangle = [\exp(-iN\theta/2) |\uparrow\uparrow\dots\uparrow\rangle + \exp(+iN\theta/2) |\downarrow\downarrow\dots\downarrow\rangle] / \sqrt{2} = (\cos N\theta/2 |\Psi_N^+\rangle + i \sin N\theta/2 |\Psi_N^-\rangle) / \sqrt{2}$, where $|\Psi_N^\pm\rangle = (|\uparrow\uparrow\dots\uparrow\rangle \pm |\downarrow\downarrow\dots\downarrow\rangle) / \sqrt{2}$ are two orthogonal NOON states. The last expression is clearly reminiscent of the phase encoded for the single qubit case. Analogous to the single qubit case, implementing a projective measurement which distinguishes $|\Psi_N^\pm\rangle$ as given by $\hat{M}_{NOON} = |\Psi_N^+\rangle\langle\Psi_N^+| - |\Psi_N^-\rangle\langle\Psi_N^-|$ (highly nontrivial to realise but a measurement yielding the same outcome distribution is possible by parity analysis [198]) yields a signal that is N times more sensitive to phase with respect to the single qubit case, given by $\langle \hat{M}_{NOON} \rangle = \cos N\theta$, and uncertainty $(\Delta \hat{M}_{NOON})^2 = \sin^2 N\theta$. This results in a vastly improved phase uncer-

tainty of $\Delta\tilde{\theta}_{\text{NOON}} = \sin N\theta/N \sin N\theta = 1/N$ by utilising the maximal entanglement between all qubits in the ensemble as in a NOON state, compared to the SQL of completely separable ensembles. Moreover the fundamental lower bound of phase uncertainty for the general N qubits system $\Delta\theta_N$ again turns out to be exactly that illustrated above such that $\Delta\theta_N \geq \Delta\theta_{\text{HL}} = 1/N$, the famous result in quantum metrology called the Heisenberg limit. The quadratic improvement in sensitivity gained from the classical SQL to the Heisenberg limited performance emphasises the usefulness of entanglement in quantum metrology: N entangled quantum yardsticks can behave as N^2 classical yardsticks. The N -fold increase in sensitivity from maximally entangled states is exhibited in a context outside sensing such as in super-resolution imaging [199] and lithography [200], where the N entangled wavepackets behave as a single wavepacket with a wavelength reduced by a factor of N . We briefly note a crucial point here that not all entangled states are useful for quantum metrology, or equivalently that there are entangled states parameterised by $\rho(\theta)$ in its evolution, where the quantum Fisher information is no greater than that of separable states such that $F_Q[\rho(\theta)] \leq N$.

Although NOON states conceptually find almost universal application to quantum technologies, such as quantum computing, quantum teleportation, and quantum key distribution, they are notoriously difficult to prepare and handle. Other entangled states useful for quantum metrology include the classes of the squeezed, Fock or Dicke states, and other nontrivial multipartite entangled states. Squeezing has become the prominent resource for quantum metrology due to the relative simplicity of preparation and the state's robustness to imperfections. Squeezed states are typically generated from a classically correlated state via an inter-particle interaction resulting in the reduction of collective fluctuation along a specific quadrature, following an increased fluctuation in the conjugate variable, below the classical uncertainty. Broadly speaking squeezed states are used in a Ramsey interferometer for the reduction provided in measurement uncertainty with respect to an uncorrelated ensemble, but performing with similar signal sensitivity to the interferometric phase. Squeezed states have been first demonstrated with light, but are now found in various physical systems including cold thermal gases, BECs, as well as in optomechanical systems. On the other hand, NOON states have been mostly restricted to quantum optics and trapped ion systems due to the exquisite control of isolated single particles and two particle interaction, and all have produced relatively small states at most up to $N = 10$ realised in nuclei spin in a molecule [201].

5.2 Quantum sensors and quantum magnetic microscopes

Diverse areas in physics harness quantum correlations to improve precision measurements. For example, these include the detection of gravitational waves by light in which the photon's time of arrival is squeezed [202], precision time keeping with spin squeezed ensembles of cold atoms [203], measurement of electromagnetic fields with spin squeezed cold atoms and BECs [204, 205], force and displacement by ul-

tracoherent optomechanical systems [206], as well as super-resolution imaging with photonic NOON states [199]. In fact, the LIGO collaboration is currently utilising squeezed light-enhanced sensitivity of their interferometer for their gravitational wave observations [24]. Among many applications in quantum enhanced sensing, magnetometry has become an active area for a variety of platforms, including superconducting circuits which utilise sophisticated phase estimation algorithms [207], nuclei in molecules prepared in spin NOON states [201], nitrogen-vacancy centres in diamond which provide subatomic spatial resolution [208], magneto-sensitive optomechanical microcavities probed with squeezed light [209], magnetic gradiometry with trapped ions in a Bell state [194], squeezed atomic vapours [204], and ultracold atoms [205, 210].

An interesting avenue in magnetometry that quantum sensors provide is the microscopic spatial detail to which the magnetic field can be mapped. Magnetic microscopes show promising applications, for instance, in medical and material science, where a precise mapping of the magnetic field is desired, requiring the combination of microscopic spatial resolution and high measurement precision [211]. Excellent wide-field measurements of magnetic fields have been investigated using nitrogen-vacancy centres in diamond [208] and ultracold atomic systems [212]. A high resolution imaging technique combining magnetically sensitive fluorescent spectroscopy of nitrogen-vacancy centres in diamond has been demonstrated to realise the 2D imaging of a magnetic field [208]. Ultracold atom microscopes so far rely on reconstruction of the magnetic field via imaging density modulations in elongated trapped ensembles [213, 212], or via in-trap atom interferometry [205], both performed while scanning the trapped ensemble over the interrogation area, or equivalently by scanning the source of the magnetic field.

So far however, demonstrations of such wide field-of-view magnetic imaging has been limited to 2D, and quantum correlations are yet to be exploited in such applications. One can envisage that a 3D magnetic field microscope may allow novel kinds of applications over the current state-of-the-art 2D devices, which are for instance limited in the reconstruction of current distributions to 2D structures [214]. Such a 3D microscope device could be able to directly reconstruct a complete internal structure of the field from local measurements, which could enable a more accurate method to investigate higher order problems such as field sources without relying on additional assumptions or restricted geometries. In the work described in this chapter, we propose and demonstrate experimentally a scheme for 3D magnetic microscopy with ultracold atomic scattering halos. Indeed, the scattering halo has metrologically useful quantum correlations for demonstrating nonclassical metrological tasks.

5.2.1 Atom pairs in a magnetic field

The Bell state $|\Psi^+\rangle$ in spin that is created in a collision of oppositely spin-polarised BECs has interesting properties for magnetometry. The two atoms, labelled by $i = 1, 2$, may experience a different magnetic field depending on their location $\mathbf{B}(\mathbf{r}_i)$, which gives the magnetic potential of the Hamiltonian $\hat{H}_{\text{mag}} = \hbar(\omega_1 \hat{\sigma}_z^{(1)} + \omega_2 \hat{\sigma}_z^{(2)})/2$,

where $\omega_i \propto B(\mathbf{r}_i)$ is the Larmor frequency of the atom. Since the eigenstates $|\uparrow^{(i)}\rangle$ ($|\downarrow^{(i)}\rangle$) accrue phase at ω_i ($-\omega_i$), the pair evolves according to $|\Psi(t)\rangle = \exp(-i\hat{H}_{\text{mag}}t/\hbar)|\Psi^+\rangle = (e^{-i(\omega_1-\omega_2)t/2}|\uparrow\downarrow\rangle + e^{+i(\omega_1-\omega_2)t/2}|\downarrow\uparrow\rangle)/\sqrt{2}$. Letting the phase parameter be the difference $\theta = (\omega_1 - \omega_2)t$, we write the transformed state in the familiar form $|\Psi(t)\rangle = \cos\theta/2|\Psi^+\rangle + i\sin\theta/2|\Psi^-\rangle$. The two Bell states $|\Psi^\pm\rangle$ can be distinguished perfectly using only local and single qubit operations and classical communication between the spatially separate parties, resembling the measurement $\hat{M} = |\Psi^+\rangle\langle\Psi^+| - |\Psi^-\rangle\langle\Psi^-|$, which we show later. Observe that this system is just an $N = 1$ case of the quantum enhanced metrology with NOON states discussed in Section 5.1.2. Therefore, this scheme achieves a phase uncertainty $\Delta\theta = 1$, from a generalisation of the Bell state to the Schrodinger cat state $|\uparrow\rangle_1^N \otimes |\downarrow\rangle_2^N + |\downarrow\rangle_1^N \otimes |\uparrow\rangle_2^N$, where the subscript labels the two position, which gives the Heisenberg scaling $\Delta\theta = 1/N$.

The Bell state created in a scattering halo offers a variety of unique advantages in magnetometry, namely Heisenberg limited sensitivity, common-mode noise rejection, and nonclassical measurement protocols. First, let us properly compare the phase sensitivity for measuring the difference in magnetic field by the $|\Psi^+\rangle$ entangled atom pair against a pair of uncorrelated atoms. The magnetic interaction is described by the Hamiltonian $\hat{H}/\hbar = \omega_1/2|\uparrow;1\rangle\langle\uparrow;1| - \omega_1/2|\downarrow;1\rangle\langle\downarrow;1| + \omega_2/2|\uparrow;2\rangle\langle\uparrow;2| - \omega_2/2|\uparrow;2\rangle\langle\uparrow;2|$, which depends on the atom's position labelled by $|1\rangle$ and $|2\rangle$. Observe that uncorrelated atoms can be used to measure the magnetic field difference $\delta B = B_1 - B_2 = (\omega_1 - \omega_2)/\gamma$, where γ is the atom's gyromagnetic ratio, in two separate ways: each atom may be localised to determine its local magnetic field independently then δB inferred, or an atom could be delocalised and the contribution from δB in the relative phase directly inferred. Letting $\theta_i = \omega_i t$ gives the phase difference as $\theta = \theta_1 - \theta_2 = \gamma\delta B t$. Then we immediately see that the standard quantum limit for the localised case gives $\Delta\theta_{i,\text{SQL}} = 1$ at each location, and therefore uncertainties from independent measurements sum to give for a pair of atoms $\Delta\theta_{\text{SQL,local}} = \Delta(\theta_1 - \theta_2)_{\text{SQL}} = \sqrt{(\Delta\theta_{1,\text{SQL}})^2 + (\Delta\theta_{2,\text{SQL}})^2} = \sqrt{2}$. In contrast, when the atoms are prepared delocalised there are 4 stationary states, 2 from spin and 2 from position. However sensitivity to θ is maximised when the superposition is set up between the maximum energy state in one location and the minimum energy state in the other, such as $|\uparrow;1\rangle$ and $|\downarrow;2\rangle$, since incorporating other states will only reduce the signal visibility corresponding to the frequency of interest $\omega_1 - \omega_2$. Following the above choice, since the unitary evolution is identical to that of single qubit, the optimal phase encoding realised by $|\psi(t)\rangle = (e^{-i\omega_1 t/2}|\uparrow;1\rangle + e^{+i\omega_2 t/2}|\downarrow;2\rangle)/\sqrt{2} = (e^{-i\theta/4}|\uparrow;1\rangle + e^{+i\theta/4}|\downarrow;2\rangle)/\sqrt{2}$, where in the last expression we have dropped the global phase. A crucial point here is that the familiar phase encoding in a qubit appears rescaled by a factor of $1/2$ for the optimal delocalised state for a single atom. Thus we find $\Delta(\theta_{\text{SQL,delocal}}/2)|_{\text{single}} = 1$ for a single atom, and finally for two uncorrelated delocalised atoms one finds $\Delta\theta_{\text{SQL,delocal}} = \sqrt{2}$. Since the Bell state has been shown to achieve $\Delta\theta = 1$, which is a factor of \sqrt{N} enhancement over the standard quantum limit, $N = 2$ in this case, and is therefore the Heisenberg limit.

Second, the phase encoded by the Bell state is only sensitive to difference in mag-

netic fields such that any collective noise in the magnetic field, such as from distant sources, is inherently rejected from the signal. This trait of the Bell state, called decoherence free subspace, is useful to quantum information technologies since the two particle state $|\Psi^\pm\rangle$ may be used to represent an effective logical qubit immune to decoherence from environmental noise when the qubits are located nearby [215]. In addition, this property can be ideal in scenarios where the background field is very large and uniform, but it is only important to measure minute variations in the field that can be orders of magnitude below the actual field magnitude.

Third, this measurement scheme is highly nonclassical since it involves a distributed measurement involving two spatially separated parties manipulating and observing their atom locally, where their individual outcomes are genuinely random as seen from tracing out one of the atoms $\hat{\rho}_{\text{single}} = (|\uparrow\rangle\langle\uparrow| + |\downarrow\rangle\langle\downarrow|)/2$ for both atoms. It is only when the two outcomes at the distributed sites are correlated that the useful information is revealed. Another interesting extension of using the Bell states would be in tests of general relativity, where certain effects may be different in quantum realm than the classical formulation of equivalence principles. In this regard, the entangled atom pairs can offer a truly quantum mechanical test mass, as in a superposition of masses or positions, to measuring a field that is yet unable to be formulated in the quantum mechanics treatment.

5.2.2 The trajectory of atoms in the scattering halo

The atoms in the scattering halo, whether prepared as spin entangled pairs or a spin-polarised state, are not fixed at two positions but rather propagate in all directions in space. These individual trajectories however can be reconstructed to a certain extent with the information gathered from the DLD-MCP detector in the far-field. By applying a short interferometric sequence mid-flight to the scattering halo and detecting the outcome in the far-field, a thin spherical slice of the magnetic field at the interrogation point may be imaged. A complete 3D map can therefore be obtained by interrogating the halo at various points in its expansion to realise 3D magnetic field tomography. Here we estimate the spatial resolution achievable by atom interferometry schemes based on a ballistically expanding model of the scattering halo. For simplicity, our analysis is in one dimension in space and gravity is ignored.

Suppose the scattering halo is created at $t = 0$ from a collision of two BECs, such that a scattered atom's initial spatial location r and velocity v are normally distributed by $r \sim \mathcal{N}(0, \sigma^2)$, and $v \sim \mathcal{N}(v_0, \sigma_v^2)$, where $\mathcal{N}(\mu, \sigma^2)$ denotes a normal distribution with mean μ and variance σ^2 . Such probability distributions of the initial position and velocity can be determined from properties of the BECs. For simplicity we take the Thomas-Fermi approximation for the colliding BECs such that $\sigma \approx R_{\text{TF}}/\sqrt{2}$ (the factor of $1/\sqrt{2}$ is due to the density-squared scaling for two-body collision rates) and $\sigma_v \approx 2\hbar/mR_{\text{TF}}$ [188], where R_{TF} is the Thomas-Fermi radius, and m is mass of the atom. Based on the parameters for our experiment, where the condensate number is $N \sim 10^5$, and trapping frequency $\bar{\omega} \approx 2\pi \cdot 20$ Hz, we obtain $R_{\text{TF}} \approx 50 \mu\text{m}$ and $\sigma_v \approx 0.6 \text{ mm/s}$.

Assuming that the scattered atoms do not interact strongly with the BECs and with each other, they propagate as free particles whereby an atom's position in the scattering halo after an arbitrary evolution time t is given by $s(t) = r + vt$, thus $s \sim \mathcal{N}(v_0 t, \sigma^2 + \sigma_v^2 t^2)$. With an ideal detection scheme at $t = T$, every scattered atom's position at this time $s(T) = S$ can be measured, whereas the magnetic field interrogation occurs at a previous time t^* .

First, given an atom's position S at detection with no uncertainty, we determine the (posterior) distribution of its position at the point of interrogation $s(t^*) \equiv s^*$.³ The spatial resolution of such scheme corresponds to the spatial uncertainty of atom's positions at the interrogation time s^* , based on all possible trajectories to the particular measurement outcome. Thus, the conditional probability distribution of the atom's location at t^* is given by

$$\begin{aligned} P(s^*|S) &= P(s(t^*) = s^*|s(T) = S) \\ &= \frac{P((s(t^*) = s^*) \cap (s(T) = S))}{P(s(T) = S)}. \end{aligned} \quad (5.4)$$

The joint event probability (numerator of Eq. 5.4) corresponds to a unique trajectory, with the initial position $r' = s^* - t^* v'$ and velocity $v' = (S - s^*)/(T - t^*)$, such that

$$\begin{aligned} P(s^* \cap S) &= P(r = r' \cap v = v') \\ &= P(r = r')P(v = v'). \end{aligned} \quad (5.5)$$

Substituting (5.5) into (5.4) and evaluating the probability function for s^* gives a normal distribution with parameters

$$\langle s^* \rangle = \frac{(\tau + \xi^2)S - \sigma\xi w^{-1}(1 - \tau)}{1 + \xi^2} \quad (5.6a)$$

$$\Delta s^* = \frac{\sigma(1 - \tau)}{\sqrt{1 + \xi^2}}, \quad (5.6b)$$

where $\tau = t^*/T$, $\xi = \sigma/\sigma_v T$ and $w = \sigma_v/v_0$ are the dimensionless parameters characterising the scheme.

In the far-field detection regime ($\xi \ll 1$) and with an ultracold scattering halo ($w \ll 1$), the mean position and spatial uncertainty at the interrogation time simultaneously simplify to first order

$$\langle s^* \rangle_\infty = \tau S \quad (5.7a)$$

$$\Delta s_\infty^* = \sigma(1 - \tau). \quad (5.7b)$$

Our experimental parameters are $\tau \approx 0.01$, $\xi \approx 0.1$, and $w \approx 0.03$, so that we can assume the evolution of the scattering halo to be a uniform expansion in time, where the uncertainty is limited by the size of the BEC (5.7). Indeed (5.7) show that the effect

³A finite detector resolution (uncertainty in S) further blurs the atom's posterior distribution by simple convolution, however this effect is shown to be negligible in the regime we operate.

of finite detector resolution, such that S has an uncertainty ΔS , is to blur the spatial distribution at interrogation by $\tau\Delta S$. In our experiment, the detector resolution in each dimension contributes to a negligible effect (< 1%) over the intrinsic uncertainty from the scattering halo's free-expansion dynamics, thereby resulting in an isotropic 3D uncertainty volume in the interrogated region.

5.3 Entanglement-based 3D magnetic gradiometry

In this section we discuss an entanglement-based sensing of magnetic field gradients, based on the result from atomic Bell states that we create in the scattering halo and their counter-propagating trajectories in space.

5.3.1 Methods and concept

The experiment starts with a BEC of metastable helium (He^*) in the 2^3S_1 state, magnetically trapped in the $m_J = +1$ Zeeman sublevel [141]. After the trap switch-off the magnetic field at the centre of the BEC chamber is actively stabilised to a nearly uniform field of $B \approx 0.5(\hat{x} + \hat{z})/\sqrt{2}$ G (see Fig. 5.1 for the coordinate system) by the nullerometer detailed in Section 2.3. This is the reference magnetic field that we wish to map out with our proposed magnetometry technique.

The atomic ensemble used is an s -wave scattering halo created in a collision of two BECs, which has been theoretically investigated for applications to quantum metrology in [178], and pairwise entanglement was experimentally verified in this thesis [101]. Using a stimulated Raman transition to impart a coherent momentum kick, we split the BEC into two daughter condensates, which are initially overlapped then separate at velocities $\pm 60\hat{z}$ mm s $^{-1}$ in the centre of mass frame (see Fig. 5.1(a)). Binary atomic collisions then scatter atoms into counter-propagating pairs (opposite in momentum) with uniform probability amplitude in all directions, such that the momentum distribution of the scattering halo resembles a thin spherical shell. The pairs can be prepared in the symmetric spin Bell state $|\Psi^+\rangle$ by inducing a spin-flip via the Raman transition, and thus oppositely spin polarising the colliding condensates. The atomic spin states in our work are $m_J = \{+1, 0\}$, which we denote by the eigenstates of the $\hat{\sigma}_z$ Pauli operator $\{|\uparrow\rangle, |\downarrow\rangle\}$, respectively.

Approximately 416 ms after trap switch-off, the 3D position and m_J of individual atoms are measured (see Fig. 5.1(a)) using a combination of a Stern-Gerlach (SG) sequence and a single-atom sensitive detector (see 2.3.4 for details). This far-field distribution of atoms can be used to reconstruct the spatial distribution at an intermediate point in its trajectory using a simple geometric argument illustrated previously. Recall that the reconstructed field-of-view of the interrogated region corresponds to the volume of the scattering halo (thin spherical shell) at that point of expansion, while the spatial resolution is ultimately limited by the corresponding width of the collision source in each dimension.

For EBMG we begin with a collision between $|\uparrow\rangle$ and $|\downarrow\rangle$ states to scatter pairs into the Bell entangled state $|\Psi^+\rangle$ [178, 101]. Recall from Section 2.2.2 that a pair

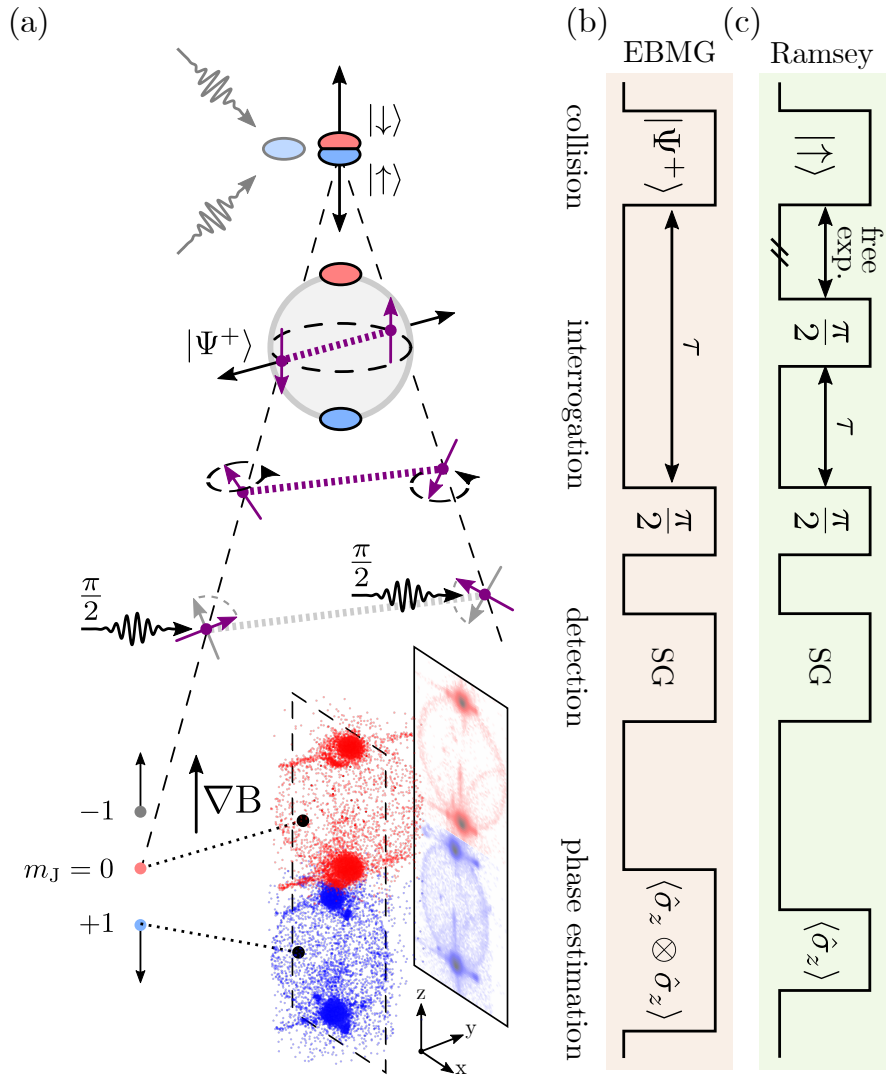


Figure 5.1: (a) Experimental schematic for entanglement-based 3D magnetic gradiometry. Raman beams (wavy arrows) induce a collision between $|\uparrow\rangle$ and $|\downarrow\rangle$ -polarised (blue/red) BECs. (Note the Raman beams can be tuned to induce a $|\uparrow\rangle$ -polarised collision for 3D magnetic field tomography shown in (c)). Pairs of atoms (purple) scatter back-to-back as $|\Psi^+\rangle$ and form a scattering halo (grey sphere). Each atom undergoes Larmor precession based on its local magnetic field. The phase evolution of the entangled pairs depends only on the difference in the magnetic field across the atoms, and can be estimated from the pairwise spin correlation properties after a $\pi/2$ -pulse. A Stern-Gerlach sequence spatially separates the Zeeman sublevels, after which individual atoms' spin and 3D position are detected in the far-field. (b) Experimental sequence for EBMG. (c) Experimental sequence for a 3D magnetic field tomography. See main text for details.

of counter-propagating modes will actually be a superposition of the unoccupied vacuum, a single entangled pair, as well as higher numbers of the pairs [178], analogous to the two-mode squeezed vacuum in quantum optics. Two-body correlations in the scattering halo were experimentally determined [101], and theoretically investigated [178] for applications to quantum metrology, and an agreement between the theory and experiments for higher order correlations was found in [112], although there was no spin degree of freedom in the latter. We note that sensitivity beyond SQL has been demonstrated by directly utilising such number fluctuations in twin Fock states of atomic ensembles [216], but this effect is negligible to the scattering halo which generally operates in the spontaneous regime with average mode occupancy well below unity.

As the entangled pairs separate, they oscillate coherently between the Bell states $|\Psi^+\rangle$ and $|\Psi^-\rangle$ at the difference in Larmor frequencies of each atom $\delta\omega = \gamma\delta B$ (which can be time dependent), where $\gamma \approx 2.8 \text{ MHz G}^{-1}$ is the gyromagnetic ratio of He*, and δB is the difference in B between the entangled atoms' locations. Therefore the pair's dynamics are independent of any symmetric perturbation to the system, but only to the asymmetric component, such as the difference in magnetic field experienced by each atom in the pair. We characterise the pair by the Bell phase Φ , such that after some time τ following the collision the pair is given by

$$|\Psi(\tau)\rangle = \cos \Phi(\tau) |\Psi^+\rangle + i \sin \Phi(\tau) |\Psi^-\rangle. \quad (5.8)$$

The Bell phase then evolves according to $\Phi(\tau) = \gamma/2 \int_0^\tau \delta B(\tau') d\tau'$ and is fully determined by the magnetic field $B(\mathbf{r})$ and each atom's trajectory $\mathbf{r}_i(t)$. Therefore, pairs scattered along different directions will undergo different time evolution, such that the entire scattering halo interrogates the 3D spatial variation in the magnetic field.

For a pair of atoms in a superposition of Bell states as in (5.8), Φ can be estimated by the correlation of their spins projected in a complementary basis to $\hat{\sigma}_z$, such as $\hat{\sigma}_x$. In our experiment the change in basis is effected by a $\pi/2$ -pulse using separate Raman beams, which act independently on each atom's spin according to $|\uparrow\rangle \mapsto (|\uparrow\rangle + |\downarrow\rangle)/\sqrt{2}$, and $|\downarrow\rangle \mapsto (-|\uparrow\rangle + |\downarrow\rangle)/\sqrt{2}$. The co-propagating Raman beam geometry used for the spin rotation ensures that the atoms' momenta are unaffected by the two-photon recoil [101]. Under the $\pi/2$ -pulse, the singlet is invariant $|\Psi^-\rangle \mapsto (|\uparrow\downarrow\rangle - |\downarrow\uparrow\rangle)/\sqrt{2}$ and remains perfectly anti-correlated, whereas the triplet becomes $|\Psi^+\rangle \mapsto (|\uparrow\uparrow\rangle - |\downarrow\downarrow\rangle)/\sqrt{2}$ and thus perfectly correlated in spin. Observe that the rotated Bell states are then distinguished by the spin correlator $(\hat{\sigma}_z \otimes \hat{\sigma}_z) |\Psi^\pm\rangle_{\pi/2} = (\pm 1) |\Psi^\pm\rangle_{\pi/2}$, where the subscript indicates that a $\pi/2$ -pulse has been applied to the state. The pairwise correlator on the state (5.8) after the $\pi/2$ -pulse therefore reveals the Bell phase, given by

$$\begin{aligned} \langle \hat{\sigma}_z \otimes \hat{\sigma}_z \rangle_{\pi/2} &= +1 \cdot \cos^2 \Phi - 1 \cdot \sin^2 \Phi \\ &= \cos 2\Phi. \end{aligned} \quad (5.9)$$

In general single pair detection events can only be guaranteed by post-selection on a

near perfect single atom detector, which also wastes useful information from culled and even undetected events. Below we introduce a mode occupation normalised measurement to incorporate all atom number fluctuations by deriving the above idealised pair correlation from generalised correlations in the collective spin projections (difference in the number of atoms with spin $|\uparrow\rangle$ and $|\downarrow\rangle$) between the counter-propagating modes.

5.3.2 Generalised collective spin correlation

From (5.9) we found that the Bell phase of a single two-qubit state in a superposition of $|\Psi^+\rangle$ and $|\Psi^-\rangle$ can be determined based on the pairs' spin correlation measured in a complementary basis such as $\hat{\sigma}_x$. In this section, we explain the method used to evaluate a single entangled pair's correlation function accounting for variations in the number of pairs in the same mode of the scattering halo. This method allows faster data acquisition by using a brighter pair source.

The collision of oppositely polarised BECs has been treated in the Bogoliubov approximation to investigate usefulness of the correlated pairs scattered back-to-back in the scattering halo for the violation of Bell inequality [178]. This physics is analogous to spontaneous four-wave mixing in quantum optics, as evident in the collision Hamiltonian for the initially empty modes in the scattering halo $\hat{H}_{\text{col}} \sim (\hat{a}_A^\dagger \hat{b}_B^\dagger + \hat{a}_B^\dagger \hat{b}_A^\dagger) + \text{h.c.}$ (each term is accompanied with a quadratic term of the classical condensate field which gives a density squared dependence in coupling strength but is omitted here for simplicity), where \hat{a}_i and \hat{b}_i are the annihilation operators for the diametrically opposite scattering modes A and B with spin- i , respectively, satisfying the canonical commutation relations $[\hat{a}_i, \hat{a}_j^\dagger] = [\hat{b}_i, \hat{b}_j^\dagger] = \delta_{i,j}$ and $[\hat{a}_i, \hat{a}_j] = [\hat{b}_i, \hat{b}_j] = [\hat{a}_i, \hat{b}_j] = [\hat{a}_i, \hat{b}_j^\dagger] = 0$. The scattered state into the counter-propagating modes is then given by

$$|\zeta\rangle = \exp\left(\zeta(\hat{a}_A^\dagger \hat{b}_B^\dagger + \hat{a}_B^\dagger \hat{b}_A^\dagger) - \text{h.c.}\right) |0\rangle = c_0 |0\rangle + c_1 (|\uparrow_A \downarrow_B\rangle + |\downarrow_A \uparrow_B\rangle) + \dots \text{(multiple pairs)}, \quad (5.10)$$

and completely characterised by the squeezing parameter ζ , or correspondingly the average mode occupancy $\bar{n} = \langle \hat{n}_i^A \rangle = \langle \hat{a}_i^\dagger \hat{a}_i \rangle = \sinh^2 |\zeta|$ (similarly at B due to symmetry).

In the general case for an arbitrary number of atoms scattered into back-to-back locations on the halo, let us extend the idealised expression (5.9) by summing the spin-1/2 operators $\vec{\alpha}$ for individual atoms, corresponding to the generalised angular momentum operators and total atom number operators at A (B follows similarly),

given by

$$\hat{J}_x^A = \frac{1}{2} (\hat{a}_\uparrow^\dagger \hat{a}_\downarrow + \hat{a}_\downarrow^\dagger \hat{a}_\uparrow) \quad (5.11a)$$

$$\hat{J}_y^A = \frac{1}{2i} (\hat{a}_\uparrow^\dagger \hat{a}_\downarrow - \hat{a}_\downarrow^\dagger \hat{a}_\uparrow) \quad (5.11b)$$

$$\hat{J}_z^A = \frac{1}{2} (\hat{n}_\uparrow^A - \hat{n}_\downarrow^A) \quad (5.11c)$$

$$\hat{N}^A = \hat{n}_\uparrow^A + \hat{n}_\downarrow^A. \quad (5.11d)$$

Then the Raman pulse applying independent local rotations on each atom at $l \in \{A, B\}$ is given by the collective rotation $\hat{R}_y^l(\theta) = \exp(-i\theta \hat{J}_y^l)$, and the unitary time-evolution operator from the EBMG Hamiltonian $\hat{H} = \hbar\omega^A \hat{J}_z^A + \hbar\omega^B \hat{J}_z^B$ is given by $\hat{U}(t) = \exp(-i\omega^A t \hat{J}_z^A) \exp(-i\omega^B t \hat{J}_z^B)$. The generalised correlation function between two regions A and B for the many-body system is then defined

$$E(\theta, \phi) = \frac{\langle \hat{J}_z^A \hat{J}_z^B \rangle_{\theta, \phi}}{\langle \frac{1}{2} \hat{N}^A \frac{1}{2} \hat{N}^B \rangle_{\theta, \phi}}, \quad (5.12)$$

where the subscript indicates that the state is rotated by angles θ, ϕ at A, B , respectively.

We measure the correlation after a $\pi/2$ -rotation to all atoms, given explicitly by

$$\begin{aligned} E(\pi/2, \pi/2) &= \frac{\langle \zeta | \hat{U}^\dagger(t) \hat{J}_x^A \hat{J}_x^B \hat{U}(t) | \zeta \rangle}{\langle \frac{1}{2} \hat{N}(A) \frac{1}{2} \hat{N}(B) \rangle} \\ &= \frac{1 + 1/\bar{n}}{3 + 1/\bar{n}} \cos(\omega^A - \omega^B)t. \end{aligned} \quad (5.13)$$

Observe that the generalised correlation function has exactly the same dependence on time-evolution as the ideal pair treatment (5.9), and the contribution from multiple pairs (characterised by average mode occupation) is conveniently factorised into the visibility. Furthermore, \bar{n} can be self-consistently estimated from a spin-unresolved back-to-back correlation measurement given by

$$G = \frac{\langle \hat{N}(\mathbf{k}) \hat{N}(-\mathbf{k}) \rangle}{\langle \hat{N}(\mathbf{k}) \rangle \langle \hat{N}(-\mathbf{k}) \rangle} = \frac{1}{2}(3 + 1/\bar{n}), \quad (5.14)$$

which is a conserved quantity under both time evolution and rotation since $[\hat{N}^l, \hat{J}_i^l] = 0$. We therefore find that the contribution of higher number of pairs on the collective correlation of the pair source (i.e. the two-mode squeezed vacuum state) is a reduction by a correlation-dependent factor on the correlation for a single entangled pair (see (5.9)) given explicitly by

$$\langle \hat{\sigma}_x \cdot \hat{\sigma}_x \rangle = (1 - 1/G)^{-1} E(\pi/2, \pi/2). \quad (5.15)$$

5.3.3 Scattering angle dependence in pairwise correlations

In order to determine the scattering angle or spatially resolved pairwise correlations, and thus magnetic field gradients, the integration volume used in our original definition of the back-to-back second order correlation function Eq. (4.17) must be localised around a specific region in the scattering halo. We introduce the localised two-particle correlation function across back-to-back pairs in \mathbf{k} -space

$$g_{ij}^{(2)}(\mathbf{q}) = \frac{\sum_{\mathbf{k} \in \delta V} \langle \hat{n}_{\mathbf{k},i} \hat{n}_{-\mathbf{k},j} \rangle_{\pi/2}}{\sum_{\mathbf{k} \in \delta V} \langle \hat{n}_{\mathbf{k},i} \rangle_{\pi/2} \langle \hat{n}_{-\mathbf{k},j} \rangle_{\pi/2}}, \quad (5.16)$$

where the localised integration volume δV around \mathbf{q} is chosen for data analysis as follows. Following our analysis of the uncertainty in the atom's trajectory at the interrogation region, we used a *double-cone* bin oriented along $\pm\mathbf{q}$ as δV , with half-cone angle $\alpha = \pi/10$ chosen so that the bin size at interrogation is equal to the near-field spatial resolution from Eq. 5.7(b). This corresponds to an angular bin over the 3D sphere that captures all atoms which scatter approximately along $\pm\mathbf{q}$ (parallel and anti-parallel) with relative angle below α .

Figure 5.2 shows the distribution of $g^{(2)}$ measured for various τ , where we clearly observe the scattering angle dependent time-evolution. Figures 5.2(a-c) reveal that shortly after their creation ($\tau = 0.8$ ms), atom pairs are mostly spin-correlated in the $\hat{\sigma}_x$ -basis, independent of their scattering angle, verifying our claim that all pairs are prepared approximately in $|\Psi^+\rangle$ when they scatter. This result was exploited in the previous chapter in the demonstration of EPR-steering, by extension the entire entangled scattering halo could be used for parallel realisations of a Bell test. At longer evolution times we observe a strong scattering angle dependent evolution between $|\Psi^\pm\rangle$ states (see Figs. 5.2(d-i)), such that by $\tau = 1.7$ ms distinct regions are occupied almost purely by either $|\Psi^+\rangle$ or $|\Psi^-\rangle$ (see Fig. 5.2(i)).

5.3.4 Entanglement-based 3D magnetic gradiometry

Figure 5.3(a) shows the observed time-evolution of the pairwise correlation at three representative locations on the scattering halo (using bins of half-cone angle $\approx 20^\circ$), and clearly shows the large range of dynamics along different scattering angles. The earliest time we have applied the $\pi/2$ -pulse to the entangled halo is 0.8 ms after the collision sequence (see Fig. 5.1(b)), which provides sufficient time for the BECs to fully separate, thus ensuring that no more pairs are scattered into the halo after the $\pi/2$ -pulse. The pairs remain close to $|\Psi^+\rangle$ for short times after the collision ($\tau \lesssim 1$ ms) regardless of their scattering angle, since there is insufficient spatial separation between the pairs, and thus relatively small differences in magnetic field. As the halo expands further, we begin to observe a gradually increasing scattering angle-dependent evolution of the Bell states, such that at $\tau = 1.7$ ms the halo simultaneously contains regions of almost stationary $|\Psi^+\rangle$ states (\circ -marker), as well as those which have almost fully evolved to the orthogonal state $|\Psi^-\rangle$ (\times -marker).

Since the interrogation region is small and well isolated from nearby current

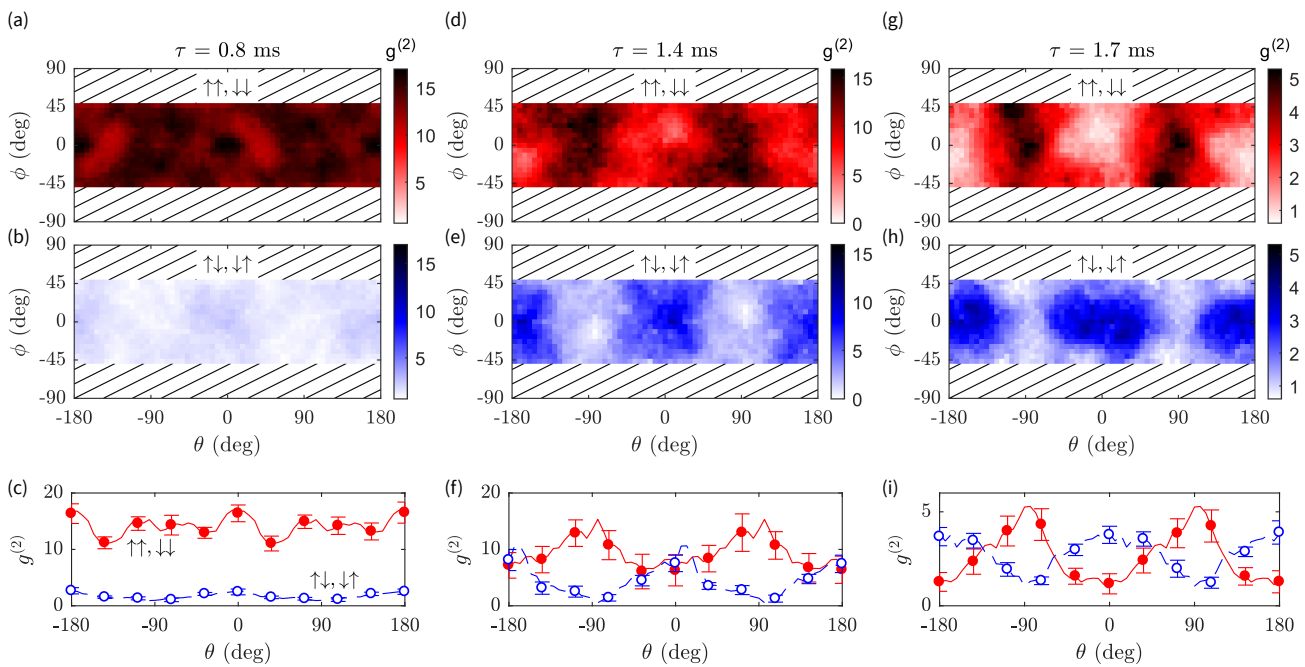


Figure 5.2: Localised second order correlation function across back-to-back momentum pairs in the scattering halo. (a) Spin correlated configuration. (b) Spin anti-correlated configuration. (c) Comparison of $g^{(2)}$ around the equator ($\phi = 0$) for correlated (red solid line) and anti-correlated configurations (blue dashed line). (a–c) are evaluated $\tau = 0.8 \text{ ms}$ after the collision pulse. (d–f) and (g–i) are similar to (a–c), for $\tau = 1.4 \text{ ms}$ and 1.7 ms , respectively. Error bars indicate a 1σ standard error in the mean estimated from bootstrapping.

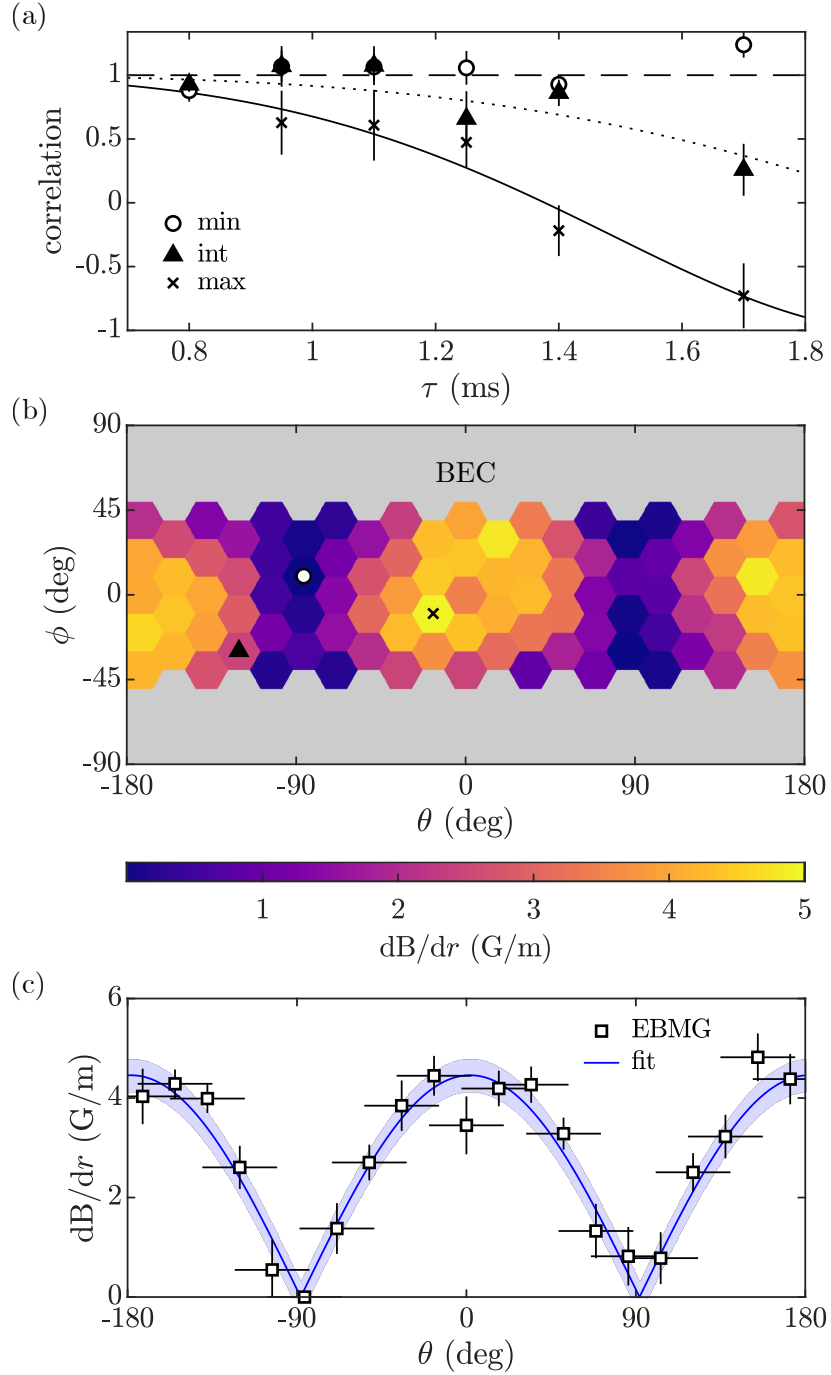


Figure 5.3: Entanglement-based 3D magnetic gradiometry. (a) Time evolution of pairwise correlation $\langle \hat{\sigma}_z \otimes \hat{\sigma}_z \rangle_{\pi/2}$ along selected scattering directions (locations indicated in (b)) and fitted models (lines). (b) Spatial distribution of dB/dr reconstructed on the scattering halo. The regions near BECs (grey) contain uncorrelated atoms, and are ignored in the data analysis. (c) Comparison of dB/dr between the measured data from entanglement-based 3D magnetic gradiometry (markers) and the fitted model of the magnetic field (line) taken around the equator. All vertical error bars and shaded regions indicate a standard error in the mean. Horizontal error bars in (c) indicate the angular size of bins.

sources, we approximate the magnetic field to first order in position around the point of collision \mathbf{r}_0 , such that $B(\mathbf{r}) = B_0 + \nabla B \cdot \mathbf{r}' + \mathcal{O}(\mathbf{r}'^2)$, where $\mathbf{r}' = \mathbf{r} - \mathbf{r}_0$. Then, an entangled pair in Eq. (5.8) counter-propagating at velocities $\pm \mathbf{v}_r$ in the centre-of-momentum frame has a Bell phase which evolves according to $d\Phi/dt = (\gamma/2)\nabla B \cdot (2\mathbf{v}_r t)$, unaffected by the free-falling frame. In terms of the gradient of magnetic field strength along the scattering axis $dB/dr = \nabla B \cdot \mathbf{v}_r / |\mathbf{v}_r|$, this gives

$$\Phi(\tau) = \frac{\gamma v_r}{2} \frac{dB}{dr} \tau^2. \quad (5.17)$$

Note that the correlation measurement (5.9) cannot reveal the sign of dB/dr , and all gradient measurements henceforth reported will be their absolute value. The above model gives an excellent fit to the observed correlation dynamics as seen in Fig. 5.3(a). The quadratic dependence of Φ on τ also qualitatively explains the transition from almost stationary states at $|\Psi^+\rangle$ regardless of the scattering angle at the start of expansion, to the diverging behaviour at later times.

Figure 5.3(b) shows the reconstructed spatial distribution of dB/dr obtained by fitting the single free parameter model, in the equirectangular projection where θ (ϕ) is the azimuthal (elevation) angle in the scattering halo-centred coordinate system. By nature of our metrology scheme, we must consider both the statistical uncertainty from a single bin, and its variability over all observed angles. Roughly speaking, the first quantity corresponds to the spatially-resolved measurement uncertainty, whereas the second reveals how spatially uniform the method is. Therefore we summarise the measurement uncertainty as a spatial-average of statistical uncertainties from individual binning regions, given by $\Delta(dB/dr) = 0.4(1) \text{ G m}^{-1}$, where the quantity in parenthesis indicates the standard deviation over the spatial distribution. The observed uncertainty from EBMG is in a reasonable agreement to the theoretical prediction (phase uncertainty $\Delta\Phi = 1/\sqrt{2N\eta^2 n}$ to Eq. (5.17), where $\bar{N} \approx 22(8)$ is the average number of atoms in a double-cone region, $\bar{\tau} \approx 1.1(2) \text{ ms}$ the average interrogation time, and $n = 7540$ the number of experiments) given by $\Delta(dB/dr) = 0.16(8) \text{ G m}^{-1}$. The reconstructed spatial distribution in Fig. 5.3(b) is consistent with our model of a uniform gradient across the halo which gives $dB/dr = |\nabla B| \cos \beta$, where β is the angle between the principal direction of the magnetic field gradient and the scattering direction. The fitted first order approximation of the magnetic field to the reconstructed data in Fig. 5.3(b) gives $\nabla B = 4.5(1)\hat{x} + 0.2(1)\hat{y} + 0.4(1)\hat{z} \text{ G m}^{-1}$, up to a flip in the sign (direction) of the vector. An independent estimation using a commercial magnetometer placed $\pm 100\hat{y} \text{ mm}$ around the interrogation region supports this result yielding $(\nabla B)_y = 0.4(2) \text{ G m}^{-1}$. We cannot make a direct comparison between these results however, since the length scales of the two methods differ by over 3 orders of magnitude. Indeed, estimating field gradients at 0.1 mm scale by a two-point absolute field measurement presents additional challenges to the spatial resolution of the magnetometer, as well as the precision of the sensor positioning system.

Fortunately our EBMG result offers a simple self-consistency check. The observed

distribution of magnetic field gradient in Fig. 5.3b is indeed maximised along the x -axis which agrees with the direction of the fitted gradient vector ∇B , given above, and steadily decreases away to a sharp minimum region around the perpendicular directions, as expected from the above cosine behaviour of gradients in a scalar field with first-order non-uniformity. Figure 5.3(c) clearly shows that the spatial distribution of dB/dr probed by the entanglement-based scheme is in excellent agreement with the simple model of an inhomogeneous magnetic field expanded to first order. The observed consistency validates the initial approximation used to estimate dB/dr from the correlation dynamics seen in Fig. 5.3(a).

In summary of this proof-of-principle demonstration, we note that EBMG provides a way to map field gradients decoupled from the absolute magnitude of the field. Higher order field gradients, neglected in our simple proof-of-concept demonstration, can be gradually incorporated by interrogating the scattering halo at finer intervals of its expansion, to reduce integration effects. It is also not restricted to sensing symmetrically around a particular point, since any field gradient at an arbitrary location in space could in principle be measured by displacing the point of collision accordingly.

5.4 3D magnetic field tomography

In the previous section, we discussed how the pairwise entanglement in the scattering halo can be a useful resource in probing spatial variations in the magnetic field. However when the absolute magnitude of the field is to be estimated, the claimed advantage of common-mode rejection by EBMG becomes a serious obstacle. Here we introduce a metrology scheme using a spin-polarised scattering halo to perform 3D magnetic field tomography (i.e. to measure the 3D distribution of absolute magnetic field) which complements EBMG by a simple reprogramming of the Raman pulse sequence.

5.4.1 Methods and concept

The proposed scheme to achieve 3D magnetic field tomography is based on standard Ramsey interferometry [25], implemented on the scattering halo at different times during its free-expansion (see Fig. 5.1(c)), such that the 3D magnetic field distribution is reconstructed in slices of spherical shells of variable radii.

In this conceptual demonstration of 3D magnetic field tomography, we let a $|\uparrow\rangle$ -scattering halo expand freely for 3 ms after a $|\uparrow\rangle$ -polarised collision, at which time the halo diameter is $D \approx 360 \mu\text{m}$, when Ramsey interferometry – two $\pi/2$ -pulses with a delay in between (τ) – is applied (see Fig. 5.1(c)). During the interrogation period τ , a relative phase accumulates between the $|\uparrow\rangle/|\downarrow\rangle$ components at the local Larmor frequency. The second $\pi/2$ -pulse maps the interferometric phase to the normalised polarisation such that $(n_\uparrow - n_\downarrow)/(n_\uparrow + n_\downarrow) \sim \cos \gamma B \tau$, where $n_{\uparrow/\downarrow}$ is the number of atoms with spin- \uparrow/\downarrow , respectively. The magnetic field distribution over the scattering

halo is then reconstructed from the oscillation frequency of this polarisation at each point on the sphere.

5.4.2 Experimental results

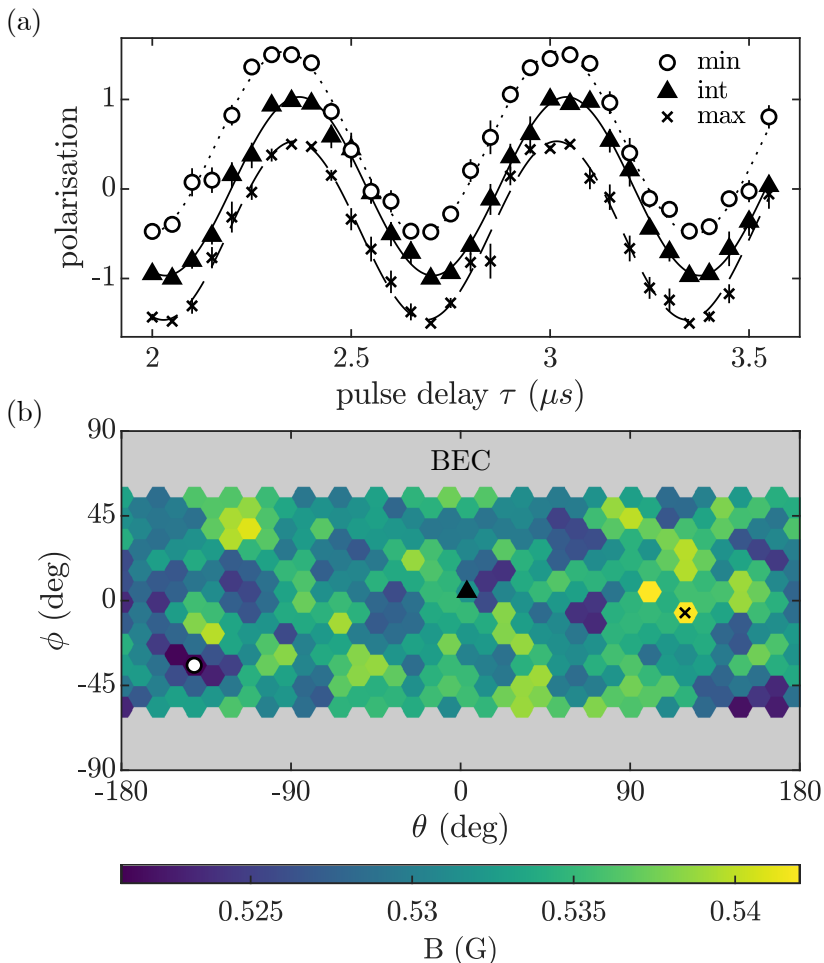


Figure 5.4: 3D magnetic field tomography. (a) Normalised polarisation P (markers offset vertically for clarity) and fitted Ramsey signal (lines) for selected regions on the scattering halo (locations indicated in (b)). The error bars indicate a standard error in the mean. (b) Spatial distribution of the measured magnetic field B on the scattering halo. The regions near BECs (grey) are affected by detector saturation, and ignored from data analysis.

Figure 5.4(a) shows the observed Ramsey signal at different locations on the scattering halo corresponding to where the maximum, minimum, and an intermediate value of magnetic fields were observed. 10 shots were taken at each interrogation time τ uniformly spaced between 2 μs and 3.55 μs , with a single-shot average of

≈ 68 atoms scattered into an individual conical bin (half-cone angle of 11° , which is smaller than that from EBMG since the halos have evolved to different sizes at the interrogation sequence), and ≈ 7200 atoms in the whole scattering halo, accounting for the detector efficiency. Using the individual spatially-resolved Ramsey signals around the halo, we reconstruct the magnetic field $B(\mathbf{r})$ over the scattering halo at the interrogation time. The projected spherical distribution is shown in Fig. 5.4(b), where the corresponding halo diameter is $\approx 360 \mu\text{m}$. The grey areas in Fig. 5.4(b) correspond to excluded regions of the scattering halo near the BECs ($|\phi| > 60^\circ$), which cause the detector to saturate. The average measurement uncertainty for an individual bin (pixel) was $\Delta B = 3.2(2) \text{ mG}$ (as before, the value in parenthesis indicates the standard deviation over the scattering halo), while the overall image histogram around the sphere is well described by a Gaussian distribution with a mean of 0.532 G and a standard deviation of $\approx 5 \text{ mG}$. An independent measurement of the magnetic field, based on the Zeeman shift to the two-photon Raman transition [152], yields $0.53(1) \text{ G}$, in good agreement with this result. Since in this demonstration the observed spatial variation is comparable to the measurement uncertainty of a single bin, we conclude that the actively stabilised magnetic field inside our vacuum chamber is uniform at the level of our noise floor.

We may compare the above result against that of EBMG, since the field gradient across the halo can be determined based on the positions of the interrogated regions (see Section 5.2.2). The Ramsey demonstration then yields an uncertainty in the magnetic field gradient of $\approx 10 \text{ G m}^{-1}$, accounting for the errors propagated in evaluating the finite difference $\delta B / \delta r$, compared to the EBMG sensitivity 0.4 G m^{-1} . Recall the magnitude of magnetic field gradient present in our experiment at this length scale was determined from EBMG to be $\approx 5 \text{ G m}^{-1}$. Therefore the poor signal to noise ratio of $\approx 1/2$ explains the nondiscrimination of spatial features by our demonstration of magnetic field tomography (see Fig. 5.4(b)).

Some key technical challenges can be addressed to improve the metrological performance demonstrated here, such as by increasing the atom number N , detector efficiency η , and interrogation time τ , based on the SQL of Larmor precession-based magnetometers $\Delta B = 1/\gamma\sqrt{N}\tau$ [217], and from a more efficient sampling strategy of τ [218]. We note that the theoretical uncertainty in the magnetic field, corresponding to the SQL phase uncertainty, from our experimental parameters for a single pixel is $\Delta B = 2.7 \text{ mG}$, and is in an excellent agreement with the observed uncertainty from the experiment.

5.5 Conclusion

Here we have demonstrated two complementary quantum metrology schemes with an ultracold atomic scattering halo where the free-expansion dynamics of the ensemble was utilised for the novel 3D spatial reconstruction of the magnetic field and its gradient. This marks the beginning of investigations utilising pairs of entangled atoms for non-classical tasks. Our proof-of-principle demonstration of magnetic gra-

diometry with freely propagating atomic Bell states may be extended to useful applications such as for quantum tests of general relativity [73] and for the demonstration of quantum nonlocality with massive particles [70, 101].

Conclusions and Outlook

6.1 Conclusions

In conclusion, this thesis presented an investigation into the nonlocal correlations between atoms arising from their collision. An experimental demonstration verified that such a simple event produces entanglement, the seed for quantum technologies and open problems in quantum physics. As a proof of principle application, we were able to demonstrate the sensing of magnetic field gradient based on entanglement. There remain a wealth of exciting challenges ahead in understanding and engineering entanglement, and we provide a few relevant for cold collisions below.

6.2 The Bell test and loopholes

Bell tests, from the stringent demonstration of nonlocality, are the experimental benchmark according to which a physical platform and its operation may be trusted to be quantum mechanical. As such, it is the basis for many device-independent (DI) quantum information processing protocols such as the DI quantum key distribution, quantum teleportation, and the generation of genuinely random numbers [1].

Demonstrating the Bell test is also of interest to validating the maturity of a quantum platform since the protocol requires a set of elementary operations in quantum information processing, namely the two-qubit entangling operation, the single qubit rotation, and the readout [219]. The violation of Bell inequality has so far been demonstrated with photons [9, 10], hadrons [58, 60], trapped ions [220, 221], neutral atoms [11], nitrogen vacancy in diamond [8], superconducting qubits [64], spin qubits in silicon [219], and optomechanical system [222]. This list continues to grow as more physical systems are exquisitely controlled to exhibit quantum mechanical coherence. For a pair of neutral atoms, the Weinfurter group [11] realised a Bell test where two atoms in separate optical dipole traps were entangled indirectly via entanglement swapping over the fluorescent photons emitted by each atom.

The Bell test is the immediate extension to the experimental demonstration of EPR-steering reported in this thesis. This requires the evaluation of pairwise correlations over the four sets of measurement angles which must be independently configured for each of the atom pairs. Recall that in the experiment reported in this thesis,

every atom was interrogated with the same measurement angle, since the phase of the Raman beam determines the measurement angle, while the Raman beam itself was applied uniformly over the scattering halo. In order to generalise the experimental protocol to a Bell test, we envisage illuminating two halves of the scattering halo (hemispheres) separately by two independent, rectangular-shaped Raman beams, for instance. The extension to a Bell test is therefore reasonably straightforward.

In the future, addressing the loopholes in our experiment is crucial to the rigorous validation of the violation of local realism [7]. Indeed there lies the two important loopholes in the experiment conducted in this thesis: the locality loophole, whereby each particle could communicate information about their choice of measurement angle to the counterpart; the efficiency loophole, whereby seemingly nonlocal correlation arises from a biased subsample of experimental realisations due to detector inefficiencies.

6.3 Hyperentanglement

By the conservation of momentum at the collision, pairs of atoms in the scattering halo are entangled in momentum, as well as their spin. A long-awaited goal in atom optics is to demonstrate such momentum entanglement by way of a Bell test, which is planned in the future based on the scattering halos. A number of experimental and theoretical challenges are currently being addressed for the demonstration of a momentum Bell test with ultracold atoms.

For continuous variables such as the motional degrees of freedom, even a measurement of an entanglement witness, not to mention a Bell test, presents non-trivial experimental challenges, since any imperfections in real operations leads to coupling into a large number of modes and causes decoherence. A number of experiments have been proposed to test for motional entanglement of massive particles, with the recent experiment by Westbrook group [130] highlighting the experimental challenges involved in the endeavour. In particular, this work builds a first step in exploring the scattering halo-based motional Bell test proposed by Lewis-Swan and Kheruntsyan [70], mirroring a seminal Bell test in quantum optics with a pair of wavevector entangled photons [55].

A system entangled in more than one of its degrees of freedom, such as the scattering halo, is called hyperentangled [185]. Entanglement between particles in such additional degrees of freedom offers improvements in various quantum information processing tasks, such as quantum dense coding [223] and quantum teleportation [224]. Hyperentanglement becomes a necessary resource to utilise, especially when the number of particles is a limiting factor, for quantum technologies to maximally encode information onto every degree of freedom and simultaneously utilise advantages gained by quantum correlation. For a pair of photons, this requires entangling their polarisation, spatial mode, and time/energy, and has been experimentally demonstrated from parametric down-conversion [225].

6.4 A quantum test of general relativity

The most important unsolved puzzle in physics is arguably the unification of quantum mechanics, the formalism underlying the modern physics of fundamental particles and interactions, and general relativity, the theory of gravity as a geometry of space-time. One approach aims to quantise the theory of gravity, where much effort has been made to formulate aspects of general relativity fully quantum mechanically, and conduct precision experiments on existing quantum mechanical systems which may test the theory.

The equivalence principles, a prerequisite condition for general relativity containing the equivalence of free fall, when formulated in quantum theory predicts experimentally observable signatures [74]. Atom interferometers are among the promising candidates in the hunt for signatures of a quantum theory of gravity. Indeed cold atoms are already paving the way towards state-of-the-art gravimeters due to their strong coupling to gravity, environmental isolation, and mature coherent control techniques [75]. Interestingly, recent experiments have investigated the accuracy to which the equivalence principle holds for quantum mechanical systems prepared in a coherent superposition of its internal states [226].

A quantum test of the weak equivalence principle has recently been proposed based on an atom interferometry using mass entangled pairs of atoms [73]. A collision between ${}^4\text{He}^*$ and ${}^3\text{He}^*$ suffices to produce the required entangled state. The technical details required to realise this experiment is indeed evident in the first step towards achieving this: the production of a degenerate Fermi gas of ${}^3\text{He}^*$. This scheme is predicted to achieve precision of the weak equivalence principle at an accuracy of 10^{-7} for the entangled species of ${}^{85}\text{Rb}$ and ${}^{87}\text{Rb}$ atoms, in addition to which the large mass ratio between the isotopes of helium and its low mass allows a previously unexplored energy regime of the parameter space in the search for the violation of the quantum formulation of the equivalence principle.

Theory of stimulated Raman transition

Here we give a detailed theoretical treatment of stimulated Raman transition, in which we derive the main results stated in Section 2.3.3. Recall the atom-light system for stimulated Raman transition described in the preamble of Section 2.3.3 and schematically illustrated in Fig. 2.15. The system Hamiltonian for the stimulated Raman transition for the Λ system is given by

$$\hat{H} = \hat{\mathbf{p}}^2/2m + \hbar\omega_i^a |i\rangle\langle i| + [\hbar\Omega_l \exp(i(\mathbf{k}_l \cdot \hat{\mathbf{r}} - \omega_l t + \phi_l)) |3\rangle\langle l| + \text{h.c.}], \quad (\text{A.1})$$

where the Einstein summation convention is implied over $i = 1, 2, 3$ and $l = 1, 2$.

Notice in Eq. (A.1) that $\exp(i\mathbf{q} \cdot \hat{\mathbf{r}}/\hbar) = \int |\mathbf{p} + \mathbf{q}\rangle\langle \mathbf{p}| d\mathbf{p} \equiv \tilde{T}(\mathbf{q})$ is the translation operator in momentum space giving $\tilde{T}(\mathbf{q}) |\mathbf{p}\rangle = |\mathbf{p} + \mathbf{q}\rangle$ [97]. The system Hamiltonian is therefore closed in a family of 3-dimensional subspaces characterised by a single momentum \mathbf{p} denoted by the new basis

$$\{|1'\rangle, |2'\rangle, |3'\rangle\} = \{|1; \mathbf{p}\rangle, |2; \mathbf{p} + \hbar(\mathbf{k}_1 - \mathbf{k}_2)\rangle, |3; \mathbf{p} + \hbar\mathbf{k}_1\rangle\}.$$

(Note that the symbol \mathbf{p} used to select a particular instance of the closed-momentum family can be arbitrary and should not be confused to mean that the atom in Fig. 2.15 need to be prepared in a specific internal state.)

The Hamiltonian in this momentum-quantised subspace can be given explicitly by

$$\hat{H} = \begin{bmatrix} \hbar\omega_1^a + \frac{\mathbf{p}^2}{2m} & 0 & \hbar\Omega_1^* e^{-i\phi_1} e^{i\omega_1 t} \\ 0 & \hbar\omega_2^a + \frac{(\mathbf{p} + \hbar(\mathbf{k}_1 - \mathbf{k}_2))^2}{2m} & \hbar\Omega_2^* e^{-i\phi_2} e^{i\omega_2 t} \\ \hbar\Omega_1 e^{i\phi_1} e^{-i\omega_1 t} & \hbar\Omega_2 e^{i\phi_2} e^{-i\omega_2 t} & \hbar\omega_3^a + \frac{(\mathbf{p} + \hbar\mathbf{k}_1)^2}{2m} \end{bmatrix} \quad (\text{A.2})$$

which explicitly includes the recoil momentum from absorption/emission of a photon as part of the atom's kinetic energy.

This system is simplified in the rotating frame of the atom given by the unitary

transformation $U(t) = \exp(i\hat{\xi}t)$ where $\hat{\xi} = H'_{ii}/\hbar |i'\rangle\langle i'|$, and H'_{ij} are the matrix elements of the Hamiltonian in the momentum-quantised basis in Eq. A.2. (Under a time-dependent unitary transformation $U(t)$ the state and Hamiltonian transform according to $|\tilde{\psi}\rangle = U|\psi\rangle$ and $\tilde{H} = U\hat{H}U^\dagger + i\hbar\dot{U}U^\dagger$.) The rotating frame Hamiltonian is found to be

$$\tilde{H} = \hbar \begin{bmatrix} 0 & 0 & \Omega_1^* e^{-i\phi_1} e^{i\Delta t} \\ 0 & 0 & \Omega_2^* e^{-i\phi_2} e^{i(\Delta-\delta)t} \\ \Omega_1 e^{i\phi_1} e^{-i\Delta t} & \Omega_2 e^{i\phi_2} e^{-i(\Delta-\delta)t} & 0 \end{bmatrix} \quad (\text{A.3})$$

where

$$\Delta \equiv \omega_1 - (H'_{33} - H'_{11})/\hbar \quad (\text{A.4})$$

$$\delta \equiv (\omega_1 - \omega_2) - (H'_{22} - H'_{11})/\hbar \quad (\text{A.5})$$

are the detuning of the single-photon transition to the intermediate state ($|1'\rangle \leftrightarrow |3'\rangle$ by laser 1), and the stimulated two-photon transition between the lower lying states $|1'\rangle \leftrightarrow |2'\rangle$, respectively. A graphical annotation of the detunings are shown in Fig. 2.15. These two detunings play an important role in the dynamics but their discussion will be withheld until we can simplify Eq. (A.3) to make their role explicit.

The key point of Raman transitions is that the excited state can be completely depopulated while Rabi oscillations are induced between the two lower states for the qubit abstraction, in a process called adiabatic elimination. It turns out that the criterion for adiabatic elimination is when the single-photon detuning is much greater than the individual single-photon Rabi frequencies, as well as the detuning of the two-photon transition (i.e. when $|\Delta| \gg |\Omega_1|, |\Omega_2|, |\delta|$), as I present below. Indeed this regime is easily realised in atomic systems. For metastable helium, the lower lying states can be the Zeeman sublevels at the RF scale, and the intermediate state the optically addressable larger orbital states, such as the 2^3P_J levels.

In the Schrodinger picture for the rotating frame, $|\psi(t)\rangle = \sum c_i(t) |\tilde{i}'\rangle$ (where $\{|\tilde{i}'\rangle\}$ is the basis for the matrix representation shown in Eq. (A.3)) evolves according to

$$\dot{c}_1 = -i\Omega_1^* e^{-i\phi_1} e^{i\Delta t} c_3 \quad (\text{A.6a})$$

$$\dot{c}_2 = -i\Omega_2^* e^{-i\phi_2} e^{i(\Delta-\delta)t} c_3 \quad (\text{A.6b})$$

$$\dot{c}_3 = -i\Omega_1 e^{i\phi_1} e^{-i\Delta t} c_1 - i\Omega_2 e^{i\phi_2} e^{-i(\Delta-\delta)t} c_2. \quad (\text{A.6c})$$

If we now assume c_1 and c_2 oscillate much more slowly with respect to c_3 , and $|\Delta| \gg |\Omega_1|, |\Omega_2|, |\delta|$, Eq. (A.6c) can be directly integrated by treating the slow evolving terms as constant [152], giving

$$c_3 \approx \frac{\Omega_1}{\Delta} e^{i\phi_1} e^{-i\Delta t} c_1 + \frac{\Omega_2}{\Delta} e^{i\phi_2} e^{-i(\Delta-\delta)t} c_2. \quad (\text{A.7})$$

(The errors incurred in this approximation require the aforementioned criteria, and

a rigorous treatment of the adiabatic elimination can be found in Ref. [227].)

Substituting Eq .(A.7) back into Eq .(A.6), the effective Hamiltonian reduces to the desired subspace spanned by $\{|\tilde{1}'\rangle, |\tilde{2}'\rangle\}$

$$\hat{H}_{\text{eff}} = \hbar \begin{bmatrix} \frac{|\Omega_1|^2}{\Delta} & \frac{\Omega_1^* \Omega_2}{\Delta} e^{i\phi} e^{i\delta t} \\ \frac{\Omega_1 \Omega_2^*}{\Delta} e^{-i\phi} e^{-i\delta t} & \frac{|\Omega_2|^2}{\Delta} \end{bmatrix} = \hbar \boldsymbol{\Omega}'(t) \cdot \hat{\sigma}, \quad (\text{A.8})$$

where $\phi = \phi_2 - \phi_1$ is the relative phase between the fields, $\hat{\sigma} = (\hat{\sigma}_x, \hat{\sigma}_y, \hat{\sigma}_z)$ is the Pauli matrix vector (such that $\hat{\sigma}_z = |\tilde{1}'\rangle\langle\tilde{1}'| - |\tilde{2}'\rangle\langle\tilde{2}'|$), and

$$\boldsymbol{\Omega}' = \left(\frac{|\Omega_1^* \Omega_2|}{\Delta} \cos(\delta t + \phi'), -\frac{|\Omega_1^* \Omega_2|}{\Delta} \sin(\delta t + \phi'), \frac{|\Omega_1|^2 - |\Omega_2|^2}{2\Delta} \right) \quad (\text{A.9})$$

is the torque vector of the Hamiltonian [228], where $\phi' = \phi + \arg(\Omega_1^* \Omega_2)$, and the term proportional to the identity is dropped in the last equality in Eq. (A.8). This driven two-state system has a simple solution, accompanied by a visual representation as a 3D vector on the Bloch sphere , as shown by Fig. 2.16(a). Observe that $\boldsymbol{\Omega}'$ rotates around the $-z$ -axis at frequency δ , which can be undone by the unitary transformation $U(t) = \exp[i(\delta t/2)\hat{\sigma}_z]$, giving the time-independent Hamiltonian $\tilde{H}_{\text{eff}} = \hbar \tilde{\boldsymbol{\Omega}}' \cdot \hat{\sigma}$, where

$$\tilde{\boldsymbol{\Omega}}' = \left(\frac{|\Omega_1^* \Omega_2|}{\Delta} \cos \phi', -\frac{|\Omega_1^* \Omega_2|}{\Delta} \sin \phi', \frac{|\Omega_1|^2 - |\Omega_2|^2}{2\Delta} - \frac{\delta}{2} \right). \quad (\text{A.10})$$

In this rotating frame, the atom represented as a Bloch vector rotates around $\tilde{\boldsymbol{\Omega}}'$ [154, 228]. The physics of stimulated Raman transitions is encapsulated in this characteristic torque vector (which we often call the rotation vector) given in Eq. (A.10), which we now analyse. The relative phase between the driving field determines the azimuthal angle of the rotation vector. The resonance condition of the Raman transition corresponds to when the rotation vector lies perpendicular to the z -axis.

The explicit form of δ is given by (from its definition Eq. (A.5) and the Hamiltonian elements from Eq. (A.2))

$$\begin{aligned} \delta &= (\omega_1 - \omega_2) - [(\omega_2^a - \omega_1^a) + ((\mathbf{p} + \hbar(\mathbf{k}_1 - \mathbf{k}_2))^2 - \mathbf{p}^2)] \\ &= (\omega_1 - \omega_2 - \omega_{21}) + \frac{\mathbf{p} \cdot (\mathbf{k}_1 - \mathbf{k}_2)}{m} + \frac{\hbar(\mathbf{k}_1 - \mathbf{k}_2)^2}{2m}. \end{aligned} \quad (\text{A.11})$$

The first term in Eq. (A.11) is the detuning between the energy of photons and the atom (the qubit states), the second term naturally introduces the Doppler shift due to the atom's motion in the lab frame, while the third term regards the change in kinetic energy for the two photon recoil. For the single-photon detuning Δ in Eq. (A.4), the Doppler shift and recoil energy terms are negligible fractions of the simple detuning between the single photon and the atom's optical transition, and can be approxi-

mated by

$$\Delta \approx \omega_1 - (\omega_3^a - \omega_1^a), \quad (\text{A.12})$$

which completes the derivation of characteristics parameters introduced in Section 2.3.3.

Notes on the ECL

B.1 Alignment procedure

This section gives details a step-by-step instruction on how to align the external-cavity laser (i.e. adjustment of the custom lens mount) for optimal performance, where the output power through the fibre is maximised.

B.1.1 Positioning the lens in XYZ degree of freedom

First, we give instructions on how to adjust the position of collimating lens in the 3 translational degrees of freedom (DOF).

The **Z axis** corresponds to the direction of free-space beam propagation. The lens position along the Z-axis is crucial in properly collimating the divergent free-space beam from the gainchip, so that the grating back-reflected light is well mode matched. A fine-pitched (0.5 mm pitch) screw on the commercial lens package (see yellow component in Fig. 3.2) is used to adjust the Z position. Note that the diffraction grating sub-assembly needs to be detached from the external-cavity block before adjusting the Z DOF of the lens. This step should be taken with care to avoid any damage to the diffraction grating.

The **XY plane** is the plane normal to the free-space beam propagation (Z axis). The collimation optics sub-assembly fixes on the laser head mount (see Fig. 3.2(b)), with a small amount of translational freedom (± 0.5 mm) in the XY plane, designed to compensate for the dimensional variability of the gainchip (0.1 mm). The XY position of the collimation optics is coarsely fixed by the three screws around the front face (see Fig. 3.2(b)). With some care, the X and Y DOFs of the collimation lens can be adjusted while the diffraction grating is mounted.

B.1.2 Aligning the collimation lens

The following procedure is ideally done once in the initial operation of the ECL, and should not need to be repeated in its lifetime:

1. **Initialise** the grating orientation and collimating lens to approximately their nominal configurations for the iterative procedure:

- Grating orientation: place in the mid-range of its motion.
 - Lens Z position: align by collimating the free-space beam from amplified spontaneous emission (ASE)¹. (Note: ASE beam is broader than the lasing mode)
 - Lens XY position: place in the mid-range of its motion.
2. **Back-couple the 1st diffraction order ($m = 1$) into the gain chip**, until the free-space output lasers, then maximise the output power by finer adjustments. (Note: Once the external-cavity is reasonably well aligned, the output power through the fibre will become measurable, and should be used for further optimisation.)
 3. **Adjust the Z position of the collimating lens.** Recommended increments should adapt from the coarsest 1/2-turn, to finer 1/32-turns as the optimum is reached.
 4. **Repeat from step 2** to maximise the output power, referring to Fig. 3.4 for the expected performance when the ECL is properly aligned.

In summary, a precise collimation of the free-space beam is critical to achieving the maximum output power. Around the optimal location of the collimating lens, the output power of the ECL is much more sensitive to displacements in Z degree of freedom (DOF), than in X and Y.

B.2 List of parts and instruments

Table B.1 provides the list of commercial and custom-built parts and instruments used in the (i) design, (ii) control, and (iii) diagnostic of the external-cavity gain chip laser system, including a brief description and identified by their manufacturer and product name. We note to the readers that any specified parts and manufacturers named here are solely for the purpose of clarity in description of the experimental apparatus.

¹No more than 200 mA of injection current is required for the alignment procedure.

Table B.1: List of parts, controllers, and miscellaneous instruments for the master laser system.

	Component	Description	Manufacturer	Product name
ECT parts	SAF gain chip module	$\lambda = 1060 \pm 150$ nm; 250 mW; PM fibre coupled output; internal TEC	Innolume	GM-1060-150-PM-250
	Collimation lens	AR (1064 nm), $f=8$ mm; NA=0.5	Thorlabs	C240TME-1064
	Diffraction grating	1200 /mm; 1 μm blaze	Thorlabs	GR13-1210
	Mirror mount	standard kinematic mirror mount; 100 TPI	Thorlabs	KMSS/M
	PZT	3.6 μm @ 150 V	Thorlabs	PA4FKW
	TEC	17 W; 15.4 V	European Thermodynamics	APH-127-10-25-S
	Thermistor	NTC; 10 k Ω ; 1% precision	Epcos	S861
Controllers	Fibre-coupled optical isolator	-50 dB; 300 mW	AFW Technologies	PISO-83-2-C-7-2-FB
	Current controller	200 mA; 15 MHz (BW); noise 18 nA rms (DC - 100 kHz)	RSPE Electronics Unit	upgraded from J697
	PZT driver	-30 to 150 V; 180 kHz (signal); noise 26 μV rms (1 μF)	PiezoDrive	PDu-150CL
	Temperature controller	—	ILX Lightwave	LDT-5100
	PI controller	—	custom-built	—
	Lock-in amplifier	100 kHz (BW)	SRS	SR510
	Fibre-coupled AOM	centre frequency 250 MHz; 50 MHz (BW)	Brimrose	TEM-250-50-10-2FP
	RF signal generator	35–4400 MHz; -70– +10 dBm out	RF-consultant	TPI-1002-A
Misc	RF amplifier	1–930 MHz; 1 mW in; 2 W max out	eBay seller	—
	Wavelength meter	700–1700 nm	Burleigh	WA-1100
	Scanning Fabry-Pérot cavity	—	custom-built	—
	Fast photodetector	12 GHz (BW); fiber optic	Newport	New Focus 1544
	Spectrum analyser	1.5 GHz (BW)	Rigol	DSA815-TG
	Fibre amplifier	1064–1083 nm; 1.0–15.0 mW in; 5W max out; free space output isolated	Nufern	NUA-1064-PB-0005-C2

Notes on correlations

C.1 Sum uncertainty relation for angular momentum

The below uncertainty relation result was first derived by Hoffman and Takeuchi in Ref. [229]. Consider a system with an angular momentum j and let \vec{J} be the angular momentum vector operators (ignoring factors of \hbar). The sum of uncertainties in the orthogonal directions give

$$(\Delta \hat{J}_x)^2 + (\Delta \hat{J}_y)^2 + (\Delta \hat{J}_z)^2 = \langle \hat{J}_x^2 + \hat{J}_y^2 + \hat{J}_z^2 \rangle - (\langle \hat{J}_x \rangle^2 + \langle \hat{J}_y \rangle^2 + \langle \hat{J}_z \rangle^2). \quad (\text{C.1})$$

The first term on the rhs of Eq. (C.1) is by definition $j(j+1)$, while the second term inside the bracket is $\leq j^2$ since the vector $\langle \hat{J}_i \rangle$ has a maximum length of j . Therefore, we have the uncertainty relation

$$(\Delta \hat{J}_x)^2 + (\Delta \hat{J}_y)^2 + (\Delta \hat{J}_z)^2 \geq j. \quad (\text{C.2})$$

Using $(\Delta \hat{J}_i)^2 \leq j^2$ there is another uncertainty relation based on a sum of only two terms

$$(\Delta \hat{J}_i)^2 + (\Delta \hat{J}_j)^2 \geq j - j^2, \quad (\text{C.3})$$

which is nontrivial for only $j = 1/2$.

For a general two level system Eq. (C.3) gives the uncertainty relation violated in the EPR-Bohm paradox

$$(\Delta \hat{\sigma}_i)^2 + (\Delta \hat{\sigma}_j)^2 \geq 1, \quad (\text{C.4})$$

for any two orthogonal directions i, j .

C.2 CHSH Bell inequality

Here we give a short derivation of the most famous Bell inequality first derived by Clauser, Horne, Shimony and Holt (CHSH) [38] for a two qubit system. The proof closely follows Bell's version in Ref. [230].

The correlation function for a LHV model is given by

$$E(\mathcal{A}, \mathcal{B}) = \sum_{a,b=\pm 1} \sum_{\lambda} ab P(a, b | \mathcal{A}, \mathcal{B}; \lambda) p_{\lambda} \quad (\text{C.5})$$

$$= \sum_{a,b=\pm 1} \sum_{\lambda} ab P(a | \mathcal{A}, \lambda) P(b | \mathcal{B}, \lambda) p_{\lambda} \quad (\text{C.6})$$

$$= \sum_{\lambda} a(\mathcal{A}, \lambda) b(\mathcal{B}, \lambda) p_{\lambda}, \quad (\text{C.7})$$

The first step to Eq. (C.6) is the factorisation based on the locality postulate discussed in Section 2.1.2. For the next step to Eq. (C.7), the LHV theory is assumed to be *deterministic* so that $P(m' | \mathcal{M}, \lambda) = \delta_{m', m(\lambda)} \in \{0, 1\}$ for the dichotomous outcomes $m' = \pm 1$, giving the λ -dependent outcome functions $a(\mathcal{A}, \lambda), b(\mathcal{B}, \lambda) = \pm 1$ ¹.

Consider the case when Alice measures \mathcal{A} , but Bob switches their measurement setting between \mathcal{B} and \mathcal{B}' . The difference in correlations observed by the two different measurement configurations can be algebraically rearranged by

$$E(\mathcal{A}, \mathcal{B}) - E(\mathcal{A}, \mathcal{B}') = \sum_{\lambda} [a(\mathcal{A}, \lambda) b(\mathcal{B}, \lambda) - a(\mathcal{A}, \lambda) b(\mathcal{B}', \lambda)] p_{\lambda} \quad (\text{C.8})$$

$$\begin{aligned} &= \sum_{\lambda} [a(\mathcal{A}, \lambda) b(\mathcal{B}, \lambda) (1 \pm a(\mathcal{A}', \lambda) b(\mathcal{B}', \lambda))] p_{\lambda} \\ &\quad - \sum_{\lambda} [a(\mathcal{A}, \lambda) b(\mathcal{B}', \lambda) (1 \pm a(\mathcal{A}', \lambda) b(\mathcal{B}, \lambda))] p_{\lambda}. \end{aligned} \quad (\text{C.9})$$

Since $|ab| \leq 1$ and the summands in the last expression is non-negative, we have

$$|E(\mathcal{A}, \mathcal{B}) - E(\mathcal{A}, \mathcal{B}')| \leq \sum_{\lambda} (1 \pm a(\mathcal{A}', \lambda) b(\mathcal{B}', \lambda)) p_{\lambda} - \sum_{\lambda} (1 \pm a(\mathcal{A}', \lambda) b(\mathcal{B}, \lambda)) p_{\lambda} \quad (\text{C.10})$$

$$= 2 \pm (E(\mathcal{A}', \mathcal{B}') + E(\mathcal{A}', \mathcal{B})), \quad (\text{C.11})$$

and finally the celebrated CHSH Bell inequality

$$|E(\mathcal{A}, \mathcal{B}) - E(\mathcal{A}, \mathcal{B}') + E(\mathcal{A}', \mathcal{B}') + E(\mathcal{A}', \mathcal{B})| \leq 2. \quad (\text{C.12})$$

Note that the appearance of the order of measurement settings, and therefore the location of the minus sign in Eq. (C.12), is arbitrary.

¹The following result holds for even *stochastic* LHV models [231], since one may represent any probabilistic distribution of outcomes as a deterministic LHV theory in a larger λ space.

C.3 Generalised bipartite correlation coefficient for many-body states

The correlation coefficient is given by definition from Eq. (4.15) by

$$E(\theta, \phi) = \frac{\langle \hat{J}_z^{(A)} \hat{J}_z^{(B)} \rangle_{\theta, \phi}}{\langle \hat{N}^{(A)} \hat{N}^{(B)} \rangle_{\theta, \phi}} \quad (\text{C.13})$$

$$= \frac{\langle (\hat{n}_{\uparrow}^{(A)} - \hat{n}_{\downarrow}^{(A)}) (\hat{n}_{\uparrow}^{(B)} - \hat{n}_{\downarrow}^{(B)}) \rangle_{\theta, \phi}}{\langle (\hat{n}_{\uparrow}^{(A)} + \hat{n}_{\downarrow}^{(A)}) (\hat{n}_{\uparrow}^{(B)} + \hat{n}_{\downarrow}^{(B)}) \rangle_{\theta, \phi}}. \quad (\text{C.14})$$

Therefore, it can be expanded in terms of products of number operators across the regions A/B

$$E = \frac{\langle \hat{n}_{\uparrow}^{(A)} \hat{n}_{\uparrow}^{(B)} \rangle + \langle \hat{n}_{\downarrow}^{(A)} \hat{n}_{\downarrow}^{(B)} \rangle - \langle \hat{n}_{\uparrow}^{(A)} \hat{n}_{\downarrow}^{(B)} \rangle - \langle \hat{n}_{\downarrow}^{(A)} \hat{n}_{\uparrow}^{(B)} \rangle}{\langle \hat{n}_{\uparrow}^{(A)} \hat{n}_{\uparrow}^{(B)} \rangle + \langle \hat{n}_{\downarrow}^{(A)} \hat{n}_{\downarrow}^{(B)} \rangle + \langle \hat{n}_{\uparrow}^{(A)} \hat{n}_{\downarrow}^{(B)} \rangle + \langle \hat{n}_{\downarrow}^{(A)} \hat{n}_{\uparrow}^{(B)} \rangle}, \quad (\text{C.15})$$

where for convenience the subscript (θ, ϕ) for labelling the general rotated state is assumed for all correlators. Since the density of the scattering halo is symmetric in momentum (*s*-wave scattering) and spin, $\bar{n} = \langle \hat{n}_m^{(\mathbf{k})} \rangle$ for all $m \in \{\uparrow, \downarrow\}$ and $\mathbf{k} \in V$, observe that each term in C.15 corresponds to a second-order correlation function

$$\langle \hat{n}_i^{(A)} \hat{n}_j^{(B)} \rangle = \bar{n}^2 g_{ij}^{(2)} \quad (\text{C.16})$$

Therefore, the general correlation coefficient $E(\theta, \phi)$ in C.15 can be written in terms of $g^{(2)}$ as

$$E(\theta, \phi) = \frac{g_{\uparrow\uparrow}^{(2)} + g_{\downarrow\downarrow}^{(2)} - g_{\uparrow\downarrow}^{(2)} - g_{\downarrow\uparrow}^{(2)}}{g_{\uparrow\uparrow}^{(2)} + g_{\downarrow\downarrow}^{(2)} + g_{\uparrow\downarrow}^{(2)} + g_{\downarrow\uparrow}^{(2)}}. \quad (\text{C.17})$$

C.4 LHV model supports EPR-steering correlation

Consider the Bell triplet

$$|\Psi^+\rangle = \frac{1}{\sqrt{2}} (|+\rangle^{(A)} \otimes |-\rangle^{(B)} + |-\rangle^{(A)} \otimes |+\rangle^{(B)}) \quad (\text{C.18})$$

and suppose that we measure the outcomes of the spins projected in $\{|+\rangle, |-\rangle\}$, the eigenbasis of σ_z , after rotating the spins by θ and ϕ for the particle at A and B , respectively, around \hat{y} -axis. Quantum mechanically, the coincidence rates when $\theta = \phi$ are given by

$$P_{++}(\theta, \theta) = P_{--}(\theta, \theta) = \frac{1}{2} \sin^2 \theta \quad (\text{C.19a})$$

$$P_{+-}(\theta, \theta) = P_{-+}(\theta, \theta) = \frac{1}{2} \cos^2 \theta \quad (\text{C.19b})$$

where for $\alpha, \beta \in \{+, -\}$ the term $P_{\alpha\beta}(\theta, \phi)$ is the coincidence rate for measuring the joint outcome α at A and β at B , when the rotation angles are configured to θ and ϕ , respectively. Then, the pair “correlator” predicted by quantum mechanics under a common rotation angle is

$$E(\theta, \theta) \equiv P_{++} - P_{+-} - P_{-+} + P_{--} = -\cos(2\theta) \quad (\text{C.20})$$

which is a distinct signature of $|\Psi^+\rangle$. I will demonstrate a simple local hidden variable (LHV) model of a pair source that reproduces the correlator in Equation C.20.

In the LHV theory, given a “complete” set of hidden variables denoted by $\lambda \in \Lambda$, all measurement outcome space-like separated must be completely determined by the configuration of the local measurement apparatus and the set of hidden variables describing the pair (plus local environment). For the relevant case of a pair of two-state system, this means that there exists a well-defined binary measurement outcome of each particle

$$O^{(i)}(\theta_i, \lambda) = \pm 1 \quad (\text{C.21})$$

where $i \in \{A, B\}$ denotes the arbitrarily separated measurement apparatus, θ_i the rotation configuration of measurement at i , and λ the hidden variable. Here of course, the outcomes ± 1 denote \pm , respectively. A general correlator is then given by

$$E(\theta, \phi) = \int_{\lambda \in \Lambda} O^{(A)}(\theta, \lambda) O^{(B)}(\phi, \lambda) \rho(\lambda) d\lambda \quad (\text{C.22})$$

where $\rho(\lambda)$ is the probability distribution of the hidden variable ².

Consider the following formulation

$$O^{(A)}(\theta, \lambda) = \begin{cases} +1 & : \lambda \in \Lambda_{++,\theta} \\ +1 & : \lambda \in \Lambda_{+-,\theta} \\ -1 & : \lambda \in \Lambda_{-+,\theta} \\ -1 & : \lambda \in \Lambda_{--, \theta} \end{cases} \quad (\text{C.23a})$$

$$O^{(B)}(\phi, \lambda) = \begin{cases} +1 & : \lambda \in \Lambda_{++,\phi} \\ -1 & : \lambda \in \Lambda_{+-,\phi} \\ +1 & : \lambda \in \Lambda_{-+,\phi} \\ -1 & : \lambda \in \Lambda_{--, \phi} \end{cases} \quad (\text{C.23b})$$

²A class of inequalities exist, which is satisfied by correlations arising from any local hidden variable theories, see for example Bell’s original proof [4], and the famous CHSH inequality [38]. If such an inequality can be violated by quantum mechanics, it is called a Bell inequality, named after Bell’s original proposal for an experiment that would demonstrate the validity of quantum mechanics and its incompatibility with local realism [8]. The “holy grail” is to realise an experiment to violate the Bell inequality, called the Bell test.

where for any given rotation angle ξ , the set of $\Lambda_{\alpha\beta,\xi}$ is a partition of Λ (our argument holds even if there is an empty subset). Thus $\Lambda_{\alpha\beta,\xi} \cap \Lambda_{\gamma\delta,\xi} = \emptyset$ unless $\alpha = \gamma$ and $\beta = \delta$, and $\bigcup_{\alpha,\beta=\pm 1} \Lambda_{\alpha\beta,\xi} = \Lambda$. Observe that the given formulation has an elegant property, such that the outcome of the particle at A (B) corresponds to the first (second) subscript of the partition subset defined by the local rotation angle, to which λ belongs to.

The construction of such partition to reproduce the common angle coincidence rates for the Bell triplet (see Eq. C.19), here denoted by \mathcal{P} to distinguish it from own outcome, is then a straightforward exercise. Let $\Lambda = [0, 1)$ and explicitly construct the partition as (see Fig. C.1)

$$\Lambda_{++,\xi} = [0, \mathcal{P}_{++}(\xi, \xi)) = \left[0, \frac{1}{2} \sin^2 \xi\right) \quad (\text{C.24a})$$

$$\Lambda_{+-,\xi} = \left[\frac{1}{2} \sin^2 \xi, \frac{1}{2} \sin^2 \xi + \mathcal{P}_{+-}(\xi, \xi)\right) = \left[\frac{1}{2} \sin^2 \xi, \frac{1}{2}\right) \quad (\text{C.24b})$$

$$\Lambda_{-+,\xi} = \left[\frac{1}{2}, \frac{1}{2} + \frac{1}{2} \cos^2 \xi\right) \quad (\text{C.24c})$$

$$\Lambda_{--, \xi} = \left[\frac{1}{2} + \frac{1}{2} \cos^2 \xi, 1\right) \quad (\text{C.24d})$$

Now since the size of the subsets, namely the length of the interval, directly correspond to the pair coincidence rate, we let $\rho(\lambda) = 1$ for simplicity and check to see if such model reproduces the correlation of $|\Psi^+\rangle$ under a common rotation angle. The expression for the general averaged joint detection rate is thus given by

$$\begin{aligned} P_{\alpha\beta}(\theta, \phi) &= \int_{\lambda \in \Lambda} \delta(O^{(A)}(\theta, \lambda), \alpha) \delta(O^{(B)}(\phi, \lambda), \beta) \rho(\lambda) d\lambda \\ &= \int_{\lambda \in \mathcal{L}} 1 \cdot d\lambda \quad \text{where } \mathcal{L} = \bigcup_{i,j=\pm 1} (\Lambda_{\alpha i, \theta} \cap \Lambda_{j\beta, \phi}) \\ &= [\text{total overlap length between } \Lambda_{\alpha i, \theta} \text{ and } \Lambda_{j\beta, \phi} \text{ where } i, j \text{ are summed over}] \end{aligned} \quad (\text{C.25})$$

from our claim that the probability distribution of the hidden variables is uniform across the range. Hence for common rotation angle it's just the full length of the corresponding subset of the partition. To conclude, by construction (see Eq. C.24) we indeed reproduce the joint detection rate of the Bell triplet under common rotation angles, which is what we set out to show.

Of course, a full description of quantum mechanical correlations arising from the Bell triplet will not be replicable by the above or any other LHV theory (see [4] for the Bell singlet case). For completeness then, I will demonstrate one family of measurement configurations where the above LHV model deviates from quantum theory. Consider the case where the rotation only occurs at B and given by angle ϕ .

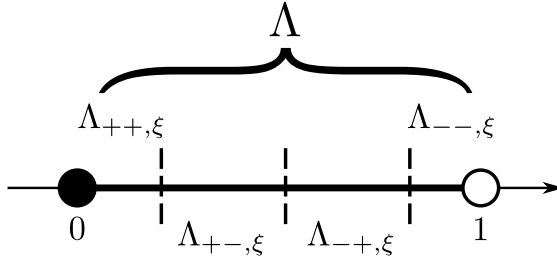


Figure C.1: Hidden variables.

The partition of hidden variable relevant at A ($\xi = 0$ in Eq. C.24) is then given by

$$\Lambda_{++,0} = [0, 0) = \emptyset \quad (\text{C.26a})$$

$$\Lambda_{+-,0} = [0, 1/2) \quad (\text{C.26b})$$

$$\Lambda_{-+,0} = [1/2, 1) \quad (\text{C.26c})$$

$$\Lambda_{--,0} = [1, 1) = \emptyset \quad (\text{C.26d})$$

and thus along with the partition at B we can evaluate every possible joint detection rates defined in Eq. C.25. A diagram in Figure C.2 clearly illustrates the calculation to give

$$\begin{cases} P_{++}(0, \phi) = \frac{1}{2} \sin^2 \phi \\ P_{+-}(0, \phi) = \frac{1}{2} \cos^2 \phi \\ P_{-+}(0, \phi) = \frac{1}{2} \cos^2 \phi \\ P_{--}(0, \phi) = \frac{1}{2} \sin^2 \phi \end{cases} \quad (\text{C.27})$$

thus the correlator is

$$\begin{aligned} E(0, \phi) &= \sum_{\alpha, \beta = \pm 1} \alpha \beta P_{\alpha \beta}(0, \phi) = \sin^2 \phi - \cos^2 \phi \\ &= -\cos 2\phi \end{aligned} \quad (\text{C.28})$$

The LHV prediction for the correlator is clearly in disagreement with the quantum mechanical prediction of the Bell triplet

$$E_{\text{QM}}(\theta, \phi) = -\cos(\theta + \phi) \quad (\text{C.29})$$

In fact, the general correlator from our LHV model is not difficult to see from generalising the particular case of $\theta = 0$. Observe from Figure C.2 that independent of the measurement configuration at A , $\lambda < 1/2 \implies O^{(A)} = +1$ and $\lambda \geq 1/2 \implies O^{(A)} = -1$. Since the joint detection rate is given by the overlap length (see Eq. C.25), we have found a surprising result about this LHV model: measurement configuration at A has no effect on the joint outcome probability! In fact, $P_{\alpha \beta}(\theta, \phi) = P_{\alpha \beta}(0, \phi)$,

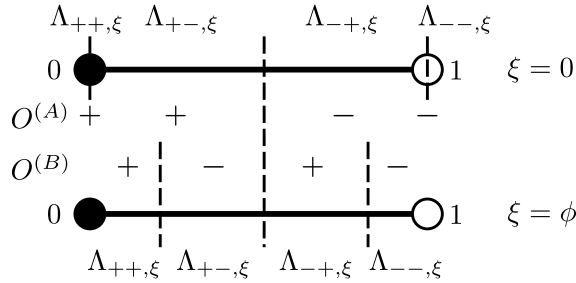


Figure C.2: Hidden variable model prediction for a single rotation measurement at B .

hence the general correlator is $E(\theta, \phi) = -\cos 2\phi$.

A final consistency check is to evaluate the CHSH parameter S based on our LHV theory.

$$\begin{aligned} S(\theta, \theta'; \phi, \phi') &\equiv |E(\theta, \phi) - E(\theta, \phi') + E(\theta', \phi) + E(\theta', \phi')| \\ &= |-2 \cos 2\phi| \\ &\leq 2, \end{aligned} \quad (\text{C.30})$$

which shouldn't be surprising.

C.5 Combinatorial algorithm for evaluating correlation functions

Correlations are central to the understanding of many-body quantum systems which admit no local theory [1], as well as to generalising the concept of classical coherence to nonclassical fields [123]. A theoretical tool for characterising correlations in quantum fields was introduced by Glauber [123] who defined the normalised n -th order correlation function as

$$g^{(n)}(\mathbf{x}_1, \mathbf{x}_2, \dots, \mathbf{x}_n) = \frac{\langle : \hat{n}(\mathbf{x}_1) \hat{n}(\mathbf{x}_2) \dots \hat{n}(\mathbf{x}_n) : \rangle}{\langle \hat{n}(\mathbf{x}_1) \rangle \langle \hat{n}(\mathbf{x}_2) \rangle \dots \langle \hat{n}(\mathbf{x}_n) \rangle}, \quad (\text{C.31})$$

where $\hat{n}(\mathbf{x})$ is the number operator for variable \mathbf{x} (e.g. position, momentum, time), and the $::$ symbol denotes normal ordering of the operator product (annihilation operators are placed to the right of creation operators). Glauber's correlation function characterises the likelihood of observing the coincidence of n -fold joint detection event $(\mathbf{x}_1, \mathbf{x}_2, \dots, \mathbf{x}_n)$ in a single experiment, therefore for a many-body system a large value of $g^{(n)}$ indicates the presence of an n -particle interaction. As a special case, if the particle numbers at all \mathbf{x}_i are uncorrelated, such that their fluctuations are independent of each other, the expectation value in the numerator of Eq. (C.31) factorises to yield $g^{(n)} = 1$. Here I describe the algorithm – based on counting all n -th order coincident events – for determining the correlation function from experimental

data. For simplicity, I present the case for second order correlation function used throughout this thesis, from which algorithms for higher order correlation functions follow by extension.

Let an *experiment* $\mathcal{E} = \{e_i\}$ (referred to as a shot) consist of a set of *events* e observed from the particular realisation (e.g. atoms/photons are detected somewhere at sometime: $e = (\mathbf{r}, t)$). The phenomenon is investigated by repeating the experiment many times, giving a set of experiments $\{\mathcal{E}_i\}$ which is the data set. We assume that any two events occurring in the same experiment are distinguishable, which is reasonable since in an experiment individual particles are resolved as separate “clicks” on a detector.

Operationally, finite sized bins of size ϵ are used in counting the number of particles $n(\mathbf{x})$ for the continuous variable \mathbf{x} , such that for the i -th shot $n_i(\mathbf{x}) = \#\{\mathbf{r} : |\mathbf{r} - \mathbf{x}| < \epsilon, \mathbf{r} \in \mathcal{E}_i\}$, where $\#A$ denotes the number of elements of a set A . By definition the second order correlation function is given by

$$g^{(2)}(\mathbf{x}, \mathbf{x}') = \frac{\langle : \hat{n}(\mathbf{x}) \hat{n}(\mathbf{x}') : \rangle}{\langle \hat{n}(\mathbf{x}) \rangle \langle \hat{n}(\mathbf{x}') \rangle} \quad (\text{C.32})$$

$$= \frac{\frac{1}{n} \sum_{i=1}^n [\#\{\mathbf{r} : |\mathbf{r} - \mathbf{x}| < \epsilon, \mathbf{r} \in \mathcal{E}_i\} \#\{\mathbf{r}' : |\mathbf{r}' - \mathbf{x}'| < \epsilon, \mathbf{r}' \in \mathcal{E}_i\}]_{\text{unique}}}{\left(\frac{1}{n} \sum_{i=1}^n \#\{\mathbf{r} : |\mathbf{r} - \mathbf{x}| < \epsilon, \mathbf{r} \in \mathcal{E}_i\} \right) \left(\frac{1}{n} \sum_{j=1}^n \#\{\mathbf{r}' : |\mathbf{r}' - \mathbf{x}'| < \epsilon, \mathbf{r}' \in \mathcal{E}_j\} \right)}, \quad (\text{C.33})$$

where the subscripted expression in the numerator indicates that no single event should belong to multiple terms in the product. The reason we must avoid such self-counting is naturally tied to the normal ordering of number product in Eq. (C.31) to properly describe correlation measurements realised in experiments [127], since physically a particle is annihilated with its detection. This is a crucial point that broadly means that a particle cannot be correlated with itself, which is evident when the numerator of Eq. (C.33), called the unnormalised correlation function and denoted by a capitalised symbol, is written as

$$\begin{aligned} G^{(2)}(\mathbf{x}, \mathbf{x}') &= \langle : \hat{n}(\mathbf{x}) \hat{n}(\mathbf{x}') : \rangle \\ &= \frac{1}{n} \sum_{i=1}^n \#\{(\mathbf{r}, \mathbf{r}') : \mathbf{r} \approx \mathbf{x}, \mathbf{r}' \approx \mathbf{x}', \mathbf{r}, \mathbf{r}' \in \mathcal{E}_i, \mathbf{r} \neq \mathbf{r}'\}, \end{aligned} \quad (\text{C.34})$$

whereas the denominator is given by

$$\langle \hat{n}(\mathbf{x}) \rangle \langle \hat{n}(\mathbf{x}') \rangle = \frac{1}{n^2} \sum_{i,j=1}^n \#\{(\mathbf{r}, \mathbf{r}') : \mathbf{r} \approx \mathbf{x}, \mathbf{r}' \approx \mathbf{x}', \mathbf{r} \in \mathcal{E}_i, \mathbf{r}' \in \mathcal{E}_j\}, \quad (\text{C.35})$$

where we have simplified the notation $|a - b| < \epsilon$ for $a \approx b$. In words, the second order correlation function formally defined in Eq. (C.32) has an equivalent definition in a combinatorial form, given by the ratio of the average number of appropriate

coincident pairs, not self-counting, observed in an individual experiment to that observed indiscriminately across all experiments in the data set. A simple extension reveals the modus operandi of the algorithm used in this thesis: evaluate the n -th order correlation function by counting n -fold coincident events occurring within the same shot, normalised by the frequency when all shots are collated.

For completeness, I give an explicit justification of the algorithm used for the back-to-back (BB) correlation function used extensively throughout this thesis. The BB correlation function is then characterised by a single variable $\Delta = \hat{\mathbf{x}} + \hat{\mathbf{x}}'$ quantifying the mismatch in the BB condition, since the absolute momenta \mathbf{x} of one of the particles is integrated over all space V , given explicitly by

$$g_{\text{BB}}^{(2)}(\Delta) = \frac{\frac{1}{V} \int_V G^{(2)}(\mathbf{x}, -\mathbf{x} + \Delta) d\mathbf{x}}{\frac{1}{V} \int_V \langle \hat{n}(\mathbf{x}) \rangle \langle \hat{n}(-\mathbf{x} + \Delta) \rangle d\mathbf{x}}. \quad (\text{C.36})$$

The numerator of Eq. (C.36) simplifies after substituting Eq. (C.34), given explicitly as follows

$$G_{\text{BB}}^{(2)}(\Delta) = \frac{1}{V} \int_V \left(\frac{1}{n} \sum_{i=1}^n \# \{ (\mathbf{r}, \mathbf{r}') : \mathbf{r} \approx \mathbf{x}, \mathbf{r}' \approx -\mathbf{x} + \Delta, \mathbf{r}, \mathbf{r}' \in \mathcal{E}_i, \mathbf{r} \neq \mathbf{r}' \} \right) d\mathbf{x} \quad (\text{C.37})$$

$$= \frac{1}{n} \sum_{i=1}^n \left(\frac{1}{V} \int_V \# \{ (\mathbf{r}, \mathbf{r}') : \mathbf{r} \approx \mathbf{x}, \mathbf{r}' \approx -\mathbf{x} + \Delta, \mathbf{r}, \mathbf{r}' \in \mathcal{E}_i, \mathbf{r} \neq \mathbf{r}' \} d\mathbf{x} \right) \quad (\text{C.38})$$

$$= \frac{1}{n} \sum_{i=1}^n \left(\frac{1}{V} \int_V \# \{ (\mathbf{r}, \mathbf{r}') : \mathbf{r} \approx \mathbf{x}, \mathbf{r} + \mathbf{r}' \approx \Delta, \mathbf{r}, \mathbf{r}' \in \mathcal{E}_i, \mathbf{r} \neq \mathbf{r}' \} d\mathbf{x} \right) \quad (\text{C.39})$$

$$= \frac{1}{n} \sum_{i=1}^n \# \{ (\mathbf{r}, \mathbf{r}') : \mathbf{r} + \mathbf{r}' \approx \Delta, \mathbf{r}, \mathbf{r}' \in \mathcal{E}_i, \mathbf{r} \neq \mathbf{r}' \}. \quad (\text{C.40})$$

The denominator of Eq. (C.36) similarly simplifies to

$$\frac{1}{n^2} \sum_{i,j=1}^n \# \{ (\mathbf{r}, \mathbf{r}') : \mathbf{r} + \mathbf{r}' \approx \Delta, \mathbf{r} \in \mathcal{E}_i, \mathbf{r}' \in \mathcal{E}_j \}. \quad (\text{C.41})$$

References

- [1] Brunner, N., Cavalcanti, D., Pironio, S., Scarani, V. & Wehner, S. Bell nonlocality. *Rev. Mod. Phys.* **86**, 419–478 (2014).
- [2] Einstein, A., Podolsky, B. & Rosen, N. Can quantum-mechanical description of physical reality be considered complete? *Phys. Rev.* **47**, 777–780 (1935). URL <https://link.aps.org/doi/10.1103/PhysRev.47.777>.
- [3] Schrödinger, E. Discussion of probability relations between separated systems. *Math. Proc. Cambridge Philos. Soc.* **31**, 555–563 (1935).
- [4] Bell, J. S. On the Einstein Podolsky Rosen paradox. *Physics* **1**, 196–200 (1964).
- [5] Freedman, S. J. & Clauser, J. F. Experimental test of local hidden-variable theories. *Phys. Rev. Lett.* **28**, 938–941 (1972).
- [6] Aspect, A., Dalibard, J. & Roger, G. Experimental test of bell’s inequalities using time-varying analyzers. *Phys. Rev. Lett.* **49**, 1804–1807 (1982).
- [7] Larsson, J.-Å. Loopholes in bell inequality tests of local realism. *J. Phys. A: Math. Theor.* **47**, 424003 (2014).
- [8] Hensen, B. *et al.* Loophole-free Bell inequality violation using electron spins separated by 1.3 kilometres. *Nature* **526**, 682–686 (2015).
- [9] Giustina, M. *et al.* Significant-loophole-free test of Bell’s theorem with entangled photons. *Phys. Rev. Lett.* **115**, 250401 (2015).
- [10] Shalm, L. K. *et al.* Strong loophole-free test of local realism. *Phys. Rev. Lett.* **115**, 250402 (2015).
- [11] Rosenfeld, W. *et al.* Event-ready bell test using entangled atoms simultaneously closing detection and locality loopholes. *Phys. Rev. Lett.* **119** (2017).
- [12] Amico, L., Fazio, R., Osterloh, A. & Vedral, V. Entanglement in many-body systems. *Rev. Mod. Phys.* **80**, 517–576 (2008). URL <https://link.aps.org/doi/10.1103/RevModPhys.80.517>.
- [13] Ekert, A. K. Quantum cryptography based on bell’s theorem. *Phys. Rev. Lett.* **67**, 661–663 (1991).
- [14] Bennett, C. H. *et al.* Teleporting an unknown quantum state via dual classical and einstein-podolsky-rosen channels. *Phys. Rev. Lett.* **70**, 1895–1899 (1993). URL <https://link.aps.org/doi/10.1103/PhysRevLett.70.1895>.

- [15] Reichardt, B. W., Unger, F. & Vazirani, U. Classical command of quantum systems. *Nature* **496**, 456–460 (2013).
- [16] Wiseman, H. M., Jones, S. J. & Doherty, A. C. Steering, entanglement, nonlocality, and the einstein-podolsky-rosen paradox. *Phys. Rev. Lett.* **98**, 140402 (2007). URL <https://link.aps.org/doi/10.1103/PhysRevLett.98.140402>.
- [17] Uola, R., Costa, A. C. S., Nguyen, H. C. & Gühne, O. Quantum steering. *Rev. Mod. Phys.* **92**, 015001 (2020). URL <https://link.aps.org/doi/10.1103/RevModPhys.92.015001>.
- [18] Branciard, C., Cavalcanti, E. G., Walborn, S. P., Scarani, V. & Wiseman, H. M. One-sided device-independent quantum key distribution: Security, feasibility, and the connection with steering. *Phys. Rev. A* **85**, 010301 (2012). URL <https://link.aps.org/doi/10.1103/PhysRevA.85.010301>.
- [19] Cronin, A. D., Schmiedmayer, J. & Pritchard, D. E. Optics and interferometry with atoms and molecules. *Rev. Mod. Phys.* **81**, 1051–1129 (2009). URL <https://link.aps.org/doi/10.1103/RevModPhys.81.1051>.
- [20] Cohen-Tannoudji, C. & Guéry-Odelin, D. *Advances in Atomic Physics* (WORLD SCIENTIFIC, 2011). URL <https://www.worldscientific.com/doi/abs/10.1142/6631>. <https://www.worldscientific.com/doi/pdf/10.1142/6631>.
- [21] Metcalf, H. & van der Straten, P. *Laser Cooling and Trapping*. Graduate Texts in Contemporary Physics (Springer New York, 2001). URL <https://books.google.com.au/books?id=i-40VaXqrjOC>.
- [22] Khakimov, R. I. *et al.* Ghost imaging with atoms. *Nature* **540**, 100 (2016).
- [23] Walls, D. F. Squeezed states of light. *Nature* **306**, 141–146 (1983).
- [24] The LIGO Scientific Collaboration. Quantum-enhanced advanced ligo detectors in the era of gravitational-wave astronomy. *Phys. Rev. Lett.* **123**, 231107 (2019). URL <https://link.aps.org/doi/10.1103/PhysRevLett.123.231107>.
- [25] Pezzè, L., Smerzi, A., Oberthaler, M. K., Schmied, R. & Treutlein, P. Quantum metrology with nonclassical states of atomic ensembles. *Rev. Mod. Phys.* **90** (2018).
- [26] Buhrman, H., Cleve, R., Massar, S. & de Wolf, R. Nonlocality and communication complexity. *Rev. Mod. Phys.* **82**, 665–698 (2010). URL <https://link.aps.org/doi/10.1103/RevModPhys.82.665>.
- [27] Giovannetti, V., Lloyd, S. & Maccone, L. Quantum-enhanced measurements: Beating the standard quantum limit. *Science* **306**, 1330–1336 (2004).
- [28] Bohm, D. *Quantum theory* (Prentice Hall, Englewood Cliffs, NJ, 1951).
- [29] Nielsen, M. A. & Chuang, I. L. *Quantum Computation and Quantum Information: 10th Anniversary Edition* (Cambridge University Press, USA, 2011), 10th edn.

-
- [30] Clauser, J. F. & Shimony, A. Bell's theorem. experimental tests and implications. *Rep. Prog. Phys.* **41**, 1881–1927 (1978). URL <https://doi.org/10.1088%2F0034-4885%2F41%2F12%2F002>.
 - [31] Werner, R. F. Quantum states with einstein-podolsky-rosen correlations admitting a hidden-variable model. *Phys. Rev. A* **40**, 4277–4281 (1989). URL <https://link.aps.org/doi/10.1103/PhysRevA.40.4277>.
 - [32] Horodecki, R., Horodecki, P., Horodecki, M. & Horodecki, K. Quantum entanglement. *Rev. Mod. Phys.* **81**, 865–942 (2009).
 - [33] Cavalcanti, E. G., Jones, S. J., Wiseman, H. M. & Reid, M. D. Experimental criteria for steering and the einstein-podolsky-rosen paradox. *Phys. Rev. A* **80**, 032112 (2009). URL <https://link.aps.org/doi/10.1103/PhysRevA.80.032112>.
 - [34] Bruß, D. Characterizing entanglement. *J. Math. Phys.* **43**, 4237–4251 (2002). URL <https://doi.org/10.1063/1.1494474>. <https://doi.org/10.1063/1.1494474>.
 - [35] James, D. F. V., Kwiat, P. G., Munro, W. J. & White, A. G. Measurement of qubits. *Phys. Rev. A* **64**, 052312 (2001). URL <https://link.aps.org/doi/10.1103/PhysRevA.64.052312>.
 - [36] Peres, A. Separability criterion for density matrices. *Phys. Rev. Lett.* **77**, 1413–1415 (1996). URL <https://link.aps.org/doi/10.1103/PhysRevLett.77.1413>.
 - [37] Clauser, J. F. Experimental distinction between the quantum and classical field-theoretic predictions for the photoelectric effect. *Phys. Rev. D* **9**, 853–860 (1974). URL <https://link.aps.org/doi/10.1103/PhysRevD.9.853>.
 - [38] Clauser, J. F., Horne, M. A., Shimony, A. & Holt, R. A. Proposed experiment to test local hidden-variable theories. *Phys. Rev. Lett.* **23**, 880–884 (1969).
 - [39] Cirel'son, B. S. Quantum generalizations of bell's inequality. *Lett. Math. Phys.* **4**, 93–100 (1980). URL <https://doi.org/10.1007/BF00417500>.
 - [40] Popescu, S. & Rohrlich, D. Quantum nonlocality as an axiom. *Found. Phys.* **24**, 379–385 (1994). URL <https://doi.org/10.1007/BF02058098>.
 - [41] Navascués, M. & Wunderlich, H. A glance beyond the quantum model. *Proceedings of the Royal Society A: Mathematical, Physical and Engineering Sciences* **466**, 881–890 (2009). URL <https://royalsocietypublishing.org/doi/abs/10.1098/rspa.2009.0453>. <https://royalsocietypublishing.org/doi/pdf/10.1098/rspa.2009.0453>.
 - [42] Acín, A., Gisin, N. & Toner, B. Grothendieck's constant and local models for noisy entangled quantum states. *Phys. Rev. A* **73**, 062105 (2006). URL <https://link.aps.org/doi/10.1103/PhysRevA.73.062105>.

- [43] Tsirel'son, B. S. Quantum analogues of the bell inequalities. the case of two spatially separated domains. *Journal of Soviet Mathematics* **36**, 557–570 (1987).
- [44] Bowles, J., Vértesi, T., Quintino, M. T. & Brunner, N. One-way einstein-podolsky-rosen steering. *Phys. Rev. Lett.* **112**, 200402 (2014). URL <https://link.aps.org/doi/10.1103/PhysRevLett.112.200402>.
- [45] Tischler, N. *et al.* Conclusive experimental demonstration of one-way einstein-podolsky-rosen steering. *Phys. Rev. Lett.* **121**, 100401 (2018). URL <https://link.aps.org/doi/10.1103/PhysRevLett.121.100401>.
- [46] Jones, S. J., Wiseman, H. M. & Doherty, A. C. Entanglement, einstein-podolsky-rosen correlations, bell nonlocality, and steering. *Phys. Rev. A* **76**, 052116 (2007). URL <https://link.aps.org/doi/10.1103/PhysRevA.76.052116>.
- [47] Reid, M. D. *et al.* Colloquium: The einstein-podolsky-rosen paradox: From concepts to applications. *Rev. Mod. Phys.* **81**, 1727–1751 (2009). URL <https://link.aps.org/doi/10.1103/RevModPhys.81.1727>.
- [48] Pironio, S., Scarani, V. & Vidick, T. Focus on device independent quantum information. *New J. Phys.* **18**, 100202 (2016). URL <https://doi.org/10.1088%2F1367-2630%2F18%2F10%2F100202>.
- [49] Pironio, S. *et al.* Random numbers certified by bell's theorem. *Nature* **464**, 1021–1024 (2010).
- [50] Brukner, i. c. v., Żukowski, M., Pan, J.-W. & Zeilinger, A. Bell's inequalities and quantum communication complexity. *Phys. Rev. Lett.* **92**, 127901 (2004). URL <https://link.aps.org/doi/10.1103/PhysRevLett.92.127901>.
- [51] Pezzé, L. & Smerzi, A. Entanglement, nonlinear dynamics, and the Heisenberg limit. *Phys. Rev. Lett.* **102**, 100401 (2009).
- [52] Giovannetti, V., Lloyd, S. & Maccone, L. Quantum metrology. *Phys. Rev. Lett.* **96**, 010401 (2006).
- [53] Masanes, L. All bipartite entangled states are useful for information processing. *Phys. Rev. Lett.* **96**, 150501 (2006). URL <https://link.aps.org/doi/10.1103/PhysRevLett.96.150501>.
- [54] Raussendorf, R. & Briegel, H. J. A one-way quantum computer. *Phys. Rev. Lett.* **86**, 5188–5191 (2001). URL <https://link.aps.org/doi/10.1103/PhysRevLett.86.5188>.
- [55] Rarity, J. G. & Tapster, P. R. Experimental violation of bell's inequality based on phase and momentum. *Phys. Rev. Lett.* **64**, 2495–2498 (1990).
- [56] Tittel, W., Brendel, J., Zbinden, H. & Gisin, N. Violation of bell inequalities by photons more than 10 km apart. *Phys. Rev. Lett.* **81**, 3563–3566 (1998). URL <https://link.aps.org/doi/10.1103/PhysRevLett.81.3563>.

-
- [57] Weihs, G., Jennewein, T., Simon, C., Weinfurter, H. & Zeilinger, A. Violation of bell's inequality under strict einstein locality conditions. *Phys. Rev. Lett.* **81**, 5039–5043 (1998). URL <https://link.aps.org/doi/10.1103/PhysRevLett.81.5039>.
 - [58] Lamehi-Rachti, M. & Mittig, W. Quantum mechanics and hidden variables: A test of bell's inequality by the measurement of the spin correlation in low-energy proton-proton scattering. *Phys. Rev. D* **14**, 2543–2555 (1976).
 - [59] Polachic, C. *et al.* Polarization correlations of 1s0 proton pairs as tests of hidden-variable theories. *Phys. Lett. A* **323**, 176 – 181 (2004). URL <http://www.sciencedirect.com/science/article/pii/S0375960104001483>.
 - [60] Sakai, H. *et al.* Spin correlations of strongly interacting massive fermion pairs as a test of bell's inequality. *Phys. Rev. Lett.* **97**, 150405 (2006).
 - [61] Eisaman, M. D., Fan, J., Migdall, A. & Polyakov, S. V. Invited review article: Single-photon sources and detectors. *Rev. Sci. Instrum.* **82**, 071101 (2011).
 - [62] Garg, A. & Mermin, N. D. Detector inefficiencies in the Einstein-Podolsky-Rosen experiment. *Phys. Rev. D* **35**, 3831–3835 (1987).
 - [63] Rowe, M. A. *et al.* Experimental violation of a bell's inequality with efficient detection. *Nature* **409**, 791–794 (2001).
 - [64] Ansmann, M. *et al.* Violation of bell's inequality in josephson phase qubits. *Nature* **461**, 504–506 (2009).
 - [65] Christensen, B. G. *et al.* Detection-loophole-free test of quantum nonlocality, and applications. *Phys. Rev. Lett.* **111** (2013).
 - [66] Giustina, M. *et al.* Bell violation using entangled photons without the fair-sampling assumption. *Nature* **497**, 227–230 (2013).
 - [67] Żukowski, M., Zeilinger, A., Horne, M. A. & Ekert, A. K. 'Event-ready-detectors' Bell experiment via entanglement swapping. *Phys. Rev. Lett.* **71**, 4287–4290 (1993).
 - [68] Gneiting, C. & Hornberger, K. Bell test for the free motion of material particles. *Phys. Rev. Lett.* **101** (2008).
 - [69] Kofler, J. *et al.* Einstein-podolsky-rosen correlations from colliding bose-einstein condensates. *Phys. Rev. A* **86**, 032115 (2012).
 - [70] Lewis-Swan, R. J. & Kheruntsyan, K. V. Proposal for a motional-state bell inequality test with ultracold atoms. *Phys. Rev. A* **91** (2015).
 - [71] Penrose, R. On gravity's role in quantum state reduction. *Gen. Relativ. Gravitation* **28**, 581–600 (1996).
 - [72] Bassi, A., Großardt, A. & Ulbricht, H. Gravitational decoherence. *Class. Quantum Grav.* **34**, 193002 (2017).

- [73] Geiger, R. & Trupke, M. Proposal for a quantum test of the weak equivalence principle with entangled atomic species. *Phys. Rev. Lett.* **120** (2018).
- [74] Zych, M. & Brukner, Č. Quantum formulation of the einstein equivalence principle. *Nat. Phys.* **14**, 1027–1031 (2018). URL <https://doi.org/10.1038/s41567-018-0197-6>.
- [75] Bongs, K. *et al.* Taking atom interferometric quantum sensors from the laboratory to real-world applications. *Nature Reviews Physics* **1**, 731–739 (2019). URL <https://doi.org/10.1038/s42254-019-0117-4>.
- [76] Hofmann, J. *et al.* Heralded entanglement between widely separated atoms. *Science* **337**, 72–75 (2012). URL <https://science.sciencemag.org/content/337/6090/72>. <https://science.sciencemag.org/content/337/6090/72.full.pdf>.
- [77] Pethick, C. J. & Smith, H. *Bose-Einstein Condensation in Dilute Gases* (Cambridge University Press, 2008).
- [78] Gerry, C. & Knight, P. *Introductory Quantum Optics* (Cambridge University Press, 2004).
- [79] Walls, D. & Milburn, G. J. (eds.) *Quantum Optics* (Springer Berlin Heidelberg, 2008).
- [80] Chin, C., Grimm, R., Julienne, P. & Tiesinga, E. Feshbach resonances in ultracold gases. *Rev. Mod. Phys.* **82**, 1225–1286 (2010). URL <https://link.aps.org/doi/10.1103/RevModPhys.82.1225>.
- [81] Lücke, B. *et al.* Detecting multiparticle entanglement of dicke states. *Phys. Rev. Lett.* **112**, 155304 (2014). URL <https://link.aps.org/doi/10.1103/PhysRevLett.112.155304>.
- [82] Gross, C., Zibold, T., Nicklas, E., Estève, J. & Oberthaler, M. K. Nonlinear atom interferometer surpasses classical precision limit. *Nature* **464**, 1165–1169 (2010).
- [83] Riedel, M. F. *et al.* Atom-chip-based generation of entanglement for quantum metrology. *Nature* **464**, 1170–1173 (2010). URL <https://doi.org/10.1038/nature08988>.
- [84] Schmied, R. *et al.* Bell correlations in a bose-einstein condensate. *Science* **352**, 441–444 (2016).
- [85] Arecchi, F. T., Courtens, E., Gilmore, R. & Thomas, H. Atomic coherent states in quantum optics. *Phys. Rev. A* **6**, 2211–2237 (1972). URL <https://link.aps.org/doi/10.1103/PhysRevA.6.2211>.
- [86] Duan, L.-M., Sørensen, A., Cirac, J. I. & Zoller, P. Squeezing and entanglement of atomic beams. *Phys. Rev. Lett.* **85**, 3991–3994 (2000).

-
- [87] Bücker, R. *et al.* Twin-atom beams. *Nat. Phys.* **7**, 608–611 (2011). URL <https://doi.org/10.1038/nphys1992>.
 - [88] Bonneau, M. *et al.* Tunable source of correlated atom beams. *Phys. Rev. A* **87**, 061603 (2013). URL <https://link.aps.org/doi/10.1103/PhysRevA.87.061603>.
 - [89] Perrin, A. *et al.* Observation of atom pairs in spontaneous four-wave mixing of two colliding bose-einstein condensates. *Phys. Rev. Lett.* **99** (2007).
 - [90] Savage, C. M., Schwenn, P. E. & Kheruntsyan, K. V. First-principles quantum simulations of dissociation of molecular condensates: Atom correlations in momentum space. *Phys. Rev. A* **74**, 033620 (2006). URL <https://link.aps.org/doi/10.1103/PhysRevA.74.033620>.
 - [91] Rosenfeld, W. *et al.* Towards long-distance atom-photon entanglement. *Phys. Rev. Lett.* **101**, 260403 (2008). URL <https://link.aps.org/doi/10.1103/PhysRevLett.101.260403>.
 - [92] Kominis, I. K., Kornack, T. W., Allred, J. C. & Romalis, M. V. A subfemtotesla multichannel atomic magnetometer. *Nature* **422**, 596–599 (2003).
 - [93] Kitagawa, M. & Ueda, M. Squeezed spin states. *Phys. Rev. A* **47**, 5138–5143 (1993). URL <https://link.aps.org/doi/10.1103/PhysRevA.47.5138>.
 - [94] Julsgaard, B., Kozhekin, A. & Polzik, E. S. Experimental long-lived entanglement of two macroscopic objects. *Nature* **413**, 400–403 (2001). URL <https://doi.org/10.1038/35096524>.
 - [95] Orzel, C., Tuchman, A. K., Fenselau, M. L., Yasuda, M. & Kasevich, M. A. Squeezed states in a bose-einstein condensate. *Science* **291**, 2386–2389 (2001). URL <https://science.sciencemag.org/content/291/5512/2386>. <https://science.sciencemag.org/content/291/5512/2386.full.pdf>.
 - [96] Kwiat, P. G. *et al.* New high-intensity source of polarization-entangled photon pairs. *Phys. Rev. Lett.* **75**, 4337–4341 (1995).
 - [97] Sakurai, J. & Napolitano, J. *Modern Quantum Mechanics* (Addison-Wesley, 2011).
 - [98] Weiner, J., Bagnato, V. S., Zilio, S. & Julienne, P. S. Experiments and theory in cold and ultracold collisions. *Rev. Mod. Phys.* **71**, 1–85 (1999). URL <https://link.aps.org/doi/10.1103/RevModPhys.71.1>.
 - [99] Lahaye, T., Menotti, C., Santos, L., Lewenstein, M. & Pfau, T. The physics of dipolar bosonic quantum gases. *Rep. Prog. Phys.* **72**, 126401 (2009). URL <https://doi.org/10.1088%2F0034-4885%2F72%2F12%2F126401>.
 - [100] Arfken, G. B., Weber, H. J. & Harris, F. E. Chapter 15 - legendre functions. In Arfken, G. B., Weber, H. J. & Harris, F. E. (eds.) *Mathematical Methods for*

- Physicists (Seventh Edition)*, 715 – 772 (Academic Press, Boston, 2013), seventh edition edn. URL <http://www.sciencedirect.com/science/article/pii/B9780123846549000153>.
- [101] Shin, D. K. *et al.* Bell correlations between spatially separated pairs of atoms. *Nat. Commun.* **10**, 4447 (2019). URL <https://doi.org/10.1038/s41467-019-12192-8>.
 - [102] Moal, S. *et al.* Accurate determination of the scattering length of metastable helium atoms using dark resonances between atoms and exotic molecules. *Phys. Rev. Lett.* **96**, 023203 (2006). URL <https://link.aps.org/doi/10.1103/PhysRevLett.96.023203>.
 - [103] Balakrishnan, N. Perspective: Ultracold molecules and the dawn of cold controlled chemistry. *The Journal of Chemical Physics* **145**, 150901 (2016).
 - [104] Liu, L. R. *et al.* Building one molecule from a reservoir of two atoms. *Science* **360**, 900–903 (2018).
 - [105] Pitaevskii, L. & Stringari, S. *Bose-Einstein Condensation and Superfluidity* (Oxford University Press, 2016).
 - [106] Huang, K. *Statistical Mechanics* (John Wiley & Sons, 1987).
 - [107] Dalfovo, F., Giorgini, S., Pitaevskii, L. P. & Stringari, S. Theory of bose-einstein condensation in trapped gases. *Rev. Mod. Phys.* **71**, 463–512 (1999). URL <https://link.aps.org/doi/10.1103/RevModPhys.71.463>.
 - [108] Ozeri, R., Katz, N., Steinhauer, J. & Davidson, N. Colloquium: Bulk bogoliubov excitations in a bose-einstein condensate. *Rev. Mod. Phys.* **77**, 187–205 (2005). URL <https://link.aps.org/doi/10.1103/RevModPhys.77.187>.
 - [109] Jaskula, J.-C. *et al.* Sub-poissonian number differences in four-wave mixing of matter waves. *Phys. Rev. Lett.* **105** (2010).
 - [110] Krachmalnicoff, V. *et al.* Spontaneous four-wave mixing of de broglie waves: Beyond optics. *Phys. Rev. Lett.* **104**, 150402 (2010). URL <https://link.aps.org/doi/10.1103/PhysRevLett.104.150402>.
 - [111] Kheruntsyan, K. V. *et al.* Violation of the Cauchy-Schwarz inequality with matter waves. *Phys. Rev. Lett.* **108**, 260401 (2012).
 - [112] Hodgman, S., Khakimov, R., Lewis-Swan, R., Truscott, A. & Kheruntsyan, K. Solving the quantum many-body problem via correlations measured with a momentum microscope. *Phys. Rev. Lett.* **118** (2017).
 - [113] Band, Y. B., Trippenbach, M., Burke, J. P. & Julienne, P. S. Elastic scattering loss of atoms from colliding bose-einstein condensate wave packets. *Phys. Rev. Lett.* **84**, 5462–5465 (2000). URL <https://link.aps.org/doi/10.1103/PhysRevLett.84.5462>.

-
- [114] Ziń, P., Chwedeńczuk, J., Veitia, A., Rzażewski, K. & Trippenbach, M. Quantum multimode model of elastic scattering from bose-einstein condensates. *Phys. Rev. Lett.* **94** (2005).
 - [115] Chwedeńczuk, J., Ziń, P., Rzażewski, K. & Trippenbach, M. Simulation of a single collision of two bose-einstein condensates. *Phys. Rev. Lett.* **97** (2006).
 - [116] Mølmer, K. *et al.* Hanbury brown and twiss correlations in atoms scattered from colliding condensates. *Phys. Rev. A* **77**, 033601 (2008). URL <https://link.aps.org/doi/10.1103/PhysRevA.77.033601>.
 - [117] Deuar, P. *et al.* Anisotropy in s-wave bose-einstein condensate collisions and its relationship to superradiance. *Phys. Rev. A* **90**, 033613 (2014). URL <https://link.aps.org/doi/10.1103/PhysRevA.90.033613>.
 - [118] Zin, P., Wasak, T., Boiron, D. & Westbrook, C. I. Pair correlation of atoms scattered from colliding bose-einstein quasicondensates. *Phys. Rev. A* **101**, 033616 (2020). URL <https://link.aps.org/doi/10.1103/PhysRevA.101.033616>.
 - [119] Castin, Y. & Dum, R. Bose-einstein condensates in time dependent traps. *Phys. Rev. Lett.* **77**, 5315–5319 (1996). URL <https://link.aps.org/doi/10.1103/PhysRevLett.77.5315>.
 - [120] Ketterle, W., Durfee, D. S. & Stamper-Kurn, D. M. Making, probing and understanding bose-einstein condensates [cond-mat/9904034v2](https://arxiv.org/abs/cond-mat/9904034v2).
 - [121] Loudon, R. & Knight, P. Squeezed light. *J. Mod. Opt.* **34**, 709–759 (1987). URL <https://doi.org/10.1080/09500348714550721>. <https://doi.org/10.1080/09500348714550721>.
 - [122] Jeltes, T. *et al.* Comparison of the hanbury brown–twiss effect for bosons and fermions. *Nature* **445**, 402–405 (2007).
 - [123] Glauber, R. J. The quantum theory of optical coherence. *Phys. Rev.* **130**, 2529–2539 (1963). URL <https://link.aps.org/doi/10.1103/PhysRev.130.2529>.
 - [124] Perrin, A. *et al.* Atomic four-wave mixing via condensate collisions. *New J. Phys.* **10**, 045021 (2008).
 - [125] Vogels, J. M., Xu, K. & Ketterle, W. Generation of macroscopic pair-correlated atomic beams by four-wave mixing in bose-einstein condensates. *Phys. Rev. Lett.* **89**, 020401 (2002). URL <https://link.aps.org/doi/10.1103/PhysRevLett.89.020401>.
 - [126] Heidmann, A. *et al.* Observation of quantum noise reduction on twin laser beams. *Phys. Rev. Lett.* **59**, 2555–2557 (1987). URL <https://link.aps.org/doi/10.1103/PhysRevLett.59.2555>.
 - [127] Reid, M. D. & Walls, D. F. Violations of classical inequalities in quantum optics. *Phys. Rev. A* **34**, 1260–1276 (1986).

- [128] Lopes, R. *et al.* Atomic hong-ou-mandel experiment. *Nature* **520**, 66–68 (2015).
- [129] Hodgman, S. S., Bu, W., Mann, S. B., Khakimov, R. I. & Truscott, A. G. Higher-order quantum ghost imaging with ultracold atoms. *Phys. Rev. Lett.* **122**, 233601 (2019). URL <https://link.aps.org/doi/10.1103/PhysRevLett.122.233601>.
- [130] Dussarrat, P. *et al.* Two-particle four-mode interferometer for atoms. *Phys. Rev. Lett.* **119**, 173202 (2017).
- [131] Opatrný, T. & Kurizki, G. Matter-wave entanglement and teleportation by molecular dissociation and collisions. *Phys. Rev. Lett.* **86**, 3180–3183 (2001). URL <https://link.aps.org/doi/10.1103/PhysRevLett.86.3180>.
- [132] Peise, J. *et al.* Satisfying the Einstein-podolsky-Rosen criterion with massive particles. *Nat. Commun.* **6**, 8984 (2015).
- [133] Lange, K. *et al.* Entanglement between two spatially separated atomic modes. *Science* **360**, 416–418 (2018).
- [134] Fadel, M., Zibold, T., Décamps, B. & Treutlein, P. Spatial entanglement patterns and einstein-podolsky-rosen steering in bose-einstein condensates. *Science* **360**, 409–413 (2018).
- [135] Kunkel, P. *et al.* Spatially distributed multipartite entanglement enables epr steering of atomic clouds. *Science* **360**, 413–416 (2018).
- [136] Bloch, I., Dalibard, J. & Zwerger, W. Many-body physics with ultracold gases. *Rev. Mod. Phys.* **80**, 885–964 (2008). URL <https://link.aps.org/doi/10.1103/RevModPhys.80.885>.
- [137] Hodgman, S. S. *et al.* Metastable helium: A new determination of the longest atomic excited-state lifetime. *Phys. Rev. Lett.* **103**, 053002 (2009). URL <https://link.aps.org/doi/10.1103/PhysRevLett.103.053002>.
- [138] Foot, C. J. *Atomic Physics* (Oxford University Press, 2005).
- [139] Robert, A. *et al.* A bose-einstein condensate of metastable atoms. *Science* **292**, 461–464 (2001). URL <https://science.sciencemag.org/content/292/5516/461>. <https://science.sciencemag.org/content/292/5516/461.full.pdf>.
- [140] Pereira Dos Santos, F. *et al.* Bose-einstein condensation of metastable helium. *Phys. Rev. Lett.* **86**, 3459–3462 (2001). URL <https://link.aps.org/doi/10.1103/PhysRevLett.86.3459>.
- [141] Dall, R. G. & Truscott, A. G. Bose-Einstein condensation of metastable helium in a bi-planar quadrupole Ioffe configuration trap. *Opt. Commun.* **270**, 255–261 (2007).
- [142] Haynes, W. M., Lide, D. R. & Bruno, T. J. (eds.) *CRC handbook of chemistry and physics : a ready-reference book of chemical and physical data* (CRC Press, Boca Raton, Florida, 2017), 97th edn.

-
- [143] Vassen, W. *et al.* Cold and trapped metastable noble gases. *Rev. Mod. Phys.* **84**, 175–210 (2012).
 - [144] Hotop, H. 11 - detection of metastable atoms and molecules. In Dunning, F. & Hulet, R. G. (eds.) *Atomic, Molecular, and Optical Physics: Atoms and Molecules*, vol. 29 of *Experimental Methods in the Physical Sciences*, 191 – 215 (Academic Press, 1996). URL <http://www.sciencedirect.com/science/article/pii/S0076695X08607930>.
 - [145] Jagutzki, O. *et al.* A broad-application microchannel-plate detector system for advanced particle or photon detection tasks: large area imaging, precise multi-hit timing information and high detection rate. *Nucl. Instrum. Methods Phys. Res., Sect. A* **477**, 244 – 249 (2002). URL <http://www.sciencedirect.com/science/article/pii/S0168900201018393>. 5th Int. Conf. on Position-Sensitive Detectors.
 - [146] Vassen, W., Notermans, R. P. M. J. W., Rengelink, R. J. & van der Beek, R. F. H. J. Ultracold metastable helium: Ramsey fringes and atom interferometry. *Appl. Phys. B* **122**, 289 (2016).
 - [147] Swansson, J., Baldwin, K., Hoogerland, M., Truscott, A. & Buckman, S. A high flux, liquid-helium cooled source of metastable rare gas atoms. *Appl. Phys. B* **79**, 485–489 (2004). URL <https://doi.org/10.1007/s00340-004-1600-9>.
 - [148] Swansson, J. A., Dall, R. G. & Truscott, A. G. An intense cold beam of metastable helium. *Appl. Phys. B* **86**, 485–489 (2007). URL <https://doi.org/10.1007/s00340-006-2472-y>.
 - [149] Dedman, C. J. *et al.* Optimum design and construction of a zeeman slower for use with a magneto-optic trap. *Rev. Sci. Instrum.* **75**, 5136–5142 (2004). URL <https://doi.org/10.1063/1.1820524>. <https://doi.org/10.1063/1.1820524>.
 - [150] Henson, B. M. *et al.* Approaching the adiabatic timescale with machine learning. *Proceedings of the National Academy of Sciences* **115**, 13216–13221 (2018). URL <https://www.pnas.org/content/115/52/13216>. <https://www.pnas.org/content/115/52/13216.full.pdf>.
 - [151] Dedman, C. J., Dall, R. G., Byron, L. J. & Truscott, A. G. Active cancellation of stray magnetic fields in a bose-einstein condensation experiment. *Rev. Sci. Instrum.* **78**, 024703 (2007).
 - [152] Moler, K., Weiss, D. S., Kasevich, M. & Chu, S. Theoretical analysis of velocity-selective raman transitions. *Phys. Rev. A* **45**, 342–348 (1992). URL <https://link.aps.org/doi/10.1103/PhysRevA.45.342>.
 - [153] Cohen-Tannoudji, C., Dupont-Roc, J. & Grynberg, G. *Atom—Photon Interactions* (Wiley, 1998).

- [154] Blum, K. *Density Matrix Theory and Applications* (Springer Berlin Heidelberg, 2012).
- [155] Hunsperger, R. G. *Integrated Optics* (Springer New York, 2009).
- [156] Henson, B. M. *et al.* Bogoliubov-Cherenkov radiation in an atom laser. *Phys. Rev. A* **97**, 063601 (2018).
- [157] Shin, D. K. *et al.* Widely tunable, narrow linewidth external-cavity gain chip laser for spectroscopy between 1.0 - 1.1 μm . *Opt. Express* **24**, 27403–27414 (2016). URL <http://www.opticsexpress.org/abstract.cfm?URI=oe-24-24-27403>.
- [158] Duarte, F. J. (ed.) *Tunable Laser Applications* (CRC Press, 2016).
- [159] Wieman, C. E. & Hollberg, L. Using diode lasers for atomic physics. *Rev. Sci. Instrum.* **62**, 1–20 (1991). URL <http://scitation.aip.org/content/aip/journal/rsi/62/1/10.1063/1.1142305>.
- [160] Bennetts, S. *et al.* External cavity diode lasers with 5kHz linewidth and 200nm tuning range at 1.55 μm and methods for linewidth measurement. *Opt. Express* **22**, 10642–10654 (2014). URL <http://www.opticsexpress.org/abstract.cfm?URI=oe-22-9-10642>.
- [161] Mroziewicz, B. External cavity wavelength tunable semiconductor lasers - a review. *Opto-Electron. Rev.* **16**, 347 (2008). URL <http://dx.doi.org/10.2478/s11772-008-0045-9>.
- [162] Duarte, F. J. (ed.) *Tunable Lasers Handbook*. Optics and Photonics (Academic Press, 1995).
- [163] Rideout, W., Holmstrom, R., Lacourse, J., Meland, E. & Powazinik, W. Ultralow-reflectivity semiconductor optical amplifiers without antireflection coatings. *Electron. Lett.* **26**, 36–38 (1990). URL <http://dx.doi.org/10.1049/el:19900024>.
- [164] Heim, P. J. S. *et al.* Single-angled-facet laser diode for widely tunable external cavity semiconductor lasers with high spectral purity. *Electron. Lett.* **33**, 1387 (1997). URL <http://dx.doi.org/10.1049/el:19970911>.
- [165] Hawthorn, C. J., Weber, K. P. & Scholten, R. E. Littrow configuration tunable external cavity diode laser with fixed direction output beam. *Rev. Sci. Instrum.* **72**, 4477–4479 (2001). URL <http://scitation.aip.org/content/aip/journal/rsi/72/12/10.1063/1.1419217>.
- [166] Saliba, S. D., Junker, M., Turner, L. D. & Scholten, R. E. Mode stability of external cavity diode lasers. *Appl. Opt.* **48**, 6692 (2009). URL <http://dx.doi.org/10.1364/AO.48.006692>.
- [167] Libbrecht, K. G. & Hall, J. L. A low-noise high-speed diode laser current controller. *Rev. Sci. Instrum.* **64**, 2133 (1993). URL <http://dx.doi.org/10.1063/1.1143949>.

- [168] Saliba, S. D. & Scholten, R. E. Linewidths below 100 kHz with external cavity diode lasers. *Appl. Opt.* **48**, 6961–6966 (2009). URL <http://ao.osa.org/abstract.cfm?URI=ao-48-36-6961>.
- [169] Torrance, J. S., Sparkes, B. M., Turner, L. D. & Scholten, R. E. Sub-kilohertz laser linewidth narrowing using polarization spectroscopy. *Opt. Express* **24**, 11396 (2016). URL <http://dx.doi.org/10.1364/OE.24.011396>.
- [170] Zhang, Z., Wang, X. & Lin, Q. A novel way for wavelength locking with acousto-optic frequency modulation. *Opt. Express* **17**, 10372 (2009). URL <http://dx.doi.org/10.1364/OE.17.010372>.
- [171] Okoshi, T., Kikuchi, K. & Nakayama, A. Novel method for high resolution measurement of laser output spectrum. *Electron. Lett.* **16**, 630 (1980). URL <http://dx.doi.org/10.1049/el:19800437>.
- [172] Thompson, D. J. & Scholten, R. E. Narrow linewidth tunable external cavity diode laser using wide bandwidth filter. *Rev. Sci. Instrum.* **83**, 023107 (2012). URL <http://scitation.aip.org/content/aip/journal/rsi/83/2/10.1063/1.3687441>.
- [173] Mercer, L. 1/f frequency noise effects on self-heterodyne linewidth measurements. *J. Lightwave Technol.* **9**, 485–493 (1991). URL <http://dx.doi.org/10.1109/50.76663>.
- [174] Gallion, P. & Debarge, G. Quantum phase noise and field correlation in single frequency semiconductor laser systems. *IEEE Journal of Quantum Electronics* **20**, 343–349 (1984). URL <http://dx.doi.org/10.1109/JQE.1984.1072399>.
- [175] Turner, L., Weber, K., Hawthorn, C. & Scholten, R. Frequency noise characterisation of narrow linewidth diode lasers. *Opt. Commun.* **201**, 391–397 (2002). URL [http://dx.doi.org/10.1016/S0030-4018\(01\)01689-3](http://dx.doi.org/10.1016/S0030-4018(01)01689-3).
- [176] Fukuda, K., Tachikawa, M. & Kinoshita, M. Allan-variance measurements of diode laser frequency-stabilized with a thin vapor cell. *Appl. Phys. B* **77**, 823–827 (2003). URL <http://dx.doi.org/10.1007/s00340-003-1286-4>.
- [177] Allan, D. W. Should the classical variance be used as a basic measure in standards metrology? *IEEE Trans. Instrum. Meas.* **IM-36**, 646–654 (1987).
- [178] Wasak, T. & Chwedeńczuk, J. Bell inequality, einstein-podolsky-rosen steering, and quantum metrology with spinor bose-einstein condensates. *Phys. Rev. Lett.* **120** (2018).
- [179] Augusiak, R., Demianowicz, M. & Acín, A. Local hidden-variable models for entangled quantum states. *J. Phys. A: Math. Theor.* **47**, 424002 (2014). URL <https://doi.org/10.1088%2F1751-8113%2F47%2F42%2F424002>.
- [180] Wootters, W. K. Entanglement of formation of an arbitrary state of two qubits. *Phys. Rev. Lett.* **80**, 2245–2248 (1998).

- [181] Bowles, J., Hirsch, F., Quintino, M. T. & Brunner, N. Sufficient criterion for guaranteeing that a two-qubit state is unsteerable. *Phys. Rev. A* **93**, 022121 (2016). URL <https://link.aps.org/doi/10.1103/PhysRevA.93.022121>.
- [182] Cavalcanti, D., Guerini, L., Rabelo, R. & Skrzypczyk, P. General method for constructing local hidden variable models for entangled quantum states. *Phys. Rev. Lett.* **117**, 190401 (2016). URL <https://link.aps.org/doi/10.1103/PhysRevLett.117.190401>.
- [183] Schwinger, J. On angular momentum. Tech. Rep. (1952).
- [184] Cavalcanti, E. G., Foster, C. J., Fuwa, M. & Wiseman, H. M. Analog of the clauser–horne–shimony–holt inequality for steering. *Journal of the Optical Society of America B* **32**, A74 (2015).
- [185] Kwiat, P. G. Hyper-entangled states. *J. Mod. Opt.* **44**, 2173–2184 (1997).
- [186] Strang, G. *Introduction to Linear Algebra* (Wellesley-Cambridge Press, Wellesley, MA, 2009), fourth edn.
- [187] Efron, B. & Tibshirani, R. Bootstrap methods for standard errors, confidence intervals, and other measures of statistical accuracy. *Statistical Science* **1**, 54–75 (1986). URL <http://www.jstor.org/stable/2245500>.
- [188] Ögren, M. & Kheruntsyan, K. V. Atom-atom correlations in colliding bose-einstein condensates. *Phys. Rev. A* **79**, 021606 (2009). URL <https://link.aps.org/doi/10.1103/PhysRevA.79.021606>.
- [189] Kozuma, M. *et al.* Coherent splitting of bose-einstein condensed atoms with optically induced bragg diffraction. *Phys. Rev. Lett.* **82**, 871–875 (1999). URL <https://link.aps.org/doi/10.1103/PhysRevLett.82.871>.
- [190] Vandersypen, L. M. K. & Chuang, I. L. Nmr techniques for quantum control and computation. *Rev. Mod. Phys.* **76**, 1037–1069 (2005). URL <https://link.aps.org/doi/10.1103/RevModPhys.76.1037>.
- [191] Mardia, K. V. & Jupp, P. E. (eds.) *Directional Statistics* (John Wiley & Sons, Inc., 1999).
- [192] Kielpinski, D. *et al.* A decoherence-free quantum memory using trapped ions. *Science* **291**, 1013–1015 (2001).
- [193] Kotler, S., Akerman, N., Navon, N., Glickman, Y. & Ozeri, R. Measurement of the magnetic interaction between two bound electrons of two separate ions. *Nature* **510**, 376–380 (2014).
- [194] Ruster, T. *et al.* Entanglement-based dc magnetometry with separated ions. *Phys. Rev. X* **7**, 031050 (2017).
- [195] Giovannetti, V., Lloyd, S. & Maccone, L. Advances in quantum metrology. *Nat. Photonics* **5**, 222–229 (2011).

-
- [196] Wiseman, H. M. & Milburn, G. J. *Quantum Measurement and Control* (Cambridge University Press, 2009).
 - [197] Braunstein, S. L. & Caves, C. M. Statistical distance and the geometry of quantum states. *Phys. Rev. Lett.* **72**, 3439–3443 (1994). URL <https://link.aps.org/doi/10.1103/PhysRevLett.72.3439>.
 - [198] Leibfried, D. *et al.* Toward heisenberg-limited spectroscopy with multiparticle entangled states. *Science* **304**, 1476–1478 (2004). URL <https://science.sciencemag.org/content/304/5676/1476>. <https://science.sciencemag.org/content/304/5676/1476.full.pdf>.
 - [199] Moreau, P.-A., Toninelli, E., Gregory, T. & Padgett, M. J. Imaging with quantum states of light. *Nature Reviews Physics* **1**, 367–380 (2019).
 - [200] Boto, A. N. *et al.* Quantum interferometric optical lithography: Exploiting entanglement to beat the diffraction limit. *Phys. Rev. Lett.* **85**, 2733–2736 (2000). URL <https://link.aps.org/doi/10.1103/PhysRevLett.85.2733>.
 - [201] Jones, J. A. *et al.* Magnetic field sensing beyond the standard quantum limit using 10-spin noon states. *Science* **324**, 1166–1168 (2009). URL <https://science.sciencemag.org/content/324/5931/1166>. <https://science.sciencemag.org/content/324/5931/1166.full.pdf>.
 - [202] The LIGO Scientific Collaboration. Enhanced sensitivity of the LIGO gravitational wave detector by using squeezed states of light. *Nat. Photonics* **7**, 613–619 (2013).
 - [203] Louchet-Chauvet, A. *et al.* Entanglement-assisted atomic clock beyond the projection noise limit. *New J. Phys.* **12**, 065032 (2010).
 - [204] Wasilewski, W. *et al.* Quantum noise limited and entanglement-assisted magnetometry. *Phys. Rev. Lett.* **104**, 133601 (2010). URL <https://link.aps.org/doi/10.1103/PhysRevLett.104.133601>.
 - [205] Ockeloen, C. F., Schmied, R., Riedel, M. F. & Treutlein, P. Quantum metrology with a scanning probe atom interferometer. *Phys. Rev. Lett.* **111**, 143001 (2013). URL <https://link.aps.org/doi/10.1103/PhysRevLett.111.143001>.
 - [206] Mason, D., Chen, J., Rossi, M., Tsaturyan, Y. & Schliesser, A. Continuous force and displacement measurement below the standard quantum limit. *Nat. Phys.* **15**, 745–749 (2019).
 - [207] Danilin, S. *et al.* Quantum-enhanced magnetometry by phase estimation algorithms with a single artificial atom. *npj Quantum Inf.* **4**, 29 (2018). URL <https://doi.org/10.1038/s41534-018-0078-y>.
 - [208] Steinert, S. *et al.* High sensitivity magnetic imaging using an array of spins in diamond. *Rev. Sci. Instrum.* **81**, 043705 (2010).

- [209] Li, B.-B. *et al.* Quantum enhanced optomechanical magnetometry. *Optica* **5**, 850–856 (2018). URL <http://www.osapublishing.org/optica/abstract.cfm?URI=optica-5-7-850>.
- [210] Muessel, W., Strobel, H., Linnemann, D., Hume, D. B. & Oberthaler, M. K. Scalable spin squeezing for quantum-enhanced magnetometry with bose-einstein condensates. *Phys. Rev. Lett.* **113**, 103004 (2014). URL <https://link.aps.org/doi/10.1103/PhysRevLett.113.103004>.
- [211] Meltzer, A. Y., Levin, E. & Zeldov, E. Direct reconstruction of two-dimensional currents in thin films from magnetic-field measurements. *Phys. Rev. Applied* **8**, 064030 (2017). URL <https://link.aps.org/doi/10.1103/PhysRevApplied.8.064030>.
- [212] Yang, F., Kollár, A. J., Taylor, S. F., Turner, R. W. & Lev, B. L. Scanning quantum cryogenic atom microscope. *Phys. Rev. Applied* **7**, 034026 (2017). URL <https://link.aps.org/doi/10.1103/PhysRevApplied.7.034026>.
- [213] Wildermuth, S. *et al.* Bose-einstein condensates: Microscopic magnetic-field imaging. *Nature* **435**, 440 (2005).
- [214] Roth, B. J., Sepulveda, N. G. & Wikswo, J. P. Using a magnetometer to image a two-dimensional current distribution. *J. Appl. Phys.* **65**, 361–372 (1989).
- [215] Roos, C. F. *et al.* Bell states of atoms with ultralong lifetimes and their tomographic state analysis. *Phys. Rev. Lett.* **92**, 220402 (2004). URL <https://link.aps.org/doi/10.1103/PhysRevLett.92.220402>.
- [216] Lücke, B. *et al.* Twin matter waves for interferometry beyond the classical limit. *Science* **334**, 773–776 (2011). URL <https://science.sciencemag.org/content/334/6057/773>. <https://science.sciencemag.org/content/334/6057/773.full.pdf>.
- [217] Budker, D. *et al.* Resonant nonlinear magneto-optical effects in atoms. *Rev. Mod. Phys.* **74**, 1153–1201 (2002). URL <https://link.aps.org/doi/10.1103/RevModPhys.74.1153>.
- [218] Ferrie, C., Granade, C. E. & Cory, D. G. How to best sample a periodic probability distribution, or on the accuracy of hamiltonian finding strategies. *Quantum Inf. Process.* **12**, 611–623 (2012).
- [219] Dehollain, J. P. *et al.* Bell’s inequality violation with spins in silicon. *Nat. Nanotechnol.* **11**, 242 EP – (2015). URL <https://doi.org/10.1038/nnano.2015.262>.
- [220] Matsukevich, D. N., Maunz, P., Moehring, D. L., Olmschenk, S. & Monroe, C. Bell inequality violation with two remote atomic qubits. *Phys. Rev. Lett.* **100** (2008).
- [221] Ballance, C. J. *et al.* Hybrid quantum logic and a test of bell’s inequality using two different atomic isotopes. *Nature* **528**, 384–386 (2015).

- [222] Marinković, I. *et al.* Optomechanical bell test. *Phys. Rev. Lett.* **121** (2018).
- [223] Barreiro, J. T., Wei, T.-C. & Kwiat, P. G. Beating the channel capacity limit for linear photonic superdense coding. *Nat. Phys.* **4**, 282–286 (2008).
- [224] Walborn, S. P., Pádua, S. & Monken, C. H. Hyperentanglement-assisted bell-state analysis. *Phys. Rev. A* **68** (2003).
- [225] Barreiro, J. T., Langford, N. K., Peters, N. A. & Kwiat, P. G. Generation of hyperentangled photon pairs. *Phys. Rev. Lett.* **95** (2005).
- [226] Rosi, G. *et al.* Quantum test of the equivalence principle for atoms in coherent superposition of internal energy states. *Nat. Commun.* **8** (2017).
- [227] Brion, E., Pedersen, L. H. & Mølmer, K. Adiabatic elimination in a lambda system. *J. Phys. A: Math. Theor.* **40**, 1033–1043 (2007).
- [228] Allen, L. & Eberly, J. *Optical Resonance and Two-level Atoms*. Dover books on physics and chemistry (Dover, 1987). URL <https://books.google.com.au/books?id=1q0ae-XNmWwC>.
- [229] Hofmann, H. F. & Takeuchi, S. Violation of local uncertainty relations as a signature of entanglement. *Phys. Rev. A* **68**, 032103 (2003). URL <https://link.aps.org/doi/10.1103/PhysRevA.68.032103>.
- [230] Bell, J. S. & Aspect, A. *Speakable and Unspeakable in Quantum Mechanics* (Cambridge University Press, 2004).
- [231] Fine, A. Hidden variables, joint probability, and the bell inequalities. *Phys. Rev. Lett.* **48**, 291–295 (1982). URL <https://link.aps.org/doi/10.1103/PhysRevLett.48.291>.